

**Suppression of Methane-Air Explosions with  
Water in the form of 'Fine' Mists**

Thesis submitted for the  
Degree of Doctor of Philosophy  
of the University of Wales Cardiff

by  
Andrew Philip Crayford  
(MEng)

April, 2004

UMI Number: U584646

All rights reserved

INFORMATION TO ALL USERS

The quality of this reproduction is dependent upon the quality of the copy submitted.

In the unlikely event that the author did not send a complete manuscript and there are missing pages, these will be noted. Also, if material had to be removed, a note will indicate the deletion.



UMI U584646

Published by ProQuest LLC 2013. Copyright in the Dissertation held by the Author.  
Microform Edition © ProQuest LLC.

All rights reserved. This work is protected against  
unauthorized copying under Title 17, United States Code.



ProQuest LLC  
789 East Eisenhower Parkway  
P.O. Box 1346  
Ann Arbor, MI 48106-1346

## **ABSTRACT**

This thesis is concerned with the combustion hazard posed when there are accidental releases of methane from plant, particularly within the petrochemical 'exploration and production' industry. At the present time, such explosion hazards are controlled using explosion suppression systems based around Halon 1301 deployment. However, due to its environmental impact, such methods are being reviewed with the objective being their replacement with environmentally friendly alternatives.

During the course of this study, the effect of water in the form of vapour and 'fine' mists has been investigated to determine its effectiveness in the containment and control of a potential methane explosion. Laminar flame/water interaction has been studied in considerable detail, and to a lesser extent the interaction with turbulent burning mechanisms has been studied through a demonstration study based on the conclusions of the laminar flame studies; the efficiency of water in various concentrations and states (vapour or liquid-droplets) has been appraised. The research studies have also necessitated fundamental studies of droplet formation via supersaturated vapours, within small-scale laboratory test facilities, and methods suitable for generating large-scale sprays deemed suitable for the replacement of Halon systems were then appraised and characterised so as safety systems of the future may be optimised.

The laminar test programme illustrated that water is a competitive explosion suppressant capable of extinguishing a fully propagating flame. It was found that water vapour and 'fine' water droplets are most effective in the mitigation of methane-air flames during early flame formation when curvature effects are a predominant factor, with 'fine' water droplets being more effective than vapour at this time. Turbulent experiments demonstrated that water in the form of 'fine' droplets can be used to fully arrest a propagating stoichiometric methane-air explosion, at concentrations probably less than the molar water concentration associated with inerting methane air explosions.

A system based on the 'flashing' concept was fully characterised to illustrate that sprays similar to those utilised in the laboratory combustion work can be produced in a full-scale release, leading to the conclusions that Halon based systems may in the near future be replaced by environmentally sound explosion suppression systems that utilise water.

## **ACKNOWLEDGEMENTS**

I would like to take this opportunity to express my deep gratitude to my supervisor Dr Philip Bowen for his continual guidance and support throughout this study.

Also special thanks to Dr Vincent Tam (BP) for his guidance, patience and financial support during the past three years.

I am also grateful to the technical staff of the Mechanical Engineering workshop, in particular Mr Paul Malpas, Mr Alan Griffiths and Mr Malcolm Seabourne for their assistance and devotion in the construction and maintenance of the experimental facilities.

Finally, I would like to express a deep gratitude to my family and friends particularly Rachel and housemates Mark, Anna and Wendy for their constant support throughout the duration of this study.

**DECLARATION**

This work has not previously been accepted in substance for any degree and is not being concurrently submitted in candidature for any degree.

Signed..... *A.P. Laxmi* .....(candidate)

Date..... *6<sup>th</sup> April 2004* .....

**STATEMENT 1**

This thesis is the result of my own investigations, except where otherwise stated.

Other sources are acknowledged by footnotes giving explicit references. A bibliography is appended.

Signed..... *A.P. Laxmi* .....(candidate)

Date..... *6<sup>th</sup> April 2004* .....

**STATEMENT 2**

I hereby give consent for my thesis, if accepted, to be available for photocopying and for inter-library loan, and for the title and summary to be made available to outside organisations.

Signed..... *A.P. Laxmi* .....(candidate)

Date..... *6<sup>th</sup> April 2004* .....

# Nomenclature

## Roman Characters

<i>Symbol</i>	<i>Unit</i>	<i>Definition</i>
<i>a</i>	1/s	strain rate
<i>A</i>	m <sup>2</sup>	area
<i>b</i>	mm	breadth
<i>B</i>	candela/cd	luminance
<i>c</i>	f	capacitance
<i>C<sub>p</sub></i>	j/kg /K	heat capacity
<i>C<sub>E</sub></i>	-	control efficiency
<i>d</i>	μm	droplet diameter
<i>Da</i>	$\frac{LS_L}{U\delta_L}$	Damkohler number
<i>D<sub>10</sub></i>	μm	mean droplet diameter
<i>D<sub>32</sub></i>	μm	Sauter mean droplet diameter
<i>e</i>	j	energy
<i>f</i>	mm	focal length
<i>h</i>	j/m <sup>2</sup> K	thermal conductivity (2.4)
<i>h</i>	mm	height (3.4)
<i>I</i>	cd/mm <sup>2</sup>	illumination
<i>k</i>	mm <sup>2</sup> /s	evaporation constant
<i>K</i>	-	constant of expansion
<i>Ka</i>	$\frac{KD_u}{S_L^2}$	Karlovitz stretch factor
<i>m</i>	-	magnification
<i>M</i>	kg	mass
<i>Mr</i>	g/cm <sup>3</sup>	molecular mass
<i>n</i>	-	number of moles
<i>n</i>	-	refractive index

<i>Symbol</i>	<i>Unit</i>	<i>Definition</i>
P	atm	pressure
P <sup>0</sup>	pa	partial pressure
P <sub>s</sub>	pa	suppressed pressure
P <sub>u</sub>	pa	highest recorded pressure
r <sub>b</sub>	mm	flame radius
r <sub>w</sub>	-	molar water fraction
R <sub>o</sub>	j/kgK	universal gas constant
R <sub>air</sub>	j/kg.K	gas constant air
Re	$\frac{\rho u D}{\mu}$	Reynolds number
S	-	sensitivity
S <sub>g</sub>	m/s	unburned gas velocity
S <sub>s</sub>	m/s	spatial flame speed
S <sub>u</sub>	m/s	burning velocity
t	s	time
T	K	temperature
u	m/s	velocity
V	m <sup>3</sup>	volume
V	v	voltage
We	$\frac{\rho u^2 d}{\sigma}$	Weber number

## Greek Characters

<i>Symbol</i>	<i>Unit</i>	<i>Definition</i>
$\delta\varepsilon$	$^\circ$	angle of deflection
$\Delta E$	j	energy transfer
$\Delta E_{\text{CON}}$	j	energy transfer by convection
$\Delta P$	mbar	pressure drop
$\Delta T$	$^\circ\text{C}$	temperature difference
$\Delta T_{\text{da}}$	$^\circ\text{C}$	temp. difference droplet-ambient
$\Delta T_{\text{EX}}$	$^\circ\text{C}$	temperature required for extinction
$\rho$	$\text{kg/m}^3$	density
$\lambda$	nm	wavelength of light
$\sigma$	N/m	liquid surface tension
$\sigma$	-	standard deviation
$\psi, \Phi$	$^\circ$	scatter angles
$\tau$	s	time constant
$\theta$	$^\circ$	intersection angle
$\emptyset$	-	equivalence ratio

## Superscripts

<i>Symbol</i>	<i>Unit</i>	<i>Definition</i>
$n$	-	polytropic coefficient

## Subscripts

<i>Symbol</i>	<i>Unit</i>	<i>Definition</i>
atm	-	ambient
<i>b</i>	-	boiling
b	-	burnt
enc	-	nominal enclosure
fuel	-	methane injected
rig	-	Cardiff Cloud chamber
sat	-	saturation
sch	-	Schlieren
SH	-	superheat
st	-	stagnation
stoich	-	stoichiometric
u	-	unburnt
w	-	water

## Abbreviations

<i>Symbol</i>	<i>Unit</i>	<i>Definition</i>
AFR	-	Air Fuel Ratio
BR	-	Blockage ratio
bsp	inches	British standard pipe
DAQ	-	Data acquisition
ECU	-	Electronic Control Unit
ER	-	Equivalence ratio
fps	1/s	frames per second
LDA	-	Laser Doppler Anemometry
PDA	-	Phase Doppler Anemometry
PLC	-	Programmable Logic Controller
SMD	µm	Sauter mean diameter
VR	-	Venting ratio

# Table of Contents

TABLE OF CONTENTS .....	IX
LIST OF FIGURES AND TABLES .....	XIII
<b>1. Introduction.....</b>	<b>1</b>
1.1 HISTORY OF EXPLOSION SUPPRESSION SYSTEMS .....	1
1.2 REPLACEMENT OF HALON SAFETY SYSTEMS .....	6
1.3 REQUIREMENTS OF NEW SAFETY SYSTEMS.....	8
1.4 PROPOSED METHOD FOR SAFETY SYSTEMS OF THE FUTURE .....	9
1.5 AIMS AND OBJECTIVES .....	10
1.6 STRUCTURE OF THESIS .....	11
<b>2. Review of Previous Relevant Research.....</b>	<b>13</b>
2.1 WATER AS AN EXPLOSION SUPPRESSION AGENT: REVIEW OF EXPERIMENTAL WORK.....	13
2.2 SUMMARY OF FINDINGS .....	48
<b>3. Facilities Required for Research.....</b>	<b>50</b>
3.1 DESCRIPTION OF MEASUREMENTS REQUIRED FOR STUDY .....	50
3.2 DROPLET MEASUREMENT.....	51
3.2.1 <i>Malvern Mastersizer <math>\chi^{\text{TM}}</math></i> .....	51
3.2.2 <i>'DANTEC' Phase Doppler Anemometry (PDA)</i> .....	55
3.2.3 <i>Direct Impact Method Using Magnesium Oxide Slides</i> .....	59
3.3 FLAME SPEED MEASUREMENT.....	61
3.3.1 <i>Schlieren Photography</i> .....	61
3.3.2 <i>Ionisation Probe Technology</i> .....	63
3.4 DATA ACQUISITION .....	64
3.4.1 <i>NAC-1000 Video Recorder</i> .....	64
3.4.2 <i>National Instruments DAQ System</i> .....	65
3.5 SUMMARY .....	66
<b>4. Generation and Characterisation of Well Defined Mists in the Cardiff Cloud Chamber.....</b>	<b>67</b>
4.1 CLOUD CHAMBER TECHNOLOGY .....	67
4.1.1 <i>Wilson Cloud Chamber</i> .....	67
4.1.2 <i>Original Cardiff Cloud Chamber</i> .....	69
4.2 CARDIFF CLOUD CHAMBER DEVELOPMENT.....	71
4.2.1 <i>Gas Mixing and Air Quality</i> .....	71

4.2.2	<i>Initial Temperature and Pressure Control</i> .....	72
4.2.3	<i>Piston Retraction</i> .....	73
4.3	EXPERIMENTAL DIAGNOSTICS .....	73
4.3.1	<i>Initial Thermodynamic Conditions</i> .....	73
4.3.2	<i>Expansion Ratio and rate</i> .....	73
4.3.3	<i>Quantification of Transient Temperature, Pressure and Piston Kinematics</i> .....	75
4.4	MIST GENERATION AND CHARACTERISATION .....	76
4.4.1	<i>Droplet cloud formation</i> .....	76
4.4.2	<i>Characterisation of Mist Formation</i> .....	78
4.5	EXPERIMENTAL PROGRAMME.....	79
4.6	RESULTS .....	80
4.6.1	<i>Dry Cases</i> .....	80
4.6.2	<i>Mist cases</i> .....	85
4.7	ANALYSIS AND DISCUSSION .....	86
4.8	SUMMARY .....	89
<b>5.</b>	<b>Benchmarking the Cardiff Cloud Chamber against other fully contained Explosion Facilities for use in the Investigation of Self- Propagating Laminar Explosions</b> .....	<b>91</b>
5.1	RIG MODIFICATIONS AND PROCEDURES .....	91
5.1.1	<i>Control of Fuel Equivalence Ratio</i> .....	91
5.1.2	<i>Ignition</i> .....	92
5.1.3	<i>Flame front Imaging</i> .....	93
5.1.4	<i>Calculation of Equivalence ratio</i> .....	96
5.1.5	<i>Development of Reliable Experimental Procedure</i> .....	97
5.2	CURRENT EXPERIMENTAL KNOWLEDGE FOR METHANE/AIR EXPLOSIONS .....	98
5.2.1	<i>Determination of Laminar Burning velocity</i> .....	98
5.2.2	<i>Current Experimental results</i> .....	101
5.3	EXPERIMENTAL PROGRAMME.....	104
5.3.1	<i>Determination of Flame speed</i> .....	105
5.3.2	<i>Derivation of Burning velocity</i> .....	109
5.4	RESULTS AND DISCUSSIONS .....	110
5.4.1	<i>Statistical Data of Flame growth and Flame speed of Methane-Air explosions initial temperature 50°C</i> .....	111
5.4.2	<i>Statistical Data of Flame growth and Flame speed of Methane-Air explosions initial temperature 100°C</i> .....	112
5.4.3	<i>Derived Flame Speed and Burning Velocity Data</i> .....	113
5.4.4	<i>Comparison of Cardiff Cloud Chamber Data with Published work</i> .....	115

5.5 FUTURE WORK.....	118
5.6 SUMMARY .....	121
<b>6. Laminar Burning Rate of Methane/Air/Water Systems .....</b>	<b>122</b>
6.1 CALCULATION OF WATER VAPOUR FRACTIONS .....	122
6.2 EXPERIMENTAL PROGRAMME.....	124
6.3 RESULTS AND DISCUSSIONS .....	125
6.3.1 Ignition Energies .....	125
6.3.2 Statistical Data of Flame growth and Flame speed of Methane-Air-Water Vapour explosions .....	129
6.3.3 Statistical Data of Flame growth and Flame speed of Methane-Air-Water Droplet explosions .....	135
6.4 DERIVED FLAME SPEED AND BURNING VELOCITY DATA.....	137
6.5 SUMMARY .....	141
<b>7. Demonstration of the Effectiveness of ‘Fine’ Water Mist in a Turbulent Environment.....</b>	<b>142</b>
7.1 TURBULENT TEST FACILITY .....	143
7.1.1 Obstacle filled Duct.....	143
7.1.2 Retractable Roof.....	145
7.1.3 Gas mixing and Analysis.....	145
7.1.4 Ignition system .....	147
7.1.5 Flame Speed Determination .....	147
7.1.6 Control Unit.....	148
7.2 BRIEF OVERVIEW OF TURBULENT FLAME PROPAGATION.....	151
7.3 RIG DEVELOPMENT .....	153
7.4 RESULTS AND DISCUSSIONS .....	157
7.4.1 Characterisation of Injectors .....	157
7.4.2 Suppression of Turbulent Flame .....	159
7.5 FUTURE WORK.....	166
7.6 SUMMARY .....	167
<b>8. Characterisation of Large Scale Releases of ‘Fine’ Mists.....</b>	<b>168</b>
8.1 CREATION OF LARGE SCALE RELEASES .....	168
8.1.1 ‘Micromist’ Flashing Jet Technology.....	168
8.1.2 Twin Fluid ‘Effervescent’ Atomisation.....	174
8.2 RESULTS OF DIFFERENT METHODS FOR CHARACTERISATION OF WATER MIST RELEASE .....	176
8.2.1 Visualisation.....	176

8.2.2 Rainout Data.....	179
8.2.3 Malvern Data-set for a Flashing Atomiser.....	183
8.2.4 PDA Data-set for a Twin Fluid Atomiser.....	187
8.2.5 PDA Data-set for a Flashing Atomiser.....	189
8.2.5.1 'Flashing' Jet results 180°C with 0.75mm Nozzle.....	190
8.2.5.2 'Flashing' Jet results 180°C with 1mm nozzle.....	193
8.2.6 Magnesium oxide data.....	196
<b>8.3 RESULTS OF DROPLET DISPERSION AND SETTLEMENT IN A CONFINED RELEASE .....</b>	<b>198</b>
8.3.1 Visualisation.....	198
8.3.2 Magnesium Oxide Data-set for a Flashing Jet.....	199
<b>8.4 DISCUSSIONS.....</b>	<b>201</b>
8.4.1 Appraisal of different techniques in the characterisation of the Micromist atomiser .....	201
8.4.2 Usefulness of Micromist atomiser as an explosion suppressant system.....	204
8.4.3 Future work.....	208
<b>8.5 SUMMARY.....</b>	<b>209</b>
<b>9. Conclusions and Suggestions for Further Work.....</b>	<b>210</b>
9.1 MAIN ACHIEVEMENTS OF WORK.....	210
9.2 FURTHER WORK.....	213
<b>REFERENCES .....</b>	<b>215</b>
<b>APPENDIX A: CALCULATION OF COMBUSTION MIXTURES FOR CARDIFF CLOUD CHAMBER.....</b>	<b>227</b>
<b>APPENDIX B: FLAME GROWTH METHANE-AIR FLAMES DRY .....</b>	<b>230</b>
<b>APPENDIX C: FLAME GROWTH METHANE-AIR-WATER FLAMES VAPOUR.....</b>	<b>234</b>
<b>APPENDIX D: FLAME GROWTH METHANE-AIR-WATER FLAMES DROPLETS.....</b>	<b>251</b>

# List of Figures and Tables

## 1. Introduction

Figure 1.1 <i>Typical management flow chart for managing the risk of large scale hazards</i> .....	1
Figure 1.2 <i>Schelkin Diagram</i> .....	3
Figure 1.3 (a&b) <i>Results of poor explosion safety systems in the cases of Flixborough and Piper Alpha disasters respectively</i> .....	5
Figure 1.4 <i>Graph depicting the decrease in ozone layer versus time</i> .....	7
Figure 1.5 <i>Offshore hydrocarbon releases and severity analysis</i> .....	8

## 2. Review of Previous Relevant Research

Figure 2.1 <i>Effects on methane-air burning velocities of nitrogen, carbon dioxide and water vapour additions</i> .....	14
Figure 2.2 (a&b) <i>Diagram of experimental apparatus for spray quenching and inerting respectively</i> .....	16
Figure 2.3 <i>Flame velocities versus volume fraction of water for the following droplet sizes and hydrogen concentrations: (1) 20<math>\mu</math>m, 29.5% H<sub>2</sub> by volume (stoichiometric); (2) 100<math>\mu</math>m, 20%; (3) 100<math>\mu</math>m, 15%; and (4) 40<math>\mu</math>m, 15%</i> .....	18
Figure 2.4 <i>Droplet break-up mechanisms</i> .....	20
Table 2.1 <i>Droplet evaporation time based on equation proposed by Sapko et al. [21]</i> .....	21
Figure 2.5 <i>Comparison of the fraction of mass stripped between a 200<math>\mu</math>m and 750<math>\mu</math>m droplet in oxy-hydrogen + 50% Ar</i> .....	22
Figure 2.6 <i>Comparison of overpressure/ time profiles recorded at the same transducer for equivalent tests with and without water deluge</i> .....	25
Figure 2.7 (a&b) <i>Pressure time profiles for slow flames and fast flames respectively</i> .....	29
Figure 2.8 <i>Nozzle capability compared with nozzle requirement for suppression</i> .....	30
Figure 2.9 <i>Effectiveness of water-spray systems as a function of the average size of water droplets they supply (schematic)</i> .....	34
Figure 2.10 <i>Design basis for explosion suppression</i> .....	35
Figure 2.11 <i>Comparison of extinction limits with plain water mist and various saline water mists</i> .....	36
Figure 2.12 <i>Comparison of extinction strain rate against droplet size for different droplet mass fractions in condensed phase at inflow</i> .....	37
Figure 2.13 <i>Number of droplets and total surface area produced by one litre of water, as a monodisperse spray with various mean droplet diameters</i> .....	38

Figure 2.14 Accuracy of mean droplet diameter as a function of sample size.....	39
Figure 2.13 (a&b) Photographs showing the catastrophic break-up of a 4mm droplet $\Delta T=1ms$ and the rapid fragmentation of a simulated water spray $\Delta T=1.3ms$ respectively.....	40
Figure 2.14 Droplet size distributions generated by air-blast atomisation for different incident flame speeds.....	44
Figure 2.15 Types of aerofoil passive systems utilised in study.....	44
Figure 2.16 Computed laminar burning velocities for a distributed energy loss calculated as a percentage of local chemical energy release rate (●) and increasing molar concentration of water vapour in the initial methane-air mixture (■).....	45
Figure 2.17 Variation in computed burning velocities in stoichiometric pre-mixed methane-air allowing for evaporation of 10, 20, 30, 50 and 100 $\mu m$ diameter water droplets.....	46
Table 2.2 Summary of mono-disperse spray characteristics at critical loading densities, just before failure of the flame solution for a range of initial droplet diameters at corresponding critical number densities for inhibition.....	46
Figure 2.18 Burning velocities as a function of initial water loading and droplet size. Inset figure provides an expanded view of the low-loading region.....	48
 <b>3. Facilities Required for Research</b>	
Table 3.1 Laser Analysis Measurement Range.....	51
Figure 3.1 Schematic Representation of the Malvern Mastersizer $\chi^{TM}$ .....	52
Table 3.2 Standard Range Lenses for Long Bed Mastersizer $\chi^{TM}$ .....	52
Figure 3.2 Schematic of how a Fourier transform occurs.....	53
Figure 3.3 Schematic representation of the effect of high obscuration on particle sizing.....	54
Figure 3.4 Schematic depicting angles of diffraction associated with different size particles that lead to vignetting problems.....	54
Figure 3.6 Control Volume Formed by intersection of two Coherent Laser Beams.....	55
Figure 3.7 Light scattering from a droplet whilst passing through PDA control volume.....	56
Figure 3.8 Light Scattering caused by a liquid droplet.....	57
Figure 3.9 Droplet Sizing by comparison to phase change.....	57
Figure 3.10 Illustration of PDA setup demonstrating scattering angles for detector placement.....	58
Figure 3.11 (a&b) Illustration of three detector PDA system and how it eliminates the $2\pi$ ambiguity.....	59
Figure 3.12 Schematic representation of method of magnesium oxide slides.....	60

Figure 3.13 Correlation derived from May [54] to convert measured to actual size of water droplets .....	60
Figure 3.14 Illustration of a typical Schlieren apparatus based around two concave mirrors ...	61
Figure 3.15 Typical ionisation probe circuit .....	63
Figure 3.16 User interface for the National Instruments data acquisition system.....	65

#### **4. Generation and Characterisation of Well Defined Mists in the Cardiff Cloud Chamber**

Figure 4.1 Schematic representation of the original Wilson cloud chamber .....	68
Figure 4.2 Schematic representation of the original Cardiff cloud chamber .....	70
Figure 4.3 Schematic representation of modified Cardiff cloud chamber .....	71
Table 4.1 Expansion ratio properties used for mist formation .....	73
Figure 4.4 Calibration curve of linear potentiometer .....	74
Figure 4.5 Schematic representation of compensated circuit used to speed up the thermocouple response .....	76
Figure 4.6 Volumes of water required for 100% saturation of the Cardiff Cloud Chamber at various Temperatures ( $v_1=910\text{cm}^3$ ) .....	77
Figure 4.7 Photograph of Cardiff cloud chamber in Malvern Mastersizer .....	78
Figure 4.8 (a&b) Typical histogram showing the number concentrations against droplet sizes within a mist generated by the Cardiff cloud chamber and Vignetting quantification results respectively .....	79
Figure 4.9 Transient recordings of temperature, pressure and piston position against time for a rapid expansion with initial temperature 30°C, expansion ratio 1.62.....	81
Table 4.2 Summary of experiments conducted with 0% humidity.....	81
Figure 4.10(a&b) Pressure versus volume plots for a rapid and slow expansion of the Cardiff cloud chamber, initial temperature 50°C and expansion ratio 1.62 .....	83
Figure 4.11(a&b) Temperature versus pressure plots for a rapid and slow expansion of the Cardiff cloud chamber, initial temperature 50°C and expansion ratio 1.62 .....	84
Figure 4.12 Transient recordings of temperature, pressure, piston position and droplet growth for a rapid expansion with initial temperature 30°C, expansion ratio 1.62 .....	85
Table 4.3 Summary of all results obtained for the wet cases .....	86
Figure 4.13 (a&b) Effect of expansion rate on the final droplet SMD, for expansion rates greater than 0.2 and complete ranges for initial temperature 50°C and expansion ratio 1.38 respectively .....	87

Figure 4.14 <i>Effect of expansion ratio on resultant droplet SMD for a variety of initial conditions</i>	88
---	----

## 5. Benchmarking the Cardiff Cloud Chamber Against Other Fully Contained Explosion Facilities for use in the Investigation of Self-Propagating Laminar Explosions

Figure 5.1 <i>Schematic representation of ignition system for combustion studies in the Cardiff cloud chamber</i>	93
Figure 5.2 <i>Photograph of Toepler Schlieren setup around Cardiff cloud chamber</i>	94
Figure 5.3 (a&b) <i>Diagram and photograph of the pinhole principle for cutting out of undisturbed light used to create a Schlieren image</i>	94
Figure 5.4 <i>Flow chart depicting full Schlieren system</i>	95
Figure 5.5 (a&b) <i>Examples of images of propagating flame front produced by Ciné camera (400fps) and Schlieren technique (1000fps)</i>	96
Figure 5.6 <i>Schematic representation of different methods used to determine burning velocity of methane-air flames</i>	99
Figure 5.7 <i>Effect of equivalence ratio on the laminar burning velocity of methane-air mixtures, P=1 bar, T=288.15-298.15k [19]</i>	102
Figure 5.8 <i>Burning velocity variation with pressure, for <math>\phi = 1</math> [77]</i>	103
Figure 5.9 <i>Effect of initial temperature on burning velocity of stoichiometric methane-air mixture; numerical, experimental: points. [89]</i>	103
Figure 5.10 <i>Schlieren photographs showing positions of flame centre and Schlieren flame front radius at times 1, 10 &amp; 16mS after Ignition</i>	105
Figure 5.11 <i>Example of Schlieren front versus time graph with five repeats</i>	106
Figure 5.12 <i>Example of Schlieren front radius versus time graph with error bars indicating 95% confidence</i>	107
Figure 5.13 <i>Graphical representation of flame speeds derived from 6th order polynomial fits of distance time graphs</i>	108
Figure 5.14 <i>Final representation of flame speed against time with error bars indicating 95% confidence</i>	108
Figure 5.15 <i>Comparison of expansion ratio used in this study</i>	110
Figure 5.16 (a&b) <i>Processed data for flame growth and flame speed respectively. Equivalence ratio 0.8, Ignition energy 1.76mJ</i>	111
Figure 5.17 (a&b) <i>Processed data for flame growth and flame speed respectively. Equivalence ratio 1.0, Ignition energy 1.76mJ</i>	111

Figure 5.18 (a&b) <i>Processed data for flame growth and flame speed respectively. Equivalence ratio 1.1, Ignition energy 1.76mJ</i> .....	111
Figure 5.19 (a&b) <i>Processed data for flame growth and flame speed respectively. Equivalence ratio 1.2, Ignition energy 5.1mJ</i> .....	111
Figure 5.20 (a&b) <i>Processed data for flame growth and flame speed respectively. Equivalence ratio 0.8, Ignition energy 1.76mJ</i> .....	112
Figure 5.21 (a&b) <i>Processed data for flame growth and flame speed respectively. Equivalence ratio 1.0, Ignition energy 1.76mJ</i> .....	112
Figure 5.22 (a&b) <i>Processed data for flame growth and flame speed respectively. Equivalence ratio 1.1, Ignition energy 1.76mJ</i> .....	112
Figure 5.23 (a&b) <i>Processed data for flame growth and flame speed respectively. Equivalence ratio 1.2, Ignition energy 1.76mJ</i> .....	112
Figure 5.24 <i>Derived expansion ratios for methane-air flames at various equivalence ratios at initial temperatures of 50°C and 100°C</i> .....	113
Figure 5.25 <i>Maximum measured flame speeds and derived burning velocity for methane-air flames within the Cardiff Cloud chamber with various equivalence ratios and initial temperatures</i> .....	114
Figure 5.26 <i>Appraisal of the accuracy of the proposed correlation for the effect of initial temperature and predicted results</i> .....	115
Figure 5.27 <i>Comparison of maximum derived burning velocity of Cardiff cloud chamber compared with other published data</i> .....	116
Figure 5.29 <i>Comparison of measured flame speeds at different flame radius in Leeds bomb and Cardiff cloud chamber for methane-air flame, <math>\Phi=1</math></i> .....	117
Figure 5.30 <i>Possible Schlieren setup capable of filming through front window of Cardiff cloud chamber</i> .....	119
Figure 5.31 <i>Flame growth within Cardiff cloud Chamber filmed using Photron digital camera (1000fps)</i> .....	120
<b>6. Laminar Burning Rate of Methane/Air/Water Systems</b>	
Figure 6.1 <i>Schematic diagram representing pre-mixing conditions of water, methane and air</i>	123
Table 6.1 <i>Schematic representation of experimental programme</i> .....	125
Figure 6.2 <i>Schlieren sequence depicting the 'quench' of a propagating flame</i> .....	126
Figure 6.3 (a&b) <i>Ignition energies used to initiate flame propagation for various combustion mixtures represented as voltage supplied (V) and theoretical spark energy (mJ) respectively</i> .....	128
Figure 6.4.1 (a&b) <i>Processed data for flame growth and flame speed respectively. Equivalence ratio 0.8, Ignition energy 3.5mJ, 5% Water Vapour, Initial temperature 50°C</i> .....	130

Figure 6.4.2 (a&b) Processed data for flame growth and flame speed respectively. Equivalence ratio 1.0, Ignition energy 2.5mJ, 5% Water Vapour Initial temperature 50°C.....	130
Figure 6.4.3 (a&b) Processed data for flame growth and flame speed respectively. Equivalence ratio 1.1, Ignition energy 3.5mJ, 5% Water Vapour Initial temperature 50°C.....	130
Figure 6.4.4 (a&b) Processed data for flame growth and flame speed respectively. Equivalence ratio 1.2, Ignition energy 15.9mJ, 5% Water Vapour Initial temperature 50°C.....	130
Figure 6.5.1 (a&b) Processed data for flame growth and flame speed respectively. Equivalence ratio 0.8, Ignition energy 3.5mJ, 5% Water Vapour Initial temperature 100°C.....	131
Figure 6.5.2 (a&b) Processed data for flame growth and flame speed respectively. Equivalence ratio 1.0, Ignition energy 2.5mJ, 5% Water Vapour Initial temperature 100°C.....	131
Figure 6.5.3 (a&b) Processed data for flame growth and flame speed respectively. Equivalence ratio 1.1, Ignition energy 3.5mJ, 5% Water Vapour Initial temperature 100°C.....	131
Figure 6.5.4 (a&b) Processed data for flame growth and flame speed respectively. Equivalence ratio 1.2, Ignition energy 13.8mJ, 5% Water Vapour Initial temperature 100°C.....	131
Figure 6.6.1 (a&b) Processed data for flame growth and flame speed respectively. Equivalence ratio 0.8, Ignition energy 10.2mJ, 10% Water Vapour Initial temperature 50°C.....	132
Figure 6.6.2 (a&b) Processed data for flame growth and flame speed respectively. Equivalence ratio 1.0, Ignition energy 5.7mJ, 10% Water Vapour Initial temperature 50°C.....	132
Figure 6.6.3 (a&b) Processed data for flame growth and flame speed respectively. Equivalence ratio 1.1, Ignition energy 10.2mJ, 10% Water Vapour Initial temperature 50°C.....	132
Figure 6.7.1 (a&b) Processed data for flame growth and flame speed respectively. Equivalence ratio 0.8, Ignition energy 10.2mJ, 10% Water Vapour Initial temperature 100°C.....	133
Figure 6.7.2 (a&b) Processed data for flame growth and flame speed respectively. Equivalence ratio 1.0, Ignition energy 5.7mJ, 10% Water Vapour Initial temperature 100°C.....	133
Figure 6.7.3(a&b) Processed data for flame growth and flame speed respectively. Equivalence ratio 1.1, Ignition energy 10.2mJ, 10% Water Vapour Initial temperature 100°C.....	133
Figure 6.7.4(a&b) Processed data for flame growth and flame speed respectively. Equivalence ratio 1.2, Ignition energy 300v, 10% Water Vapour Initial temperature 100°C.....	133
Figure 6.8.1(a&b) Processed data for flame growth and flame speed respectively. Equivalence ratio 0.8, Ignition energy 28.2mJ, 15% Water Vapour Initial temperature 100°C.....	134
Figure 6.8.2(a&b) Processed data for flame growth and flame speed respectively. Equivalence ratio 1.0, Ignition energy 15.9mJ, 15% Water Vapour Initial temperature 100°C.....	134
Figure 6.8.3(a&b) Processed data for flame growth and flame speed respectively. Equivalence ratio 1.1, Ignition energy 28.2mJ, 15% Water Vapour Initial temperature 100°C.....	134
Figure 6.8.4(a) Processed data for flame growth and flame speed respectively. Equivalence ratio 1.2, Ignition energy 86.4mJ, 15% Water Vapour Initial temperature 100°C.....	134
Figure 6.9.1(a&b) Processed data for flame growth and flame speed respectively. Equivalence ratio 1.0, Ignition energy 13.8mJ, 5% Water Droplets (10µm) Initial temperature 34°C..	135

Figure 6.9.2(a&b) Processed data for flame growth and flame speed respectively. Equivalence ratio 1.0, Ignition energy 13.8mJ, 5% Water Droplets (20 $\mu$ m) Initial temperature 34 $^{\circ}$ C..	135
Figure 6.10.1(a&b) Processed data for flame growth and flame speed respectively. Equivalence ratio 1.0, Ignition energy 55.3mJ, 10% Water Droplets (5 $\mu$ m) Initial temperature 48 $^{\circ}$ C..	136
Figure 6.10.2(a&b) Processed data for flame growth and flame speed respectively. Equivalence ratio 1.0, Ignition energy 55.3mJ, 10% Water Droplets (15 $\mu$ m) Initial temperature 48 $^{\circ}$ C	136
Figure 6.11 (a&b) Derived values of expansion ratio at initial temperatures of 50 $^{\circ}$ C and 100 $^{\circ}$ C respectively .....	137
Figure 6.12 Effect of water concentration, temperature and equivalence ratio on flame speed and burning velocity of methane-air flames .....	138
Figure 6.13 Effect of water vapour fraction on the burning velocity of different methane-air flames .....	139
Figure 6.14 Graph showing the effect of water in the form of vapour and 'fine' droplets on the mitigation of a stoichiometric methane-air flame corrected for initial temperature 50 $^{\circ}$ C and pressure 1013mbar.....	140
<b>7. Demonstration of the Effectiveness of 'Fine' Water Mists in a Turbulent Environment</b>	
Figure 7.1 Photographs of turbulent duct showing action of retractable roof and positioning of ignition system, obstacles, ionisation probes and roof vent .....	143
Figure 7.2 Gas mixing system of turbulent test rig.....	145
Figure 7.3 (a&b) Internal and external views of control unit of the turbulent duct rig.....	148
Figure 7.4 Pre-programmed automated flow diagram .....	150
Figure 7.5 Visual depiction of flame front showing crest and trough structure .....	151
Figure 7.5 Photograph sequence of flame passing over an obstacle array.....	152
Figure 7.6 Borghi phase diagram showing different regimes in premixed turbulent combustion [11].....	153
Figure 7.7 Schematic representation of rig and spray pattern used by Thomas [10] .....	154
Figure 7.8 Proposed water delivery system for turbulent duct rig.....	156
Figure 7.9 (a&b) Effect of injection duration and initial pressure on droplet size .....	157
Figure 7.10 Effect of drive pressure and injection duration on mass of water ejected .....	159
Figure 7.11 Film sequence of turbulent methane flame in conducted in the SHELL duct rig with no water (25fps) .....	160
Figure 7.12 Film sequence of turbulent methane flame in conducted in the SHELL duct rig with water mist barrier .....	162

Figure 7.13 (a&b) <i>Film sequences of turbulent methane flame in conducted in the SHELL duct rig with water mist barrier and without water barrier respectively</i> .....	164
Figure 7.14 <i>Film sequence showing total quench of a propagating turbulent flame</i> .....	165
<b>8. Characterisation of Large Releases of 'Fine' Mists</b>	
Figure 8.1 <i>Technical Drawing of Micromist system used for this report</i> .....	169
Figure 8.2 (a&b) <i>Thermodynamic boundary conditions in relation to saturated conditions required for (a) flashing liquid release and (b) two phase flashing</i> .....	170
Figure 8.3 <i>Dependence of spray characteristics on upstream flow conditions</i> .....	172
Figure 8.4 <i>Schematic of flashing and non-flashing regions in relation to droplet size</i> .....	173
Figure 8.5 <i>Flashing release from Micromist atomiser</i> .....	174
Figure 8.6 <i>Schematic diagram of twin phase atomiser used for PDA appraisal</i> .....	175
Figure 8.7 <i>Illustration of camera setup to enable visualisation of shape of flashing jet</i> .....	177
Figure 8.8 <i>Graphic showing effects of both stagnation temperature and orifice diameter on flashing jet</i> .....	178
Figure 8.9 <i>Photograph of rainout experiment conducted with Micromist atomiser</i> .....	180
Figure 8.10 <i>Rainout against stagnation temperature for Micromist atomiser orifice diameter 4mm</i> .....	181
Figure 8.11 <i>Rainout fraction compared with discharge orifice for Micromist atomiser at stagnation temperature of 160°C</i> .....	182
Figure 8.12 <i>Representation of data produced from Malvern Mastersizer<math>\chi^{\text{TM}}</math> for Micromist atomiser</i> .....	184
Table 8.1 <i>Volume Analysis for Micromist atomiser using Malvern Mastersizer<math>\chi^{\text{TM}}</math></i> .....	184
Figure 8.13 (a&b) <i>ENEL Malvern mastersizer<math>\chi^{\text{TM}}</math> large scale spray rig (a) and close up of the spray zone (b)</i> .....	185
Figure 8.14 <i>Malvern Mastersizer results obtained for Micromist atomiser</i> .....	186
Figures 8.15 (a&b) <i>Fixed PDA System Utilised for the Appraisal of Characterisation of Large-scale Water Spray work with Fire Branch and Twin Fluid Atomiser Respectively</i> .....	187
Figure 8.16 (a&b) <i>PDA Droplet velocity distributions for a fire hose demonstrating the need for large data sets</i> .....	188
Figure 8.17 (a&b) <i>PDA Droplet size distribution for a twin fluid 'effervescent' jet demonstrating the need for the correct optical arrangement</i> .....	188
Figure 8.18 <i>PDA setup around the Micromist atomiser</i> .....	189
Figure 8.19 <i>PDA control volume passing through a full scale 'flashing' release</i> .....	190

Figure 8.20 Processed Results for $D_{10}$ values 180°C with 0.75mm nozzle .....	191
Figure 8.21 Processed Results for $D_{32}$ 180°C with 0.75mm nozzle .....	192
Figure 8.22 Processed validation rates for 180°C with 0.75mm nozzle .....	193
Figure 8.23 Processed results $D_{10}$ 180°C with 1mm nozzle .....	194
Figure 8.24 Processed results for $D_{32}$ 180°C with 1mm nozzle .....	195
Figure 8.25 Processed validation rates 180oC with 1mm nozzle.....	196
Figure 8.26 View of craters left by water droplets on a Magnesium Oxide slide .....	197
Figure 8.27 Droplet distribution from Micromist atomiser as determined.....	197
Figure 8.28 Video sequence of enclosed release .....	199
Figure 8.29 Droplet diameter versus time for confined release at different internal positions .	200
Figure 8.30 High speed close up of 'flashing' jet illustrating large droplets that may sway $D_{32}$ values .....	203
Figure 8.31 (a&b) PDA data for spray using standard PDA and dual PDA respectively .....	204
Figure 8.32 Photograph showing the maximum extent of flame through water mist barrier generated by Micromist atomisers .....	206
Figure 8.33 Image of droplets using particle interferometry sizing technique .....	209

## 1.1 History of Explosion Suppression Systems

Safety systems have been implemented progressively since the start of the industrial revolution. Health and Safety guidelines have been imposed on working practices here within the UK in order to make all environments, but particularly potentially hazardous workplaces, safer. Historically, these guidelines were largely based on lessons learned from previous accidents, though more recently, and particularly after the introduction of nuclear power generation in the latter half of the 20<sup>th</sup> century, risk and hazard analysis has become more commonplace. For example, Figure 1.1 shows a typical management flowchart for managing the risk associated with large scale hazards [1].

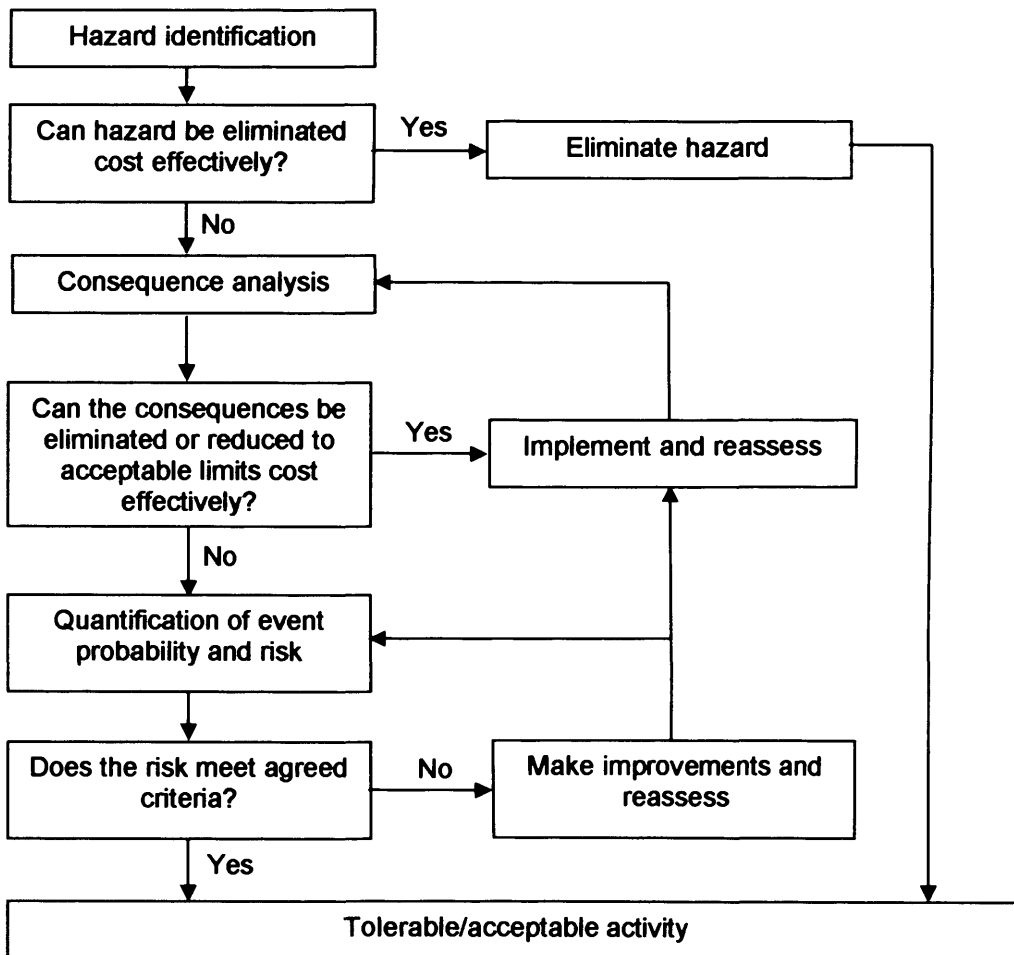
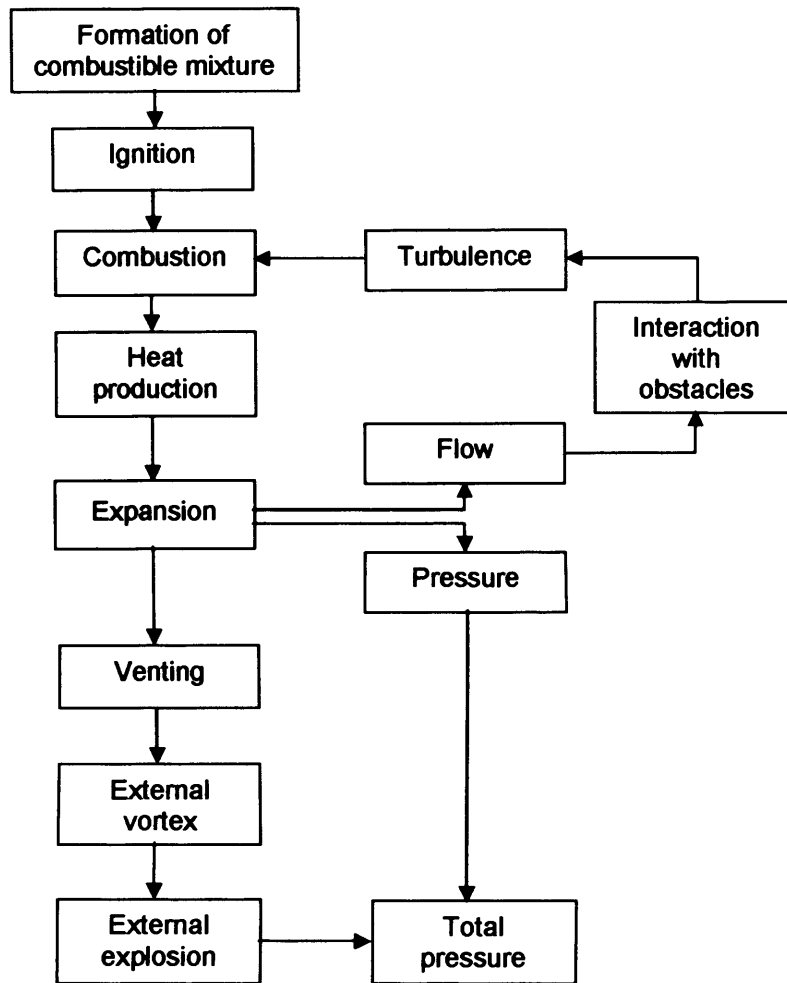


Figure 1.1 Typical management flow chart for managing the risk of large scale hazards

Note the emphasis on mitigating or eliminating hazards at each stage of assessment. International companies such as British Petroleum are even now taking a lead in integrating safety and 'green' environmental issues within their company policies, emphasising the complex nature of assessing risk in its broadest context i.e. aspects of safety, environment and public perception/image. These general issues are true for the specific application of designing and implementing explosion and suppression/mitigation systems, and this is the general context of this thesis.

In order to appreciate what constitutes an explosion suppression system, it is first necessary to define the characteristics of an explosion. An explosion is an event in which a combustible mixture is given enough energy in order that further reactants can be formed into combustion products whilst undergoing a violent reaction releasing sufficient amounts of heat to generate pressure. The 'thin' region – often approximated to an infinitely thin surface for modelling purposes - where the conversion of reactants into products takes place is defined as the propagating flame front. On release of this energy the combustion products rapidly expand and in so doing can create a pressure wave, depending upon various parameters such as the characteristics of the release environment, the fuel and its initial fluid mechanic state. The characteristics of the pressure wave determine the primary hazard effect associated with explosions, namely damage and injury. Contemporary explosion research attempts to predict the characteristics of the pressure wave from a given release scenario (Figure 1.2 – Schelkin diagram [2]), which can then be used in risk analysis models.



**Figure 1.2 Schelkin Diagram**

There are two types of explosion namely detonations and deflagrations and both are capable of devastating consequences. The criterion that discriminates one from the other is the flame position in respect to the aforementioned pressure wave. Detonations are often regarded as the more hazardous category, though this in fact depends upon the context, and sees the flame front coupled to the shock wave which can generate supersonic flame speeds, often in excess of 2000-3000m/s. Deflagrations on the other hand occur when the flame front travels behind the pressure wave, thus exhibiting slower flame speeds typically between 0.1-200m/s.

Historically explosion hazards have been found in many industrial work places especially in such industries as mining, chemical, oil & gas exploration and production (E&P), steel manufacture and aeronautical to name just a few. Throughout time these industries have endeavoured to make the work place a safer place usually with help from

their governing bodies. The primary application of work in this thesis lies within the oil & gas E&P sector.

Early methods of avoiding loss of life due to explosion hazards were seen as far back as the 1700's, when 'hit or miss' technology was used in coal mines to detect either low levels of oxygen or increasing levels of explosive gases such as methane. Primitive methods then included such things as carrying small birds such as Canaries, which literally fell off their perch if gas levels were not favourable. Early miners also carried naked flames down the mines with them as a source of light, however, they also used the size and colour of the flame to determine differing levels of oxygen and methane, unfortunately often these flames on warning of the hazard would ignite them.

Technologies have evolved and advanced over time, so now early detection in rising levels of an explosive source can be used to activate a safety system designed to either prevent the explosion or lessen the effect if an explosion should occur.

In modern coal mining explosions are rare, yet many safety systems are involved to ensure workers safety. These systems although simple are very effective and simply rely on either ensuring there are no explosive compounds (methane or coal dust) in the atmosphere by ensuring good ventilation to remove methane and the application of plenty of rock dust to control the coal dust. However, these primitive methods cannot be relied on solely to safeguard the life of personnel so more complicated gas detection units are used to cut all power to machinery thus eliminating ignition sources in the event of methane being detected. It is accepted that even with the most stringent preventative measures explosions in mines may still occur and this is why safety systems such as active and passive barriers are constructed to stop propagating explosions reaching the working areas of the mines. This particular example can be related the management flowchart (Figure 1.1) by the box 'eliminate the hazard' in the case of removing the explosive mixtures and 'can the consequences be eliminated or reduced' in the case of the positioning of active and passive barriers thus making the activity tolerable.

Other industries have learned that even with safety systems in place an unthinkable chain of reactions can still lead to a disaster. Such events have happened in the case of

the Flixborough (Nypro UK) Explosion 1974 (Figure 1.3a). This disaster resulted in the deaths of some 28 workers with a further 36 sustaining injury [3]. An immediate Health and Safety Executive (HSE) investigation led to changes in codes concerning the design and testing of pipe-work, control rooms, plant layout, operating procedures and the use of 'inerting' safety systems to try and ensure that such an event didn't happen again.

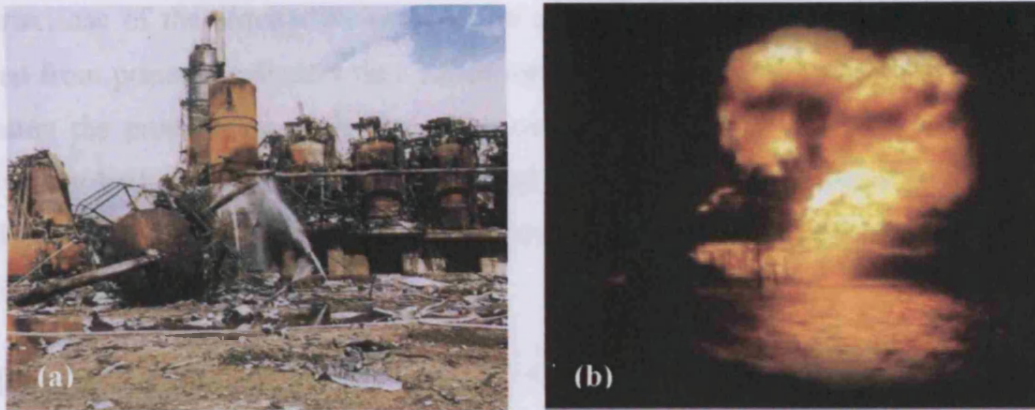


**Figure 1.3 (a&b) Results of poor explosion safety systems in the cases of Flixborough and Piper Alpha disasters respectively**

The Piper Alpha disaster 1988 (Figure 1.3b) which took the lives of 167 lives once again demonstrated the need for continual improvement in explosion safety systems [4]. The Cullen report published after the enquiry blamed inadequate safety management by the operators Occidental. The recommendations of the report led to a thorough review in the way offshore safety is governed with control being taken from the Department of Energy (DEn) and given to a newly formed body of the HSE which was more capable of managing offshore safety.

Within certain areas of industry it is not possible to eliminate the risk by introducing good safety management thus systems have needed to be designed that are capable of rendering an explosive mixture non-flammable or mitigating a fully propagating explosion. The most common form of such a system is based around the rapid flooding of the problem airspace with a fully inerting gas. Many gases can be used for such applications ranging from nitrogen to a range of industrially prepared halons. The word halon is derived from the two components of their production **Halogenated Hydrocarbon**. As a group they are very capable of rendering an airspace inflammable, the most commonly used is Halon 1301 ( $\text{CF}_3\text{Br}$ ), this chemical is capable of rendering an airspace inert with its volume fraction being as small as 3% [5]. For the above reason

it has been used extensively in the aeronautical and naval industries owing to the fact that small volumes of the chemical need to be stored to protect large volumes of space which is critical in such applications as fighter aircraft and commercial jet engines.

Halon-based systems are ideal for their use in the protection of plant or workspaces from fire or explosions especially in the vicinity of electrical equipment. They rely on the detection of rising levels of flammable gas or on detection of a fire/explosion, followed by the release of the required volume of the inerting gas, which can be very rapidly released from pressure cylinders thus either rendering the airspace inactive or instantly mitigating the propagating explosion. Also owing to their high stability, high liquid density, low boiling point, low electrical conductivity, low toxicity and corrosiveness, they do not damage any of the components they are there to protect [6]. However such effective systems come at a price.

## **1.2 Replacement of Halon Safety Systems**

Due to the Montreal protocol of 1987, the use of halon is now strictly governed. The reason for these strict regulations of their use as a fire or explosion suppressant is due to their long-term detrimental effect on the ozone layer.

The ozone layer is a thin layer of gas that occupies the space approximately 20-40km above the earth's surface. The reason this layer needs to be protected is because it blocks out a large fraction of the harmful Ultra Violet B radiation (UVB). Without this protection humans would see an increase in eye disorders and skin cancers with other detrimental effects such as immune system damage. Other species of animals, plant life and marine life would also suffer harmful effects [6].

The major problem is that Halon 1301 is stable enough at low altitudes to be transported by natural means up into the planet's stratosphere; at this level high levels of solar radiation are capable of breaking the vulnerable Carbon Bromine bond releasing bromine atoms into the surrounding gases. The released bromine atom can then react with ozone ( $O_3$ ) thus resulting in the depletion of the ozone layer as shown in equation (1.1), but also it acts as a catalyst further instigating the destruction of ozone as demonstrated by equation (1.2) [7&8].



In 1994 EC Council Regulation 3093/94 imposed a complete ban in the production of Halon 1301 and this was brought into force in the developed world as a means to limit the depletion of the ozone layer as shown in Figure 1.4 [9].

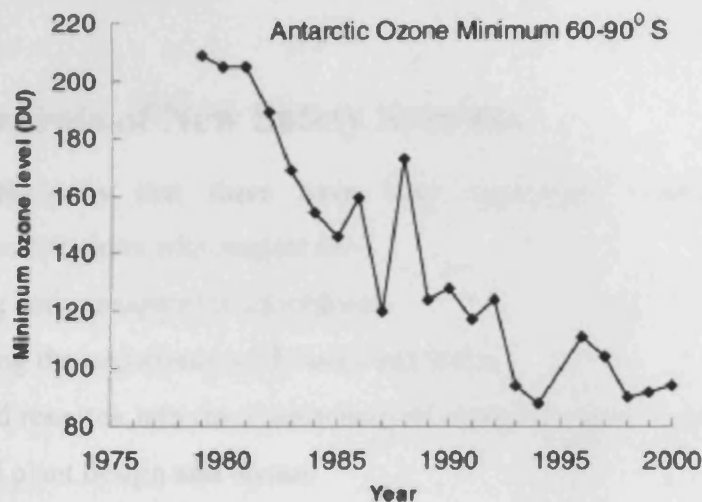


Figure 1.4 Graph depicting the decrease in ozone layer versus time

The Kyoto protocol (1997) then dictated that the sales and use of recycled Halon 1301 were only permitted until 1st January 2003, with all non-critical fire and explosion systems to be decommissioned by 31st December 2003. However a number of uses for Halon 1301's use as listed below [6] were deemed essential:

- In Aircraft for the protection of crew compartments, engine nacelles, cargo bays and dry bays
- In military vehicles and naval vessels for the protection of spaces occupied by personnel and engine compartments
- For inerting occupied spaces where flammable liquid and/or gas release could occur in the military and oil, gas and petrochemical sector, and in existing cargo ships.

- For inerting manned communication and command centres of the armed forces or otherwise essential for national security.
- For inerting spaces where there may be the risk of dispersion of radioactive matter
- In the channel tunnel, associated installations and rolling stock.

Hence, the use of Halon 1301 may currently be considered essential in critical applications, but as newer more environmentally friendly safety systems are developed it is hoped that there could come a time when the need for Halon 1301 is totally eliminated.

### 1.3 Requirements of New Safety Systems

Thomas [10] discusses that there have been significant improvements in the management of installations with respect to:-

- Operating and management procedures;
- Minimising the occurrence of failures and leaks;
- Continued research into the mechanisms of explosion development;
- Improved plant design and layout.

However, even with these improvements there are endless possibilities in which problems can arise leading to the accidental formation of a flammable cloud. This fact is illustrated by Figure 1.5 [11].

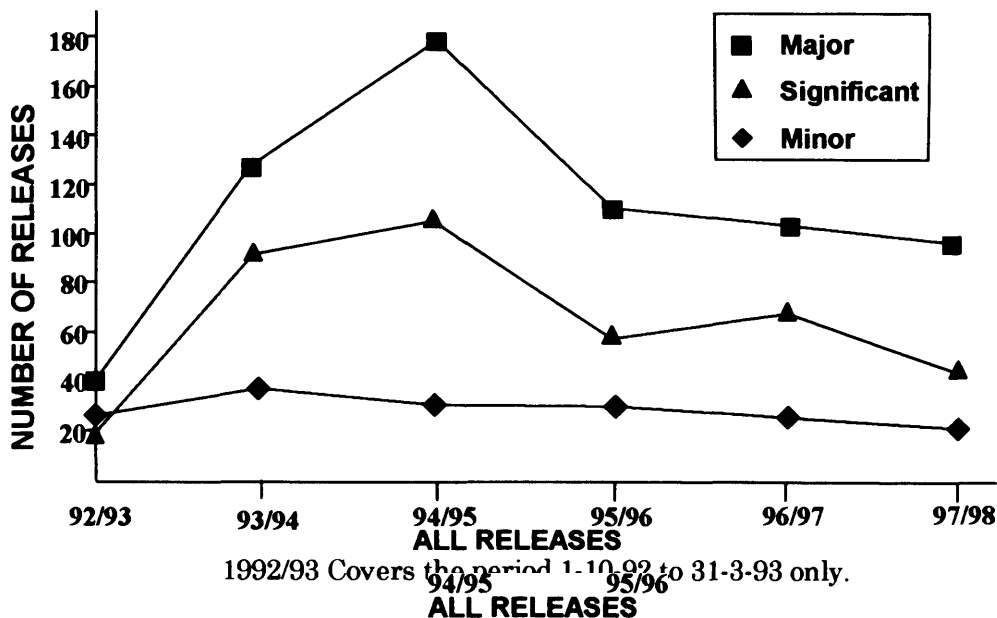


Figure 1.5 Offshore hydrocarbon releases and severity analysis

It can be seen even after a much needed 'shake-up' in safety procedures brought about by the Piper Alpha incident there were still 1271 reported incidents during 1992-1998 of which 670 were classed as major, these incidents could have led to another fatal disaster.

Owing to the fact that potential releases cannot be totally eradicated by improved management and maintenance, safety systems are still required to safeguard personnel in the event of an accidental release. At present there is no exact government legislation regarding the protection of all plant run by major companies. For this reason each company is required to develop its own codes of conduct with regard to explosion suppression systems. Due to the fact that this study is being sponsored by British Petroleum (BP) it is their objectives that will be discussed.

At present a large proportion of explosion safety systems utilised by BP are halon-based. However, owing to their 'green' policies it is considered that all halon systems should be removed as soon as a suitable replacement is found. It is stipulated in their objectives [12] that the new systems must be capable of 'inerting' a combustible environment for a minimum of 10 minutes, which is the perceived time necessary for the complete shut down of plant which could supply the ignition source and the removal of all personnel from the potential hazard. The new safety systems should also be non-hazardous to personnel and should be at least as effective as the systems they are replacing in the retardation of a propagating explosion.

## **1.4 Proposed method for Safety Systems of the Future**

It has been proposed that new explosion safety systems be developed that employ water which is readily available and environmentally friendly. However, this apparently 'simple' replacement solution is considerably more complicated than it may at first seem. Considerable work was undertaken in the 1990s; post Piper-Alpha, to better understand the interaction of water within an explosive environment. British Gas research conducted by Acton et al. [13] showed that standard sprinkler systems such as those already in use offshore for deluge systems could in fact increase the initial burning rates of an explosion. It has since been found that this is due to the increased turbulence induced ahead of the propagating flame front when coarse sprays are introduced. Bowen et al. [14] working for Shell Research, in collaboration with Kidde-Graviner Ltd.,

showed in large-scale demonstration studies (550m<sup>3</sup>) that even relatively high-pressure water releases (circa 60bar) are not sufficient to retard explosions within semi-confined/moderately congested environments. The conclusion from these and other petrochemical research programmes in the 1990s was that high-technology atomisation processes would have to be employed to mitigate/quench explosions at source, in situations when the secondary droplet break-up mechanism would not be invoked – see later. In this context, systems based on the principles of ‘flashing’ or ‘superheated’ technology, which show promise in terms of generating mists with characteristics considered appropriate for mitigation, have already been acquired by BP, and it is proposed that these systems are developed so that they are capable of replacing the existing halon-based systems.

A number of factors need to be appreciated in order that the new systems may be incorporated as smoothly as possible. The new systems should be delivered using pipe work currently installed for the halon systems, as this means drastic changes to plant are not necessary which would reduce the installation costs. However, the most important factor for the successful introduction of new systems is the confidence of current personnel in the new systems, given that halon systems have on a number of occasions performed effectively saving the lives of current employees. For this reason the new systems must be rigorously designed and tested to a level proving them to be at least as effective as the current systems.

## **1.5 Aims and Objectives**

The aim of this thesis is to develop scientific knowledge into the effect of water in the form of vapour/fine mists, for use in explosion suppression units capable of replacing existing Halon 1301 systems.

In order that the above aim can be achieved, a number of objectives must be fulfilled:-

- Thoroughly review previous work to determine what type of system is most likely to achieve the thesis aim.

- Determine whether the Cardiff cloud chamber is appropriate for the research study of water as an explosion suppressant, and if so, develop the facility accordingly.
- Quantify the influence of water in the form of both vapours and ‘fine’ mists in suppressing laminar propagating methane flames presenting data in a form which facilitates comparison with thermo-fluid/chemical-kinetic models.
- Demonstrate the conclusions of the laminar water-mist study in a fully turbulent flame field
- Appraise whether current superheated-water atomisation technology is capable of producing water mists capable of satisfying the requirements of an inerting/suppression system

## **1.6 Structure of Thesis**

The work necessary for the completion of this thesis is discussed in a number of different chapters. Chapter 1 takes the form of a general introduction to the thesis outlining the need for this research to be undertaken. Chapter 2 is a comprehensive literature review of relevant previous research into water as an explosion suppression agent, and dictates the way in which research should be pursued throughout the remainder of the thesis.

The facilities required to carry out the entire experimental programme are detailed and discussed in Chapter 3 with the aim of providing an understanding into the use and problems associated with each method. Chapter 4 then details the methods and apparatus necessary for the generation of laboratory-scale water mists with attention given into the requirements needed to generate favourable environments for the study of water mists within the Cardiff cloud chamber. Benchmarking the Cardiff cloud chamber for use in the study of laminar methane flame propagation is discussed in Chapter 5, thus ensuring that all subsequent data produced is of scientific value and consistent with other test facilities. The Cardiff cloud chamber is once again utilised in Chapter 6, the effect of water as an explosion suppressant in both vapour and droplet forms is rigorously studied with particular attention being given to fundamental combustion in a small-scale well-defined explosion medium.

On the appraisal of conclusions determined by the laminar explosion work a demonstration is conducted in Chapter 7 to determine whether similar water mists to those used in the laminar regime may be used to 'quench' a flame in a fully turbulent regime. The characterisation of large-scale atomisers capable of delivering such water mists is conducted in Chapter 8, with the intention of determining whether such devices may be developed for the replacement of current Halon 1301 systems.

Finally all the preceding conclusions reached are discussed in Chapter 9 with data drawn from all previous chapters being used to determine whether suggested atomising techniques are applicable for use in explosion suppression units of the future.

This chapter takes the form of a literature review that will describe all relevant studies previously undertaken and draw any relevant conclusions that may be useful in the development of an explosion suppression system.

Water seems an obvious choice for the suppression of methane explosions, as it is not harmful to the environment, plentiful and inexpensive. For these reasons there have been numerous studies quantifying its effectiveness as a suppressant.

There have been many different ways in which the effectiveness of water has been studied. These techniques include small-scale laboratory studies, shock-tube studies, full-scale offshore studies and finally computer simulations. Owing to the fact that some studies bridge more than one of the above techniques, this review will be conducted in a chronological order then summarised in a discussion. As this study is to be of an experimental nature, only the most useful and latest computer simulations will be discussed.

## **2.1 Water as an Explosion Suppression Agent: Review of Experimental work**

Interest in water as a suppressant can be shown as far back as the 1950's. Gerstein et al [15] used a large-scale shock tube which had a diameter of 0.61m and length of 93m. This large diameter coupled with low pressures of 0.2-0.4atm meant that wall effects were minimised, and the long length ensured a stable detonation. Natural gas-air mixtures were used for the study, and swirl nozzles were used to produce a water spray 15m down the tube.

It was concluded that 'sufficient' volumes of water mitigated both flames and detonations, however, it is noted that 'some sort of disturbance evidently carried on

down the pipe.’ It was also noted that the spacing of the nozzles from one and other within the pipe was influential in their effectiveness, and a distance of 1.5m seemed to be most efficient.

Fells and Rutherford [16] used a stationary flame to determine the effects of many factors on the burning velocity of methane-air flames. Within their remit, they investigated the retardation effects of nitrogen, water vapour and carbon dioxide, and determined that carbon dioxide was most effective, whilst nitrogen the least effective at slowing the burning rate of methane – air flames as shown in Figure 2.1.

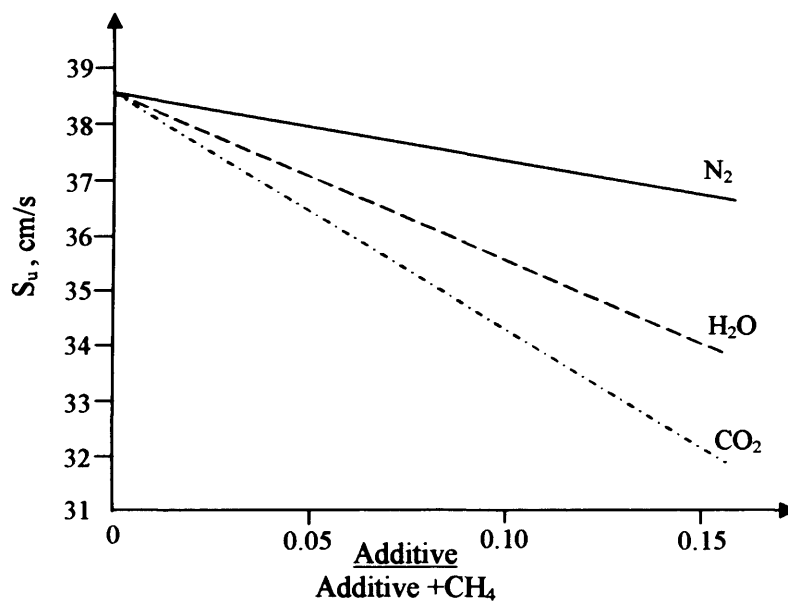


**Figure 2.1 Effects on methane-air burning velocities of nitrogen, carbon dioxide and water vapour additions**

As can be seen in the simplified graph above a value of reduction of  $0.31 \text{ cm s}^{-1} (\% \text{H}_2\text{O})^{-1}$  was observed when water vapour is added to a stationary flame and this effect is explained by dilution and heat abstraction.

Other shock-tube studies were conducted by Carlson et al. [17]. In this study a 12m long pipe of diameter 0.41m was used to study the effect of water sprays on hydrogen explosions. A back-to-back setup of sprinklers which run down the central axis of the shock-tube was utilised which supplied a water mist of a nominal  $D_{50} = 500 \mu\text{m}$ .

It is concluded that detonations were ‘rapidly attenuated’ by the water sprays. Lower values for both pressure and flame-speed, are observed. However, surprisingly the speed at which the peak pressure is reached is considerably increased when experiments

were conducted with the sprays on. This phenomenon is thought to be observed owing to the fact that there is an 'increase in the reaction manifest' brought about by the turbulence induced as a result of the spray action. A major conclusion of this work is that if a detonation ignition source was used instead of a normal initiation, then lower over-pressures were observed, and this effect is thought to be achieved owing to a shattering of the droplets at higher flow velocities.

During the 1970's there was particular interest in the controlling of self-propagating explosions in coal mine environments. Liebman et al. [18] used a 396m long shaft of cross sectional area  $5.3\text{m}^2$ . Coal dust and gas explosions were used to generate flame-speeds of  $>150\text{m/s}$ . Water was used in different systems which were either activated during the explosion, or remotely triggered. The passive barriers used consisted of basic troughs filled with water that were released/toppled by the sonic wind that travels in front of an explosion. It is stated that full quenching of the flame was witnessed for flame-speeds between 23 and  $137\text{m/s}$ . This was witnessed when the water was released in a time frame of 0.6secs just in front of the flame front.

Two types of triggered barriers were tested. These systems relied on being triggered remotely after an explosion had been detected electronically, mechanically or optically by a device prior to passing the barrier. It was found that a 'Cardox' dispenser which delivered 40kg of water in 20ms at high velocity in two directions was capable of suppressing a coal dust explosion travelling at  $150\text{m/s}$ . However, owing to the very rapid discharge rates this system was deemed dangerous to surrounding personnel. A safer nitrogen-pressurised system was also tested and was also found to be effective when releasing 27kg of water in 200ms in the path of a coal dust explosion.

Water sprays interacting with a flame front were filmed by Eggleston et al. [19]. This study used ethylene-air and vinyl chloride-air flames within a polythene tent of dimensions  $9\text{m}^2 \times 4.6\text{m}$ . The mixtures were ignited in the presence of water sprays and it was observed through high-speed photography that the flames turned non-luminous and the flame-speed increased when they interacted with the water sprays. It concludes that turbulent-enhanced burning is brought about by the water sprays, and this effect

meant that under no conditions were the water sprays successful in quenching the resultant explosion.

The effectiveness of water sprays compared to other suppressants such as 3 different halons and purple-k powder were examined by Richards and Sheehan. [20]. They used the forward pump room of the 150m long Rhode Island tanker, to conduct a series of tests using a propane-air mixtures. The studies used a UV detection system to release the different suppression systems and some major conclusions were drawn showing that suppressant systems were possible, but relied heavily on early detection and rapid releases of suppressant to fully saturate the entire airspace. It was shown that ideally full release of suppressants should be deployed in less than 150ms especially in the case of highly confined environments.

Sapko et al. [21] finally tried to actually quantify the effect of water on a propagating methane-air explosion. Two laboratory-scale facilities were constructed to investigate the effectiveness of water in quenching and inerting a propagating methane-air explosion as shown in Figures 2.2 (a&b).

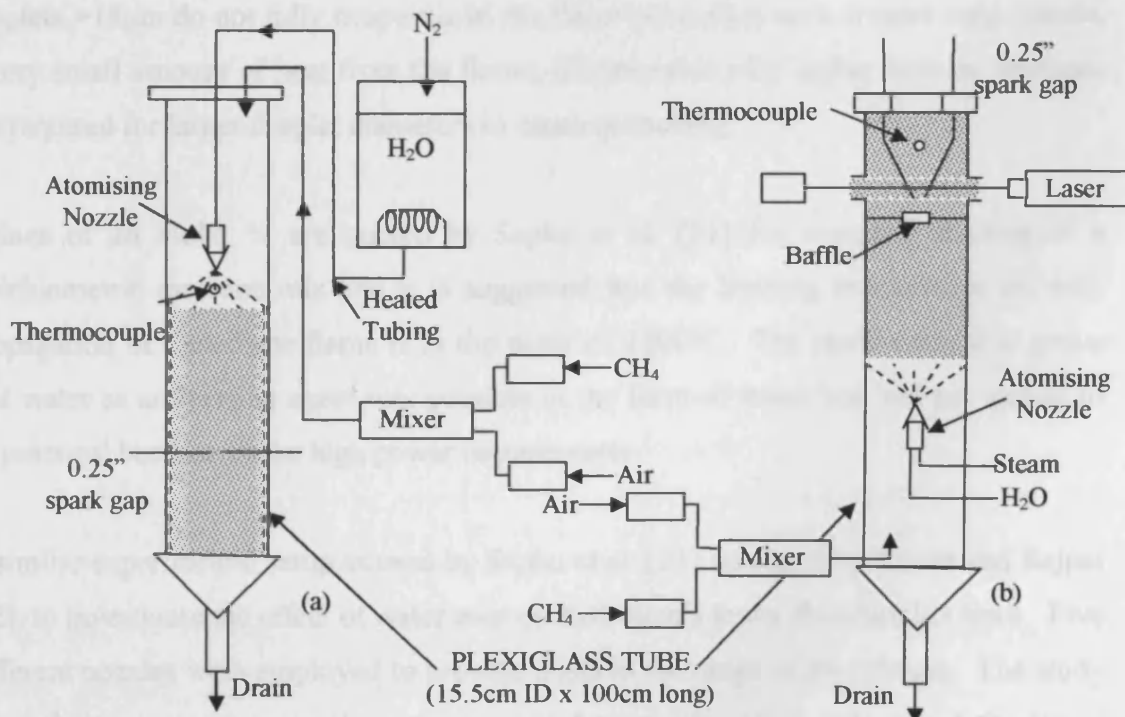


**Figure 2.2 (a&b) Diagram of experimental apparatus for spray quenching and inerting respectively**

As can be seen in Figure 2.2, this research attempted to investigate fully the effects of water as both a quenching and inerting agent. The apparatus used allowed investigation of parameters such as water vapour fraction, water droplet size, methane concentration and liquid temperature to be examined.

The results from these experiments show that the volumes of water required to inert an environment are much less than those required to quench a self-propagating flame. It also states that droplets of  $<10\mu\text{m}$  are as effective as vapour when being used as an inerting agent. The quenching experiments suggest that by reducing the droplet size and increasing the mixture temperature, the effectiveness of the water can greatly increase in order to affect the quench of a propagating flame. It is stated that by reducing the droplet diameter from  $106\mu\text{m}$  to  $56\mu\text{m}$  the droplet concentration required to bring about a full quench is reduced from  $68\text{mg}/\text{cm}^3$  to  $35\text{mg}/\text{cm}^3$ . This data can be used to predict that by using droplets of  $20\mu\text{m}$  as little as  $10\text{mg}/\text{cm}^3$  may be required. It is also shown that methane mixtures lower than that of stoichiometry are easier to quench.

Mathematical modelling of the droplets evaporation by Sapko et al. [21] shows that droplets  $>18\mu\text{m}$  do not fully evaporate in the flame zone, thus each droplet only absorbs a very small amount of heat from the flame, this explains why higher volume fractions are required for larger droplet diameters to cause quenching.

Values of 26 molar % are quoted by Sapko et al. [21] for complete inerting of a stoichiometric methane mix and it is suggested that the limiting temperature for self-propagation of a methane flame is in the order of  $1200^\circ\text{C}$ . The study seemed to prove that water as an inerting agent was possible in the form of steam but 'did not appear to be practical because of the high power requirements.'

A similar experimental setup as used by Sapko et al. [21] was used by Zalosh and Bajpai [22], to investigate the effect of water mist on hydrogen's lower flammability limit. Five different nozzles were employed to provide mists in the range of  $20\text{-}1156\mu\text{m}$ . The study showed that at room temperature even very dense water mists only raised the lower flammability of hydrogen very slightly. The effect of raising the mixtures temperature however, did increase the lower flammability noticeably. It is thought that this increase was brought about by an increase in the vapour concentration along with a decrease in

the size of the average droplet, which made the mists effectiveness in acting as a heat sink much greater.

A 1-D computer model, concerning the interaction of water droplets with a hydrogen flame was studied by Lutz et al. [23]. The model was intended to provide knowledge of water droplets as a flame retardant. Transport equations for mass, thermal energy and volume, were calculated with varying ranges of droplet sizes and a variety of hydrogen-air mixes of less than or equal to stoichiometry. Droplet sizes of 20, 100 and 400 $\mu\text{m}$  were used as volumes and surface areas could then be independently varied within the water fog. Aerodynamic effects acting on droplets were neglected and only evaporation taken into account, which causes the effect of turbulence to be ignored.

Approximate droplet loadings at particular droplet sizes suggested the propagation limits for hydrogen, thus the requirements necessary for the quenching of a hydrogen flame can be represented as depicted by Figure 2.3.

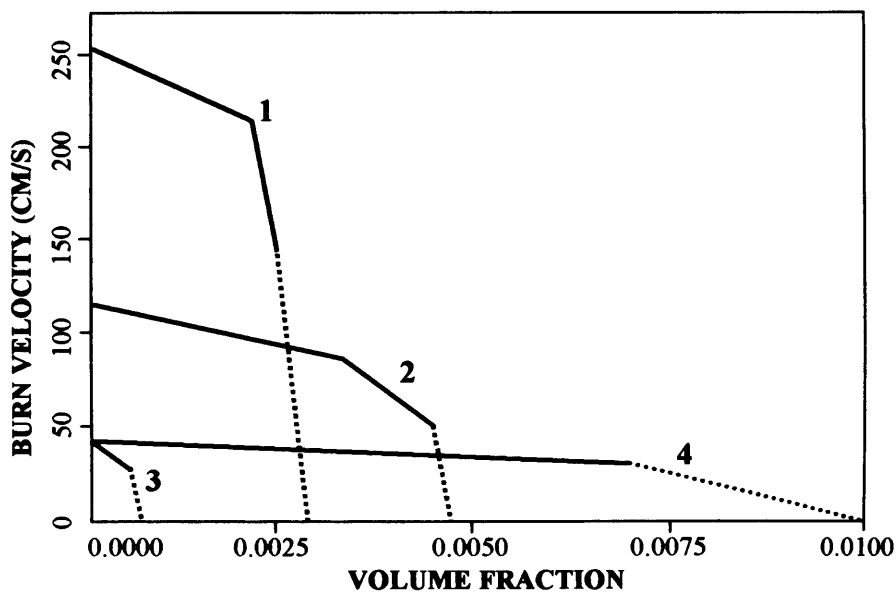


**Figure 2.3** Flame velocities versus volume fraction of water for the following droplet sizes and hydrogen concentrations: (1) 20 $\mu\text{m}$ , 29.5%  $\text{H}_2$  by volume (stoichiometric); (2) 100 $\mu\text{m}$ , 20%; (3) 100 $\mu\text{m}$ , 15%; and (4) 40 $\mu\text{m}$ , 15%

As can be seen from the figure above, the results from this computer model show that smaller droplets are more capable of quenching hydrogen explosions. For a stoichiometric mixture, only small droplets i.e. <100 $\mu\text{m}$  could supply a high enough heat sink to achieve quenching. For leaner mixtures of hydrogen larger droplets were effective as a mitigating agent; however in all cases, smaller droplets were more

effective and required lower droplet loading density, thus lower volumes of water are required when droplets are small.

Comprehensive studies investigating the break-up of large water droplets in moving air were conducted by Pilch and Erdman, [24]. Previous data was re-worked in order to determine what affects the break-up of a water droplet. It was proposed that droplet break-up could be described as a function of Weber number. Weber number ( $We$ ) can be defined as:-

$$We = \frac{\rho u^2 d}{\sigma} \quad (2.1)$$

where, as can be seen the Weber number is a function of the density of flow field ( $\rho$ ), the initial relative velocity ( $u$ ), initial droplet diameter ( $d$ ) and the surface tension of the drop ( $\sigma$ ). The qualitative description of the break-up mechanisms could then be given as shown in Figure 2.4. As is illustrated there are six different mechanisms for break-up. The first called vibrational break-up, does not always occur, and causes the formation of large fragments over a long break-up time. As the Weber number is increased towards 50, bag break-up becomes the mode of break-up, with many small fragments being produced, coupled with large drops formed by the disintegration of the rim. As Weber number is increased still further, a similar mechanism occurs with the addition of an added stamen. This causes the formation of a few larger droplets.

As the Weber number increases to over 100, sheet stripping becomes the prevalent mode of break-up. In this form, small droplets strip off the periphery of the coherent central drop. Wave crest stripping at higher Weber number, and occurs due to the formation of high amplitude low wavelength waves on the windward side of the drop, the tops of the waves then stripping to form lots of small droplets. Finally, when the Weber number exceeds 350, catastrophic break-up is witnessed. This is similar to the above, but a few waves of long wavelength form, which penetrate the drop, which creates several smaller droplets that are then totally stripped causing the formation of many very small droplets. Given that the area of concern is in the case of water sprays in air, then both the density of the flow medium, and the surface tension of the droplets are constant, therefore it follows that in the case of an explosion, high velocities and large initial droplets are most likely to induce the most effective water droplets to quench a propagating gaseous

explosion. This effect can be witnessed in various experiments discussed later in this chapter.

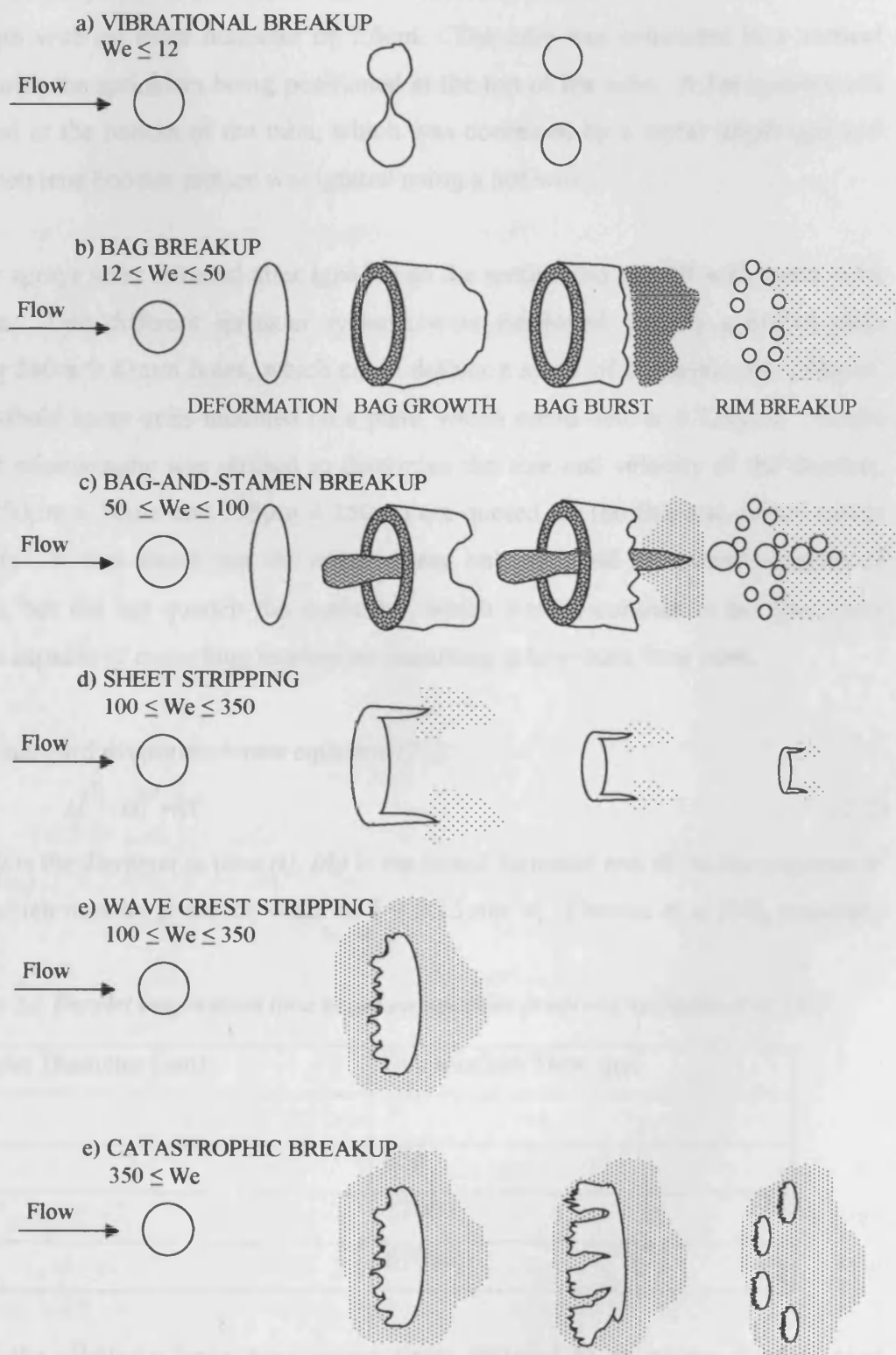


**Figure 2.4 Droplet break-up mechanisms**

A study to investigate the effectiveness of a triggered water barrier, with the proposal that they may be used to replace standard problematic arrestors was conducted by Thomas et al. [25]. The experiments were conducted in a detonation tube of dimensions 4.5m length with an inner diameter of 7.6cm. The tube was orientated in a vertical direction with the sprinklers being positioned at the top of the tube. A 1m ignition cell was formed at the bottom of the tube, which was contained by a mylar diaphragm and the oxy-acetylene booster section was ignited using a hot wire.

The water sprays were initiated after ignition so the section did not fill with water prior to ignition. Two different sprinkler systems were employed, namely a drilled plate containing 240 x 0.43mm holes, which could deliver a spray of concentration 1.6kg/m<sup>3</sup> and 5 handheld spray units mounted on a plate, which could deliver 0.72kg/m<sup>3</sup>. Strobe and streak photography was utilised to determine the size and velocity of the droplets. Sizes of 250µm ± 50µm and 775µm ± 250µm are quoted for the fine and coarse sprays respectively. It was found that the coarse spray only reduced the overall impulse of detonation, but did not quench the explosion, which was in contrast to the fine spray which was capable of quenching explosions occurring at low mass flow rates.

Using the standard evaporation-rate equation [21]:

$$d^2 = d_i^2 - kt \tag{2.2}$$

where, ( $d$ ) is the diameter at time ( $t$ ), ( $d_i$ ) is the initial diameter and ( $k$ ) is the evaporation constant which may be given for water as  $k = 0.15\text{mm}^2/\text{s}$ , Thomas et al [25], presented Table 2.1 :

**Table 2.1 Droplet evaporation time based on equation proposed by Sapko et al. [21]**

Droplet Diameter (µm)	Evaporation Time (µs)
1	7
10	670
50	17000
100	67000

Owing to the relatively large evaporation times required to evaporate droplets over 10µm, the authors proposed that due to the size of the sprays used in this study, that evaporation cannot be the sole mechanism instigating the quenching of a detonation.

It was proposed that in order to quench a detonation there must be a decoupling of the reaction zone/ flame front from the shockwave. Four mechanisms by which energy loss could be removed from the detonation by the water sprays were given as;

- Energy required in breaking the surface tension in order to strip droplets whilst forming a ‘micro’ mist.
- Energy required in accelerating the ‘micro’ mist to the velocity of the detonation.
- Energy required to raise the temperature of the droplets
- Energy required in the latent heat required to vaporise the ‘micro’ mist

The authors also demonstrated that the initial size of droplet was critical in determining the type of ‘micro’ mist formed in the resulting explosion, as shown Figure 2.5.

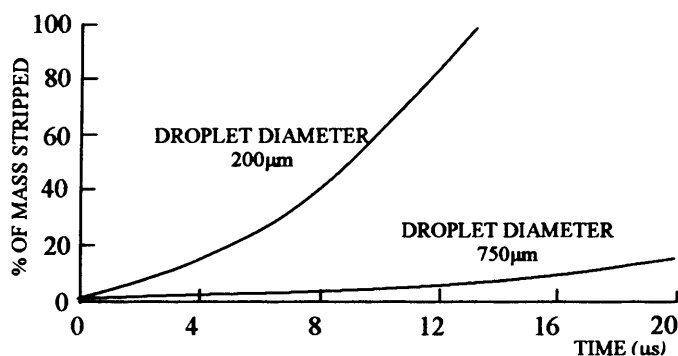


**Figure 2.5 Comparison of the fraction of mass stripped between a 200µm and 750µm droplet in oxy-hydrogen + 50% Ar**

It may be observed that the smaller droplets are stripped totally within 12µs, which would explain the ability of the fine spray to fully quench the slow moving detonations. The last concern raised was that if there was a non-instantaneous evaporation, then the movement of the acoustic field behind the detonation could affect the shattering and hence the subsequent quenching.

After the Piper Alpha disaster (discussed in Chapter 1), there was a drive in understanding the effects of water sprays for use offshore. A large-scale test was carried out by Acton et al. [13], where current deluge systems present on offshore modules were examined to assess their effect on propagating gaseous flames. Three different experiments were conducted in three different rigs. The first experiment utilised a 46.5m x 3m duct fitted with an initial 15m confined section. Obstructions in the form of 0.18m diameter pipes and planks were arranged to form a blockage ratio of 42% was erected. Two fuels namely methane and propane were investigated. The first experiment

testing water deluge utilised two different standard sprinklers supplying the water sprays. The sprinklers may be thought as low and high velocity discharges, created by a 10mm open pendant head, and a 126 high velocity head, respectively.

The results of the primary experiment were promising, with both types of sprinklers reducing the effects of the explosion. When the tests were undertaken without water, the subsequent methane explosion reached flame speeds of 500m/s and an overpressure of 10bar. The propane explosion reached detonation after 15m, travelling at a speed of 1800m/s with an overpressure of 30bar. When the sprays were instigated, fully deluging the congested area with 6x pendant nozzles, and a methane explosion reinitiated, lower flame speeds down to 100m/s, coupled with reduced overpressures of 0.35bar were recorded.

When the propane explosion was reappraised with the pendant nozzles, detonation did not occur and overpressures were reduced down to 1.7bar. In these experiments, the high velocity nozzles were not as effective as the pendant design, but did reduce both flame speeds and overpressures. After leaving the deluge section the flames reaccelerated.

Conclusions derived from this experiment were that cooling of the combustion products was only one factor in the reduction of the overpressure, as the theoretical reduction in expansion ratio/ overpressure should have been of the order of 30% whereas a considerably greater reduction was witnessed. It was proposed that quenching of the flame reaction zone by the vaporisation of droplets within the flame front reduced the reaction rate. It was then calculated that only droplets of  $<30\mu\text{m}$  would have been capable of full evaporation in the flame zone, therefore as the droplets supplied by the nozzles were in the order of  $900\mu\text{m}$ , there was evidence of droplet break-up.

A very important observation in the context of the current research programme was that flames in uncongested areas were by contrast initially accelerated when passing through the water sprays; this illustrates the fact that sprinkler systems can cause turbulence in the flow field. Eventually there was a reduction in both flame speed and overpressure, thus these sprays are effective overall even though there is an initial doubling of flame speed. It was concluded that this early enhancement could be negated by designing a

better nozzle capable of supplying smaller initial droplets, which of course is the focus of this research programme.

The second experiment was conducted in an obstructed area of 25m x 4.7m x 2.5m within a pipe rack typical of an onshore storage unit. A polythene tent was used to contain the flammable mixture. Tests were carried out to determine the size of a water curtain necessary to decouple the flame front from the shockwave. Three types of nozzles were investigated, namely: a 120° full cone generating a Sauter mean diameter of 480µm at 3bar supply pressure, a 120° flat type nozzle that produced a similar droplet size but in a sheet like spray. The final nozzle was a twin fluid atomising nozzle capable of supplying droplets of 100µm SMD, delivered at 2.5bar.

Conclusions drawn from this study are that both the full cone and flat type nozzles were capable of decelerating the flame speed to such a level as to decouple the flame front from the shockwave providing there were more than 1 row of sprinklers 0.5m apart. The atomising nozzle was found to be more effective than the other nozzles, with one row of nozzles being sufficient to decouple the shockwave from the flame front.

The final experiment used a 4m x 10m x 2.1m rig representative of an offshore module. Pipes and girders were used to provide a supply blockage ratio of 10%. A stoichiometric methane mix was ignited in the presence of a total area deluge, supplied by 36 x 90° cone nozzles that delivered water droplets of 430µm at 12 L/min. A pictorial representation of the resultant pressure traces recorded with and without water deluge is presented in Figure 2.6.

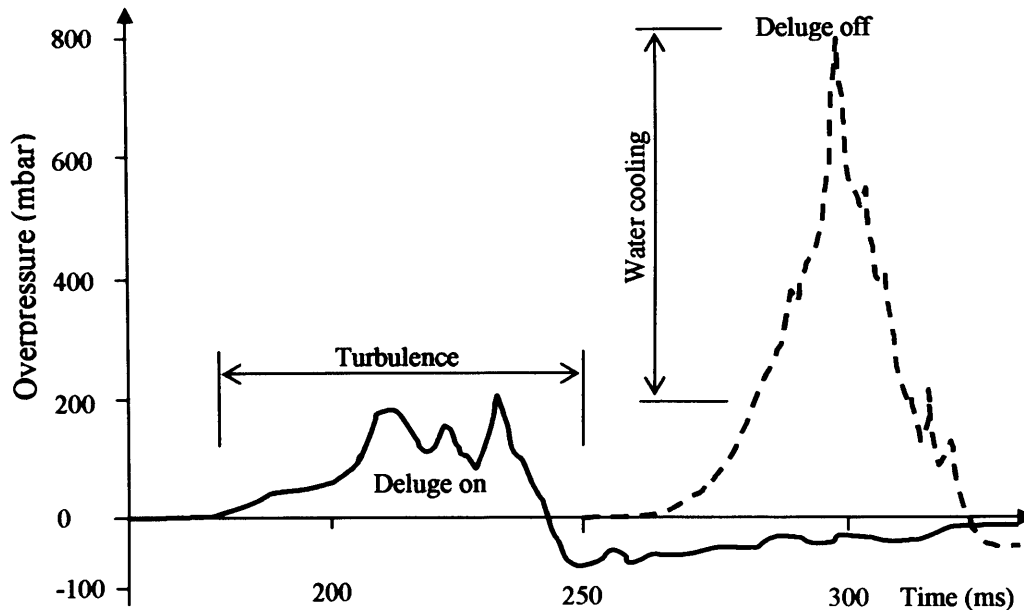


**Figure 2.6 Comparison of overpressure/ time profiles recorded at the same transducer for equivalent tests with and without water deluge**

It can be seen the water deluge reduced the peak overpressure from approximately 800mbar to 200mbar. This, as discussed earlier, is due to cooling effects of the combustion products. However, the time taken to reach the peak pressure is decreased from 300ms to between 200ms-240ms, this is assumed to occur owing to the fact that the turbulence generated by the sprays enhances the initial burning rate as discussed earlier.

Another large-scale offshore replica set of experiments was conducted by Bjerketvedt and Bjorkhaug, [26]. A 1:5 scale replica of an offshore module measuring 8m x 2.5m x 2.5m was used to determine the effect of standard water sprays on the mitigation of fuel rich methane and propane explosions. The results found in this study were in agreement with those discussed by Acton et al [13]. Once again there was evidence of initial flame acceleration enhancement, identified by a decreased time taken to reach the peak overpressure; this was more noticeable for the high-velocity nozzle, which supports the theory of increased flow field turbulence induced by the sprinklers leading to an increase of initial reaction rate.

The deluge caused a reduction in the peak overpressure due to the mitigating effect of the water on the explosion. Once again the large reduction in overpressure supports the evidence of droplet stripping causing a ‘micro’ mist capable of acting as a highly efficient heat sink, whilst the vapourisation of droplets in the flame zone lead to

retardation in reaction rate. Other conclusions drawn from this work are that the larger the gas cloud, the more effective the mitigation, and increasing the density of spray made little difference to the mitigation, indicating that fragmentation of the droplets is the primary influence.

Thomas and Jones et al. [27&28] conducted an experimental programme using two different explosion test facilities. The work aimed to examine the effect of length to diameter ratio of the test volume, on the effectiveness of water sprays. The first rig had dimensions of 50.5cm length with a diameter of 24.7cm ( $L/D=2$ ), and had sprinklers fitted at one end and a vent on the opposite wall. Two types of nozzle were used; a fine 100 $\mu\text{m}$  spray was generated from a standard garden hose, and a coarse (350 $\mu\text{m}$ ) spray was generated using 2 x Delavan<sup>TM</sup> B18 PVC nozzles, both providing flow rates of 3.5 L/min.

The second test facility was a shock-tube of length 5m with a diameter of 7.6cm ( $L/D=66$ ), mounted in a vertical plane with ignition being initiated at the top. A 30cm central slug of water spray was generated using two different sprinkler systems; a so-called 'fine' (150 $\mu\text{m}$ ) mist was generated using Lumark<sup>TM</sup> 0.8 FN Brass nozzles and a coarser (350 $\mu\text{m}$ ) mist generated via Delavan<sup>TM</sup> B18 brass nozzles at flow rates of 7.2L/min. An acceleration section could also be added to the ignition section of the rig, giving a range of methane flame speeds of 8m/s (non-accelerated) to 400m/s (accelerated).

Fuels of methane, ethylene and propane were investigated, and pressure traces recorded in both rigs. The second rig was also fitted with 6 light detectors, which were used to generate flame speed histories.

The results from the two facilities presented very different conclusions concerning the use of water sprays in the mitigation of propagating explosions. The first set of experiments showed that the use of water spray increased the reaction rate and raised the maximum overpressures attained, with the fine spray causing the fastest explosion with worst overpressure. In the shock-tube experiments, overpressures and particularly the shock impulses were decreased in the cases of experiments conducted with water sprays. The accelerated flames saw the largest decrease in measured impulses.

It is proposed that there are two mechanisms in which water spray quenches an explosion, namely: i) dilution and ii) acting as a heat sink. However, as quenching occurs in the order of *microseconds*, and the evaporation of droplets >100µm is in the order of tens of milliseconds, then droplet-stripping must be occurring. These experiments support the fact that high flow field velocities and large droplets are conducive to droplet break-up and the formation of a 'micro' mist, which is then capable of quenching an explosion.

A preliminary study with respect to liquids as an explosion suppressant is discussed by Ewan and Swithenbank, [29]. This report states that there are four major factors responsible for flame extinguishment namely:-

- Absorption of flame enthalpy through the addition of a heat sink such as water in bulk or atomised form.
- Dilution of the combustion vapour concentration below the lower flammable limit by non-flammable gas addition.
- Addition of specific gas phase materials, which provide radicals and soak up some of the chain carriers in the flame.
- Increasing local gas velocity beyond the local flame speed, thus blowing out the flame.

The study carries out simple mathematical modelling to demonstrate how droplet heat up and evaporation could bring about flame extinguishment. This simple model is given by:-

$$\Delta E = C_p \Delta T_{ex} \rho \text{ (energy absorbed by flame front)} \quad (2.3)$$

$$\Delta E_{con} = h A \Delta T_{da} \text{ (energy transfer to droplet surface)} \quad (2.4)$$

Substituting appropriate values for the equation parameters into (2.3/2.4) shows that in order for a 50µm droplet diameter with convective velocity of 10m/s to extinguish a flame, a droplet loading of  $1.9 \times 10^{10}$  droplets/m<sup>3</sup> would be necessary. It can be seen that this value is very high, but as surface area is proportional to droplet size, this value could be reduced considerably for smaller droplets or a higher vapour fraction utilised. The

authors comment that small droplets may be swept away from the flame front making them ineffective. Simple FLUENT models were then run and the following conclusions drawn. It is stated that smaller droplets are more effective for a fixed spray density due to the fact that mass transfer is proportional to surface area, hot water is more effective owing to higher vapour pressures supplying greater volumes of water that acts as a diluent, location and direction of sprays is of key importance and the competing effect of turbulence generation resulting in flame speed increase sometimes dominates the positive mitigation effect.

A comprehensive review of experimental work concerning water sprays as an inhibitor is presented by Jones and Thomas [30]. This reviewed the majority of work discussed earlier in this chapter, and concluded that water sprays can act positively in the case of gaseous explosions, possibly leading to total mitigation if the air entrainment and cooling effects are sufficiently high. It was also conceded that in certain circumstances, water sprays could act in a negative way, causing increased turbulence and electrical ignition on contact with live equipment. The importance of droplet fragmentation/break-up was also highlighted in the case of explosion suppression. The final conclusion was that there was still the need for further experimental work in order that spray behaviour in the flame zone could be understood so as this important factor can be incorporated into prediction models.

A full-scale study at the British Gas test facility, concerning the effects of obstacles, water supply, and foaming agents on explosion mitigation for offshore application, was conducted by Catlin et al. [31]. Following on from work conducted by Acton et al. [13], once again total area deluge was considered, however the rig used in this study was a large box type structure of dimensions 4.5m x 4.5m x 9m, with only one of the end walls being vented. It was speculated that confined explosions, which by nature are slower, would be less likely to cause 'stripping' of droplets, thus the purpose was to assess the limits of deluge as a protection system. Flame speed within the vessel was varied by changing the size of the vent in the end wall, with fast flame speeds achieved by using a large vent area, and slower flame speeds by closing the vent area.

Two types of nozzle were used at high and low pressures, hence varying the type of water droplet size and distribution, and by using the different nozzles, similar droplet

sizes could be achieved whilst varying the turbulence characteristics. The results from the two vessel setups are represented pictorially by Figures 2.7 (a&b).

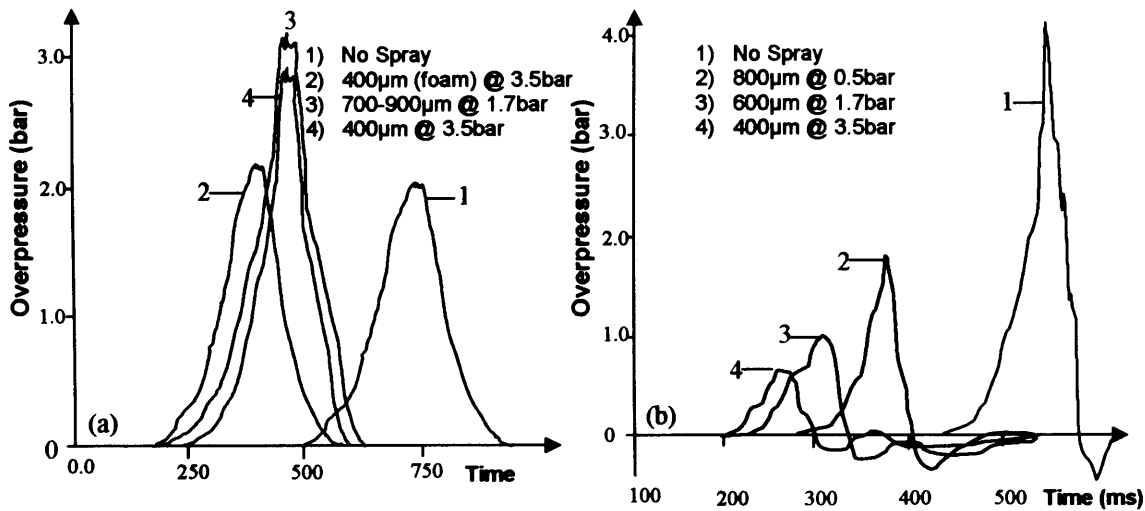


Figure 2.7 (a&b) Pressure time profiles for slow flames and fast flames respectively

The effects of droplet ‘stripping’ are once again illustrated. In Figure 2.7(a) where the flame speed is slow owing to low obstruction ratio and small end venting, it can be seen that the water sprays speed up reaction rate, and exacerbate the peak overpressure. The highest peak pressure occurs when the largest droplets are employed, and it can be seen that the foaming agent used mitigates the severity of the overpressure.

When high obstruction ratios and large end venting are employed, as in the case of Figure 2.7(b), it can be seen that the effect of deluge on the explosion reduces the peak overpressures attained. Once again it can be seen that the smaller the droplets, the less severe the event, although the effect of high spray velocity initially speeds up the reaction rates. Thus conclusions of this study indicate that the mitigating efficiency of water is dependant on droplet ‘stripping’, which is totally dependant on the type of explosion and spray characteristics.

Following on from the studies undertaken by Catlin et al. [31], the Health and Safety Executive in collaboration with British Gas and Chubb Fire Protection PLC [32], decided to test newly-designed high-pressure Chubb nozzles along with Bete PJ40 and P120 misting nozzles, to determine whether the inefficiencies of deluge techniques at high confinement/low flame speeds could be overcome by supplying smaller droplets within the combustion zone. Although literature at the time was claiming misting

nozzles could supply 50µm droplets, spray characterisation studies confirmed that these sprays were formed from droplets of nearer 300µm.

Once again in the highly confined flow obstruction set up, overpressures and reaction rates increased by the use of water spray deluge. The worst case witnessed occurred using the misting nozzles, which required a supply pressure of 10bar and only delivered a 1/10<sup>th</sup> of the water volume of a standard nozzle. The perceived characteristics required for successful mitigation, compared with those commercially available were depicted as shown by Figure 2.8.

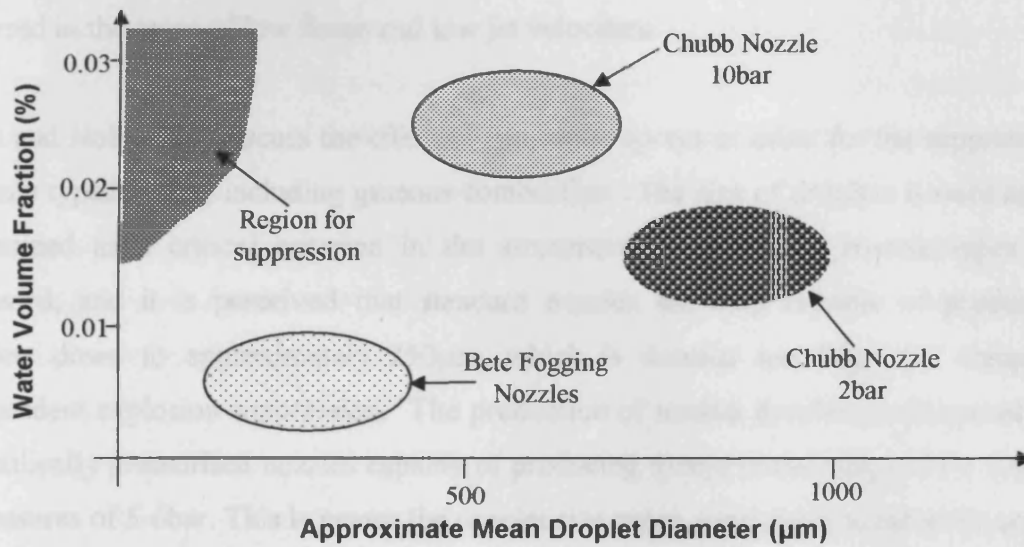


Figure 2.8 Nozzle capability compared with nozzle requirement for suppression

As can be seen from the illustration, at the time of publication standard nozzle designs were not capable of delivering the required characteristics necessary for comprehensive explosion suppression that is not reliant on droplet ‘stripping’.

Brenton et al. [33], using a small-scale 5m long 7.6cm horizontal shock-tube, examined the effect of Delevan<sup>TM</sup> BIM 8 nozzles capable of delivering a spray of approximate Sauter mean diameter 110µm. The shock tube was split into 3 distinct areas comprising an initial 2m accelerator ignition cell, coupled to a 1m long spray section, followed by a 2m section where the ensuing explosion could be studied. Flame velocities of 7-146m/s were recorded when the tests were run dry, compared with a range of 1 - 233m/s with varying levels of water spray. The highest flame speeds were reached when a combustion mix just rich of stoichiometry was utilised, with open ended shock-tubes.

There were a number of interesting conclusions with respect to wet conditions, namely; flame speed is not proportional to spray speed, flame extinction always occurred within the spray field, low speed flames are harder to extinguish than fast moving flames, extinction is generally preceded by an increase in flame speed as the flame entered water spray, extinction is more likely in lean or rich flames with a moderate water jet flow. In some cases droplets accelerated at a sufficiently fast rate to ensure the pursuing flame never caught up with the water slug, and the final conclusion drawn was that if the flame overtook the water slug, the highest flame speed reached was always within the spray field, i.e. the flame accelerated through the water cloud. This phenomenon usually occurred in the cases of low flame and low jet velocities.

Jones and Nolan [34] discuss the effect of fine water sprays or mists for the suppression of many types of fire, including gaseous combustion. The size of droplets is once again determined as a critical criterion in the arrestment of a flame. Nozzle types are discussed, and it is perceived that standard nozzles are only capable of producing droplets down to approximately 250µm, which is deemed too large for complete independent explosion suppression. The production of smaller droplets is discussed via hydraulically pressurised nozzles capable of producing sprays in the range of 90-100µm at pressures of 5-6bar. This is nearer the droplet size range considered suitable for active suppression. Two twin fluid atomisers developed by BP and Marioff are briefly mentioned, and although no details are provided, it is proposed that these types of systems may be capable of producing sprays with a large number of very fine droplets.

The difficulties associated with quantifying a spray are discussed, and a number of different means defined and discussed with the general formula for mean diameter given as:

$$(D_{mn})^{m-n} = \frac{\int_{D_0}^{D_m} D^m (dN/dD)dD}{\int_{D_0}^{D_m} D^n (dN/dD)dD} \quad (2.5)$$

Where, the maximum and minimum diameters are given by  $D_m$  and  $D_0$  respectively and the variation between these is given by  $(dN/dD)$ , the integers  $m$  and  $n$  can vary between 0 and 4 and is dependant on the particular mean being defined. The sum of these two integers gives the order of the mean diameter being defined. It is stated that the two mean diameters most often quoted are the 5<sup>th</sup> order i.e.  $m=3$  and  $n=2$  called the  $D_{32}$  or

Sauter mean diameter, as this gives a volume to surface area comparison which is of particular interest in the field of combustion and the volume mean diameter  $D_{v,0.5}$  which is the diameter below which 50% of the sprays volume/mass resides.

The last area of interest discussed by the authors is the ability of fine mists to co-exist with live electrical equipment. There are several incidents reported where the possibility of the water sprays providing the initiation source for the explosion itself due to interaction with electrical equipment is suggested. The findings of two technical workshops are discussed and it is found that Hi-fog systems are able to operate in open cabinets involving live switchgear at 690V and 24kV with no problems being encountered. Also up to six twin-fluid nozzles were used in telecommunication switchgear cabinets; tap and distilled water propelled by nitrogen at between 2-100bar were used. It was found that by adding electrical safety trips - which often were tripped by the smoke before water was even initiated - all electric shock hazards were eliminated. The water had no destructive action on the circuit board providing suitable droplet diameters, droplet velocities were utilised.

A two part publication by van Wingerden et al., studied the effect of water sprays on gas explosions. The first publication [35] focuses on spray-generated turbulence. A 15m<sup>3</sup> box, with a plexi-glass front panel allowing full visual axis was utilized, with the propane and methane mixes being ignited at the base, and 4 different types of nozzles being released from the top, 10 seconds before ignition.

The different nozzles allowed a variety of different spray characteristics, with typical mean droplet diameters of 50-200µm, 500µm and 600-800µm being released at a variety of different flow rates. The flame speed was recorded at 200 fps. There were some visual observations made by the authors who state that in the case of explosions with water spray, the flames became more cellular and the flames became redder in colour. In all nozzle cases, the flame speeds increased typically in the order of 1.5-2.0 times for propane and 1.4-2.3 times for methane. Lower flame speeds were recorded however when the spray was switched off prior to ignition, proving that the water had a positive mitigating effect but was negated by the dominant turbulence.

It is concluded that turbulence is mostly derived by the bulk flow of the water, and not attributed to the individual droplets. This is deduced from the fact that the bulk flow disturbance is in the region of 1-2 orders of magnitude higher than those attributed with single wake disturbances. This theory is backed up by the fact that droplet size and droplet velocity were not proportional to the resultant flame speed. The final proof of this phenomenon is illustrated by the large-scale disturbances (0.2m), which are much larger than disturbances that could be associated with single wakes.

The second paper of this series van Wingerden et al. [36] is concerned with actually mitigating gaseous explosions. The paper relies on statements made by Sapko et al. [21] who concludes that a water vapour concentration of 31.5% ( $234\text{g/m}^3$ ) is required to quench a propagating methane flame. The authors however concede that they are 'unaware of any measurements performed on the influence of water vapour on the burning velocity of hydrocarbon-air flames', and propose that water vapour would have similar trends to an inert gas such as nitrogen, which is in slight disagreement with the work of Fells and Rutherford [16] as shown by Figure 2.1 which demonstrates that water vapour is more effective than nitrogen.

The experimental rig used in this study was identical to that used by Bjerketvedt and Bjorjhaug [26]. Mixtures of 9.8% methane and 4.2% propane, prepared using an Infra Red gas analyser, and a 2 x 100 Joule central ignition was most commonly used. Four different nozzles were utilised, supplying Sauter mean diameters of  $500\mu\text{m}$ ,  $600\text{-}800\mu\text{m}$ ,  $200\mu\text{m}$  and  $50\text{-}70\mu\text{m}$ . The deluge was instigated 15 seconds before ignition. Quantification of the explosion was provided by 6 pressure sensors positioned throughout the test facility, and by high-speed video recording.

There were a number of conclusions derived. First, the position of the deluge curtain from the ignition source is very influential on the speed of the resultant flame - if the curtains were positioned close to the ignition then resultant overpressures and their rate-of-pressure rise increased, the largest increases observed were for the fastest sprays containing the largest droplets that created greater turbulence intensity. When the curtains were positioned in the far field away from the point of ignition, the sprays consisting of droplets  $>500\mu\text{m}$  were able to reduce the severity of the resultant shock wave, whereas the  $50\text{-}200\mu\text{m}$  sprays showed little effect. It is thought that these smaller

droplets simply get swept away in front of the flame front because they are easily accelerated (a 50 $\mu\text{m}$  droplet accelerates 20x faster than its 500 $\mu\text{m}$  counterpart), this decrease in the relative velocity between the droplet and mass flow means that a Weber number of  $\geq 10$  is not achieved within the rig for droplets of less than 200 $\mu\text{m}$ , thus there is no resultant droplet break-up and no 'micro' mist formation.

The authors demonstrated this lack of efficiency of 50-200 $\mu\text{m}$  droplets as an effective deluge curtain graphically as presented in Figure 2.9.

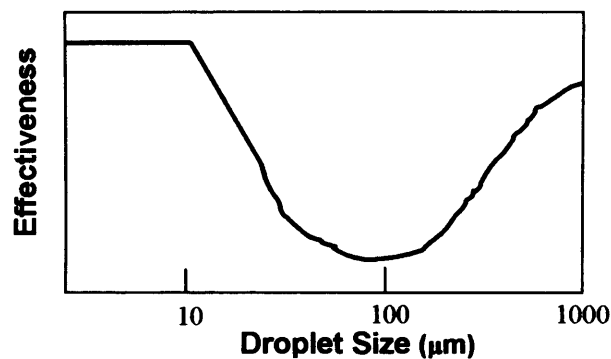


**Figure 2.9** *Effectiveness of water-spray systems as a function of the average size of water droplets they supply (schematic)*

This figure shows that droplets of  $<10\mu\text{m}$  are as effective as a vapour as stipulated by Sapko et al. [21], and then illustrates the importance of droplet size in determining its likelihood to disintegrate as predicted by Pilch and Erdman [24].

Moore [37] hypothesises that a suppression system needs to deploy the suppressant into the combustion wave of the incipient explosion so as to reduce the combustion zone temperature to below a limiting adiabatic flame temperature, so that the combustion reactions are no longer self-sustaining. This hypothesis means that a minimum critical mass of suppressant must be introduced into the system in order to quench a flame at a particular pressure level lower than the value at which an overpressure is reached that is deemed harmful to plant/personnel.

The author summarises the above statements graphically given by Figure 2.10.

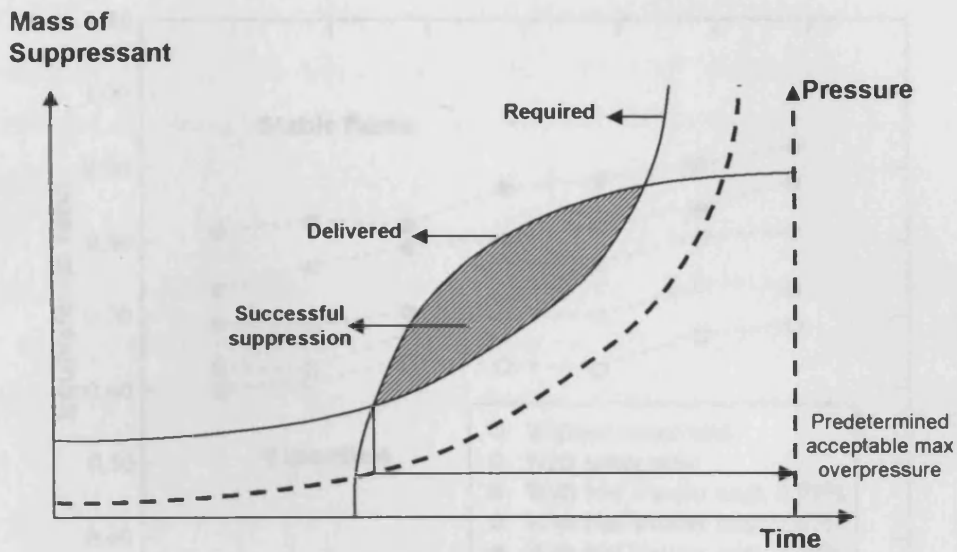
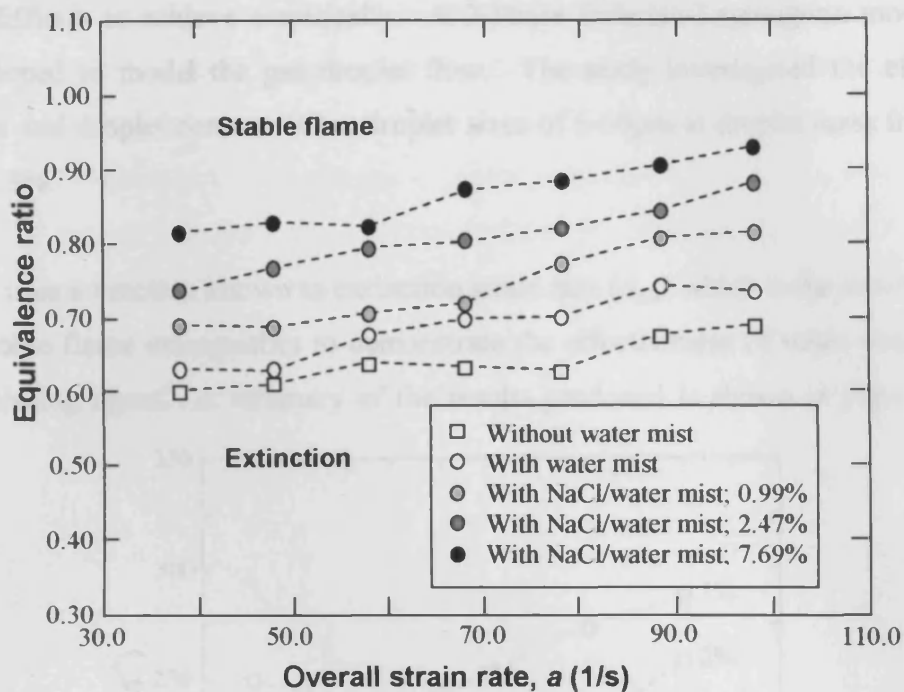


Figure 2.10 Design basis for explosion suppression

It is stated that suppression system design can be very complex, and many factors including the volume of vessel, shape of vessel, explosive material, homogeneity and turbulence should be carefully considered. The author in his summary of water as an explosion suppressant expresses that he feels it is of little use in the suppression of flammable gas explosions and against hybrid gas/dust explosions, owing to the fact that it has no chemical specificity and acts strictly as a thermal heat sink quenching agent.

However, it is conceded that if deployed very early during an explosion water can have a level of effectiveness in inerting flammable gases, highly sensitive UV-type radiation detectors are suggested in order to ensure that the explosion is detected in its earliest stages allowing for the required rapid deployment of water sprays.

A laboratory-scale study utilising a counter-flow burner was undertaken by Zheng et al. [38]. The effects of pure water droplets and NaCl-water droplets were studied with respect to the strain rates at which extinction of the flame occurred. A summary of their results is given by Figure 2.11.



**Figure 2.11** Comparison of extinction limits with plain water mist and various saline water mists

The graph shows that water mists can significantly reduce the resistance of a methane-air flame to extinction especially in cases of higher rates of strain. Also it is noted that extinction occurs more readily by the addition of NaCl. This is thought to occur due to chloride ions produced forming into chlorine which is an inhibitor, and also acting as a catalyser in the formation of water from oxides and hydroxides, which reduces the active oxygen present in the flame zone. Also the sodium may have a contributory effect but this apparently was not analysed or discussed.

This study is of particular interest for the case of offshore applications, as these concentrations of saline mixtures are of the order of those found in sea-water which is obviously plentiful for offshore applications. Unfortunately due to time constraints, this study only considered lean methane mixtures, and before this effect could be considered reliable, further investigations through stoichiometric and into rich mixtures would be necessary.

A comprehensive numerical study examining the effect of water droplets on flame extinction in a counter-flow type burner has been undertaken and documented by Lentati and Chelliah [39]. Although computer modelling is not within the remit of this study, it is considered appropriate to discuss briefly such studies as they provide insights which

are often difficult to achieve empirically. A 2-Phase Eulerian-Lagrangian model has been developed to model the gas droplet flow. The study investigated the effect of droplet size and droplet concentration, droplet sizes of 5-50 $\mu\text{m}$  at droplet mass fractions of 1, 2 and 3%.

This study uses a function known as extinction strain rate ( $a_{ext}$ ) which is the strain rate at which a stable flame extinguishes to demonstrate the effectiveness of water droplets as an extinguishing agent. A summary of the results produced is shown in Figure 2.12.

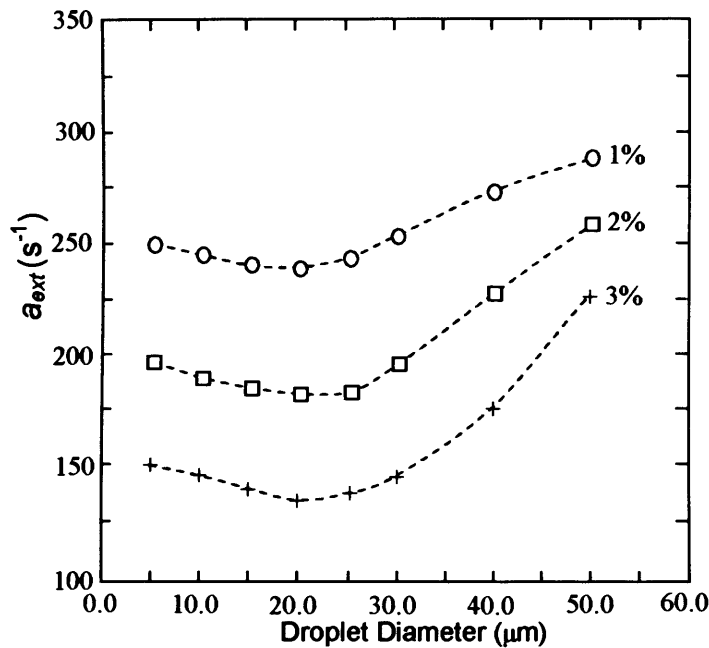


**Figure 2.12 Comparison of extinction strain rate against droplet size for different droplet mass fractions in condensed phase at inflow**

It can be seen that extinction is not directly proportional to droplet size, though for all cases it is noted that the 50 $\mu\text{m}$  droplets are least effective, whilst the most effective are in the 15-25 $\mu\text{m}$  range. It can be shown that droplets smaller than 20 $\mu\text{m}$  follow the gas closely and evaporate fully in the hot mixing layer, thus never travel into the flame zone, whereas the 50 $\mu\text{m}$  droplets travel in an oscillatory manner back and forth through the stagnation flame before they are totally vaporised. An increase in droplet mass fraction reduces the extinction strain rate almost uniformly. It is also stated that saturated water vapour alone is also capable of reducing the flame extinction strain rate by 25%, this effect being due to a dilution effect as the water displaces oxygen. This is enhanced particularly in the case of droplets by the high thermal capacity of water.

A thorough overview of the use of water as a suppressant of fire is published by Grant et al. [40]. Although this report is concerned the extinguishment of fires which require a very different spray characteristic, there are some relevant conclusions concerning the effectiveness of droplet size in creating a large surface area. This is given by Figure 2.13, which illustrates how the size of a droplet affects the effective surface area, which is of great importance for heat loss via evaporation.

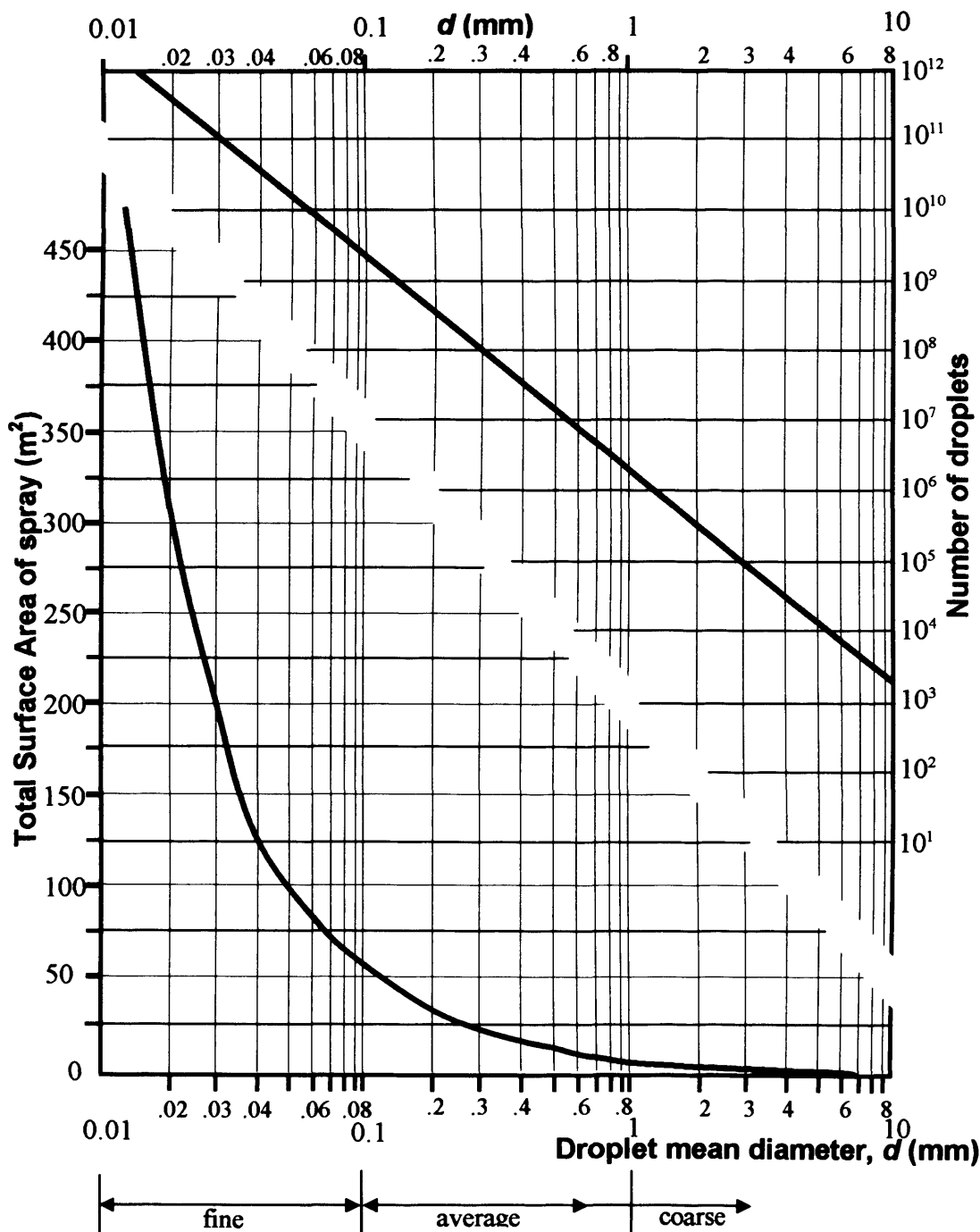
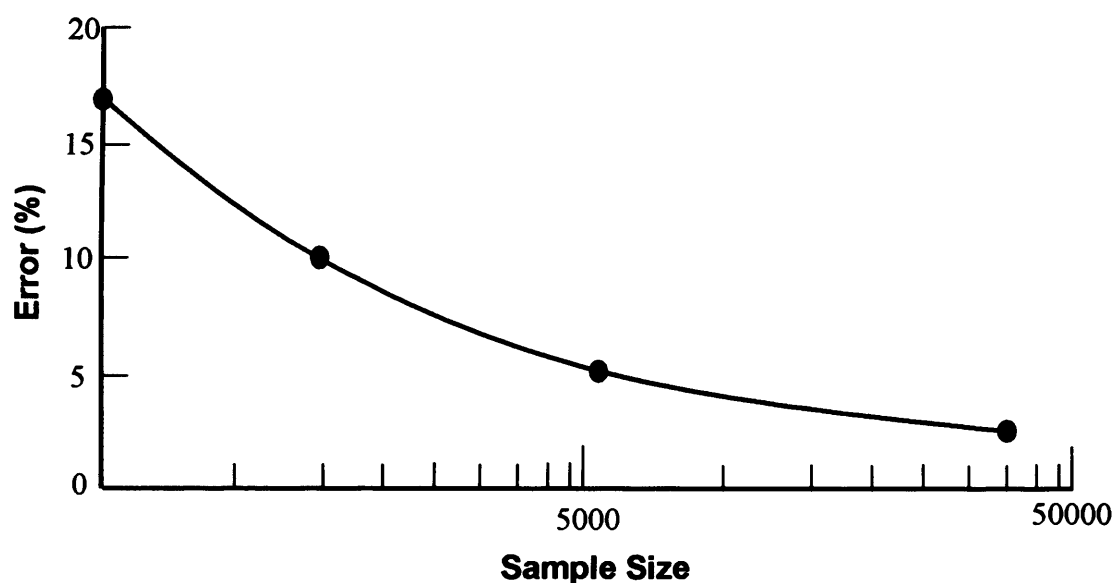


Figure 2.13 Number of droplets and total surface area produced by one litre of water, as a monodisperse spray with various mean droplet diameters.

Due to the diameter-squared dependence of surface area on droplet size, at  $10\mu\text{m}$  the line is almost vertical this may explain why it acts as a vapour. The number of droplets also increases as would be expected. This graph enables us to determine that droplets of  $<30\mu\text{m}$  are most likely to be of use as this is when the surface area starts to increase exponentially.

Droplet quantification is also discussed in this report and an interesting trend correlating the number of samples taken against the percentage error likely to be attributed to the data. This correlation is presented in Figure 2.14.



**Figure 2.14 Accuracy of mean droplet diameter as a function of sample size**

Another experimental programme concerning non-premixed flames and their interaction with ‘fine’ droplets was conducted by Lazzarini et al. [41]. This study incorporated a computer model and experimental programme simultaneously. The model and experimentation showed that the addition of vapour reduced the extinction strain rate by 12% and 13% respectively, thus showing good agreement.  $20\mu\text{m}$  droplets at a mass concentration of 3% were shown in the computer model to reduce the extinction strain rate by 55%. It was found that the addition of mono-dispersed droplets in an experimental apparatus is ‘rather difficult’.

Less agreement is found between the model and experiments as the water droplet mass fraction increases, which may be due to the poly-dispersed nature of practical work becoming more influential at higher droplet mass fractions. An interesting factor raised by this work is that the addition of NaOH into the water can dramatically improve

water's ability to act as a suppressant. It is suggested that water can become five times more efficient if a 17.5% NaOH solution is used. The explanation for this vast improvement is that water still acts as a very efficient heat sink and coupled with this effect is the ability of NaOH to act as a chemical inhibitor in radical recombination.

Thomas [10] conducts another thorough investigation into the conditions required for explosion mitigation by water sprays. The effect of droplet break-up is shown by photography of individual and spray type applications and is shown by Figures 2.13 (a&b).

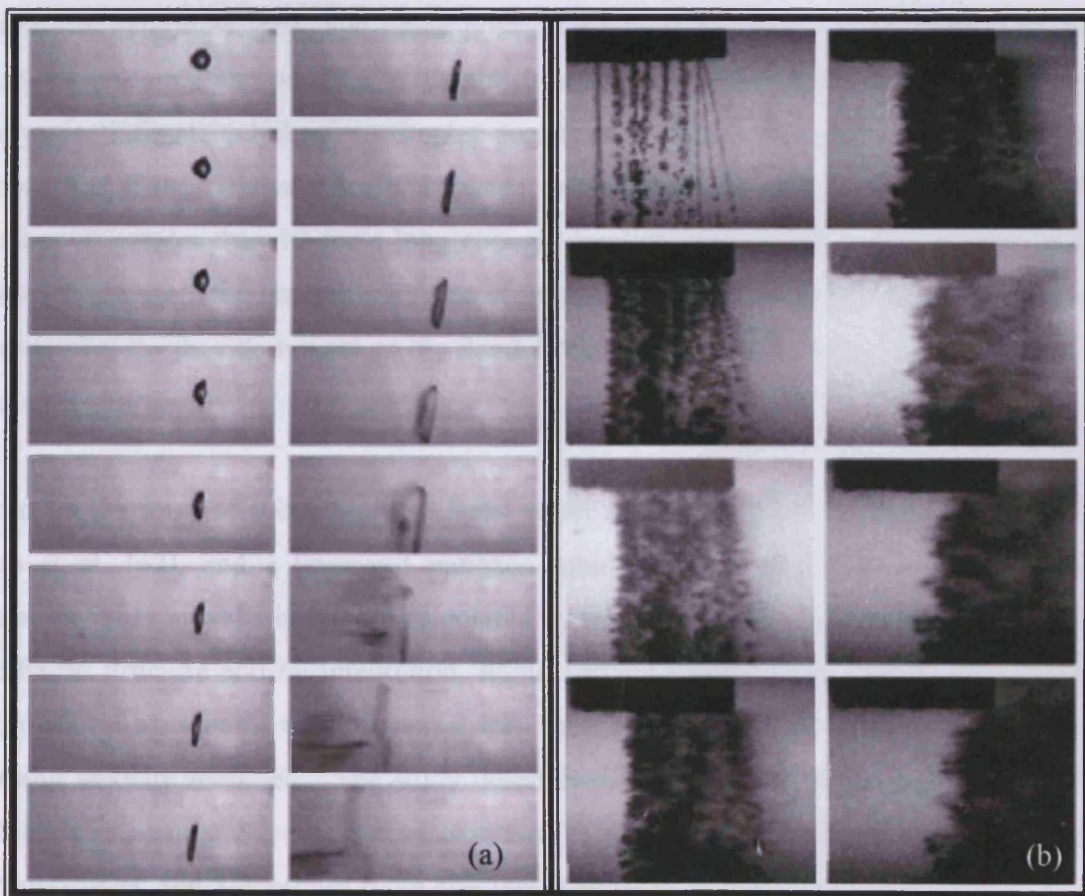


**Figure 2.13 (a&b) Photographs showing the catastrophic break-up of a 4mm droplet  $\Delta T=1ms$  and the rapid fragmentation of a simulated water spray  $\Delta T=1.3ms$  respectively**

These images show exactly how a 'micro' mist is formed in the case of a severe explosion impacting on a deluge sprinkler type system.

Thomas then discusses his computer predictions, but these results will be examined later in the chapter in a further publication [46], so will not be discussed further at this stage. An experimental programme detailing the mitigation of small-scale explosion is then

discussed. A 5.32m duct of cross-sectional dimensions 175 x 275 mm was used fitted with a 1.2m ignition cell of cross-section 0.247m. A central section fitted with water sprays and with full optical access, is used to determine the effect of water sprays on methane explosions. Visualisation of the sprays was recorded using a high-speed video camera (1000fps), and photodiodes, pressure gauges and thermocouples were used to determine flame speed and pressure rises. A variety of different nozzles in different configurations was used and was activated 5 seconds before ignition.

By examining pressure traces and comparing this with data from the laser photodiodes which can determine spray and flame position along with video tape recordings of the droplet break-up it was possible to 'demonstrate unequivocally' that mitigation by water sprays is 'intimately linked' to droplet acceleration characteristics. It is once again shown that if the relative velocity between the gas and droplet can generate a Weber number of greater than 12 for a long enough duration then break-up of the spray will occur. Once again the issue of very fine droplets being swept ahead of the flame front is raised, whereby they do not act on the flame front and are ineffective in the mitigation of methane explosions.

Water in the form of submicron ( $<0.5\mu\text{m}$ ) water mist was utilised as a suppressant by Fuss et al. [42], and a premixed methane tubular burner was used at atmospheric pressure. Burning velocities were calculated by taking 6<sup>th</sup> order polynomial functions of the flame structure and by integration, flame surface area was calculated. Water was supplied via an aerosol type generator into the combustion mixture, and its effect on burning velocity recorded. The study determined that in order to bring about a 20% reduction in burning velocity, the water was as effective as that of Halon 1301 on a mass for mass basis, and 2-2.5 times more efficient than  $\text{N}_2$  and  $\text{CF}_4$ .

The efficiency of water mist in the extinction of turbulent premixed flames was investigated by Mesli and Gökalp [43]. A counter-flow burner delivering a premixed methane air mixture from one side, and atomised water and air from the other, was used in conjunction with a PDA setup to measure the effects of water flow rate on the effect of burning velocity. Water droplets supplied by the atomiser were in the order of  $4\mu\text{m}$ . It was found that the extinction efficiency increases with water flow rate, however a plateau was reached and an efficiency of over 50% could not be achieved under any

condition in this setup. The application time of the water mist in the flame zone was also found to be an important factor and the time required for extinction seems to decrease as the water fraction increases. Stable flames could only be extinguished by applying a strong water flow, as opposed to unstable flames, which only required a low water flow rate.

A comparative study between experimental and numerical simulation was undertaken by Shimizu et al. [44], examining the effect of water mist on quenching a methane flame. An experimental chamber of 500 x 500 x 500mm using a gas burner at the base and a water mist nozzle at the top was utilised with gas flow rates of 0-2.5L/min, and water mist pressures of 0.4-0.44MPa at atmospheric conditions. Water droplet sizes of 45 $\mu$ m are quoted, but the monodispersity of this spray is not quantified. The methane concentrations are also not quoted. Schlieren photographs at 40000fps were taken and it was found that at high water flow pressures (0.5MPa) and low gas flow rates (0.018L/min) the entire flame is quenched. It can be seen that the water mist evaporated absorbing the heat of the flame then the lower flame temperature causes the flame to extinguish due to the fact that the flame is starved of oxygen by the vapour and further mist.

By increasing the gas flow rate and decreasing the water flow pressures it was noted that 'holes' appeared in the mist curtain and burning continued through these holes. It was shown that higher gas flow rates needed higher water supply pressures to bring about quenching of the flame. Also it is noted that higher supply pressures of water brought about more rapid flame extinction. The reasons given for flame extinction are (i) absorption of flame energy by latent heat needed for evaporation and (ii) suffocation of the flame by the water curtain which displaces oxygen from the flame.

An Eulerian and full Navier Stokes model was run and showed that evaporation caused a reduction in the flame temperature and it demonstrated once again that droplet diameter is a critical factor in the extinguishment of a gaseous flame.

A passive explosion suppression system was designed and rigorously tested by Catlin [45]. The study describes a number of reasons why passive suppression could be a superior method compared with active suppression. Namely:

- Passive systems don't rely on 'complex electro-mechanical infrastructure' that have the capability of failing.
- Active systems require a rapid detection to ensure system is activated before the flame front passes the point of deluge.
- Low pressure active systems whose time of activation is relatively long in the order of a few seconds are not required.
- A reduction of testing and maintenance compared to active systems.

For the above reasons the author states 'Water spray deluge, therefore, cannot absolutely guarantee that an explosion will be suppressed. Since it is possible that gas release and ignition could occur before the deluge system were activated.' Caution is also brought about such systems bringing their own hazards when activated without an explosion such as reduced visibility and electrical shock hazards.

The author discusses the facts that if deluge systems are used they must cover all areas and not just areas of particular concern owing to the fact that the sonic wind can carry water sprays away from the area they are supposed to be protecting. For all of the above reasons the author describes a study conducted on passive systems that rely only on the effect of an explosion to cause full flame extinction. Experimental programmes using a wind tunnel and a 5.1m long explosion duct of cross sectional area  $0.3\text{m}^2$  were used to study passive systems that rely on air-blast atomisation.

It is perceived that air-blast atomisation may be capable of supplying water droplets of the size range deemed effective in the suppression of a propagating flame front, this generation is shown by Figure 2.14.

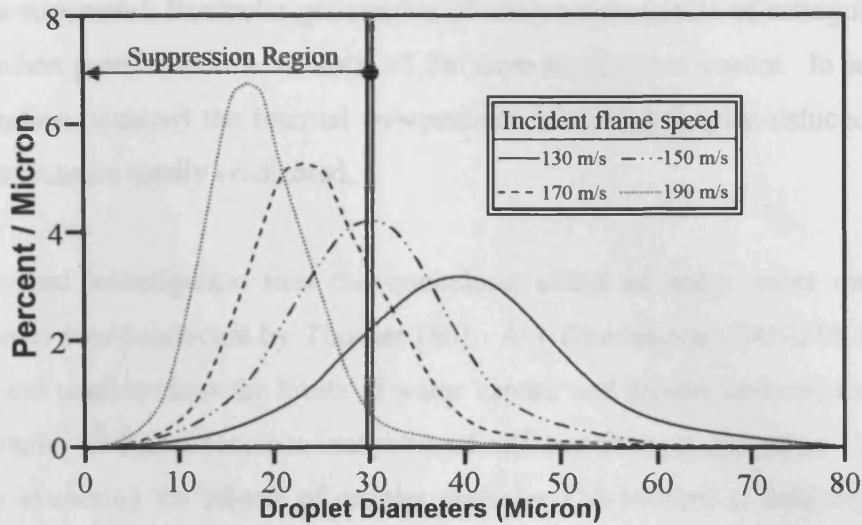


**Figure 2.14** Droplet size distributions generated by air-blast atomisation for different incident flame speeds

As can be seen, very fine mists can be formed from such a technology. For a 150m/s flame speed the droplet formation time is substantially less than 0.005ms but is rapid enough compared with a typical offshore explosion which has a typical duration of approximately 1s.

The system proposed for this study employed a multiple array of aerofoil type water containers of the type illustrated in Figure 2.15. The system relies on the sonic wind causing airflow to travel through the aerofoil, this airflow causes a film-stripping effect that produces a mist of small droplets to be generated and form in front of the array.

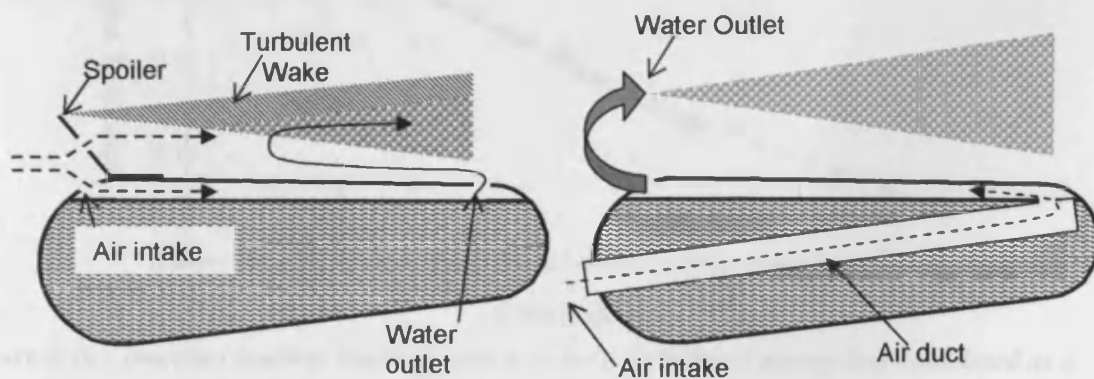


**Figure 2.15** Types of aerofoil passive systems utilised in study

The conclusions of the study showed that the droplet size and minimum flame speed necessary to instigate a full suppression of a propagating explosion was dependant on many variables such as the size, shape and number of containers within an array, also it was seen that in distances  $>1.3\text{m}$  from ignition that the use of the container with spoiler

proved more successful. Particular geometries of array were capable of extinguishing all explosions when positioned at a distance  $>1.7\text{m}$  from the ignition source. In such cases where mitigation occurred the internal overpressure was substantially reduced and the external overpressure totally eradicated.

A computational investigation into the quenching effect of water mists on laminar methane flames was conducted by Thomas [46]. A 1-Dimensional SANDIA PREMIX flame code was used to show the limits of water vapour and droplet concentration below which a methane-air flame becomes incapable of self-sustaining propagation. The remit of the study evaluated the effects of droplet diameter ( $10\text{-}100\mu\text{m}$ ) at differing number concentrations and determines their effectiveness in mitigating a methane flame. The potential improvements brought by adding alkali salts in the mitigation of a flame are also studied.

An initial study was conducted to show the effect of adding water vapour on the burning velocity of methane, the results derived are presented in Figure 2.16.

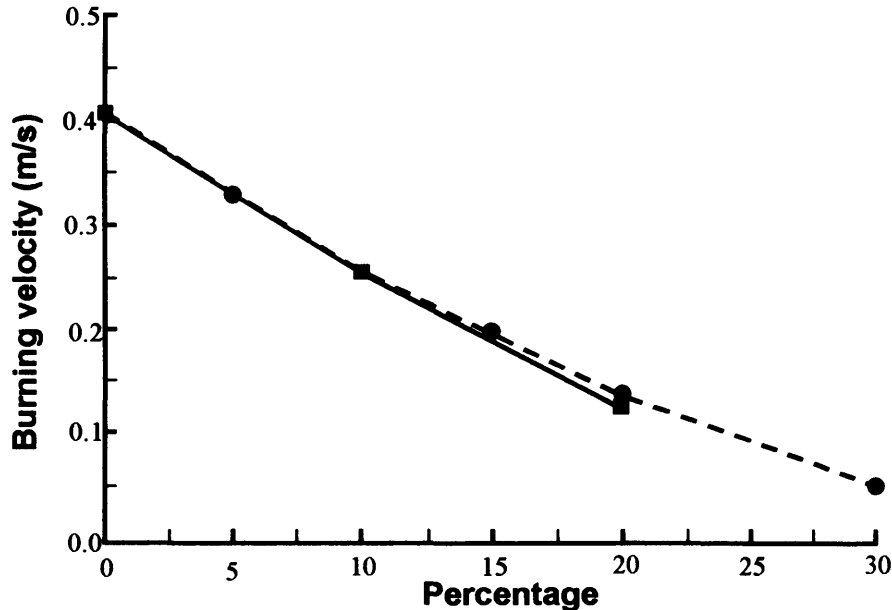


**Figure 2.16** *Computed laminar burning velocities for a distributed energy loss calculated as a percentage of local chemical energy release rate (●) and increasing molar concentration of water vapour in the initial methane-air mixture (■)*

As expected the burning velocity decreases as the molar fraction of water increases. A steady state solution was not achievable for the 25% water vapour case, which implies

that the dilution limit is reached between 20-25% which is in good agreement with the experimental value quoted throughout literature of 26%.

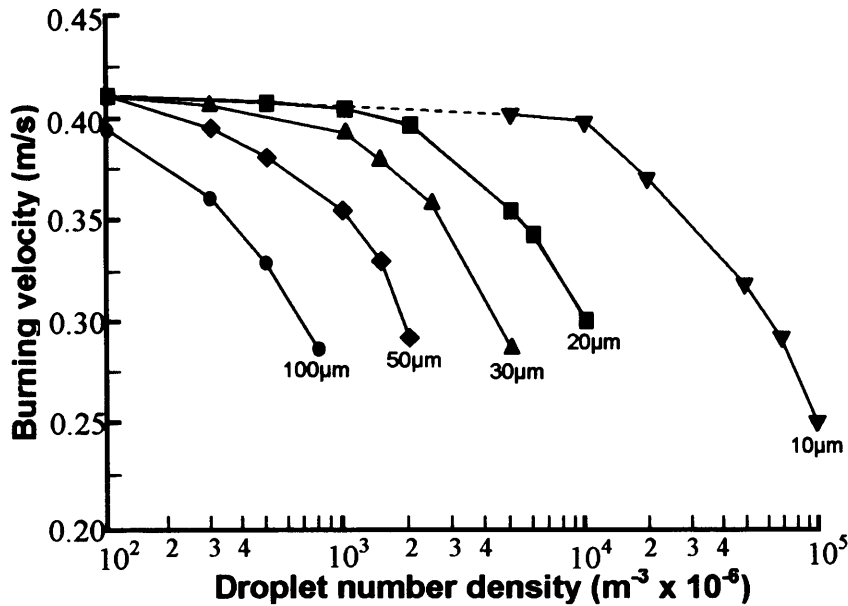


**Figure 2.17** Variation in computed burning velocities in stoichiometric pre-mixed methane-air allowing for evaporation of 10, 20, 30, 50 and 100µm diameter water droplets

Droplet evaporation was computed via a d-squared law, with the k value being time resolved. Clearly the smaller the droplet size, the larger the droplet number density required for quenching. It was assumed that when a higher number density was utilised, and no meaningful result could be calculated then the quenching limit had been reached. A summary of these results is given by Table 2.2.

**Table 2.2** Summary of mono-disperse spray characteristics at critical loading densities, just before failure of the flame solution for a range of initial droplet diameters at corresponding critical number densities for inhibition

Droplet Diameter (µm)	Number density (m <sup>-3</sup> ) x 10 <sup>-10</sup>	Volume Fraction x 10 <sup>4</sup>	Loading Density kg m <sup>-3</sup>
10	11	0.6	0.06
20	1.2	0.5	0.05
30	0.65	11	0.1
50	0.25	1.7	1.7
100	0.08	4.2	4.2

As can be seen from the graph and table the basic trend is that the larger the droplet the higher the volume/mass of liquid required to cause mitigation however, below 20µm this is not the case owing to the fact that very small droplets fully evaporate in the preheat zone thus have no further effect down stream.

Therefore this study seems to suggest that droplets of between 10-20 $\mu\text{m}$  are most effective at mitigating a laminar methane flame and a loading density of 0.05-0.06 $\text{kg}/\text{m}^3$  is required to bring about total mitigation of a flame. The effectiveness of the droplets is increased as an inhibitor by the addition of alkali salts, and this effect is thought to be of purely chemically based, whereby the alkali metals could act as a catalyst (M) as illustrated by the following equations:-



This illustrates the potential benefits of using sea water as a suppressant in offshore applications, as demonstrated and discussed earlier by Zheng et al [38].

Another computer model investigation of the effect of mono-dispersed water mists on the extinction behaviour of freely propagating, stoichiometric, premixed, methane-air flames was conducted by Yang and Kee [47]. An adaptive Eulerian mesh was used to calculate the gas-phase conservation equations, and the droplet dynamics are expressed in a Lagrangian framework. The model was then used to predict how burning velocity and extinction conditions are influenced by the number concentration and size of droplets present. A summary of their results is presented in Figure 2.18.

Again it is demonstrated that the most effective size of droplets in the suppression of a methane-air flame is between 10-20 $\mu\text{m}$ , and droplets in this range appear to be more effective than water vapour. A value of approximately 0.16 by mass seems to be sufficient to quench a flame, which seems low in comparison to other studies conducted. However, once again the general conclusion that laminar burning velocity is dependent on both initial water loading and droplet diameter with smaller droplets being more effective is consolidated, whilst it is also shown that there is no advantage seeking droplets smaller than 10 $\mu\text{m}$ .

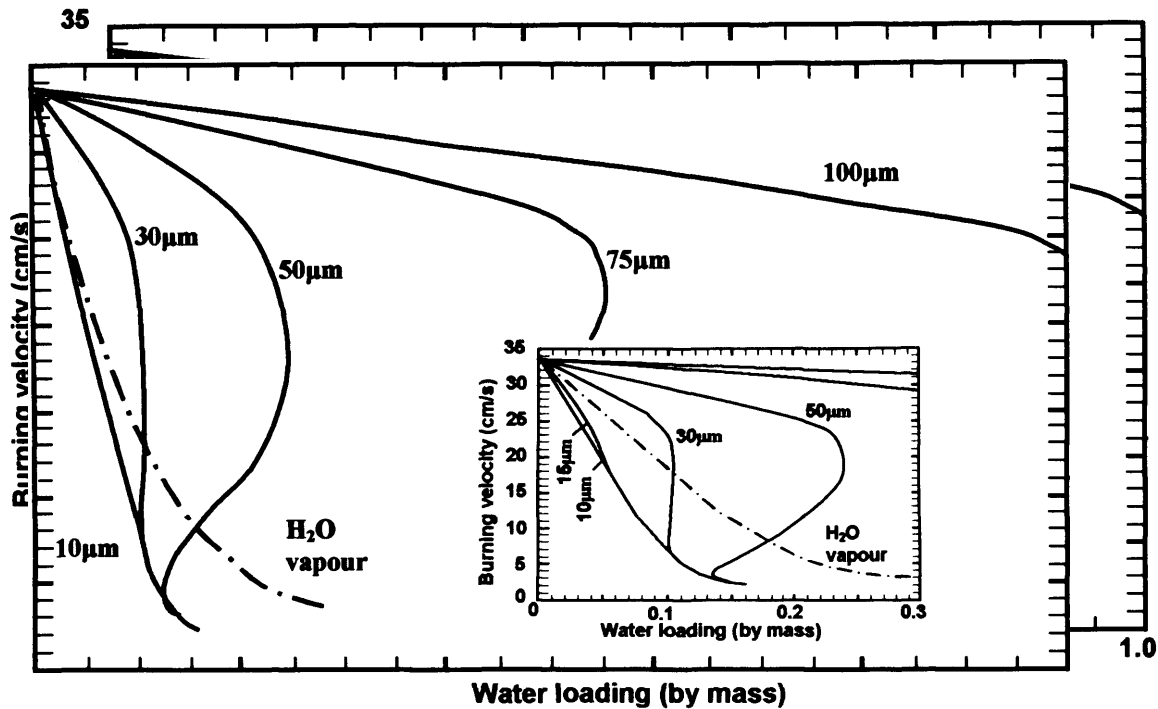


Figure 2.18 *Burning velocities as a function of initial water loading and droplet size. Inset figure provides an expanded view of the low-loading region*

A summary of both Fuss et al [42] and Yang and Kee [47], is given by Fuss et al [48]. This study demonstrates the usefulness of laboratory-scale experimental studies in the appraisal of computer models.

## 2.2 Summary of findings

The molar concentration of water vapour required to inert a stoichiometric methane-air mixture is about 25%. However, the literature suggests that to quench an established propagating flame is a more demanding criterion requiring larger masses of water. This effect could be explained by work illustrating the effects of flame strain which can decrease as a flame grows thus making the extinction of a developed flame harder. The introduction of water through water sprays or mists introduces an evaporation timescale via the size of constituent droplets, and so the droplet size population of water sprays for the purpose of explosion suppression becomes a critical characteristic.

A broad range of previous studies – both numerical and experimental - have shown that for use of water sprays in suppressing explosions, the optimum constituent droplet size is between 10-30µm. In the context of this research study, there are two ways in which

water sprays can be introduced into a gaseous explosive environment to provide this type of mist and hence reduce the severity of an explosion; first utilising sprays with larger mean droplet sizes (several hundred microns), which then break down aerodynamically into a micromist providing the droplet Weber number is sufficiently high, and secondly, providing a water mist with suitable characteristics at source. It is important to note that the aerodynamic break-up approach requires prescribed characteristics of the explosion itself, so is not always successful in reducing explosion flame speeds and overpressures, and indeed in some situations, can exacerbate the situation. Hence, in some practical industrial environments, providing the water mist at source is the only possible option available.

All previous water mitigation research studies of propagating rather than stationary flames have investigated the aerodynamic break-up approach, leaving the study of generation of fine water mist and their interaction with propagating flames relatively unexplored. There are practical reasons for this, in that providing sub-30 $\mu\text{m}$  mists in large quantities at source is extremely difficult, and requires non-standard atomisation methodologies. Generating such fine mists for controlled laboratory studies of their interaction with propagating flames is also a demanding proposition, given that most practical atomisation technologies provide turbulent, inhomogeneous, polydispersed sprays.

Hence, it is concluded that the aim and objectives of this programme are very well posed, and extremely timely. The interaction of fine-mist from source interacting with propagating laminar and turbulent flame fronts will be explored for the first time, whilst a novel practical thermodynamic method for generating very large quantities of fine mist will be appraised quantitatively.

### **3.1 Description of Measurements Required for Study**

To realise the objectives set out in Chapter 1, it is necessary to develop appropriate experimental facilities, diagnostics and methodologies. Many variables will need to be measured so that meaningful, quantified conclusions may be determined.

In order that suitable water mist can be both generated and characterised, there is first the need to measure the size of water droplets produced in the purpose of experiments in Chapters 4, 6, 7 & 8. Due to the different rigs utilised, a number of different sizing techniques are required and these are described in section 3.2.

To determine the effect of water (vapour and mist) on flame speed, it is necessary in Chapters 5, 6 & 7 to quantify the flame speed within two test rigs. Therefore methods capable of doing this are described in section 3.3

Instruments necessary for the transient recording of both flame growth - in Chapters 5 & 6 - and voltage signals - particularly useful in recording pressure and temperature measurements for Chapter 4, and in readings for flame speed quantification in Chapter 7 are detailed in section 3.4. The NAC-1000 video recording unit and National Instruments Data Acquisition (DAQ) system are thus discussed.

## 3.2 Droplet Measurement

### 3.2.1 Malvern Mastersizer $\chi^{\text{TM}}$

The Malvern Mastersizer  $\chi^{\text{TM}}$  is a laser-based system that relies on a light diffraction technique to determine the size of particles, as originally proposed by Swithenbank et al. [50]. This technique is of considerable use within this work as it is capable of measuring particles in the 1-100 $\mu\text{m}$  range, is capable of '*temporally-based*' droplet size distribution characterisation, and its errors are minimised within the environment of the Cardiff cloud chamber, due to its original design (discussed later).

There is a range of possible solids and media that may be investigated, utilising the Malvern Mastersizer  $\chi^{\text{TM}}$  as detailed below in Table 3.1.

**Table 3.1 Laser Analysis Measurement Range**

<b>Suspension</b> \ <b>Solid</b>	<b>Gas</b>	<b>Liquid</b>	<b>Solid</b>
<b>Gas</b>		Fuel sprays; Paint sprays; aerosols; inhalers	Powders not liquid dispersible; Pneumatic transport
<b>Liquid</b>	Bubbles	Emulsions; Two phase liquids	Powders easily liquid dispersed; Cohesive powder
<b>Solid</b>			

As can be seen in Table 3.1 there are unlimited applications for which this apparatus may be used to size particles, with only a selection of these possibilities presented. The application utilised in this thesis is liquid in gas.

A description of the basic configuration and theory utilised by the Malvern Mastersizer  $\chi^{\text{TM}}$  is presented in Figure 3.1 [51]. A coherent Helium-Neon (He-Ne) laser beam is transmitted through a beam expander, the expanded beam of light then travels through a sight channel, which is encapsulated to minimise any background pickup.

Depending upon the properties of the particles to be measured, the laser beam then travels through the measurement volume followed by a Fourier lens, or a reverse Fourier

lens followed by the measurement volume. In the latter case, the measurement volume is contained within a specialised cell mounted to the back of the lens.

After passing through the measurement volume and lens, the light is focused onto two different detectors; the first detector, known as the obscuration detector detects the non-diffracted light, and the second named the Multi-element detector picks up the diffracted light patterns. The readings of these detectors are fed to specialised software on a standard PC, where the signals can be manipulated into data sets, which can be used to fully characterise the particles.

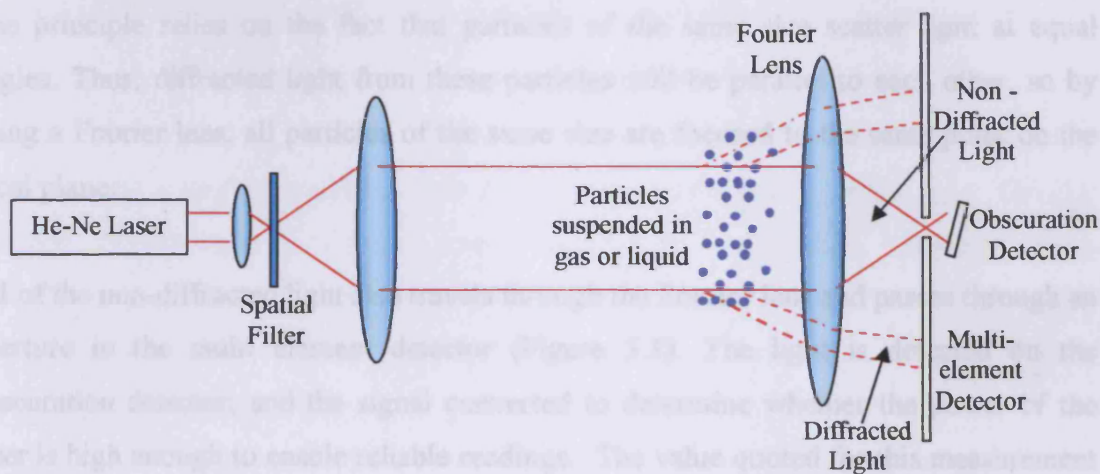


**Figure 3.1 Schematic Representation of the Malvern Mastersizer  $\chi^{\text{TM}}$**

Depending on the type of particles being measured, there is a choice of different lenses that may be used each giving a differing size sample range, as specified below in Table 3.2.

**Table 3.2 Standard Range Lenses for Long Bed Mastersizer  $\chi^{\text{TM}}$**

Configuration	Focal Length	Size Range
Reverse Fourier	45 mm	0.1 – 80 $\mu\text{m}$
Fourier	100 mm	0.5 – 180 $\mu\text{m}$
Fourier	300 mm	1.2 – 600 $\mu\text{m}$
Fourier	1000 mm	4.0 – 2000 $\mu\text{m}$

For the purposes of experiments conducted within this thesis, only Fourier lenses are required and thus discussed. The way in which a Fourier lens works can be easily illustrated by Figure 3.2.

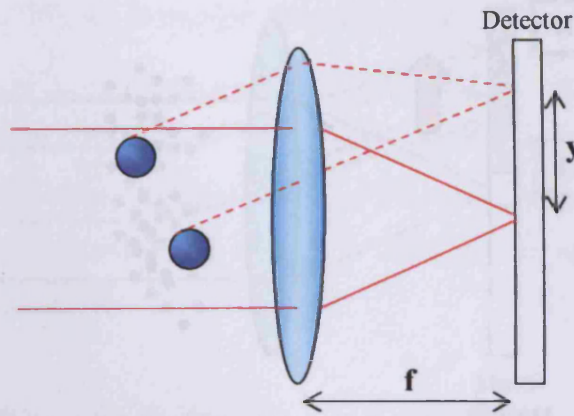


**Figure 3.2 Schematic of how a Fourier transform occurs**

The principle relies on the fact that particles of the same size scatter light at equal angles. Thus, diffracted light from these particles will be parallel to each other, so by using a Fourier lens, all particles of the same size are focused to the same point on the focal plane.

All of the non-diffracted light also travels through the Fourier lens and passes through an aperture in the multi element detector (Figure 3.1). The light is detected on the obscuration detector, and the signal converted to determine whether the power of the laser is high enough to enable reliable readings. The value quoted for this measurement within the software is the obscuration limit, and this value should be kept within the range of 6-50% to ensure accurate measurements.

If the obscuration (concentration) limit is too low, then there are not enough data points to ensure valid, accurate measurements, however if the obscuration is too high, then a phenomena known as multiple scattering is likely. This effect (Figure 3.3) leads to a higher scattering angle, consequently the reading quoted for particle size will be smaller than the actual size of the particles.

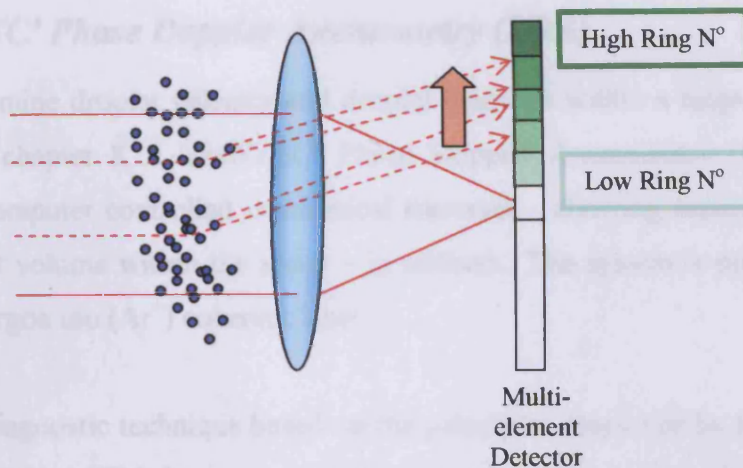


**Figure 3.3 Schematic representation of the effect of high obscuration on particle sizing**

Another associated problem with the type of light scattering technique utilised by the Malvern Mastersizer  $\chi^{\text{TM}}$  is the effect known as ‘vignetting’. This effect happens due to differing scatter angles associated with different sizes of droplets (Figure 3.4). Smaller droplets diffract light at a larger scatter angle than larger ones. Therefore if the measurement volume is located too far away from the Fourier lens, then the light scatter from the smaller droplets may be lost from the processed data, thus biasing the data in favour of the larger droplets.

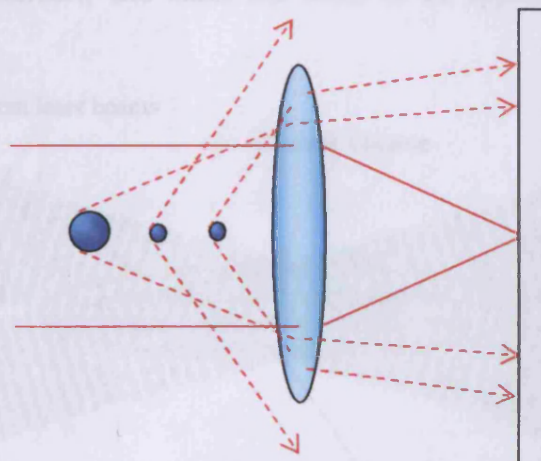


**Figure 3.4 Schematic depicting angles of diffraction associated with different size particles that lead to vignetting problems**

### 3.2.2 'DANTEC' Phase Doppler Anemometry (PDA)

In order to determine droplet velocity and droplet diameter within a large-scale release as discussed in chapter 8, a 'DANTEC' Phase Doppler Anemometry (PDA) system mounted on a computer controlled mechanical traverses - allowing accurate control of the measurement volume within the spray - is utilised. The system is powered by a 5 Watt 'Innova' Argon ion ( $\text{Ar}^+$ ) coherent laser.

PDA is a laser diagnostic technique based on the principles employed by Laser Doppler Anemometry (LDA). PDA is a non-intrusive laser based technique that enables the simultaneous measurement of diameter, velocity (up to 3 components), mass flux and concentration of spherical particles within a flow. The technique was first proposed by Durst and Zaré in 1975 [52]. Due to its usefulness within many applications, commercially available systems were released as early as 1984.

The system relies on a particle, which in this case is a water droplet, passing through a control volume. The control volume shown in Figure 3.5 is made at the point where two coherent laser beams intersect, and takes the form of an approximate 3 dimensional ellipsoidal.

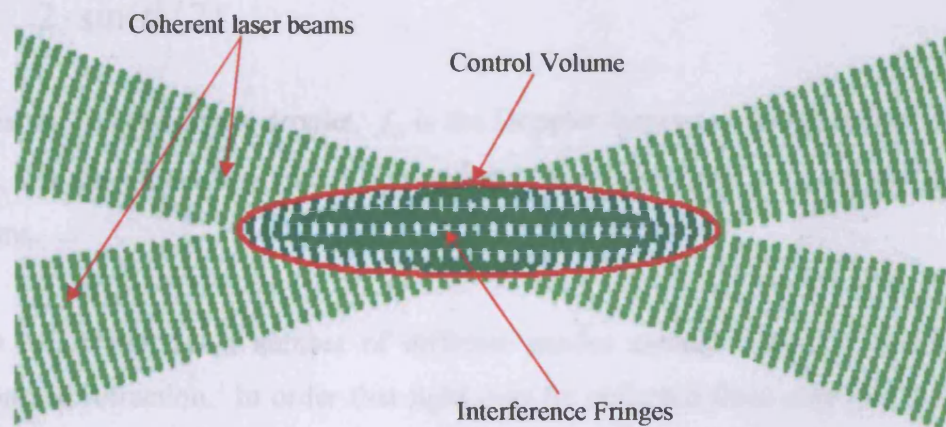


**Figure 3.6 Control Volume Formed by intersection of two Coherent Laser Beams**

The number of fringes, size and shape of the control volume are governed by a number of factors, primarily the wavelength of light used, and the angle of intersection. Spatial resolution and the velocity and size ranges that can be measured are determined by the dimensions of the control volume, thus by adjusting the focal length and beam separation of the laser source, it is possible to produce a suitable system for differing sprays.

When a droplet passes through the control volume (Figure 3.7) in a perpendicular direction to the fringes, it scatters light.

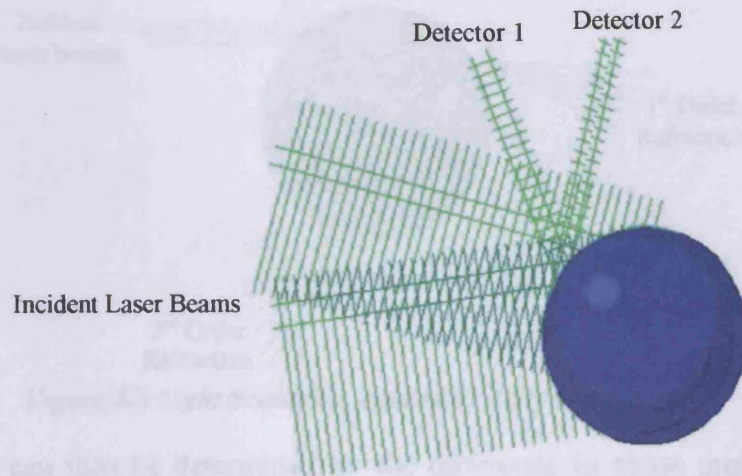


**Figure 3.7** Light scattering from a droplet whilst passing through PDA control volume

The droplet passing through the control volume results in a signal pulse having a specific frequency, which can be used to determine the droplets velocity as given by (3.1):-

$$u = \frac{f_D \cdot \lambda}{2 \cdot \sin(\theta/2)} \quad (3.1)$$

where  $u$  is the velocity of the droplet,  $f_D$  is the Doppler frequency detected at any of the detectors,  $\lambda$  is the wavelength of the light and  $\theta$  is the intersection angle of the incident laser beams.

The light can scatter via a number of different modes namely reflection, diffraction, absorption and refraction. In order that light may be collected from only the dominant mode of scattering, the receiving optics must be positioned so that only light from either reflection or refraction dominates (Figure 3.8). Studies by Bates et al. [53] have indicated that for refractive indices greater than unity, the first order refraction should be used, thus for water which has a refractive index of 1.33, a 'Brewster' angle of approximately  $72^\circ$  is optimal.

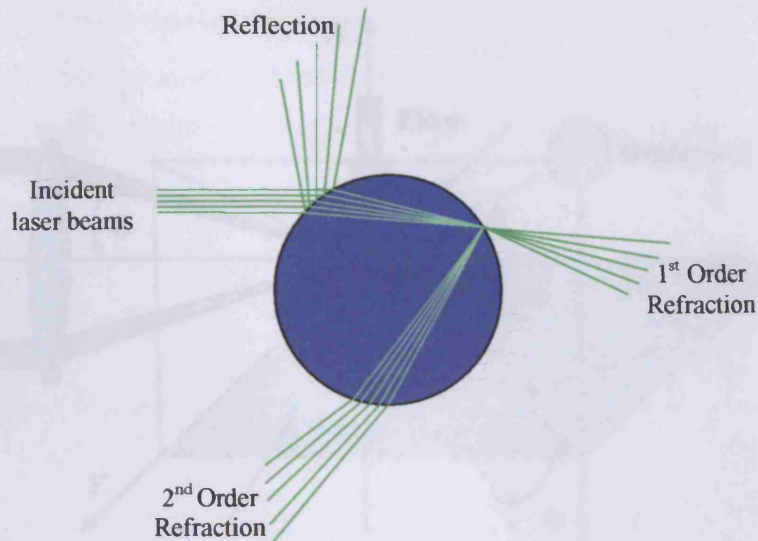


**Figure 3.8** *Light Scattering caused by a liquid droplet*

The droplet size can then be determined by the difference in phase measured by the detectors (Figure 3.9).

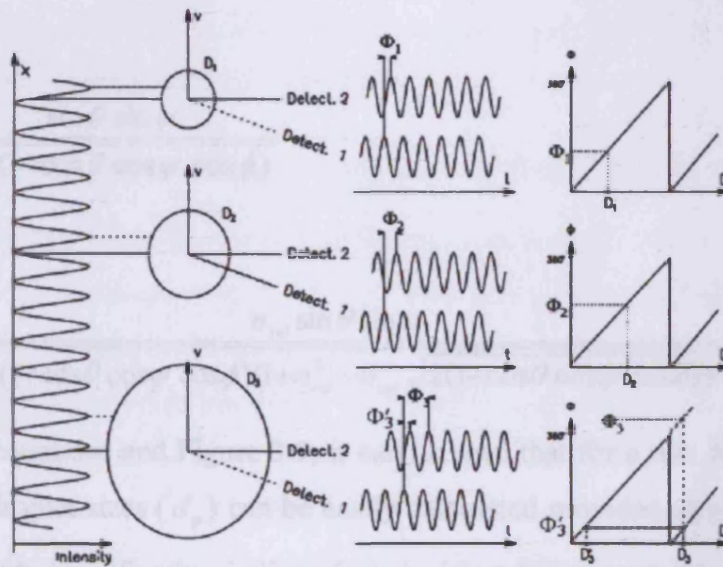


**Figure 3.9** *Droplet Sizing by comparison to phase change*

For a PDA setup (Figure 3.10), it can be shown that the phase change for reflection and 1<sup>st</sup> order refraction can be expressed by equations 3.2 and 3.3 respectively.

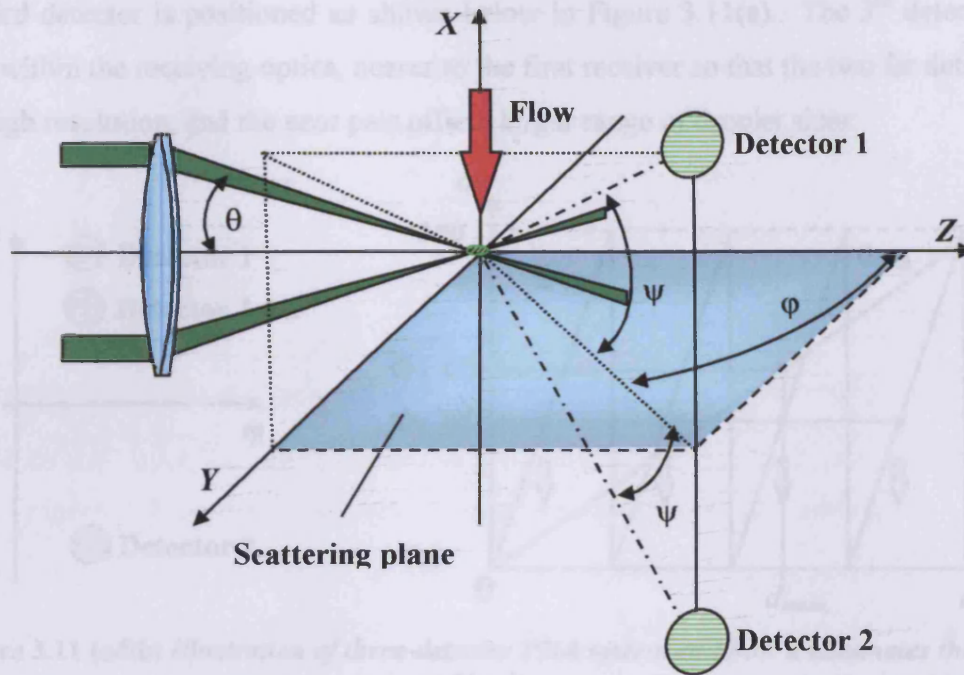


**Figure 3.10** Illustration of PDA setup demonstrating scattering angles for detector placement

$$\Phi = \frac{2\pi d_p}{\lambda} \frac{\sin \theta \sin \psi}{\sqrt{2(1 - \cos \theta \cos \psi \cos \phi)}} \quad (3.2)$$

$$\Phi = \frac{-2\pi d_p}{\lambda} \frac{n_{rel} \sin \theta \sin \psi}{\sqrt{2(1 + \cos \theta \cos \psi \cos \phi)(1 + n_{rel}^2 - n_{rel} \sqrt{2(1 + \cos \theta \cos \psi \cos \phi)})}} \quad (3.3)$$

From the above equations and Figure 3.9, it can be seen that for a two detector system, relatively small droplet sizes ( $d_p$ ) can be easily calculated provided parameters such as scatter angles ( $\psi$  &  $\phi$ ), refractive indices ( $n$ ), incident beam angle ( $\theta$ ) and the laser beams wavelength ( $\lambda$ ) are specified.

However, there is a fundamental deficiency of this system, which is illustrated by the largest droplet shown in Figure 3.9. As can be seen, the droplet can be misrepresented as a small droplet owing to the fact that the phase change is greater than  $2\pi$  ( $360^\circ$ ). This phenomena is known as the  $2\pi$  ambiguity, and is overcome relatively simply by adding a third detector.

The third detector is positioned as shown below in Figure 3.11(a). The 3<sup>rd</sup> detector is placed within the receiving optics, nearer to the first receiver so that the two far detectors offer high resolution, and the near pair offer a larger range of droplet sizes.

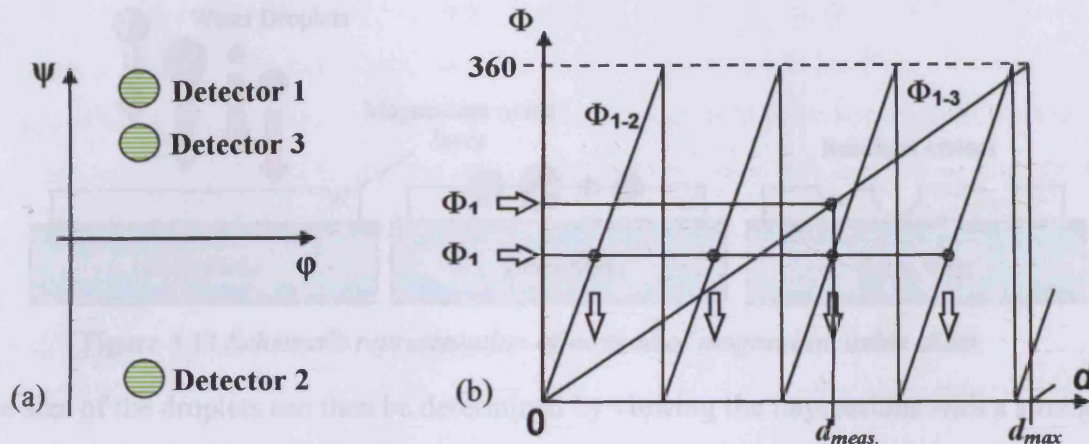


Figure 3.11 (a&b) Illustration of three-detector PDA system and how it eliminates the  $2\pi$  ambiguity

The third detector as shown in Figure 3.11(b) removes the ambiguity, and increases the diameter range that can be accurately measured.

### 3.2.3 Direct Impact Method Using Magnesium Oxide Slides

This method of droplet sizing pre-dates laser techniques, but still has its relative merits. Namely the method is cheap, easy to set-up, hard copies of the results can be kept indefinitely, and the method can work in 'moist' environments with no fear of 'fogging' lenses or damaging equipment. Moreover, in principle multiple systems can be set up cheaply, to facilitate spatial resolution.

The Magnesium Oxide slides can be made relatively easily in a laboratory by simply lighting a strip of magnesium and waving the tip of the flame backwards and forwards under a clean glass microscope slide. The magnesium oxide layer adheres to the glass slide, giving a soft and smooth white surface, with the oxide grain size being approximately  $0.5 \mu\text{m}$  [54]. The thickness of the coating should be varied by increasing the number of passes of the flame tip, and should be at least as thick as the diameter of the droplets measured [54 & 55].

The method relies on a particle, in this case a water droplet, actually hitting a prepared surface of Magnesium Oxide (Figure 3.12). The droplets impact upon the oxide layer they penetrate the surface, thus leaving a well-defined circular crater.

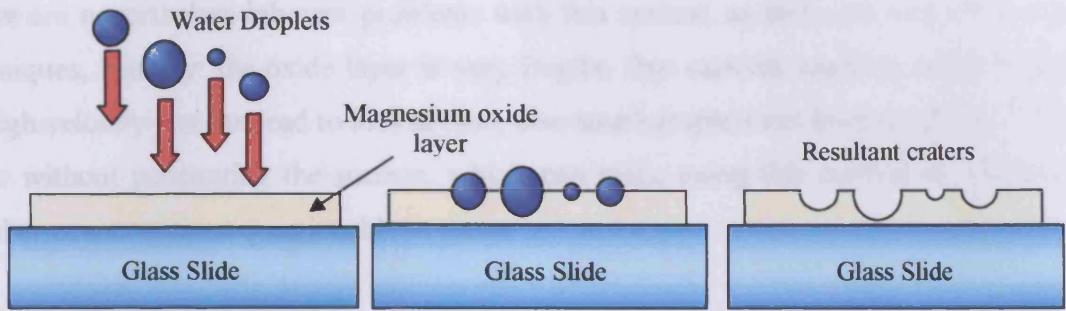


Figure 3.12 Schematic representation of method of magnesium oxide slides

The size of the droplets can then be determined by viewing the impressions with a strong transmitted light into a suitably powerful microscope. Because the size of the crater will always exceed the original size of the droplet, calibration factors as demonstrated by Figure 3.13 should be applied.

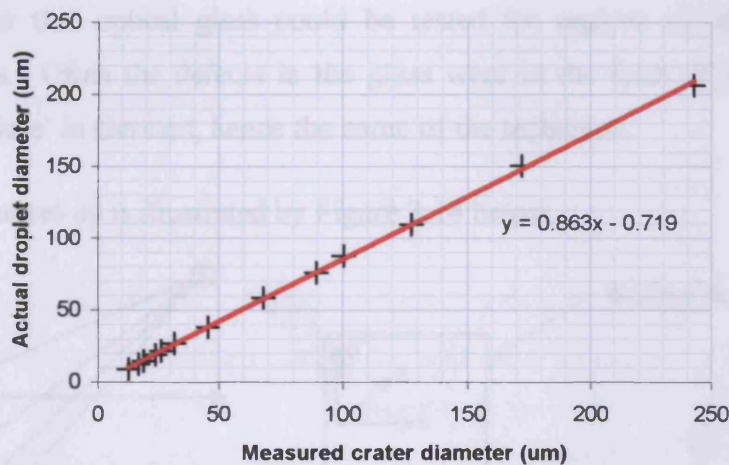


Figure 3.13 Correlation derived from May [54] to convert measured to actual size of water droplets

As can be seen from the figure above, correction factors of 0.86 should be applied to droplets > 20µm, 0.8 for droplets between 15-20µm and 0.75 for droplets of 10µm or less [54]. Droplets of less than 10µm are hard to record for low impact rates but at high impact rates, it is possible to measure droplets as small as 5µm.

It is suggested by DalaValle [56] that for non-homogeneous sprays over 200 sample points should be taken, and for rigorous droplet size distributions, several thousand

samples are usually sought. However in the case of homogenous sprays this number may be reduced significantly.

There are nevertheless inherent problems with this system, as there are with all sizing techniques, Namely: the oxide layer is very fragile, thus careless handling of the slides or high velocity jets can lead to loss of data, also small droplets can bounce off the oxide layer without penetrating the surface, which can make using this method to calculate number concentrations questionable at times.

### 3.3 Flame Speed Measurement

#### 3.3.1 Schlieren Photography

Schlieren photography is a technique that has been used extensively to examine flow fields in a number of different applications [57]. The method was developed in Germany in order that optical glass could be tested for regions of inhomogeneous internal structures. Often the defects in the glass were in the form of streaks, which translates to 'schliere' in German, hence the name of the technique.

A typical Schlieren set-up is illustrated by Figure 3.14 below.

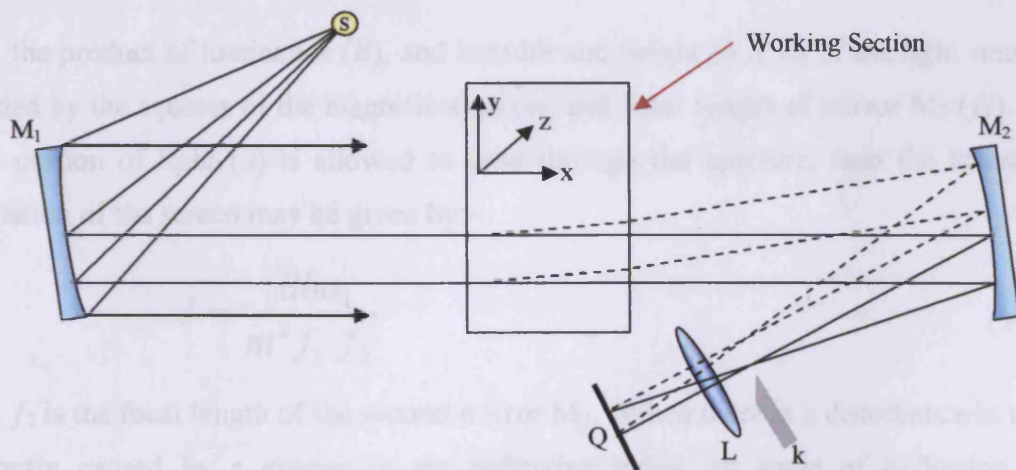


Figure 3.14 Illustration of a typical Schlieren apparatus based around two concave mirrors

A Schlieren system as demonstrated above in Figure 3.14, is constructed by positioning a light source at a distance of the focal length of the first mirror ( $M_1$ ). This causes the working section to be fully illuminated by a collimated beam of parallel light.

The collimated beam of light is then passed onto a second concave mirror ( $M_2$ ), which can be positioned at a convenient distance after the working section. This causes an image of the source to be formed at the focal point of the second mirror, at the point depicted by the tip of the knife edge ( $k$ ).

The image of the working section can then be focused using a lens onto a viewing screen or photographic plate, so the image may be viewed or recorded. If there is no refractive gradient within the working section, then there will be no difference in image compared with that of normal photography. However, if there is a gradient change in or across a small area of space, then there is a deflection of light ( $\epsilon$ ). This deflection of light causes the image of the source to move a small distance on the focal plane. This movement of the focal point can be given by  $f_2\epsilon$ , where,  $f_2$  is the focal length of the mirror  $M_2$ . The image of deflected light is then brought to focus at a corresponding point on the viewing screen Q.

The sensitivity of this system can be determined by examining the illumination ( $I_o$ ) of the screen Q. The illumination may be given by the following:-

$$I_o = \frac{Bbh}{m^2 f_1^2} \quad (3.4)$$

where, the product of luminance ( $B$ ), and breadth and height ( $b$  &  $h$ ) of the light source is divided by the squares of the magnification ( $m$ ) and focal length of mirror  $M_1$  ( $f_1$ ). If only a portion of light ( $a$ ) is allowed to pass through the aperture, then the lowered illumination of the screen may be given by:-

$$I = \frac{Bba}{m^2 f_1 f_2} \quad (3.5)$$

where,  $f_2$  is the focal length of the second mirror  $M_2$ . When there is a disturbance in the light beam caused by a change in the refractive index, an angle of deflection is introduced  $\delta\epsilon$  then a movement of the focal point of  $f_2\delta\epsilon$  is observed. Therefore another change in illumination is observed on the screen, and this may be given by:-

$$\delta I = \frac{Bb \delta\epsilon}{m^2 f_1} \quad (3.6)$$

The contrast ( $c$ ) of the system can thus be given by:

$$c = \frac{\delta I}{I} = \frac{f_2 \delta \epsilon}{a} \quad (3.7)$$

The sensitivity ( $S$ ) of the system can then be shown to be:

$$S = \frac{dc}{d\epsilon} = \frac{f_2}{a} \quad (3.8)$$

Thus, it can be seen that to improve the sensitivity of a particular system, it may be necessary to increase the focal length of the second mirror  $M_2$ , or to decrease the portion of light passing the knife edge.

In order that Schlieren photography may be used to determine the flame speed of a methane flame within the cloud chamber, it is necessary to film the event with a high-speed camera. For the purpose of this experimental programme, the NAC-1000 system discussed in section 3.4.1 was used.

### 3.3.2 Ionisation Probe Technology

Ionisation probes have been used extensively to measure flame speeds in numerous studies, many of which are discussed in Chapter 2. An ionisation probe may be represented by the following Figure 3.15.

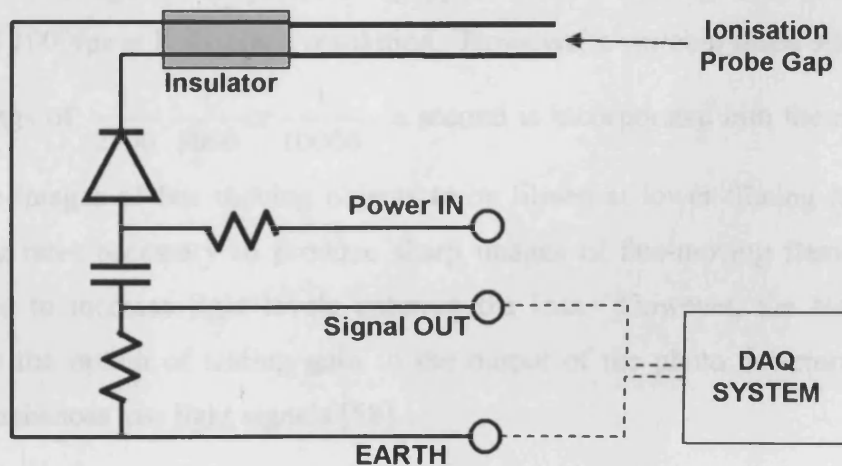


Figure 3.15 Typical ionisation probe circuit

The systems work on the principle that within the reaction zone of a propagating flame, there is a large ionisation effect. This phenomenon causes a brief short circuit across the ionisation probe gap as the flame passes. This short circuit causes the capacitor to discharge for the duration of the short, and this discharge may be measured using a suitable oscilloscope or data acquisition system.

By locating a number of ionisation probes at set distances from one and other, it becomes possible to accurately measure the time differences between the voltage spikes produced by each probe and hence possible to derive a flame speed for a propagating flame. The ionisation probes used for this study were utilised in conjunction with the National Instruments Data Acquisition system described in section 3.4.2.

## **3.4 Data Acquisition**

### ***3.4.1 NAC-1000 Video Recorder***

In order that the data acquisition of visual images could be undertaken for flame structure and flame speed measurements required in Chapters 5 & 6, it was necessary that a high speed filming technique be employed. A high speed NAC-1000 video system, donated by Shell Research Ltd., was available and suitable for such an application.

The system consists of high-speed camera which connects to a VHS video based recording unit. The high-speed system is equipped to allow filming rates of 500fps at full-screen and 1000fps at half-screen resolution. However, a variable speed shutter that has three settings of  $\frac{1}{2500}$ ,  $\frac{1}{5000}$  or  $\frac{1}{10000}$  a second is incorporated into the apparatus allowing sharp images of fast moving objects to be filmed at lower filming rates. At high shuttering rates necessary to produce sharp images of fast-moving flame fronts, there is a need to increase light levels entering the lens. However, the NAC-1000 system affords the option of adding gain to the output of the photo detectors, which electronically enhances low light signals [58].

### 3.4.2 National Instruments DAQ System

The data acquisition system used to monitor pressure and temperature traces in Chapter 4 and ionisation probe outputs in Chapter 7 is of the form of a National Instruments PC based data acquisition system. The system is built around AT-MIO-16E2 DAQ board [59], which is fitted to a standard Pentium II PC. This board allows 12 bit resolution with 8 differential channels sampling at 500 kHz.

Voltages of  $\pm 10\text{V}$  can be monitored directly via the board, although for the applications in this study, it is necessary to use a terminal block. During this study, a SCXI-1303 terminal block which was wired to the front of a SCXI-1100 analogue multiplexer allowed up to 32 temperature readings to be sampled at 250 kHz through one of the 8 channels. A SCXI-1302 terminal block coupled to a SCXI-1180 feed-through panel then afforded up to 6 voltage based sensors to be monitored.

The processed signals are then accessed by specialist National Instruments software and transformed into a user-friendly operating format using LabView diagrammatic programming. A view of the operating system screen developed for this study is given by Figure 3.16.

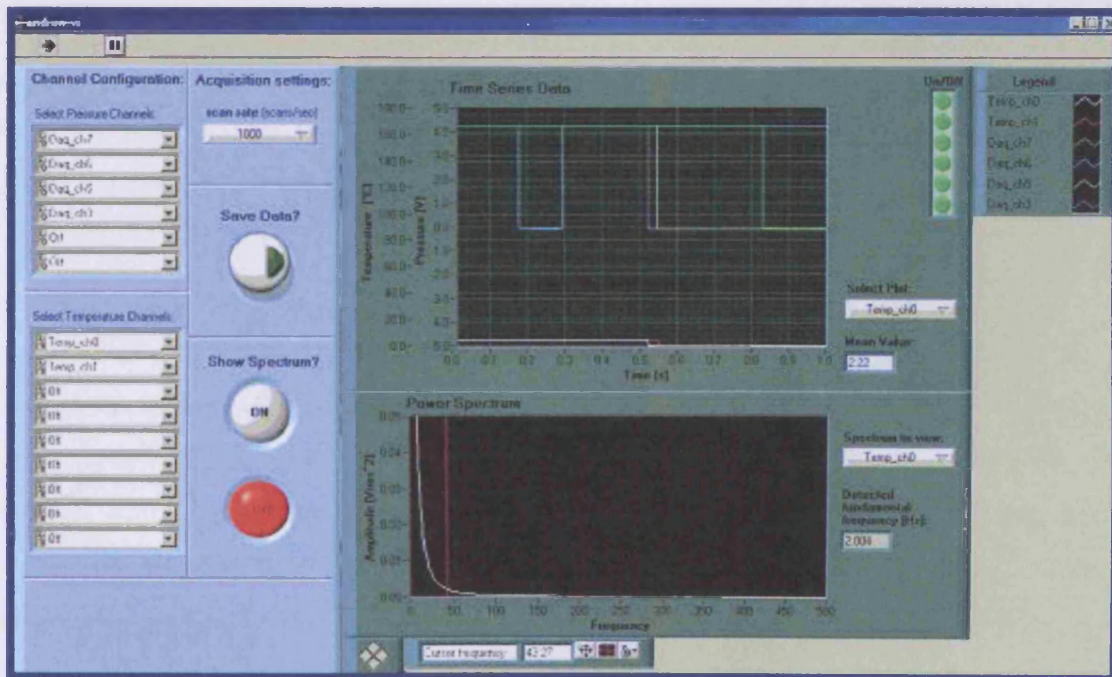


Figure 3.16 User interface for the National Instruments data acquisition system

This particular logger programme allows real time visualisation of the voltage and temperature channels, and allows data recording of 6 voltage signals and 9 temperatures simultaneously at sampling rates of 500, 1000, 5000 and 10000 samples per second. A power spectrum allows the viewing of power traces on each individual channel, thus allowing 'noise' to be monitored and conditioned out of the final data.

The data can then be readily exported to Microsoft Excel, where scaled plots of the sensors outputs can be generated, allowing the accurate measurement of temperature and pressure changes for the purposes of Chapter 4, and the calculation of flame speed from the ionisation probe readings used for Chapter 7.

### **3.5 Summary**

The various advanced measurement diagnostic facilities required and utilised to meet the objectives of this thesis have been introduced and described in this chapter. These techniques and the results they generate will now be referenced at various stages throughout the thesis, with minimal description. However, applicability, inherent limitations and validity/accuracy of data generated will be discussed.

## Generation and Characterisation of Well Defined Mists in the Cardiff Cloud Chamber

### 4.1 Cloud Chamber Technology

In order to generate quiescent mono-dispersed mists within a laboratory style test facility, it is necessary to develop a cloud chamber that relies on basic thermodynamics to create droplets. A number of such facilities have been designed and built over the past century and knowledge gained from these has been used to develop a cloud chamber capable of producing water droplets in the size range considered most effective for the extinction or suppression of propagating flames (10-30 $\mu\text{m}$ ).

#### 4.1.1 Wilson Cloud Chamber

The thermodynamic processes that govern generation of clouds and mists, such as occur in the natural environment, have intrigued scientists for over a century. Wilson (1897) was so inspired that he attempted to simulate such conditions in his Cambridge laboratory; the series of experimental devices he developed became known as 'Wilson Cloud Chambers' [60]. The cloud chamber used to produce water droplets is illustrated by Figure 4.1.

The airspace to be expanded is contained within the cylindrical upturned beaker (*A*), which is fitted like a 'diving bell' beneath the water level in the vessel (*B*), the water level in vessel (*B*), is controllable via the use of tube (*C*). The air space at the top of vessel (*B*) can be evacuated through tube (*D*) when the cork is lifted using string (*M*). This movement of air occurs due to the fact that there is a partial vacuum present in the earthenware vessel (*F*), and the floating cork (*E*) ensures that water cannot leave vessel (*B*).

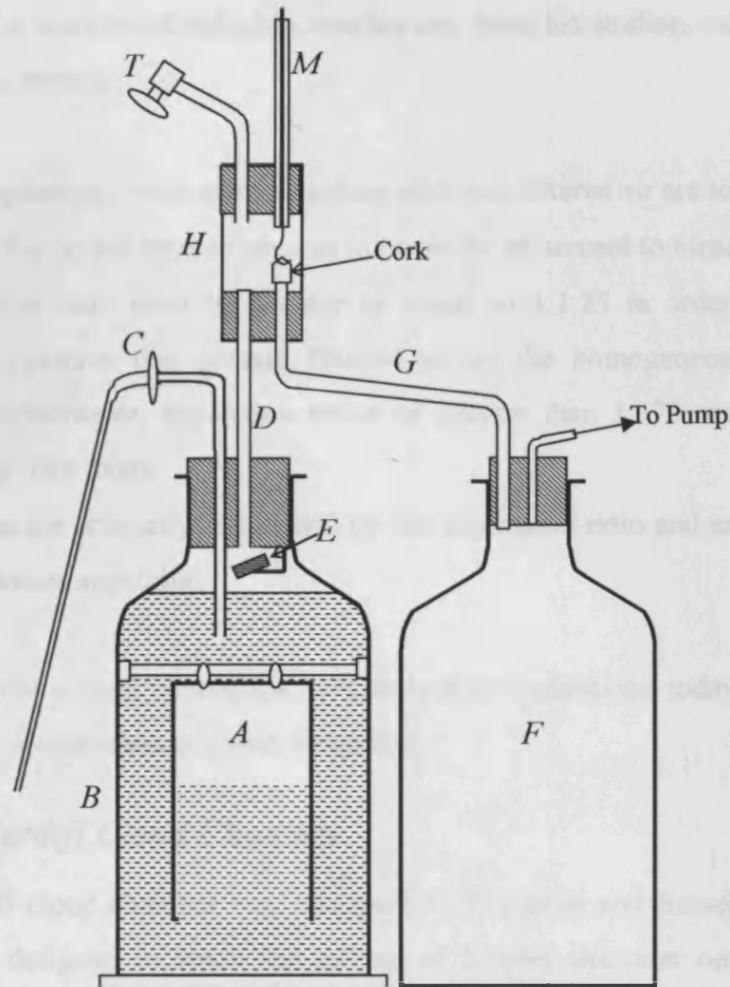


**Figure 4.1** Schematic representation of the original Wilson cloud chamber

The rapid removal of the air from vessel (B) causes the liquid in vessel (A) to drop, thus expanding the airspace in vessel (A). This rapid expansion of the airspace causes there to be a rapid drop in both pressure and temperature. If the airspace in the upturned beaker is totally saturated with water vapour then during the expansion water is forced out of saturation as the temperature drops, and for this reason a mist is observed within the airspace (A); this mist consists of quasi mono-dispersed water droplets. After expansion, the water levels can be returned to normal by opening tap (T) which is open to atmosphere.

By varying the size of the airspace in (B) and the level of vacuum in (F) it was possible to vary the expansion ratio and expansion rate of the airspace in beaker (A), thus allowing a study to be undertaken into the formation of water droplets.

Wilson determined a number of valuable conclusions from his studies, most of which hold true to this day, namely;

- Repeated expansions when experimenting with non-filtered air are to be avoided.
- ‘Dust’ particles do not have to be present in order for an aerosol to form.
- The expansion ratio must be greater or equal to 1:1.25 in order to generate droplets in mixtures that contain filtered air by the homogeneous nucleation process. Furthermore, expansion ratios of greater than 1.375 are required to produce ‘fog’ like mists.
- Droplet sizes are primarily influenced by the expansion ratio and expansion rate in cloud chamber apparatus.

Note in particular the second conclusion, which is still contentious today in terms of understanding fully mechanisms of cloud formation.

#### ***4.1.2 Original Cardiff Cloud Chamber***

The original Cardiff cloud chamber was designed by Cameron and Bowen [61 & 62]. The chamber was designed to study the effects of droplet diameter on the burning velocity of fuel droplet/vapour-air flames. The technology is extrapolated from the fundamentals illustrated by Wilson [60], and new technologies developed by Hayashi et al. [63-65], whilst developing mists with droplet sizes greater and smaller than those of interest in this study.

The original chamber as depicted by Figure 4.2, comprised a 120mm inner diameter stainless steel cylinder fully enclosed by a quartz window at one end, and a piston, edged circumferentially with non-lubricated seals, at the other. The piston was pneumatically-driven such that it may be retracted from an initial position to a pre-set final position at variable speed. Hence, by varying the final piston position post-retraction, and the speed of retraction, independent control of two primary mist control variables was afforded. Temperature within the rig was varied primarily via a heated jacket, and further optical access achieved by two diametrically-opposed quartz windows. Liquid was added into the confined rig using accurate micro-pipettes, though a deficiency of the previous

design was that the rig was slightly vented to atmosphere in the original design as the liquid was added.

As can be seen from Figure 4.2, the original cloud chamber was operated by injecting a known volume of liquid fuel into the chamber. This liquid was then allowed to evaporate fully, saturating the airspace, after which the piston was then retracted causing a pre quantified quiescent mono-dispersed aerosol cloud to form. This vapour/droplet cloud was then ignited using an electrical spark and the resultant explosions recorded using a high- speed cine camera.

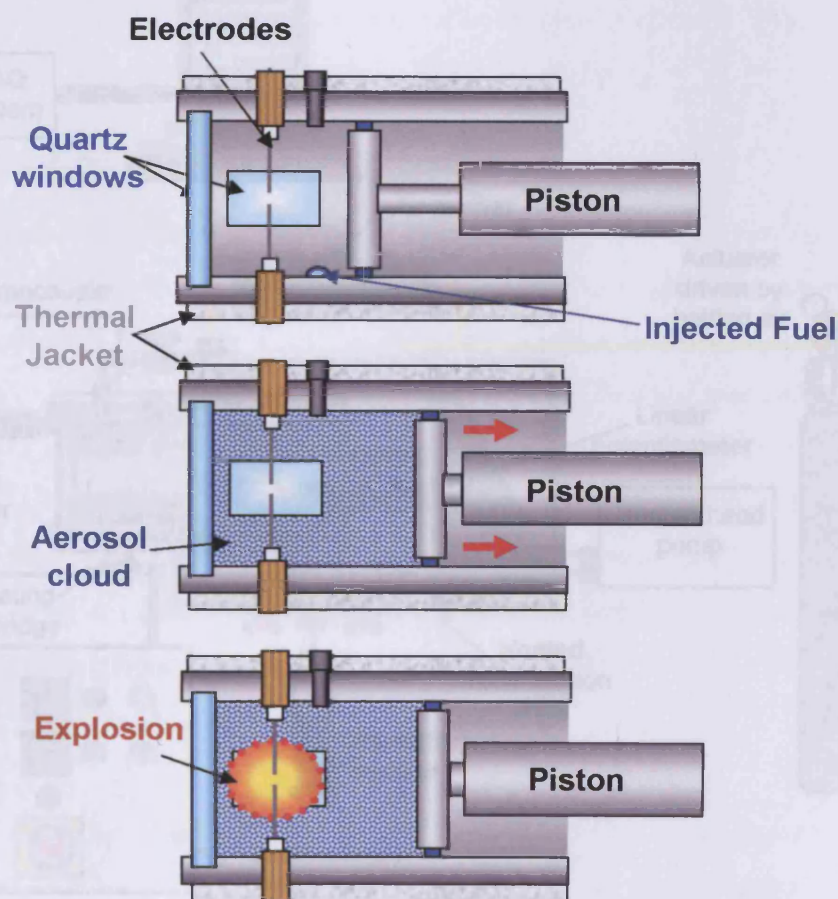


**Figure 4.2** Schematic representation of the original Cardiff cloud chamber

The original Cardiff cloud chamber was a 'novel' technique for generating suitable 'transition-size' fuel mists. The quartz windows facilitated accurate sizing of the droplets using a Malvern Mastersizer<sup>TM</sup>, as documented by Cameron and Bowen [62].

However, there were a number of modifications required to convert this original fuel-mist facility into one that would be suitable for the generation of water mists in the suggested area of interest (10-30 $\mu\text{m}$ ), in a well-defined methane-air environment.

## 4.2 Cardiff Cloud Chamber Development

Before studies could be undertaken into the characterisation of a water mist within a well-defined atmosphere, a number of modifications were required to eliminate perceived weaknesses in the original Cardiff cloud chamber design. These modifications are discussed in the following sections and illustrated by Figure 4.3.

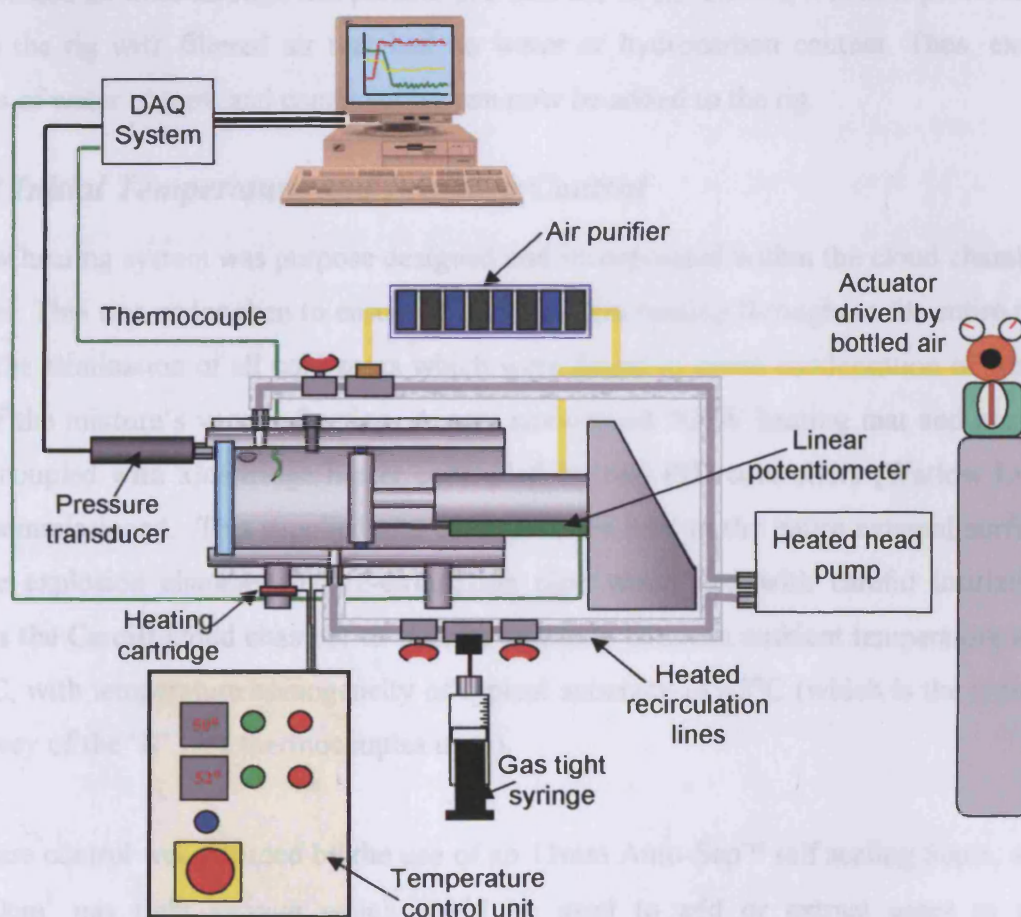


Figure 4.3 Schematic representation of modified Cardiff cloud chamber

### 4.2.1 Gas Mixing and Air Quality

The first modification was the introduction of a new re-circulation system suitable for simultaneous gas-water-air mixing. This consisted of a 5 L/min oil free heated (up to 200 $^{\circ}\text{C}$ ) head diaphragm pump (KNF Neuberger) which allowed the gases to be re-

circulated through the explosion chamber via 6mm stainless steel piping, as shown in Figure 4.3. This modification facilitates a number of improvements, namely better mixing of gaseous or vaporised fuel, suitable locations for introduction of the methane, and a simple entry point for the purging of the rig before and after each experiment set-up. The mixing of the gases was a necessary improvement as it ensured that the air/water mixtures were more homogeneous in terms of mixture ratio and temperature throughout the rig.

An air purifier was built in-house, and consists of a number of silica gel and active charcoal traps with a series of filters in between. By feeding air from the 'clean' compressed air lines through this purifier and into the re-circulation, it is now possible to purge the rig with filtered air that had no water or hydrocarbon content. Thus, exact values of water content and combustibles can now be added to the rig.

#### ***4.2.2 Initial Temperature and Pressure Control***

A new heating system was purpose designed and incorporated within the cloud chamber system. This was undertaken to ensure a more uniform heating throughout the entire rig, with the elimination of all cold spots which were found to cause condensation of water out of the mixture's vapour fraction. A new customised 500W heating mat and heated lines coupled with a cartridge heater controlled by two PID controllers (Watlow Ltd.) was commissioned. This supplied and controlled the heat to the entire external surface of the explosion chamber and re-circulation pipe work, and with careful insulation allows the Cardiff cloud chamber to operate currently between ambient temperature and 120°C, with temperature homogeneity of typical accuracy of  $\pm 2^\circ\text{C}$  (which is the typical accuracy of the 'K' type thermocouples used).

Pressure control was afforded by the use of an 11mm Auto-Sep™ self sealing Septa, and a 100cm<sup>3</sup> gas tight syringe which could be used to add or extract gases to the atmosphere, thus increasing or reducing the pressure within the chamber. An off-the-shelf actual pressure cell (detailed in section 4.3.1) could be used to give an accurate pressure within the system.

### 4.2.3 Piston Retraction

The air supply to the actuator was changed from compressed ‘line’ air from a local compressor, to a bottle source, which improved the range and control of pressure supplied to the actuator. As the actuator pneumatic pressure controls the speed of piston retraction, this in turn induces more reproducible mist generation, with a greater range of quasi-monodisperse droplet sizes, as discussed later

## 4.3 Experimental Diagnostics

### 4.3.1 Initial Thermodynamic Conditions

The remaining diagnostics that required specification before the start of each experiment were the initial thermodynamic conditions. The temperature could be monitored to within 0.1 °C within the chamber so the only other reading necessary was the initial pressure. A ‘Sensym Temperature-Compensated Cell’ –19C series, specified for the range 0-15psia (Farnell Ltd) was integrated into the rig via a self-sealing valve that allowed internal and external pressure readings to be taken from the same sensor. This meant that by using the syringe-system for introducing methane into the rig in reverse, it was possible to add or withdraw gas from the rig to give the exact initial pressure required to within approximately 1mbar.

### 4.3.2 Expansion Ratio and rate

The expansion ratio defined as  $\left(\frac{v_2}{v_1}\right)$ , the volume of the chamber after expansion,

divided by the volume of chamber before expansion, can be controlled using three different aluminium tubes that are placed over the actuator the following expansion ratios within the Cardiff cloud chamber were made possible as illustrated by Table 4.1

**Table 4.1 Expansion ratio properties used for mist formation**

Tube Number	Initial volume (cm <sup>3</sup> )	Final volume (cm <sup>3</sup> )	Stroke length (cm)	Expansion ratio
1	870	1627	6.7	1.87
2	870	1409	4.77	1.62
3	870	1200	2.92	1.38

It should be noted that all of the values are over the value of 1.25 suggested by Wilson [60] as necessary for the formation of a mist.

The expansion rate could be reproducibly changed by varying the supply pressure to the pneumatic actuator, by varying the supply pressure from 4-12bar it was possible to generate retraction speeds of between 0.15-0.45m/s. It was anticipated that this range of expansion rates would enable the required sizes of water droplets to be achieved.

The expansion rate and ratio was recorded by using a linear potentiometer, which was positioned at the back of the piston as shown in Figure 4.3. The potentiometer works by placing a known voltage (0.5V) across the potentiometer then the amount moved by the piston is representative of the output of the potentiometer as shown by Figure 4.4.

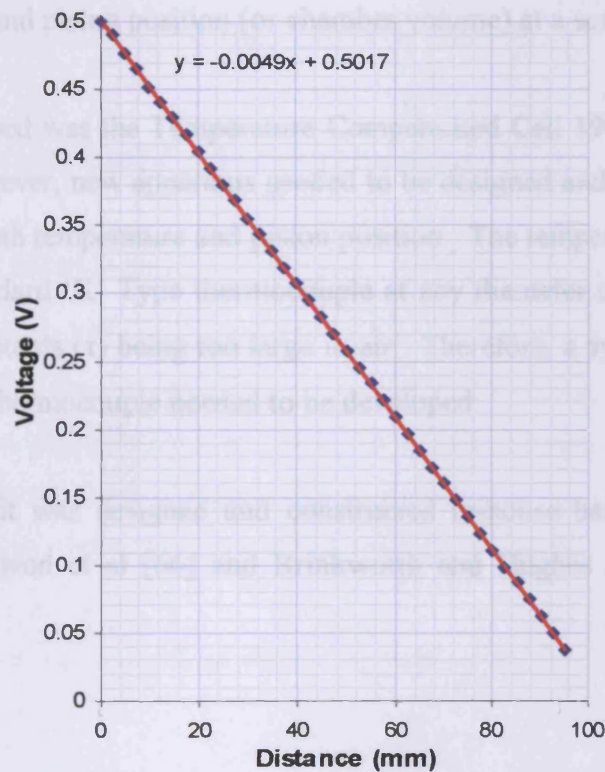


Figure 4.4 Calibration curve of linear potentiometer

By rearranging the calibration equation, the distance moved by the piston could be expressed in terms of voltage. This value coupled with the time scale taken could be used to give an accurate expansion rate, and due to the chamber being constructed in the form of a uniform 120mm diameter cylinder it was thus possible to calculate the effective rate of volume change  $(\frac{dv}{dt})$ .

### ***4.3.3 Quantification of Transient Temperature, Pressure and Piston Kinematics***

Previous studies by various authors [60-65] determined a number of factors affect the size and density of the water mist generated after a rapid expansion. These parameters include initial temperature, initial pressure, expansion ratio, expansion speed and initial water loading. Understanding better the influence of these parameters on mist formation was necessary for further studies into the quenching of laminar methane explosions.

In order that the droplet work could be utilised to compare with model predictions, it was first necessary to devise a system for measuring the aforementioned variables i.e. the initial conditions for any modelling approach. A 'National Instruments' DAQ (as discussed in section 3.5) was utilised which enabled the simultaneous measurement of pressure, temperature and piston position (or chamber volume) at a scan rate of 1 kHz.

The pressure sensor used was the Temperature Compensated Cell 19C series (SenSym) specified earlier. However, new apparatus needed to be designed and commissioned for the measurement of both temperature and piston position. The temperature could not be measured using a standard 'K' Type thermocouple at any diameter currently available, owing to the time constants ( $\tau$ ) being too large in air. Therefore, a system to accelerate the response of a fine thermocouple needed to be developed.

A compensation circuit was designed and constructed in-house based on a previous circuit designed by Kwon et al [66] and Brinkworth and Hughes [67], as shown in Figure 4.5.

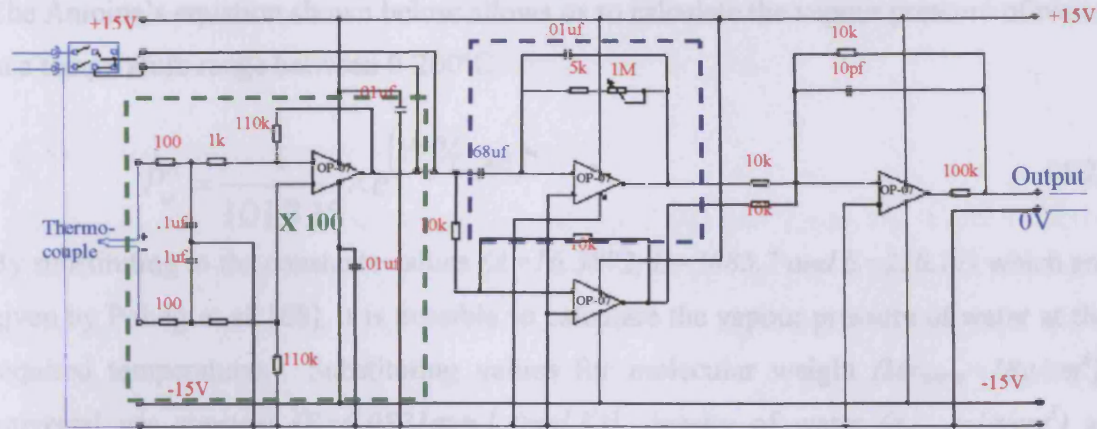


Figure 4.5 Schematic representation of compensated circuit used to speed up the thermocouple response

The circuit first conditions and amplifies the thermocouple input by a factor of 100 (area in green dashed box) then speeds up the response to a level (navy dashed box), enabling a faster response thus, the actual temperature drop to be measured.

## 4.4 Mist Generation and Characterisation

### 4.4.1 Droplet cloud formation

As explained earlier, a cloud of small droplets is formed in the cloud chamber when the piston is retracted causing the saturated mixture to be rapidly cooled, taking the mixture into the wet region of its saturation curve. Hence, to form as dense a cloud as possible it is necessary to calculate the exact volume of liquid that is required for the correct water loading required to achieve 100% humidity at the required temperature.

Thus the following equation is required where the volume to be injected is in units of  $\mu\text{L}$ .

$$V_w = \left( \frac{V_{\text{rig}} \times P_w^{\circ} \times M_{r_w}}{R \times T_{\text{rig}} \times \rho_w} \right) \times 1000 \quad (4.1)$$

As can be seen the volume of water to inject ( $V_w$ ) is dependant on a number of factors most of which are fairly constant. A major problem in the calculation is that the vapour pressure of water ( $P_w^{\circ}$ ) changes with temperature, thus another calculation is required.

The Antoine's equation shown below allows us to calculate the vapour pressure of water in a temperature range between 0-200°C.

$$P_w^o = \frac{1}{101.325} \times e^{\left(\frac{A-B}{T_{rig}+E}\right)} \quad (4.2)$$

By substituting in the constants values ( $A=16.3872$ ,  $B=3885.7$  and  $E=230.17$ ) which are given by Poling et al. [68], it is possible to calculate the vapour pressure of water at the required temperatures. Substituting values for molecular weight ( $Mr_{water}=18g/cm^3$ ), universal gas constant ( $R=0.0821atm.l(mol.K)$ ), density of water ( $\rho_{water}=1g/cm^3$ ) as given by [69] and the volume of the cloud chamber in its current form ( $V_{rig}=910cm^3$ ), it was then possible to generate the curve shown as Figure 4.6. The curve shows the maximum volumes of water than can be evaporated over the temperature range available within the Cardiff cloud chamber.

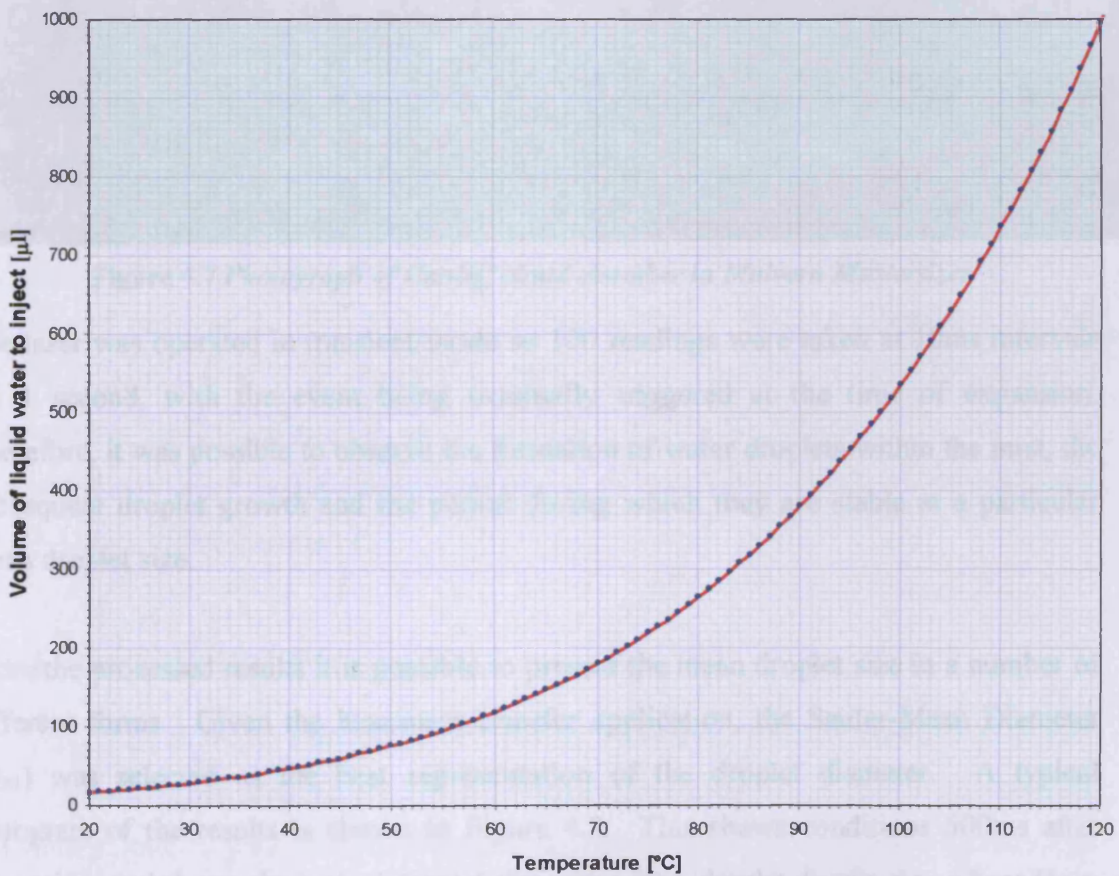


**Figure 4.6 Volumes of water required for 100% saturation of the Cardiff cloud chamber at various temperatures ( $v_i=910cm^3$ )**

To ensure the maximum volumes of water go through the phase change from vapour to liquid, and the densest mist possible is produced, it is essential that the maximum water

loading is injected into the cloud chamber prior to expansion. This can be found by reading off the line of saturation at the temperature to be used.

#### 4.4.2 Characterisation of Mist Formation

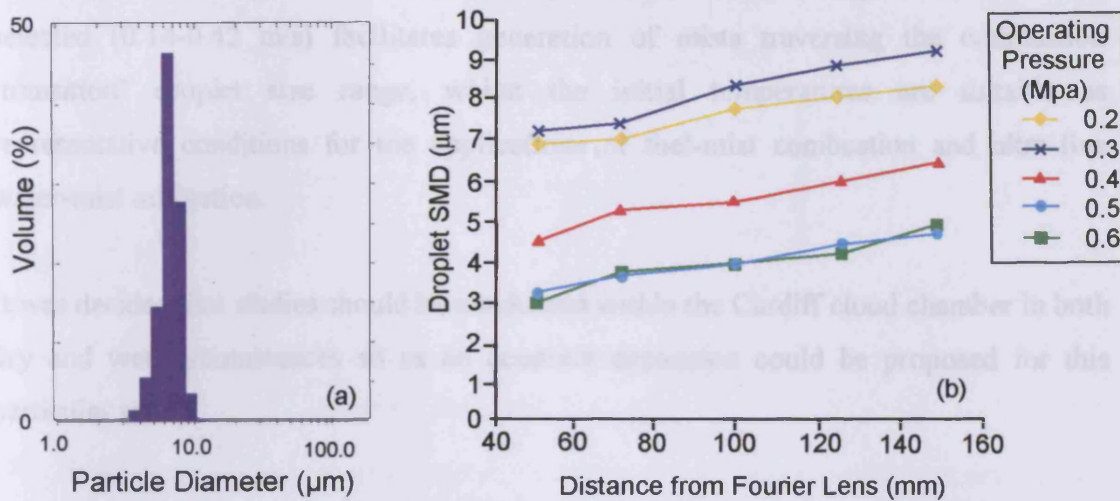
After establishing that a water cloud could be developed using the Cardiff cloud chamber, it was then required to characterise the size of the droplets. This was undertaken using the laser diffraction methodology for particle sizing currently available as a commercial system as the Malvern Mastersizer<sup>TM</sup>. (discussed earlier in section 3.2.1.) The long bench laser type was positioned around the Cardiff cloud chamber as shown by Figure 4.7.



Figure 4.7 Photograph of Cardiff cloud chamber in Malvern Mastersizer

The laser was operated in transient mode so 100 readings were taken at 10ms intervals for 1 second, with the event being externally triggered at the time of expansion. Therefore, it was possible to observe the formation of water droplets within the mist, the subsequent droplet growth and the period during which they are stable at a particular mean droplet size.

From the processed results it is possible to present the mean droplet size in a number of different forms. Given the heat/mass transfer application, the Sauter-Mean Diameter ( $D_{32}$ ) was selected as the best representation of the droplet diameter. A typical histogram of the results is shown in Figure 4.8. This shows conditions 500ms after expansion, and shows the typical droplet size range for a droplet distribution where  $D_{32} = 7\mu\text{m}$ .



**Figure 4.8 (a&b)** Typical histogram showing the number concentrations against droplet sizes within a mist generated by the Cardiff cloud chamber and Vignetting quantification results respectively

By extracting each of these sizes from the Malvern software into a graphical package, it is possible to identify the transient growth and stabilisation of the droplets within the mist.

To ensure vignetting did not effect results within the Cardiff cloud chamber Cameron [61] carried out a series of experiments to determine the effect of ‘vignetting’ on the Cardiff cloud chamber. The results from these experiments as shown by Figure 4.8(b) demonstrates that by keeping the cloud chamber between 50- 150 mm from the Fourier lens would only alter the results by a maximum of 2μm which for the purpose of these studies was considered acceptable.

## 4.5 Experimental Programme

The experimental programme for this chapter and the publication by Crayford et al. [70] was designed to characterise the thermodynamic characteristics of the cloud chamber, and furthermore, to gain a better qualitative understanding of the physical processes that affect the formation of mono-dispersed mists within Cardiff’s cloud chamber. This facilitates better control and predictability of mist generation in the future. The expansion ratio was always chosen to be in excess of that representing Wilson’s supersaturated limit for ‘cloud-like’ generation (1.375) [60], to ensure repeated mist

formation, which was confirmed for each experimental case. The range of expansion rate selected (0.14-0.42 m/s) facilitates generation of mists traversing the combustion ‘transition’ droplet size range, whilst the initial temperatures are suitable as representative conditions for the applications of fuel-mist combustion and ultra-fine water-mist mitigation.

It was decided that studies should be conducted within the Cardiff cloud chamber in both dry and wet circumstances so as an accurate expansion could be proposed for this particular set up.

For each case, three repeats were undertaken, with only the mean values presented and discussed. The initial pressure for each experiment was set at 1013mbar before expansion, and a constant initial volume of 870cm<sup>3</sup> utilised throughout. As detailed in the previous section, transient measures of pressure, temperature and piston kinematics were recorded. For wet studies, droplet growth is also quantified.

## **4.6 Results**

### ***4.6.1 Dry Cases***

To develop understanding of the processes governing droplet formation, the characteristics of the expansion process of the cloud chamber first requires investigation. As a benchmark, a preliminary programme was undertaken utilising a ‘dry’ airspace within the cloud chamber, thus removing inherent complications associated with phase changes. A representative example of temporal experimental data for a dry case is presented in Figure 4.9.

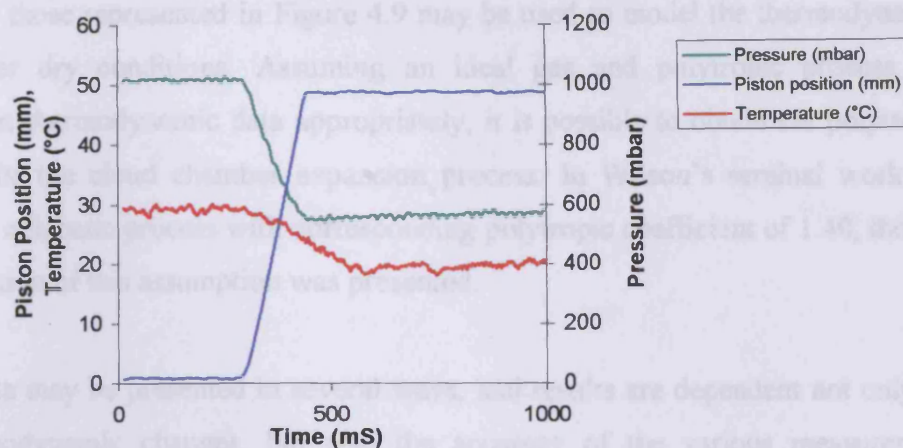


**Figure 4.9** Transient recordings of temperature, pressure and piston position against time for a rapid expansion with initial temperature 30°C, expansion ratio 1.62

Electrical noise is an inherent problem for these measurements, and so a moving average line of best fit was required to facilitate a transient characterisation of the thermodynamic response of the expansion process. Table 4.2 specifies the ‘dry’ experimental programme. Experiments were conducted with initial temperatures of 30°C and 50°C, respectively. And three expansion ratios of 1.38, 1.62 and 1.87, were chosen for compatibility with the perceived areas of interest in droplets as a mitigation tool.

Expansion rate was also systematically varied to assess its influence on mist formation as this as discussed earlier is an important factor in the resultant mist produced by a rapid expansion.

**Table 4.2** Summary of experiments conducted with 0% humidity

Initial Temp.(°C)	Expansion Ratio	Piston speed (m/S)	$\Delta T$ (°C)	$\Delta P$ (mbar)
30	1.87	0.38	11.5	545
30	1.87	0.18	9.5	545
30	1.62	0.42	10	491
30	1.62	0.16	8	491
30	1.38	0.35	7	336
30	1.38	0.16	6	336
50	1.87	0.37	9	545
50	1.87	0.19	8	545
50	1.62	0.33	10.5	491
50	1.62	0.19	9.5	491
50	1.38	0.38	7.5	336
50	1.38	0.17	6	336

Data such as those represented in Figure 4.9 may be used to model the thermodynamic process under dry conditions. Assuming an ideal gas and polytropic process, by presenting the thermodynamic data appropriately, it is possible to obtain the polytropic coefficient for the cloud chamber expansion process. In Wilson's seminal work, he presumed an adiabatic process with corresponding polytropic coefficient of 1.40, though no corroboration of this assumption was presented.

Here, the data may be presented in several ways, and results are dependent not only on actual thermodynamic changes, but also the accuracy of the various measurement techniques proposed, and thus can be used as a measure of reliability. Due to the inherently faster response times of the pressure sensor and linear potentiometer, pressure/volume correlations are considered the most accurate, whereas correlations involving temperature have been used for comparison, to assess the new improved methodology for temperature measurement in this challenging environment whilst also offering insights of qualitative trends.

For an expansion or compression of a gas as occurs within the cloud chamber to be considered as a polytropic case then the following equation must be assumed.

$$PV^n = K_o = P_oV_o^n \tag{4.3}$$

The above equation may be developed further as shown below:

$$P = \frac{P_oV_o^n}{V^n} = K_oV^{-n} \tag{4.4}$$

On the production of a data set in the form of  $P=P(V)$  it becomes possible to calculate the unknown coefficient (n). By applying a simple power law approximation ( $y = Ax^B$ ) to the measured pressure and volume data as shown by Figures 4.10 (a&b).

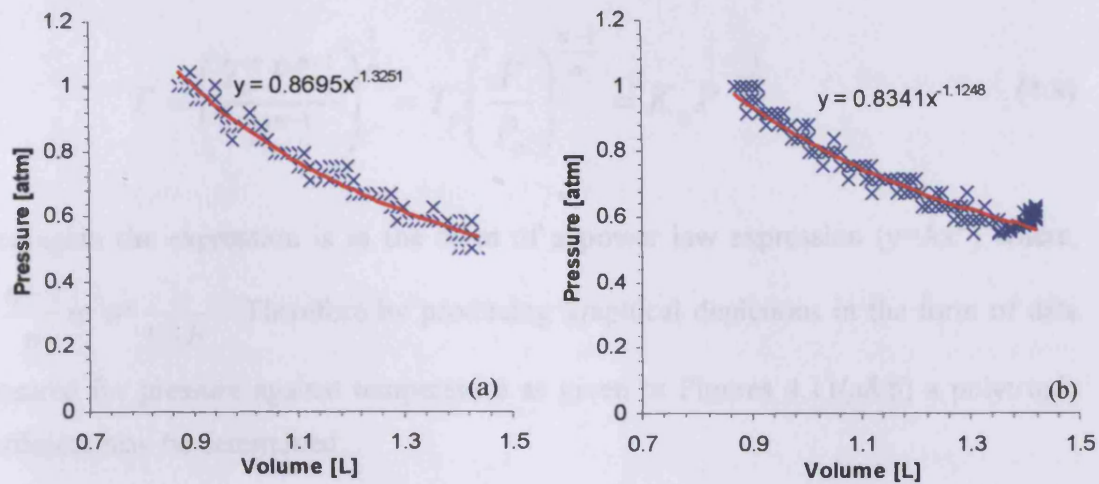


**Figure 4.10(a&b) Pressure versus volume plots for a rapid and slow expansion of the Cardiff cloud chamber, initial temperature 50°C and expansion ratio 1.62**

Thus, polytropic coefficients of 1.33 and 1.12 can be derived for the fast and slow expansions respectively. As the air within the cloud chamber can be assumed as a bi-atomic medium comprising largely of Nitrogen and Oxygen, then as discussed earlier an adiabatic expansion of 1.4 would have been expected, the fast retraction speed case is characterised by a polytropic expansion closer to the adiabatic value compared with the slow retraction speed case. This may be explained owing to the fact that the slower the expansion, the larger the heat exchange between the rig wall and the gas bulk.

Polytropic coefficients were also investigated using data derived from pressure and temperature. In this case temperature can be given in terms of pressure as given below:

$$PV = nRT \Rightarrow V = \frac{nRT}{P} \quad (4.5)$$

This equation can then be incorporated into the polytropic equation as given below:

$$P \left( \frac{nRT}{P} \right)^n = P_o \left( \frac{nRT_o}{P_o} \right)^n \quad (4.6)$$

On simplifying it is possible to derive:

$$\frac{T^n}{P^{n-1}} = \frac{T_o^n}{P_o^{n-1}} \quad (4.7)$$

Therefore a relationship between pressure and temperature can be given as follows:

$$T = \left( \frac{T_o^n P^{n-1}}{P_o^{n-1}} \right)^{\frac{1}{n}} = T_o \left( \frac{P}{P_o} \right)^{\frac{n-1}{n}} = K_o P^{\frac{n-1}{n}} \quad (4.8)$$

Once again the expression is in the form of a power law expression ( $y=Ax^B$ ) where,  $B = \frac{n-1}{n}$  or  $n = \frac{1}{1-B}$ . Therefore by producing graphical depictions in the form of data measured for pressure against temperature as given in Figures 4.11(a&b) a polytropic coefficient may be determined.

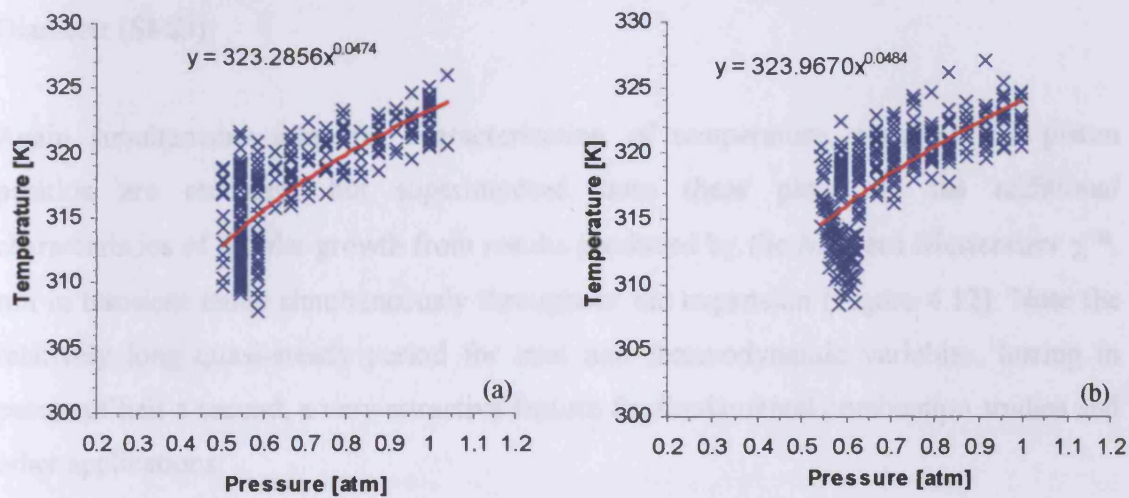


**Figure 4.11(a&b) Temperature versus pressure plots for a rapid and slow expansion of the Cardiff cloud chamber, initial temperature 50°C and expansion ratio 1.62**

From the above figures (PT) coefficients of 1.05 were derived for both fast and slow expansion cases.

These aforementioned (PV) coefficients approach the expected isothermal conditions. However, the nature of the (PT) correlations suggests that the thermocouple is still not reacting as quickly as the transient response times of both the pressure sensor (1ms for 10% to 90% of step change) and potentiometer (with quasi-instantaneous response). Clearly further work is required to improve the temperature characterisation technique.

#### 4.6.2 Mist cases

Similar studies to those described in section 4.6.1 but for 'wet' conditions have been undertaken, so that the effects of initial temperature, expansion ratio and expansion rate may be investigated with respect to droplet growth and ultimate droplet size.

It has been previously shown and discussed that mists produced by the Cardiff cloud chamber are reasonably homogeneous and mono-disperse [61 & 62]. Again, reasonably mono-dispersed mists were consistently measured in the new improved rig as discussed earlier. Henceforth, mist quality is characterised by a single parameter, the Sauter Mean Diameter (SMD).

Again simultaneous temporal characterisation of temperature, pressure and piston position are recorded, but superimposed onto these plots are the additional characteristics of droplet growth from results produced by the Malvern Mastersizer  $\chi^{\text{TM}}$ , run in transient mode simultaneously throughout the expansion (Figure 4.12). Note the relatively long quasi-steady period for mist and thermodynamic variables, lasting in excess of half a second, a very attractive feature for fundamental combustion studies and other applications.

Again a comprehensive programme was undertaken and a series of graphical representations of the format of Figure 4.12 were generated and analysed.

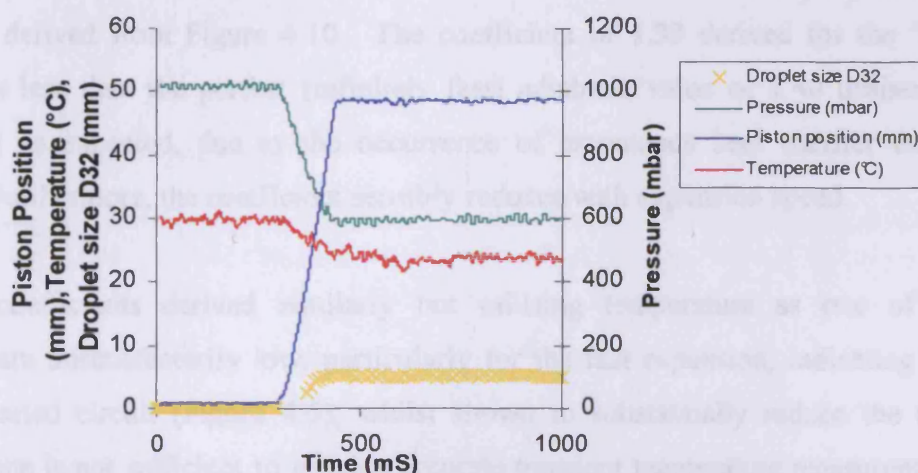


Figure 4.12 Transient recordings of temperature, pressure, piston position and droplet growth for a rapid expansion with initial temperature 30°C, expansion ratio 1.62

A summary of all results for the mist generation programme is presented in Table 4.3 below.

**Table 4.3 Summary of all results obtained for the wet cases**

<b>Initial Temp. (°C)</b>	<b>Expansion Ratio</b>	<b>Piston vel. (m/s)</b>	<b><math>\Delta T</math> (°C)</b>	<b><math>\Delta P</math> (mbar)</b>	<b>Droplet Diameter <math>D_{32}</math> (<math>\mu\text{m}</math>)</b>	<b><math>\frac{dD_{32}}{dt}</math> (<math>\mu\text{m}/\text{ms}</math>)</b>
30	1.87	0.4	7.5	502	5.4	0.1123
30	1.87	0.23	6.5	502	8.5	0.0972
30	1.62	0.33	7	419	5.1	0.0917
30	1.62	0.18	5.5	419	7.7	0.0846
30	1.38	0.38	7	336	8.4	0.124
30	1.38	0.16	6	336	12.6	0.0609
50	1.87	0.38	5.5	502	6.4	0.0933
50	1.87	0.23	5.5	502	9.9	0.0622
50	1.62	0.33	6	419	6.2	0.0954
50	1.62	0.2	5.5	419	8.6	0.0828
50	1.38	0.39	4.5	293	5.7	0.0807
50	1.38	0.18	4	293	10.4	0.0617
50	1.38	0.17	4	293	15.7	-
50	1.38	0.14	4	293	21.6	-

## 4.7 Analysis and Discussion

First, the results of the ‘dry’ test programme are informative in characterising the thermodynamic process and assessing the applicability of the various diagnostic techniques proposed and developed for this application. Figures 4.9 and 4.12 indicate that the transient pressure and volume diagnostic techniques appear to perform well for this application, and this qualitative assessment is endorsed by the polytropic coefficients derived from Figure 4.10. The coefficient of 1.33 derived for the ‘fast’ expansion is less than the perfect (infinitely fast) adiabatic value of 1.40 utilised by Wilson [60] as expected, due to the occurrence of extraneous heat transfer during expansion. Furthermore, the coefficient sensibly reduces with expansion speed.

Polytropic coefficients derived similarly but utilising temperature as one of the diagnostics are unsatisfactorily low, particularly for the fast expansion, indicating that the compensated circuit (Figure 4.5), whilst shown to substantially reduce the time constant, alone is not sufficient to provide accurate transient temperature measurements in this quiescent environment. Since the principle and advantages of the compensated circuit has now been proven for this application, a smaller (e.g. 50 $\mu\text{m}$ ) sheathed and grounded thermocouple should be utilised in future work to progress towards more

accurate, less noisy, temperature measurements. However, for the remainder of this chapter, useful qualitative trends concerning temperature measurements are discussed.

Tables 4.2 and 4.3 show that there is a smaller temperature drop observed in the wet cases compared with the corresponding dry cases; the recorded temperature drops are of the order of 30-40% less for the wet cases. This reduction in temperature drop is an indication of the influence of the latent heat of formation of the droplets. Further evidence is provided by noting that the associated reduction for the 50°C initial temperature case is smaller in comparison to that for the 30°C initial temperature, due to there being a larger volume of water changing phase as the gradient of the saturation curve for water gets steeper the higher the initial temperature.

The results presented in Table 4.3 can be represented to provide an insight into the influence on droplet growth of three primary control variables; initial temperature, expansion ratio and expansion rate.

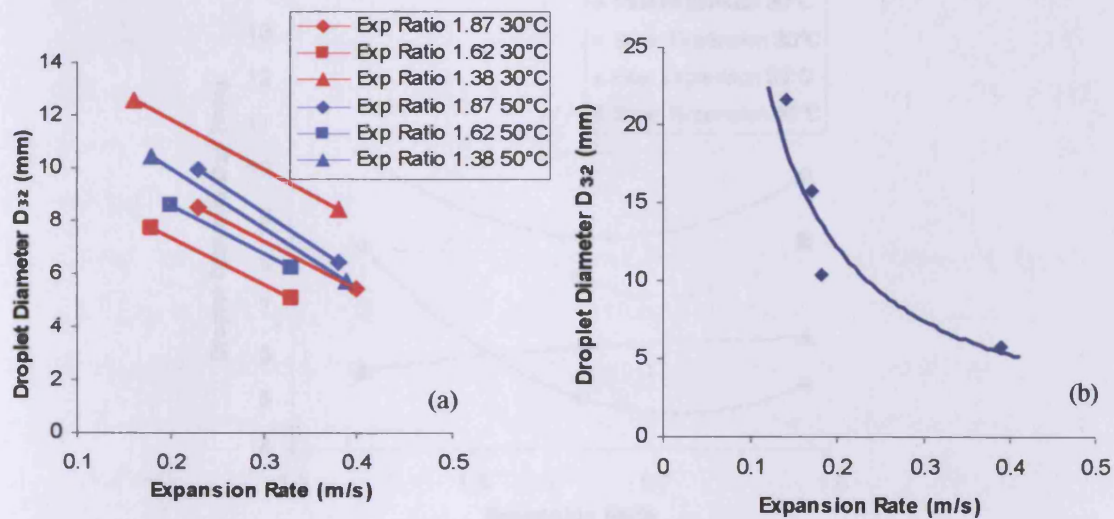


**Figure 4.13 (a&b) Effect of expansion rate on the final droplet SMD, for expansion rates greater than 0.2 and complete ranges for initial temperature 50°C and expansion ratio 1.38 respectively**

Figure 4.13(a) shows that reduction in expansion rate results in increase in SMD droplet size for all cases considered, which is in agreement with previous studies [61]. However, combined with the earlier conclusion that slower expansion rates reduce the temperature drop, this indicates that less water changes phase, leading to the conclusion that there should be fewer nucleation sites. This conclusion requires direct validation, as Malvern measurements proved inappropriate for this purpose.

### 4.3 Summary

The droplet growth rate has been measured from the Malvern data and recorded in Table 4.3. Growth rates for this experimental programme vary between 0.06-0.124  $\mu\text{m}/\text{ms}$ , increasing with expansion rate. The gradients between initial and final conditions presented for all expansion rates between 0.2-0.4m/s in Figure 4.13(a) are very similar, ranging between  $-1.9 \times 10^{-5}$  and  $-2.1 \times 10^{-5}$  seconds, and perhaps indicating a characteristic time for the droplet growth process within this range. Further experiments to establish the extent of this range are presented in Figure 4.13(b), which shows that a further reduction in expansion rate below 0.2m/s induces a significant increase in droplet growth, showing this trend to be certainly lower-bounded. It is not possible to assess the upper bound of this apparent characteristic time using the current apparatus without modification.

Figure 4.14 shows the influence of expansion ratio and initial temperature of the system.

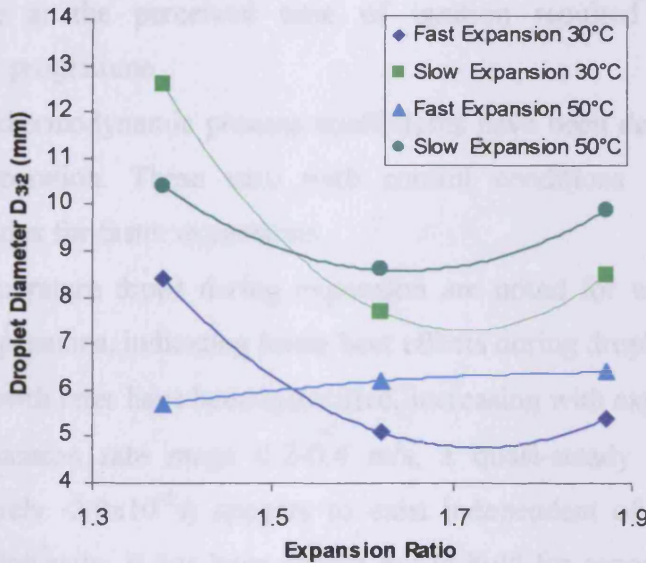


Figure 4.14 Effect of expansion ratio on resultant droplet SMD for a variety of initial conditions

Reducing the expansion ratio between 1.3-1.9 has a non-linear effect on SMD droplet size. A pronounced non-linear trend indicating a droplet size minimum is evident for the lower initial temperature cases (30°C), whereas this variation diminishes for the higher initial saturated temperature condition (50°C), so that a variation of only about 2 $\mu\text{m}$  or less was attainable using expansion ratio control at 50°C.

## 4.8 Summary

This work has shown that with considerable design improvements, the Cardiff cloud chamber is capable of being used to generate water mists in the range of droplet sizes assumed plausible for flame quench or mitigation. A number of different conclusions can be drawn detailing the creation of water droplets by a rapid expansion of a saturated airspace, namely;

- Appropriate diagnostic techniques have been developed for accurate transient quantification of chamber pressure, rate of expansion, droplet growth rate and ultimate droplet size in a novel cloud chamber/combustor facility.
- Circuit compensated electronics designed and integrated to accelerate the transient response of thermocouple temperature measurements in the rig require further development to improve on the current qualitative data. However, measurements are sufficient for the purpose of approximating ambient temperature at the perceived time of ignition required in the following combustion programme.
- Polytropic thermodynamic process coefficients have been derived for the cloud chamber operation. These vary with control conditions, and approach the adiabatic index for faster expansions.
- Lower temperature drops during expansion are noted for wet cases compared with dry expansions, indicating latent heat effects during droplet formation.
- Droplet-growth rates have been quantified, increasing with expansion rate.
- In the expansion rate range 0.2-0.4 m/s, a quasi-steady characteristic time (approximately  $2.0 \times 10^{-5}$  s) appears to exist independent of initial temperature and expansion ratio. It has been shown not to hold for expansion rate less than 0.2 m/s.
- A non-linear relationship between droplet size and expansion ratio exists, which diminishes for higher initial temperatures.

However, there is still a weakness in this system, which at the present time has not been resolved. The major concern in this work in respect to both quantification of mist generation and the droplet cloud that may be used for explosion suppression is the

inability to accurately calculate the actual droplet density and thus, the vapour/droplet ratio within the airspace after a rapid expansion. This should be developed to improve understanding as part of future studies on this elegant facility.

## CHAPTER

# 5

# **Benchmarking the Cardiff Cloud Chamber against other fully contained Explosion Facilities for use in the Investigation of Self-Propagating Laminar Explosions**

In order that the cloud chamber discussed in Chapter 4 could be used to investigate self-propagating laminar methane explosions, with the additions of water in the forms of vapour and droplets, it was first necessary to develop a suitable experimental procedure to accurately quantify flame-speed/burning rate which is comparable to other fully appraised test facilities for methane-air burning rate quantification.

## **5.1 Rig Modifications and procedures**

Before the Cardiff cloud chamber could be used as a fully confined combustion vessel, a number of modifications needed to be implemented. These are discussed in the following sections and include the control of methane concentration, ignition and flame speed determination.

### ***5.1.1 Control of Fuel Equivalence Ratio***

Before studies could be undertaken on the determination of flame-speed within the Cardiff cloud chamber, first it was necessary to establish an accurate method for the introduction of methane into the chamber to allow evaluation of initial mixture composition.

The introduction of methane was facilitated by utilising the 100cm<sup>3</sup> scaled gas tight syringe discussed in section 4.2.2., which could be filled directly from a high CP grade (99.97%, SIP Analytical Ltd.) methane bottle via a self sealing 11mm Auto-Sep™ self sealing septa. A predetermined volume of methane could then be passed into the recirculating airflow through another 11mm self sealing septa built into the re-circulation pipe work, as shown by Figure 4.3. This method of gas-mixture preparation, used

throughout these studies, induces a possible error in methane volume measurement of  $\pm 0.25\text{cm}^3$ . This gives accuracy in equivalence ratio of approximately  $\pm 0.0035$ .

### **5.1.2 Ignition**

A variable energy capacitive-discharge ignition system was developed based on that used by Cameron [61], in order that a flame could be initiated at the centre of the cloud chamber. The system which was all built into a screened aluminium die cast box consisted of three  $0.47\mu\text{f}$  rapid-discharge capacitors positioned in series that were charged by a variable high voltage (DC) power supply (0-350V). Using the energy equation (5.1) given below, a theoretical discharge of between 0-85mJ was afforded.

$$e = \frac{1}{2}cV^2 \quad (5.1)$$

The rapid discharge of the stored energy to the primary coil of a tightly bound automobile ignition coil (AIC) was initiated by the supply of a 5V TTL pulse to a controlling thyristor. The AIC then acted in a similar manner to that of a standard (AC) transformer, boosting the energy on the secondary side by the ratio of turns in the primary to secondary turns (100:1), thus providing a theoretical peak voltage of between 0-35000V.

The 'boosted' voltage, which can be termed the 'breakdown' voltage, on discharge between the spark gap, is capable of bringing about ionisation of the air allowing a spark to propagate between the two electrodes. The electrodes used for this study are based on a configuration used by Dreizler et al. [71], and are constructed from 1mm diameter stainless steel ground to a  $60^\circ$  point. The use of a fine electrode minimised the effects on the propagating flame, and the ground tip provided a more repeatable spark gap and thus spark to be attained. This system is shown schematically in Figure 5.1

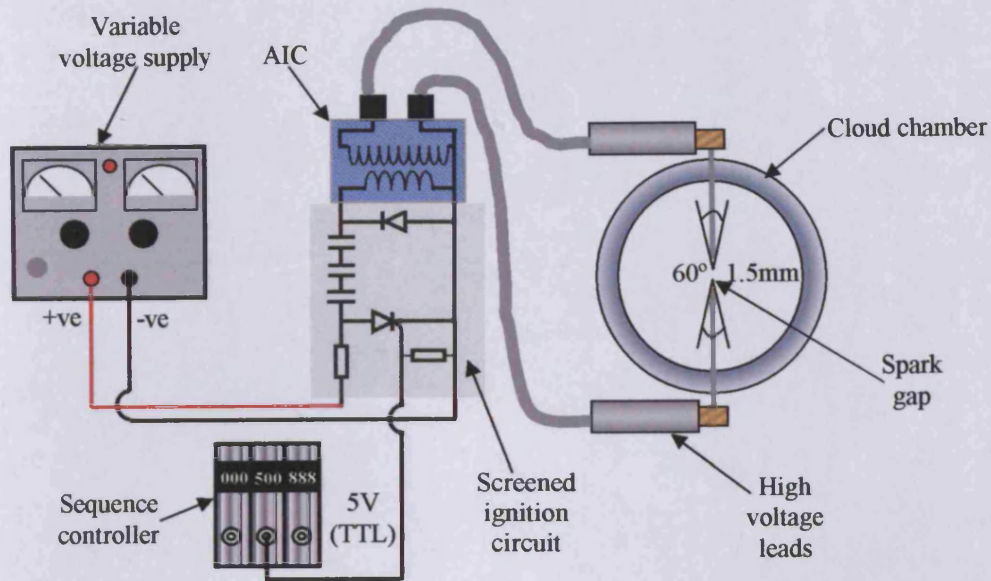


**Figure 5.1 Schematic representation of ignition system for combustion studies in the Cardiff cloud chamber**

On testing the circuit it was found that sparks could only be reliably created if the supply voltage was set at 40V. This meant that the approximate energy levels at the primary coil could be accurately controlled from approximately 1.5-85mJ.

### 5.1.3 Flame front Imaging

The calculation of flame speed within the cloud chamber is reliant on the recording of the flame front position with respect to time, and from this flame speed and burning rates may be derived. The original method for determining flame speed within the chamber was to use a high-speed Photon Ciné camera. Due to low levels of luminosity generated by the 'bluish' methane flames, filming rates of <400fps were still insufficient to achieve an exposure of the film, particularly during the highly influential early flame initiation. In order that early flame structure could be visualised at a higher filming rate of 1000fps, it was necessary to develop a Schlieren photographic technique around the Cardiff cloud chamber.

A standard Toepler style system as discussed in Chapter 3 was deemed suitable and was setup around the Cardiff cloud chamber as shown in Figure 5.2.

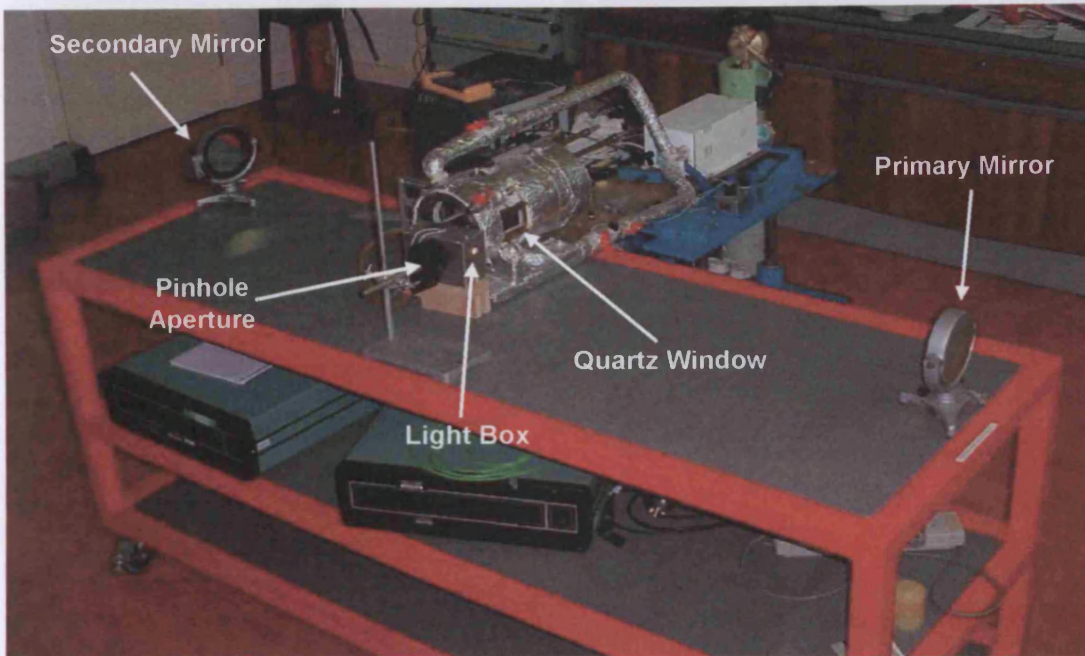


**Figure 5.2** Photograph of Toepler Schlieren setup around Cardiff cloud chamber

The light source used was built from a 100watt projector bulb with a straight filament, collimated and focused using two 4" diameter concave mirrors with focal lengths of 36.8" (O.W.L).

In this setup, a large portion of the undisturbed light source (solid line) from the second/focusing mirror is stopped using an adjustable camera aperture as a knife edge, as illustrated in Figure 5.3. This enables an image of the diffracted light to be captured.

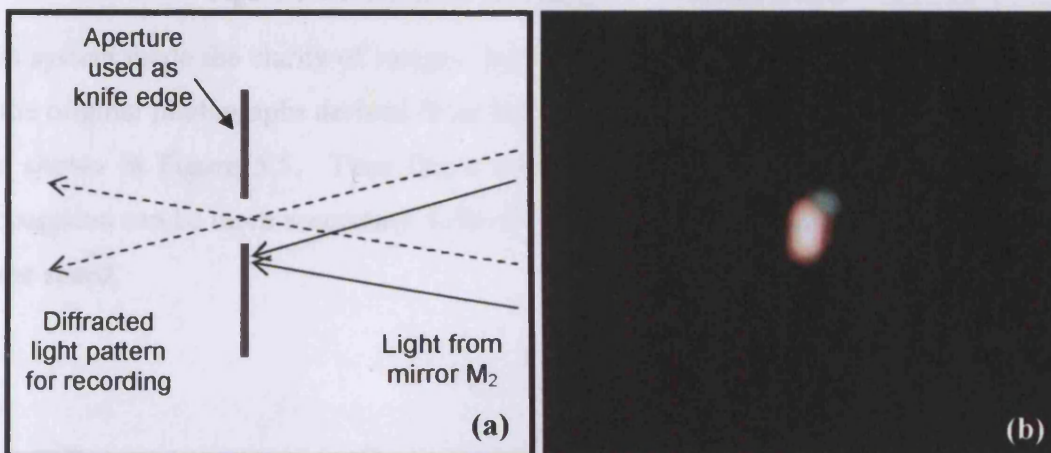


**Figure 5.3 (a&b)** Diagram and photograph of the pinhole principle for cutting out of undisturbed light used to create a Schlieren image

The NAC-1000 system which is detailed in section 3.4.1, filming at a rate of 1000fps with a shutter speed of  $\frac{1}{10000}$  second allowed a sharp image to be recorded onto normal vhs video format. In order that flame speed could be determined it was necessary to convert the recordings into a more suitable format. This is achieved as detailed below in Figure 5.4.

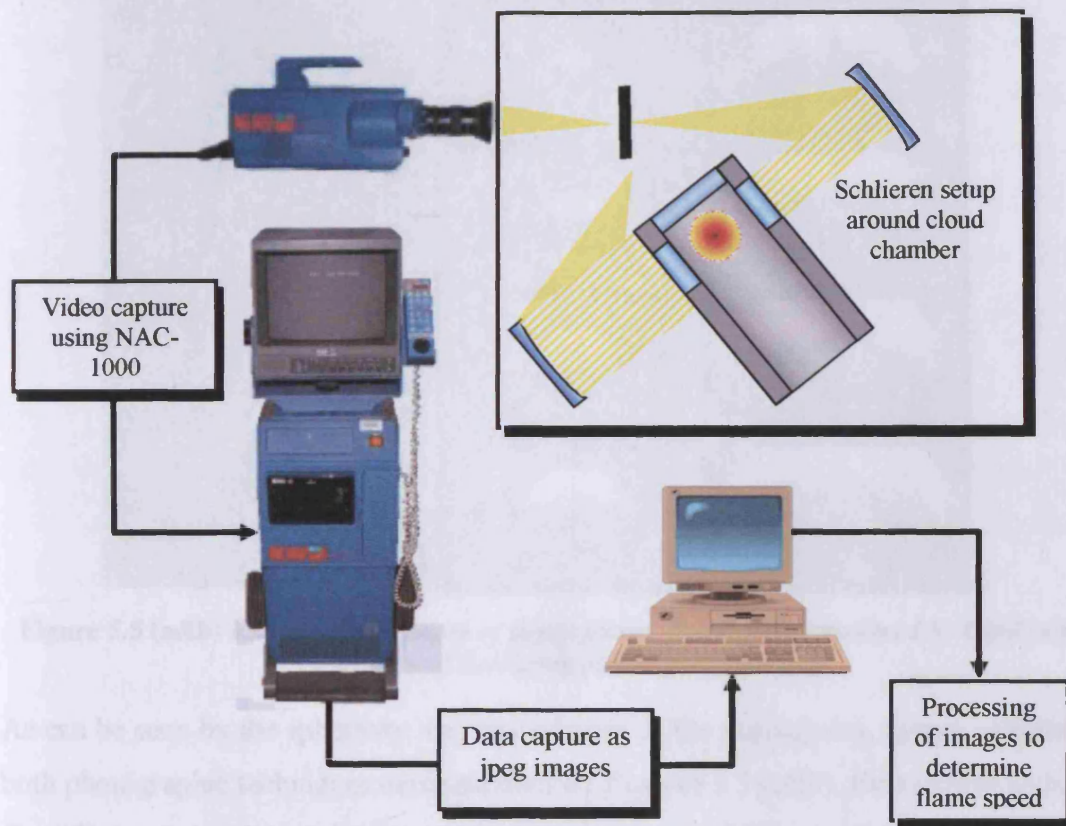


**Figure 5.4** Flow chart depicting full Schlieren system

This system made the clarity of images depicting flame growth much sharper compared to the original photographs derived from the high-speed Ciné technique used previously and shown in Figure 5.5. Thus flame edge location particularly during early flame propagation can be more accurately defined facilitating a more accurate determination of flame speed.

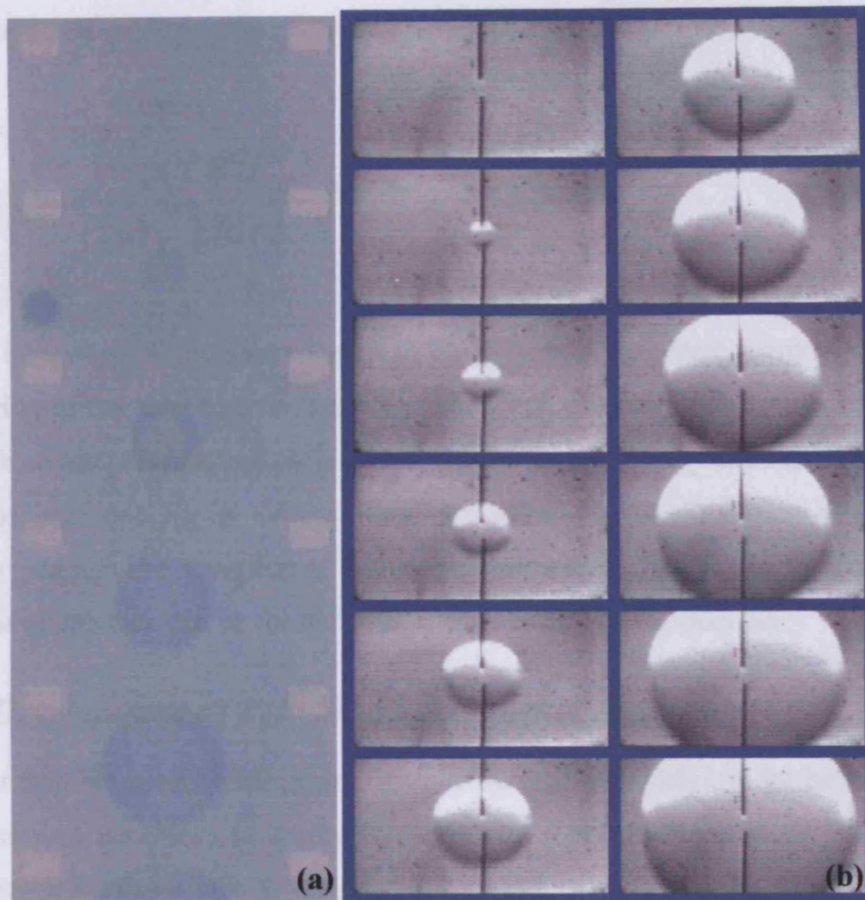


**Figure 5.5 (a&b) Examples of images of propagating flame front produced by Ciné camera (400fps) and Schlieren technique (1000fps).**

As can be seen by the sphericity and smoothness of the propagating flames exhibited by both photographic techniques demonstrated by Figures 5.5 (a&b), the mixture within the Cardiff cloud chamber at the time of ignition is very well mixed producing truly laminar flame propagation.

#### **5.1.4 Calculation of Equivalence ratio**

Before any meaningful results could be achieved using the cloud chamber it is first necessary to determine a method for the calculation of accurate equivalence ratio. So as repeatability may be ensured, ambient conditions must be accounted for in the calculations. These are presented in detail in Appendix A.

The final equation derived is given (5.2):-

$$V_{fuel} = \frac{(ER)P_{rig}V_{rig}T_{fuel}Mr_{air}}{(17.12708335)P_{fuel}T_{rig}Mr_{fuel}} \quad (5.2)$$

As can be seen from the above equation the volume of methane required can be derived and owing to the nature of the container in which the fuel is measured being vented to atmosphere the pressure and temperature of the fuel in the equation can be given as that of atmospheric conditions. Therefore an accurate volume of methane can be calculated for any pre-mixture conditions, which should ensure that a repeatable and reliable combustion mixture can be formed within the Cardiff cloud chamber.

### ***5.1.5 Development of Reliable Experimental Procedure***

In order that an experimental programme be conducted efficiently for both Chapters 5 & 6 it was first necessary to devise a procedure that would optimise repeatability and reliability of the experiments. The basic procedure of each experiment was:

- i). Purge the rig with 'clean and dry' air for at least fifteen minutes to ensure that all moisture and prior combustion products are removed from inside the chamber.
- ii). Seal the rig from the atmosphere, and allow the air to be re-circulated throughout the rig until the required initial temperature is attained throughout the combustion chamber and re-circulation lines.
- iii). After temperature equilibrium has been attained throughout the rig and ancillary pipe work, the pressure inside the rig is corrected to 1013mbar using the gas syringe.
- iv). The volume of methane required for the particular experiment (calculated as specified in section 5.1.4) is then injected into the rig and allowed to mix for a further 15 minutes.
- v). The ambient pressure inside the chamber is then again reduced to 1013mbar.
- vi). If required the desired volume of water is injected.
- vii). After complete evaporation of the water into the air space, the rig is once again reduced to 1013mbar using the gas syringe.
- viii). The re-circulation system switched off.

- ix). After all safety valves have been manually turned off, the mixture is ignited using a *single* ‘low’ energy spark, and the resulting flame growth is recorded using the Schlieren system described earlier. Ignitions via repeated sparks were avoided, as agreed at sponsor progress meetings.
- x). The rig is then purged with ‘clean and dry’ air for 10 minutes in order to remove all combustion products and reduce the temperature of the chamber walls.

## **5.2 Current Experimental Knowledge for Methane/Air Explosions**

### ***5.2.1 Determination of Laminar Burning velocity***

Burning velocity is defined by Andrews and Bradley [72] as ‘a physiochemical constant for a given combustible mixture. It is the velocity, relative to the unburnt gas, which a plane, one-dimensional flame front travels along the normal to its surface. It is the eigenvalue of the one-dimensional flame equations.’ It is also conceded. ‘Unfortunately, although its theoretical definition is simple, the same cannot be said of its practical measurement.’

There have been numerous studies in the determination of burning velocity of methane-air flames. These studies have utilised many different experimental methods as summarised by Figure 5.6. It may be noted that these methods may be grouped into two distinct categories namely; stationary flames in which pre-mixed combustion gas flow enters into a stationary flame zone; and non-stationary flames whereby the flame moves through an initially quiescent combustion mixture.

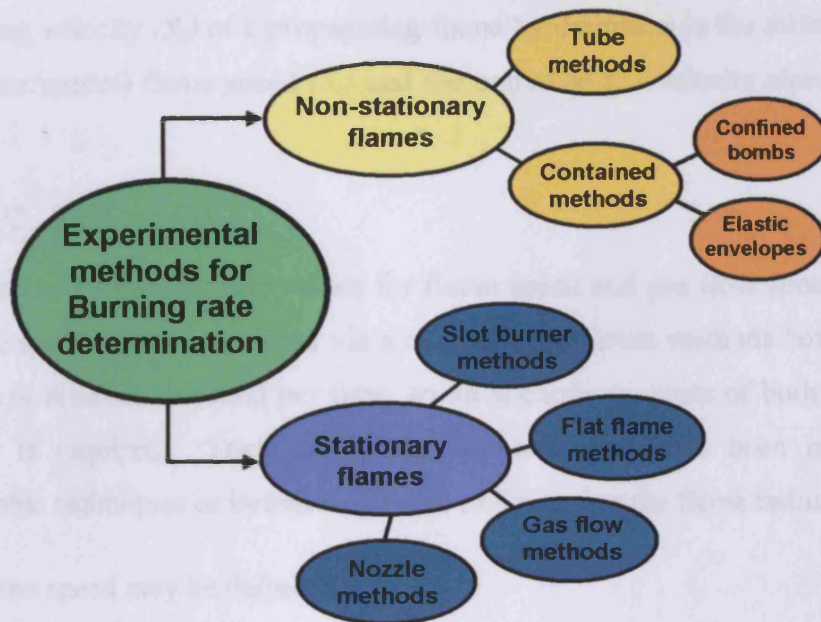


**Figure 5.6** Schematic representation of different methods used to determine burning velocity of methane-air flames

A number of publications describing the methods in the determination of burning velocities of each of the different methods are available elsewhere, most noticeably reviews conducted by Andrews and Bradley [72] and Rallis and Garforth [73].

Owing to the fact that this study will be carried out utilising the fully confined Cardiff cloud chamber, only methods generated from use of confined bombs will be further discussed.

Most confined bombs are of the form of spherical constant-volume vessels, there are a number of such apparatus described in the literature although this method seems to be less utilised in comparison with stationary flame techniques. During the early 1950's Linnett [74] concluded that this method is "potentially a powerful method for determining burning velocities", and ever since various techniques in deriving burning velocities have been developed and appraised [72, 73&75-88].

To calculate the laminar burning velocity various equations have been developed, and hence an immediate problem in the literature is the lack of consistency in the nomenclature used to denote each of the factors necessary for the correct determination. It has been decided that within this study the nomenclature originally utilised by Andrews and Bradley [72] will be adopted.

The burning velocity ( $S_u$ ) of a propagating flame by definition is the difference between the (laminar/spatial) flame speed ( $S_s$ ) and the unburned gas velocity ahead of the flame (5.3):

$$S_u = S_s - S_g \quad (5.3)$$

Thus, to calculate burning rate values for flame speed and gas flow speed are required. The flame speed may be measured via a number of different methods however speed by definition is distance travelled per time, so an accurate measure of both flame position and time is required. Traditionally the flame location has been measured using photographic techniques or ionisation probes to determine the flame radius ( $r_b$ ).

Hence flame speed may be defined (5.4):

$$S_s = \frac{\partial r_b}{\partial t} \quad (5.4)$$

Likewise there are different approaches available in measuring the gas flow ahead of the flame. The flow rate was originally derived indirectly relying on accurate pressure measurements; however these methods lead to obvious sources of error as the pressure transducers required would need to be 'impossibly sensitive'. As techniques developed, more accurate direct measurement of flow was achieved using hot wire anemometry [76&77] and current (LDA) laser techniques, which require a 'seeded' gas to allow elastic scattering of the laser source.

However due to the difficulties associated with the accurate measurement of the gas flow ahead of the flame, most studies derive the burning velocity via use of the expansion ratio between the burnt and unburned gases (5.5):

$$S_u = S_s \left( \frac{\bar{\rho}_b}{\rho_u} \right) \quad (5.5)$$

Determination of the average burnt gas density ( $\bar{\rho}_b$ ) is very difficult and requires accurate rapid measurements of temperature gradient. For this reason it seems customary for researchers to derive the average burnt gas density from uniform temperatures equal to the adiabatic flame temperature behind the flame front.

It is suggested [72] that simply applying the adiabatic flame temperature to derive the mean burnt gas density does not give an accurate density measure capable of deriving accurate burning rate. The study showed from first principles that the average burnt gas density can be expressed (5.6).

$$\rho_b = \frac{3}{r_b^3} \int_0^{r_b} r_b^2 dr \quad (5.6)$$

By substituting in the relevant values for substituting into (5.5) it can be shown that for a flame radius ( $r_b$ ) equal to 25mm the actual value of expansion ratio can be expressed (5.7).

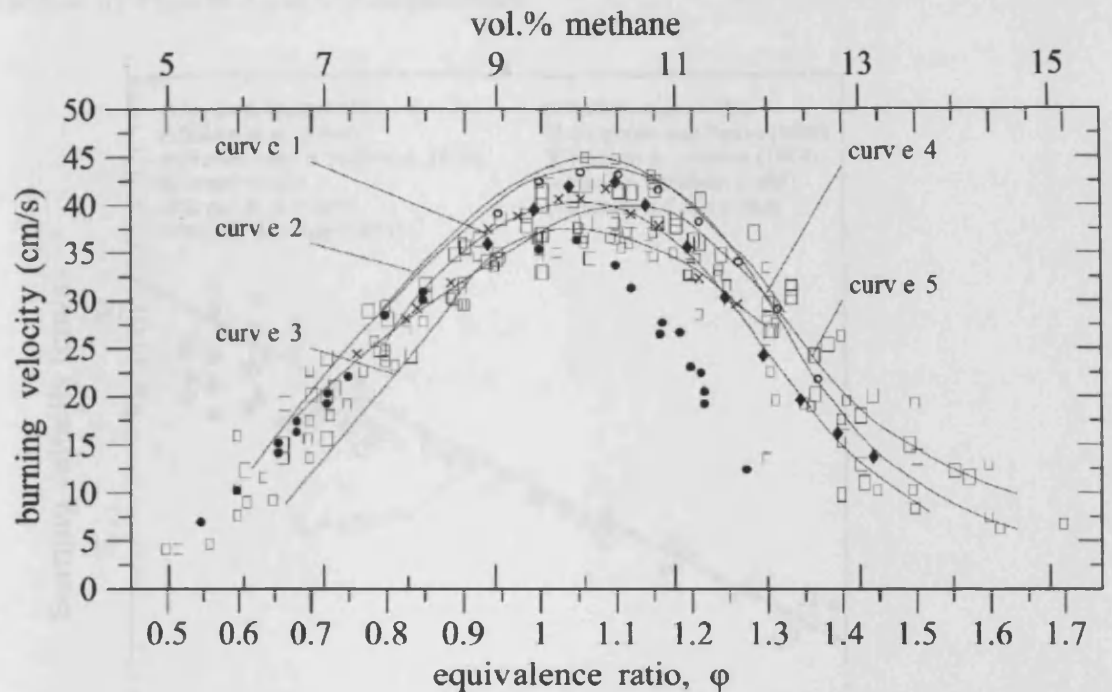
$$\frac{\bar{\rho}_b}{\rho_u} = 1.22 \frac{T_u}{T_b} \quad (5.7)$$

As can be seen if adiabatic flame temperatures were simply used then there would be an under estimation in the expansion ratio and hence, an underestimation of approximately 20% in the values of burning rates quoted.

Recent methods developed by Dahoe and de Goey [88] rely solely on pressure time traces, and do not require observation of the rapidly moving flame front. Their results compare favourably with current data however, due to the lack of certainty in this method it is thought that the use of a more traditional method is of most use in the ‘benchmarking’ of the Cardiff cloud chamber.

### ***5.2.2 Current Experimental results***

As discussed earlier there are numerous different studies to determine the burning velocity of methane-air mixtures. In order that the Cardiff Cloud chamber may be benchmarked, it is first necessary to compare all of the available data in terms of a graphical presentation, showing the effects of equivalence ratio on the laminar flame speeds. Various authors have generated such graphs [72, 77, 81, 82, 86, 87 & 88] of which the most thorough and up to date is that constructed by Dahoe and de Goey [88], and this graphical comparison is given in Figure 5.7.



×	Clingman et al. (1953)	●	Karpov & Sokolik (1961)	△	Barassin et al.(1967)
○	Lindow (1968)	▽	Edmondson & Heap (1969)	□	Edmondson and Heap (1970)
◆	Reed et al. (1971)	▨	Andrews & Bradley (1972)	▲	Günther & Janisch (1972)
□	van Maaren et al.(1994)	⊕	Clarke et al. (1995)	★	Wu and Law (1984)
▨	Iijima and Takeno (1986)	*	Kawakami et al. (1988)	⊗	Egolfopoulos et al. (1989)
●	Flamelet Library	curve 1	Scholte and Vaags (1959)	curve 2	Gibbs and Cacote (1959)
curve 3	Egerton and Lefebvre (1954)	curve 4	Warnatz (1981)	curve 5	Tsatsaronis (1978)

**Figure 5.7 Effect of equivalence ratio on the laminar burning velocity of methane-air mixtures,  $P=1$  bar,  $T=288.15-298.15k$  [19]**

It can be clearly seen from the figure that the data produced from 21 different data sets produces a disparity in the derived burning velocities of typically 10cm/s for any particular equivalence ratio, with some studies being even further from the mean. There are many different explanations for why this data should have such a deviation, namely; burning velocity derivation as discussed earlier, errors in measurement, and the properties of the test facilities used. Figure 5.7 emphasises the fact that the measurement of the laminar burning velocity is fraught with difficulties.

It is also presently understood that other factors such as initial temperature and pressure can greatly influence the burning rates of methane-air flames. And extensive studies to determine these effects have been undertaken [77, 79, 80, 81, 86, 87, 89, 90 & 91]. The general trends seen from these studies are that increasing pressure has an inversely proportional effect on burning velocity, and that increasing the unburned gas

temperature brings about an increase in the laminar burning rate. These trends are represented by Figures 5.8 & 5.9 respectively.

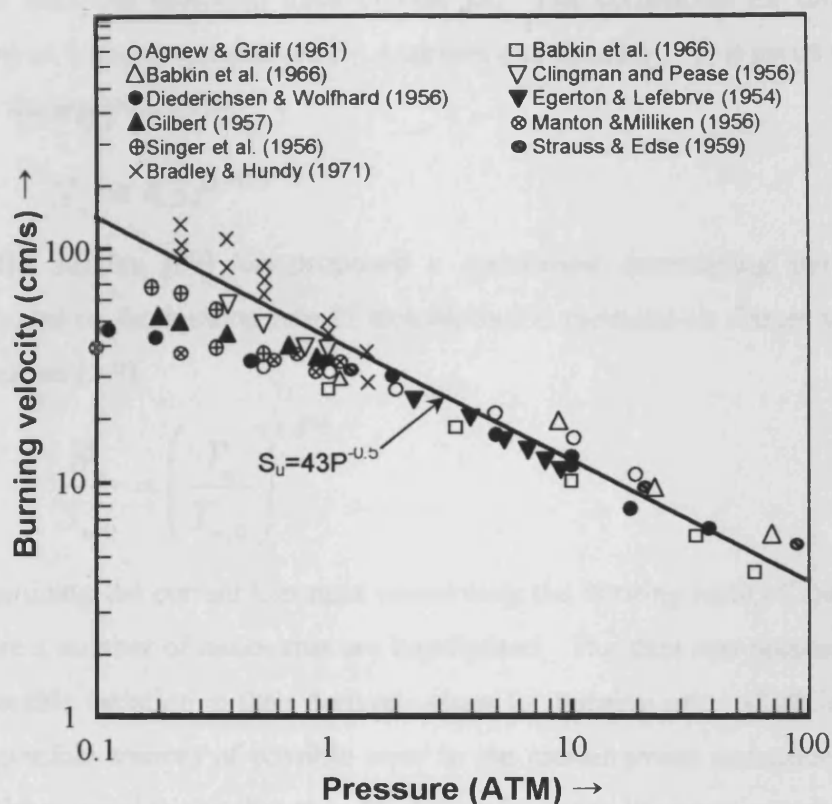


Figure 5.8 Burning velocity variation with pressure, for  $\phi = 1$  [77]

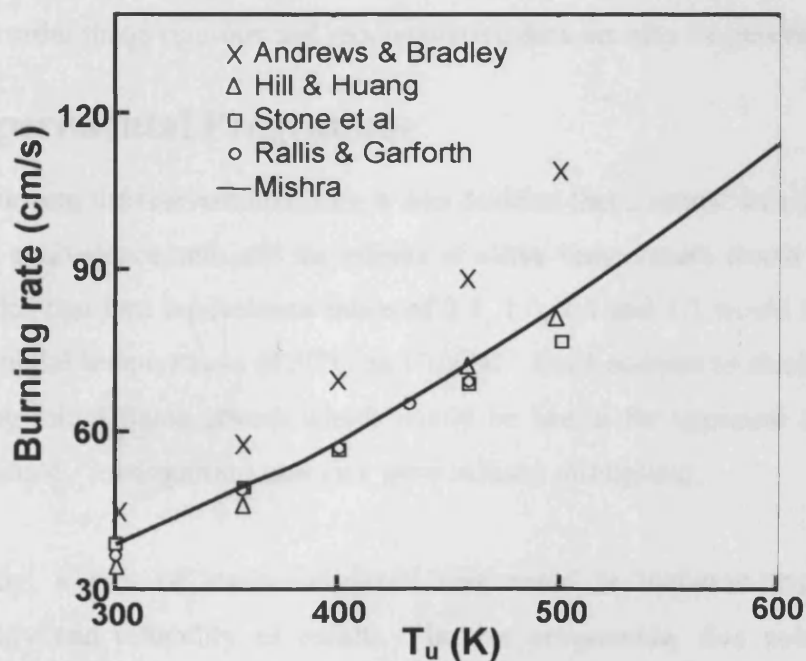


Figure 5.9 Effect of initial temperature on burning velocity of stoichiometric methane-air mixture; numerical, experimental: points. [89]

As can be seen the Figures 5.8 & 5.9 are taken straight from the literature thus do not include all data from the relevant literature. However some useful correlations are derived from the projected lines of best fit. The correlation for the effect of initial pressure on burning rate derived by Andrews and Bradley [77] is given within Figure 5.8 and by the equation (5.8).

$$S_u = 43P^{-0.5} \quad (5.8)$$

Similarly, Mishra [89] has proposed a correlation determining the effect of initial temperature on the burning rate of stoichiometric methane-air flames which is given by the equation (5.9).

$$\frac{S_u}{S_{u,0}} = \left( \frac{T_u}{T_{u,0}} \right)^{1.575} \quad (5.9)$$

On examining the current literature concerning the burning rates of methane-air flames, there are a number of issues that are highlighted. The data sets presented are subject to considerable variation in their derived values for burning rate, which indicates there are many possible sources of possible error in the measurement and calculation of burning rate. Other conclusions that may be drawn from the literature prove that the accurate definition of initial conditions with respect to temperature, pressure and air/fuel ratio is crucial in order that a rigorous and representative data set may be generated.

### 5.3 Experimental Programme

After reviewing the relevant literature it was decided that a robust data set evaluating the effects of equivalence ratio and the effects of initial temperature would be examined. It was decided that four equivalence ratios of 0.8, 1.0, 1.1 and 1.2 would be studied at two different initial temperatures of 50°C and 100°C. In an attempt to elucidate information concerning initial flame stretch which would be useful for appraisal of computational models, single, 'low' ignition energies were utilised throughout.

Importantly, a lack of statistical detail was noted in literature studies concerning repeatability and reliability of results. In this programme, five nominally identical repeats of each experiment were undertaken to allow a reasonable statistical analysis of the data.

### 5.3.1 Determination of Flame speed

As discussed earlier flame speed is simply the first derivative of flame front radius with respect to time (5.4). Thus in order to calculate flame speed a measure of spatial flame position is required. In the case of this study this value is afforded by the use of Schlieren images captured in the form of a movie at a framing rate of 1000fps as discussed earlier (section 5.13).

The flame radius measured throughout this work is that of the Schlieren front radius ( $r_{sch}$ ) which is defined as the 450 K isotherm [92]. It is proposed by Gu et al. [87] and Bradley et al. [92] that the most accurate representation of flame front is that of the cold flame front ( $r_u$ ) which is defined as the isotherm at 5 K above the temperature of the reactants. This value attempts to take into account the effect of varying flame thickness. However studies by Karpov et al. [85] and numerical studies by Bradley et al. [84] suggest that the effect of flame thickness fluctuations is of minor importance compared with other errors that are introduced at other stages of calculation. For this reason there has been no correction factors added to convert to the cold flame front radius ( $r_u$ ). Thus the flame speed used for this study as used by Karpov et al. [85] may be defined as (5.10).

$$S_s = \frac{\partial r_{sch}}{\partial t} \quad (5.10)$$

Figure 5.10 below provides an example of Schlieren images showing a propagating flame; the lines indicate the points at which the Schlieren front radius ( $r_{sch}$ ) and the point of ignition are taken:

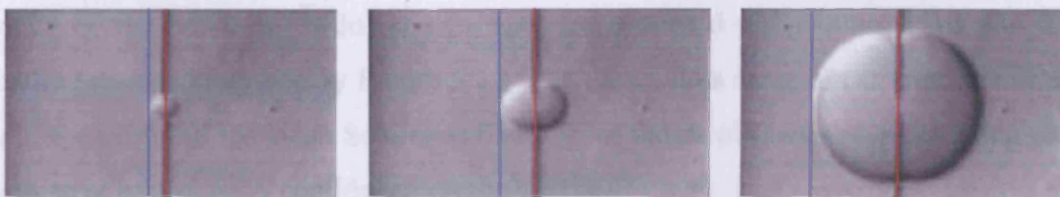


**Figure 5.10 Schlieren photographs showing positions of flame centre and Schlieren flame front radius at times 1, 10 & 16mS after Ignition**

The measurement of the Schlieren front radius was always taken on the left-hand side of the electrodes, as this was the direction of the front wall that remains a constant distance from the electrodes throughout the entire data set.

It was decided that the best way to represent the data was to take the data from the five repeats of each experiment, and draw a graph of all data points comparing Schlieren front radius against time as demonstrated in Figure 5.11:

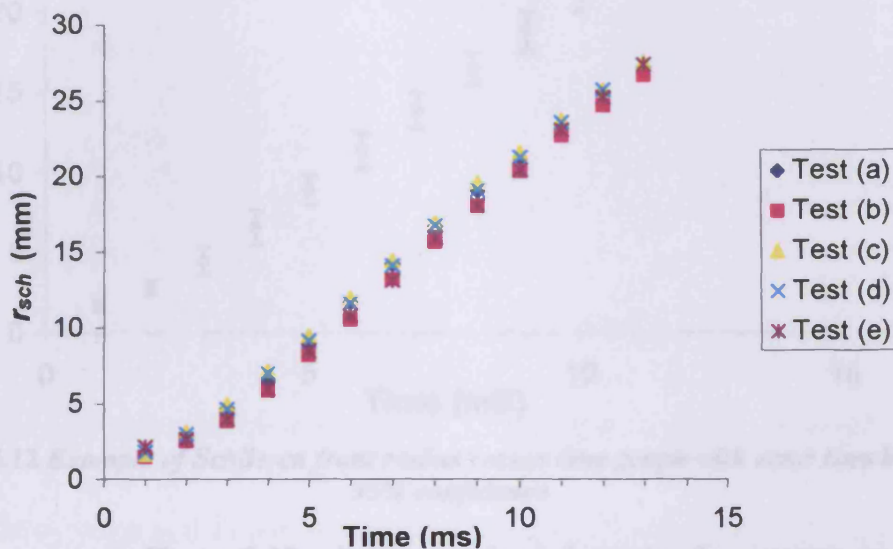


Figure 5.11 Example of Schlieren front versus time graph with five repeats

For better presentation of the data, graphs were then presented in terms of the mean ( $\bar{x}$ ) and the standard deviation around the arithmetic mean of the data, where  $\bar{x} = \frac{\sum x}{n}$ , and  $n=5$  for the majority of this dataset.

The standard deviation is defined by (5.11):

$$\sigma = \left( \frac{(x - \bar{x})^2}{n} \right)^{1/2} \quad (5.11)$$

A confidence limit of 95% was chosen as a representation of the dispersion of the data, which occurs between  $(\bar{x}-2\sigma)$  and  $(\bar{x}+2\sigma)$  for a normal distribution. Thus, the data is finally presented as given by Figure 5.12. The data points are given at 1ms time intervals on the x axis, and the mean Schlieren flame front radius of the five repeats being plotted with error bars of 95% confidence on the y axis.

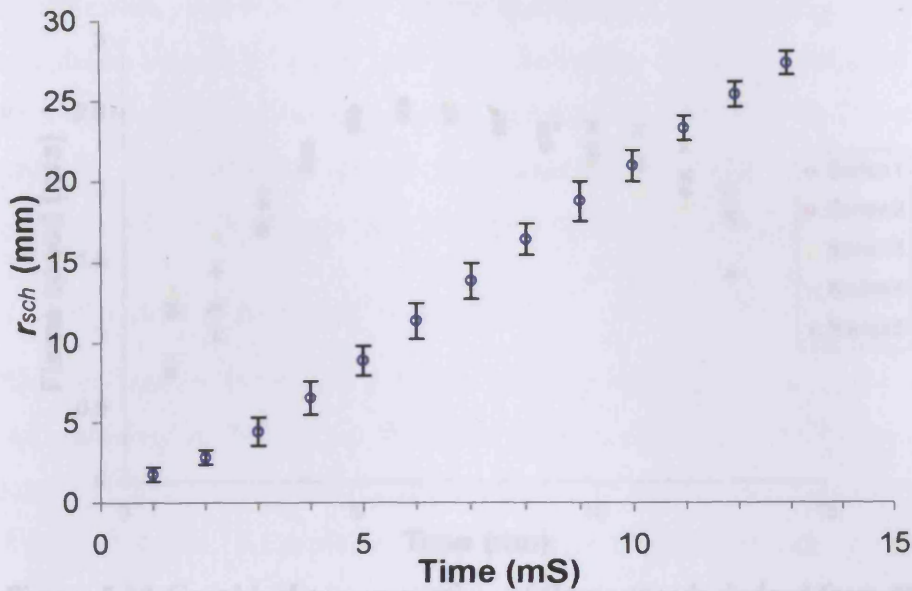


**Figure 5.12** Example of Schlieren front radius versus time graph with error bars indicating 95% confidence

As can be seen in Figure 5.12, all data attained from the five repeats is expressed together in an easy to read format and with the error bars being relatively compact, suggesting a high level of repeatability.

Taking the results from Figure 5.12 and fitting a 6<sup>th</sup> order polynomial line of best fit to each of the data sets as utilised by Fuss et al. [42], it is possible to obtain equations giving an excellent representation of the dataset. This polynomial may then be differentiated with respect to time producing a polynomial of flame speed against time. By substituting the time values back into the polynomial data series it becomes possible to represent flame speed with respect to time. Figure 5.13 shows such series with series 1-5 representing each of the five experimental repeats.

Few of the published studies discuss the statistical appraisal of their results. Toshio and Taduo [81] however state that they repeated each experiment 10 times and show error bars around their data but fail to discuss how such error bars were derived. Gu et al. [87] also briefly discuss their statistical appraisal applied to the results derived from the

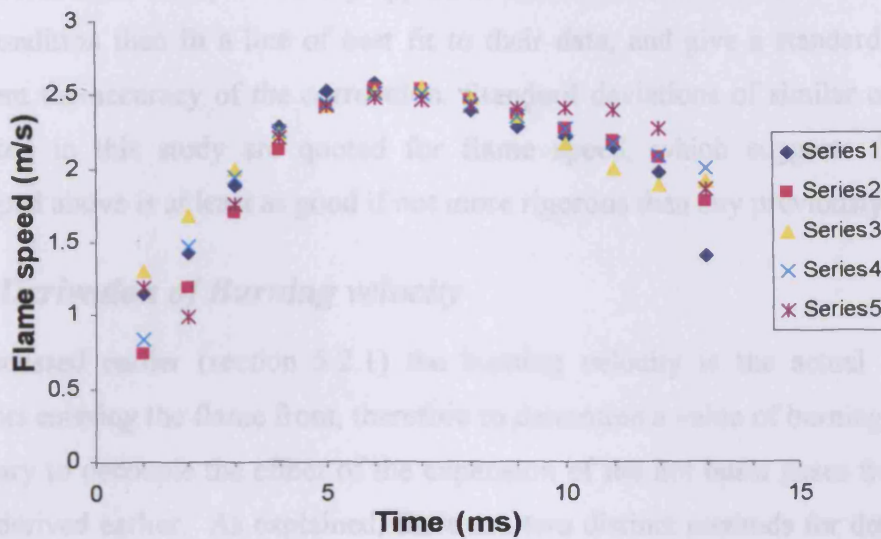


**Figure 5.13** Graphical representation of flame speeds derived from 6th order polynomial fits of distance time graphs

From these curves it is then possible to generate an arithmetic mean value for each time step as shown by Figure 5.14. To this value it is possible to calculate the standard deviations of the other five data points around this mean then multiply these by two in order to ensure a 95% confidence of data within the error bars.

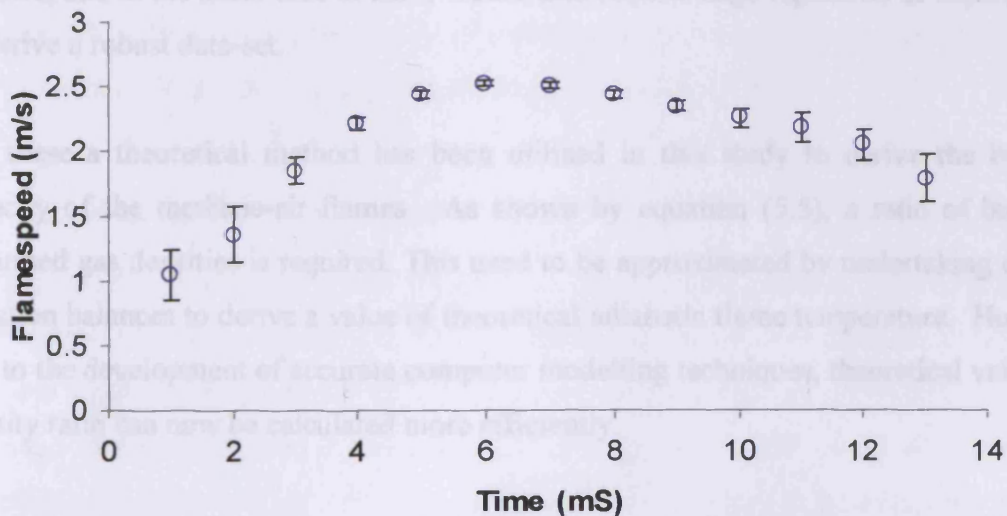


**Figure 5.14** Final representation of flame speed against time with error bars indicating 95% confidence

Few of the published studies discuss the statistical appraisal of their results. Toshio and Tadao [81] however state that they repeated each experiment 10 times and show error bars around their data but fail to discuss how such error bars were derived. Gu et al. [87] also briefly discuss their statistical appraisal applied to the results derived from the

Leeds bomb data. They invariably appear to undertake a maximum of 2 data points for each condition then fit a line of best fit to their data, and give a standard deviation to represent the accuracy of the correlation. Standard deviations of similar order to those presented in this study are quoted for flame speed, which suggests the technique developed above is at least as good if not more rigorous than any previously adopted..

### ***5.3.2 Derivation of Burning velocity***

As discussed earlier (section 5.2.1) the burning velocity is the actual speed of the reactants entering the flame front, therefore to determine a value of burning velocity it is necessary to decouple the effect of the expansion of the hot burnt gases from the flame speed derived earlier. As explained, there are two distinct methods for determining the expansion rate, experimentally or theoretically.

Due to the geometrical design of the Cardiff cloud chamber, actual measurement of the velocity of the unburned gases would be very problematic relying on either intrusive methods such as ionisations probes that would effect the flame structure or non-intrusive laser techniques such as PIV or LDA which would both require the seeding of the mixture, and in the latter case of LDA would also require huge repetition of experiments to derive a robust data-set.

For these a theoretical method has been utilised in this study to derive the burning velocity of the methane-air flames. As shown by equation (5.5), a ratio of burnt to unburned gas densities is required. This used to be approximated by undertaking energy equation balances to derive a value of theoretical adiabatic flame temperature. However due to the development of accurate computer modelling techniques, theoretical values of density ratio can now be calculated more efficiently.

For this study expansion ratios using a premix model in CHEMKIN modelling package were calculated by Kwon [93]. The results obtained are compared against other expansion ratios quoted in the literature and given by Figure 5.15.

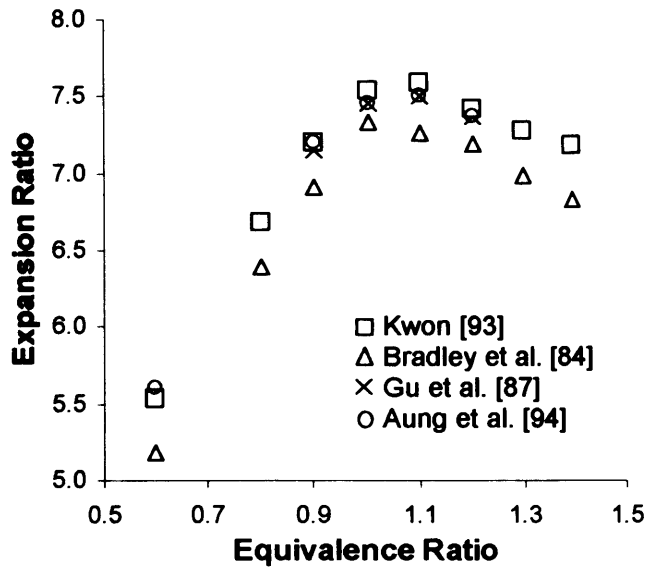


Figure 5.15 Comparison of expansion ratio used in this study

As can be seen from Figure 5.15, there is a variation in the expansion ratios derived by various studies, however the values produced by Kwon [93] are very close to those generated by other notable authors, and as such the model produced is deemed appropriate for use in this study.

Thus as values for the expansion ratio of unburned to burnt gas densities are achievable it is possible to derive the burning rate from equation (5.5).

## 5.4 Results and Discussions

After conducting the experimental programme (raw images given in Appendix B) and applying the relevant processing techniques discussed earlier, it is possible to construct data sets capable of showing the effect of equivalence ratio and initial temperature on the resultant flame speeds and burning velocity within the Cardiff cloud chamber. By comparing the data obtained with current scientific knowledge, it is anticipated that the test facility and techniques employed will be shown to be useful in the investigation of propagating methane-air and methane-water-air flames.

The data for both initial temperatures are presented in the forms of flame growth and flame speed curves in sections 5.4.1 & 5.4.2. The maximum derived flame speed is then used to determine a burning velocity for each case.

### 5.4.1 Statistical Data of Flame growth and Flame speed of Methane-Air explosions initial temperature 50°C

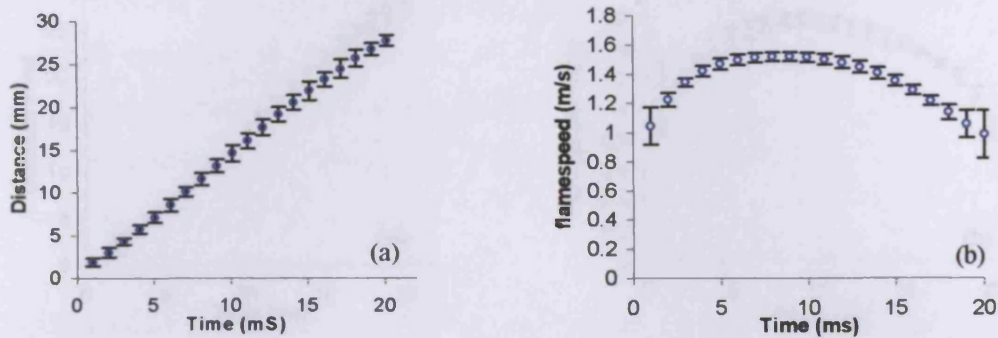


Figure 5.16 (a&b) Processed data for flame growth and flame speed respectively. Equivalence ratio 0.8, Ignition energy 1.76mJ

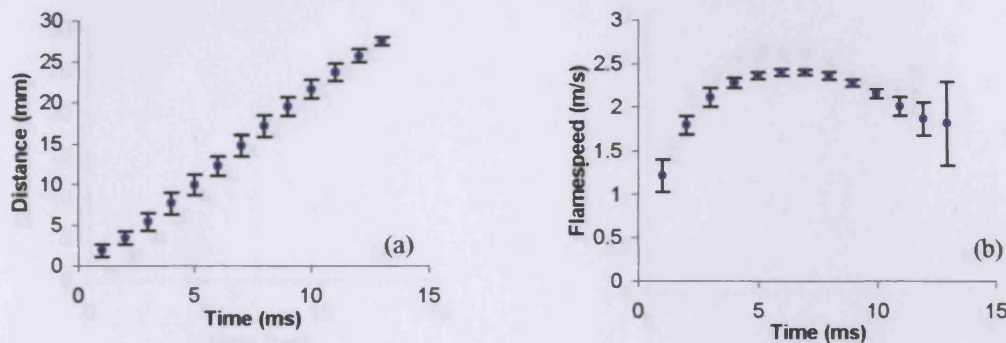


Figure 5.17 (a&b) Processed data for flame growth and flame speed respectively. Equivalence ratio 1.0, Ignition energy 1.76mJ

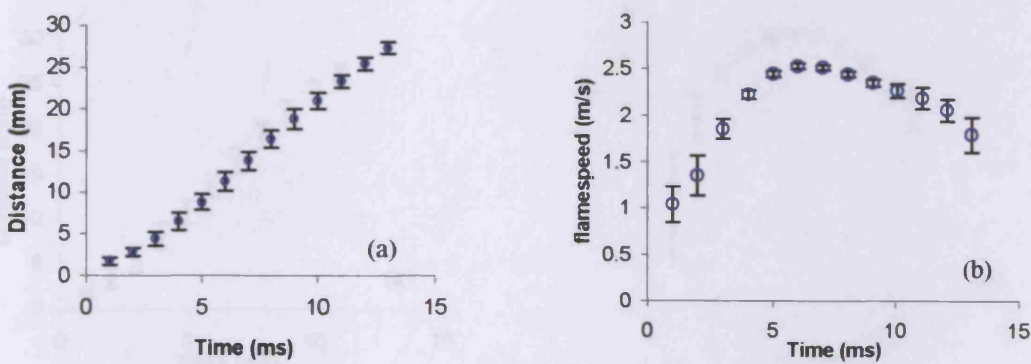


Figure 5.18 (a&b) Processed data for flame growth and flame speed respectively. Equivalence ratio 1.1, Ignition energy 1.76mJ

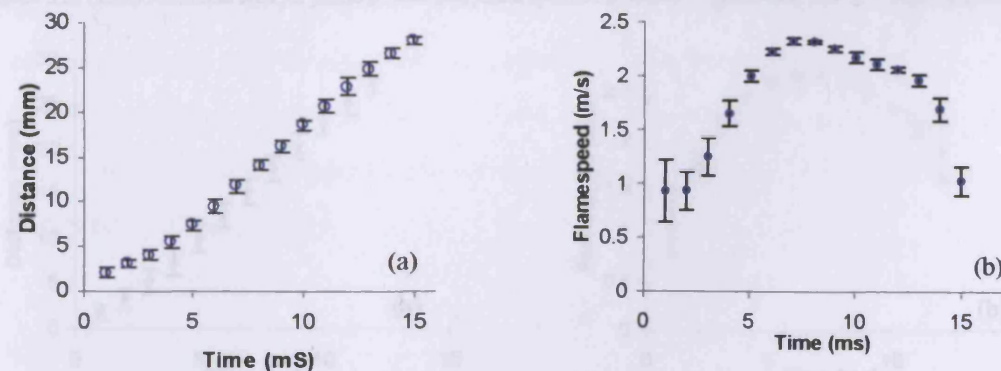


Figure 5.19 (a&b) Processed data for flame growth and flame speed respectively. Equivalence ratio 1.2, Ignition energy 5.1mJ

### 5.4.2 Statistical Data of Flame growth and Flame speed of Methane-Air explosions initial temperature 100°C

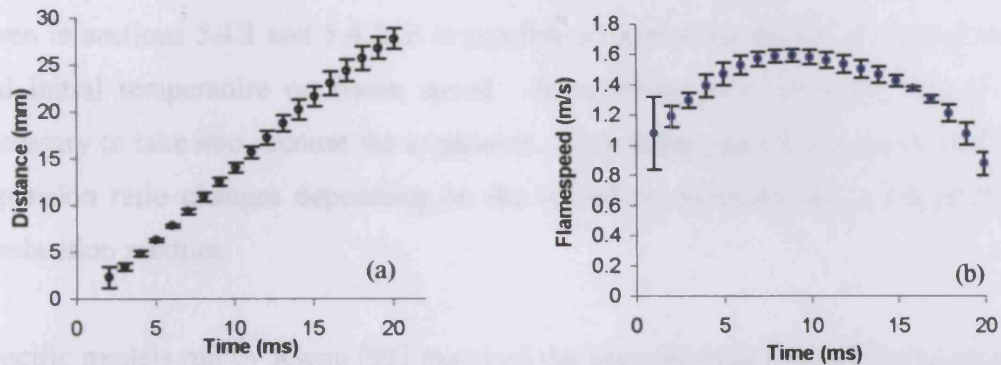


Figure 5.20 (a&b) Processed data for flame growth and flame speed respectively. Equivalence ratio 0.8, Ignition energy 1.76mJ

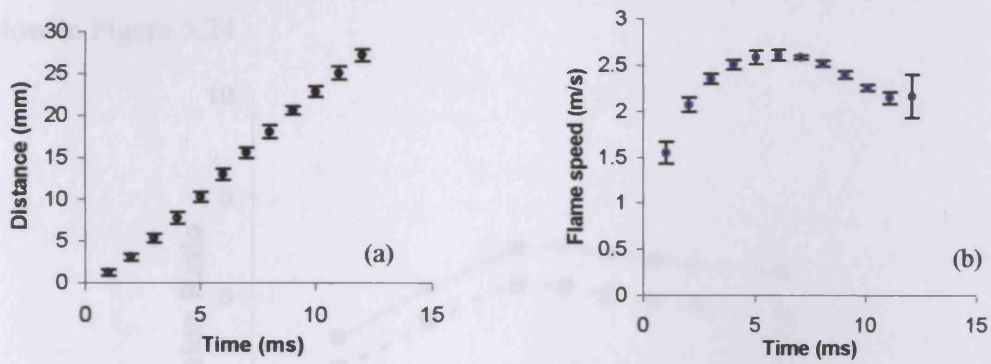


Figure 5.21 (a&b) Processed data for flame growth and flame speed respectively. Equivalence ratio 1.0, Ignition energy 1.76mJ

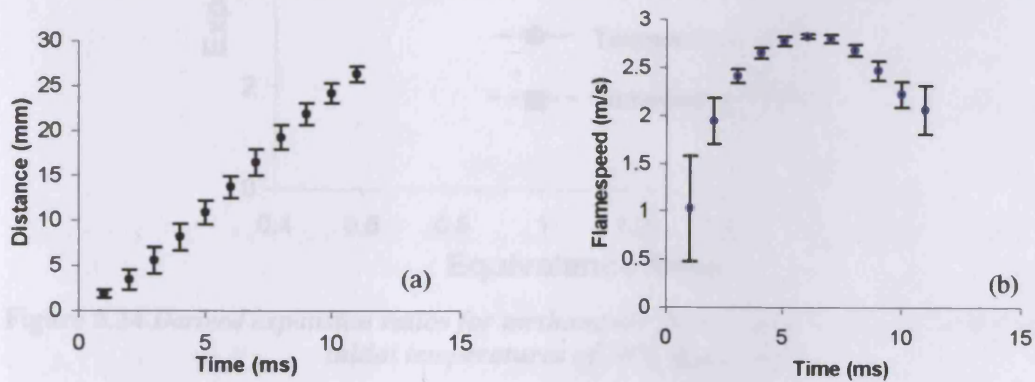


Figure 5.22 (a&b) Processed data for flame growth and flame speed respectively. Equivalence ratio 1.1, Ignition energy 1.76mJ

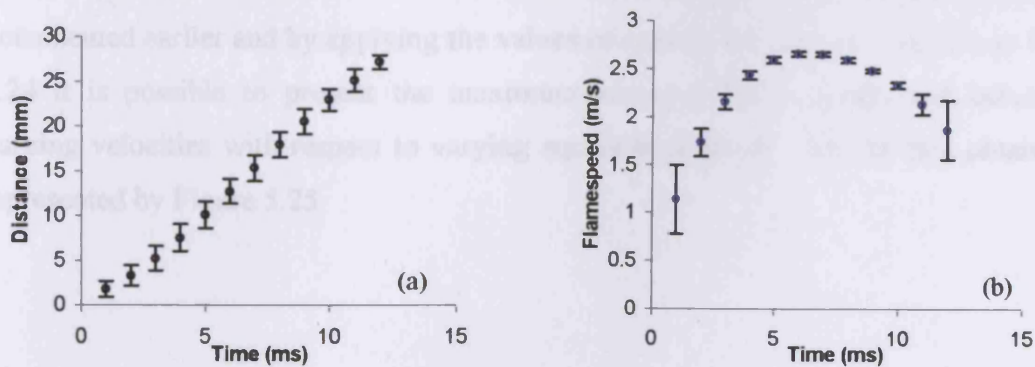
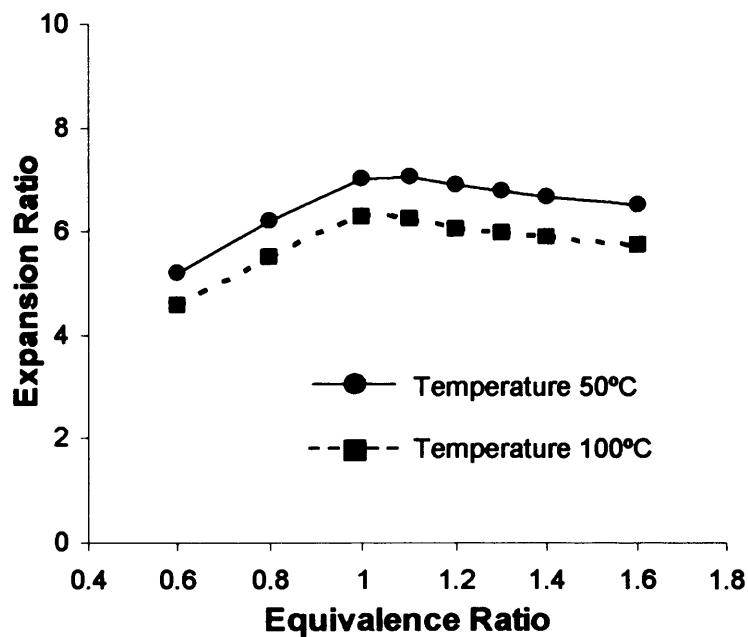


Figure 5.23 (a&b) Processed data for flame growth and flame speed respectively. Equivalence ratio 1.2, Ignition energy 1.76mJ

### 5.4.3 Derived Flame Speed and Burning Velocity Data

By taking the highest value for flame speed exhibited in each of the flame speed graphs given in sections 5.4.1 and 5.4.2, it is possible to derive the effects of equivalence ratio and initial temperature on flame speed. In order to derive burning rate, it is then necessary to take into account the expansion of the burnt gases as discussed earlier. The expansion ratio changes depending on the initial composition and temperature of the combustion mixture.

Specific models run by Kwon [93] matched the experimental programme needed for the remit of this study, and the expansion ratios needed to derive burning velocity is given below in Figure 5.24.



**Figure 5.24** Derived expansion ratios for methane-air flames at various equivalence ratios at initial temperatures of 50°C and 100°C

After derivation of the maximum measured flame speed in each of the experiments documented earlier and by applying the values of expansion ratios given above in Figure 5.24 it is possible to present the maximum recorded flame speeds and subsequent burning velocities with respect to varying equivalence ratios. All the data obtained is represented by Figure 5.25.

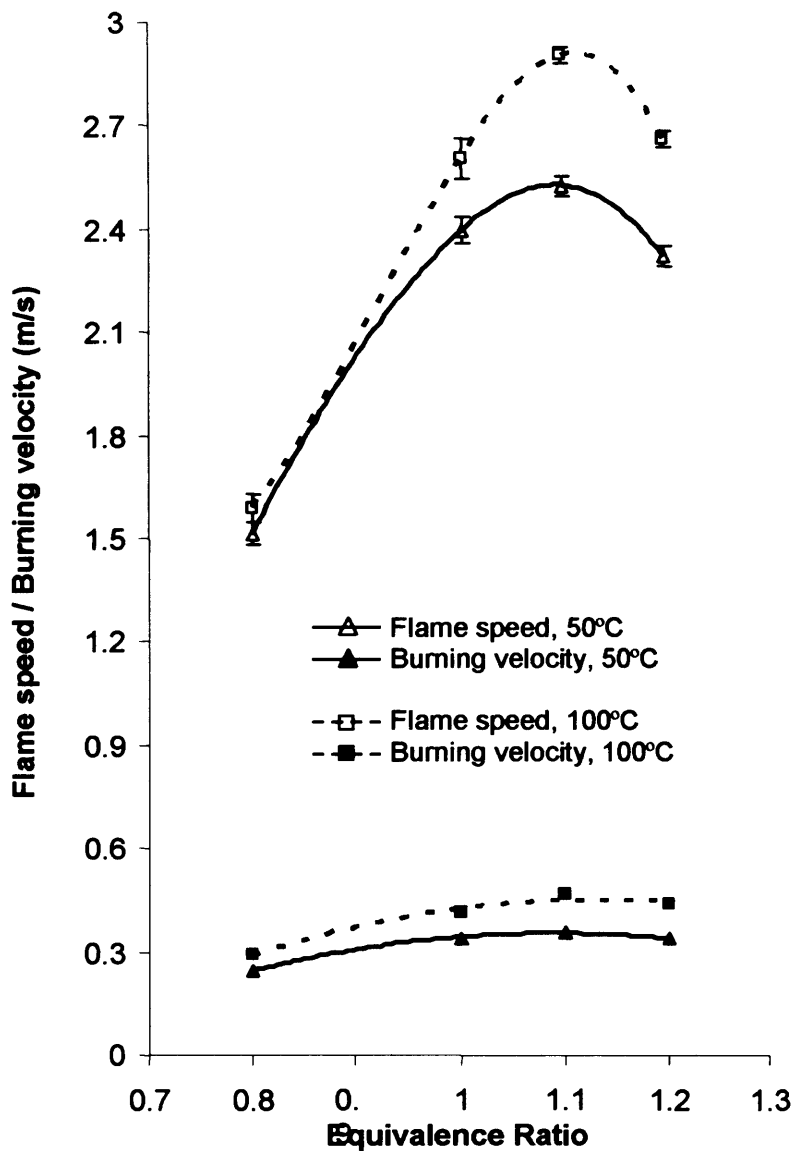


**Figure 5.25** *Maximum measured flame speeds and derived burning velocity for methane-air flames within the Cardiff cloud chamber with various equivalence ratios and initial temperatures*

As can be deduced from Figure 5.25 the initial temperature as expected is proportional to the observed flame speed/ burning velocity. The equivalence ratio causes a polynomial trend on flame speed with a maximum flame speed and burning rate being observed at just rich of stoichiometry, with lean and rich flames burning at a slower rate.

#### 5.4.4 Comparison of Cardiff Cloud Chamber Data with Published work

As discussed in section 5.2.2 there is considerable data in the literature contributing to the understanding of the burning velocity of methane-air flames. In order to confirm that the Cardiff cloud chamber is capable with current facilities and procedures of producing competent data it is necessary to compare data sets.

Before the data obtained for this research can be compared with other data, it is first necessary to correct the data with respect to initial temperature to derive a burning rate corresponding to an initial temperature of 25°C, which is then comparable with the literature data generated between 15-25°C. The correlation proposed by Mishra [89] (5.9) is appraised against data generated from the Cardiff cloud chamber at different initial temperatures and equivalence ratios. If this appraisal proves satisfactory, then this methodology can then be utilised to generate data for comparison with previous methane-air studies. The results of measured against predicted results are presented in Figure 5.26. The Mishra criterion was used to predict a 100°C data set from the 50°C data so a comparison may be made with the actual obtained data. The data is then used to predict a burning rate curve for a 25°C case.

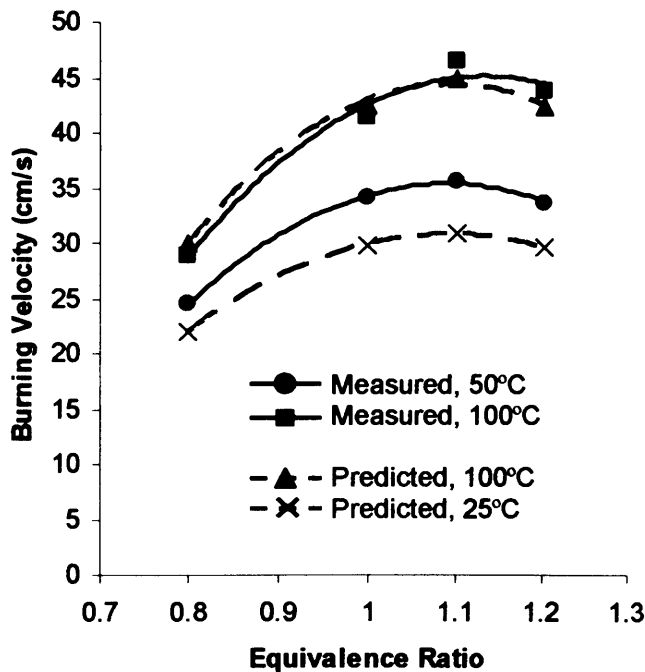
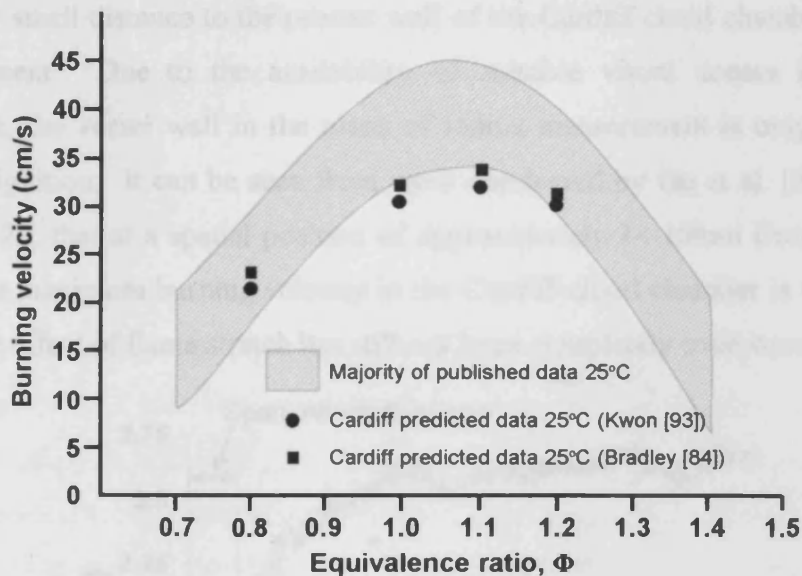


Figure 5.26 Appraisal of the accuracy of the proposed correlation for the effect of initial temperature and predicted results

It can be seen from the above Figure 5.26 that the correlation proposed by Mishra [89] from the 50°C baseline data-set produces a predicted result for 100°C that is within  $\pm 1.5\text{cm/s}$  of the measured values obtained within the Cardiff cloud chamber. Thus it is surmised that the data produced within the remit of this study compares favourably with other data demonstrating the effect of initial temperature on the burning velocity of methane-air flames. In this knowledge, the 50°C dataset was then used to extrapolate back to predict the burning rate at 25°C. It was thus possible to predict the burning velocities that would have been obtained with an initial temperature of 25°C.

The burning velocities may then be compared on a like for like basis with other studies previously conducted.



**Figure 5.27 Comparison of maximum derived burning velocity of Cardiff cloud chamber compared with other published data**

It is clearly visible from Figure 5.27 that the maximum derived burning velocities for the Cardiff cloud chamber are lower than those derived in other studies. However the shape of the curve suggests that the mixing methodology is suitable.

There are a number of factors that are contributing to these low burning velocities including the measurement of the Schlieren flame front instead of the cold front radius. Andrews and Bradley [72] state that this error is most prolific when the rate of change of flame thickness with radius becomes significant. It is known that flame thickness decreases with increasing pressure, thus in the small geometry of the Cardiff cloud

chamber there will be a rise in pressure as the flame propagates and this will cause an underestimation of the flame speed.

Another possible source of error could be in the expansion ratios used. As was shown in Figure 5.15 the values generated by Kwon [93] are higher than those published by other authors. If values of expansion ratio produced by Bradley et al. [84] had been used which are typically 3-4% lower then burning velocities approximately +2cm/s compared with those published in this study would have been generated as is shown by the squares in Figure 5.28.

It is thought, however that the largest contribution to the low burning rates is brought about due not to measurement or processing techniques associated with this work but the relatively small distance to the nearest wall of the Cardiff cloud chamber in the plane of measurement. Due to the availability of suitable visual access for the Schlieren technique, the vessel wall in the plane of radius measurement is only 35mm from the point of ignition. It can be seen from work conducted by Gu et al. [87], and shown in Figure 5.29, that at a spatial position of approximately 14-16mm from ignition source, where the maximum burning velocity in the Cardiff cloud chamber is witnessed (Figure 5.18), the effect of flame stretch has still not been completely overcome.

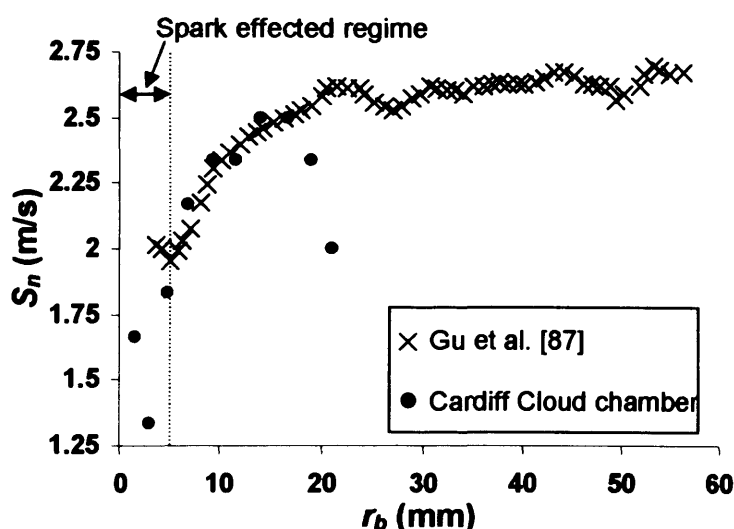


Figure 5.29 Comparison of measured flame speeds at different flame radius in Leeds bomb and Cardiff cloud chamber for methane-air flame,  $\Phi=1$

It can be seen from Figure 5.29 that when the raw data from an experiment undertaken within the Cardiff cloud chamber is superimposed onto the data provided by Gu et al. [87], there is a very close match in the flame speed until the flame radius reaches 15mm.

Beyond this point, the flame speed within the Leeds bomb carries on increasing compared to the falling Cardiff cloud chamber data, this fall in flame speed occurs owing to a rising pressure in the rig as the flame front approaches the cylinder front window. Thus it may be deduced that the flames are behaving as in other test facilities but because of the smaller propagation distance to nearest wall, the flame doesn't reach a maximum flame speed as flame stretch is not fully overcome. Thus flame speeds measured in this study are only approximately 90% of the maximum flame speed as indicated by other researchers.

It may also be noted that there is a difference in the spark effected regime, owing to the lower ignition energies of approximately 2mJ used in this study which are an order of magnitude lower than those quoted by Gu et al. [87]. For this reason there is a significant reduction in the influence of ignition overdrive, which is very beneficial for rigorous study of the effects of flame stretch.

## **5.5 Future work**

Due to the fact that the remit of this study is to investigate the effect of water on propagating methane-air flames, particularly during early flame propagation for comparison with detailed chemical-kinetic computer models, then the cloud chamber serves its purpose. However, use of the Cardiff cloud chamber could be improved by simply moving the electrodes backwards and filming the event through the front window instead of the smaller side windows. This would afford a combustion area of flame radius 60mm compared to the 35mm used in this study. By referring to Figure 5.29, it may be seen that this would allow the flame speed to reach its maximum value.

In order that the above modification could be made viable, different filming equipment would be required. At present there are two possible solutions to this filming issue. First, a new Schlieren system could be designed which would allow filming through the front window, as indicated in Figure 5.30.

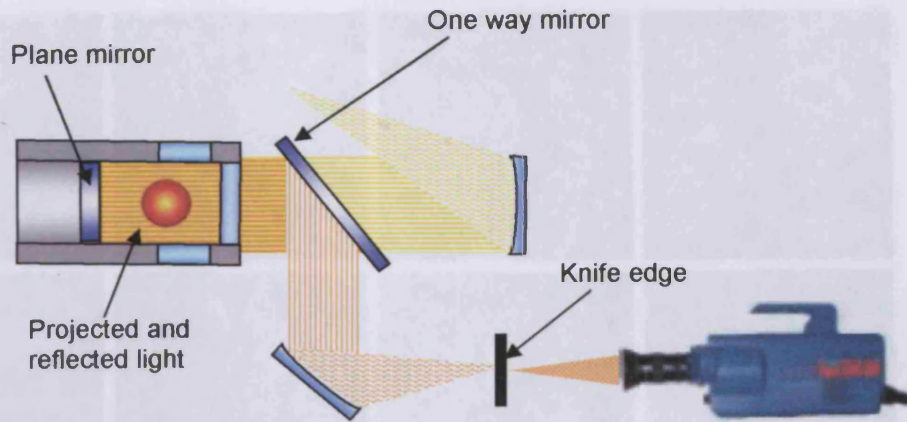


**Figure 5.30 Possible Schlieren setup capable of filming through front window of Cardiff cloud chamber**

The system relies on a one way mirror set at  $45^\circ$  allowing collimated light to be passed into the chamber, reflected off a plane mirror positioned on the piston then reflected via the one way and second concave mirror into the recording apparatus via a knife edge.

The aforementioned system however does not remove ambiguity in measurement brought about because of the various Schlieren isotherms, thus a filming technique relying solely on the flames luminosity for recording could be utilised if its light dependency was low enough. Recent advancements in high speed digital cameras may have made this technique possible. A trial has been undertaken using the new PHOTRON APX camera and as can be seen from the series of images produced, it now appears possible to film directly through the front window and observe the flame growth to a flame radius of 60mm at higher filming rates than those used for this study.

There is also further valuable data on flame stretch that could be derived from the data produced for this study. Flame stretch model/data appraisal is ongoing with the Imperial College Thermofluid research group (Lindstedt), and will be published in due course.

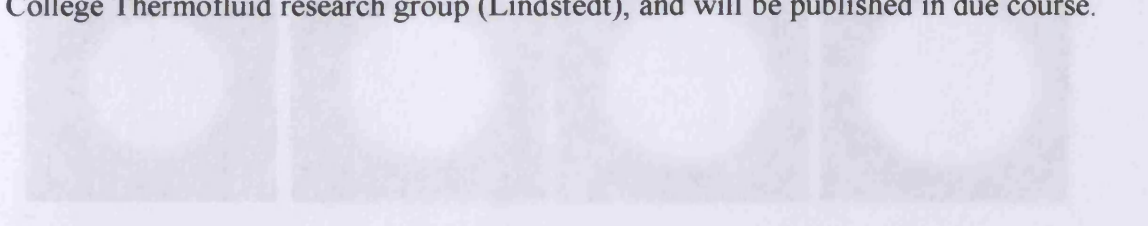


*Figure 5.31 Flame growth within Cardiff cloud chamber filmed using Photron digital camera*

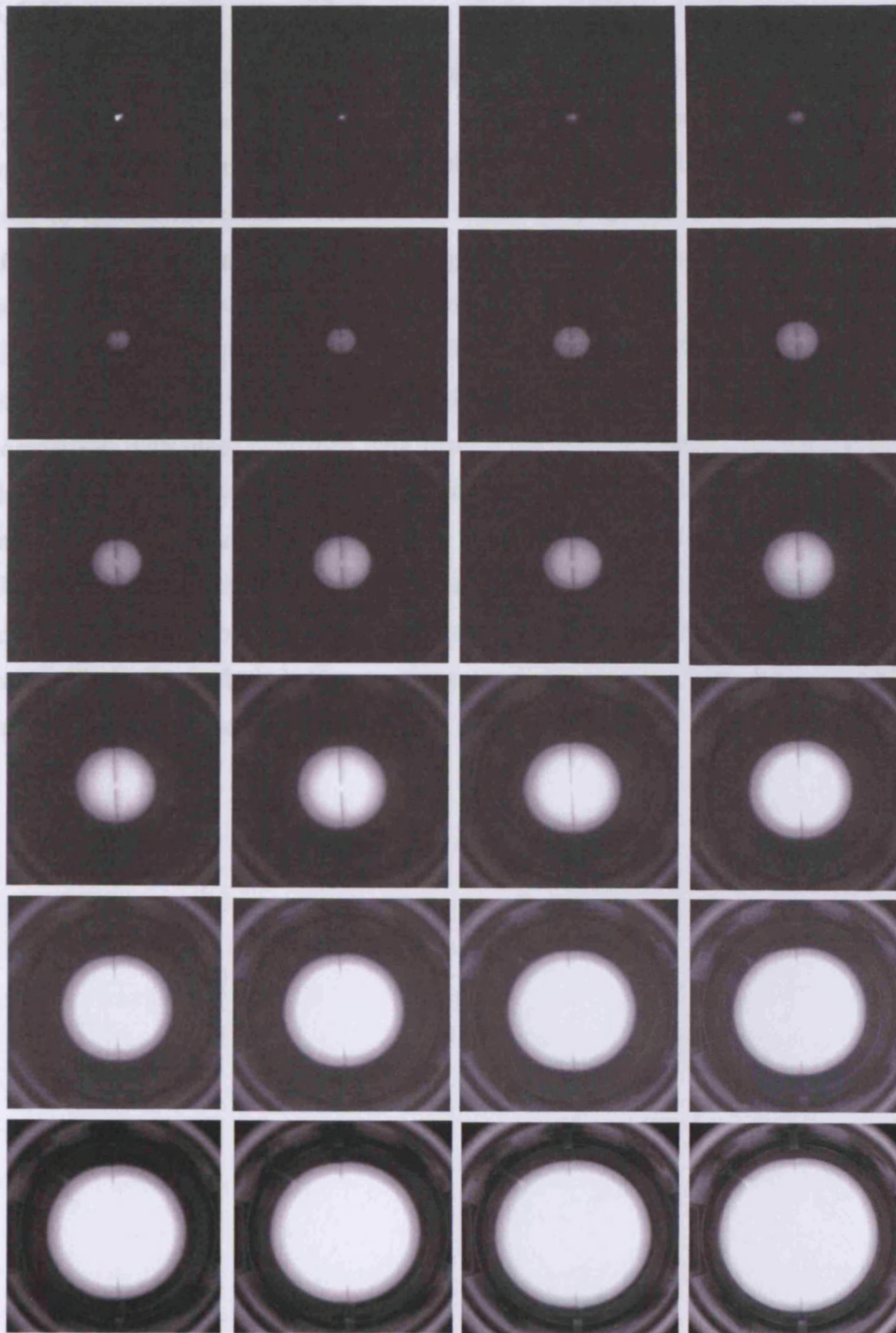


**Figure 5.31** *Flame growth within Cardiff cloud Chamber filmed using Photron digital camera (1000fps)*

## 5.6 Summary

After conducting an experimental programme to investigate the feasibility of using the Cardiff cloud chamber as a combustor for the study of methane-air flames, a number of conclusions can be drawn. It has been shown that the Cardiff cloud chamber can be used to quantify/benchmark methane-air flame propagation rates, and is particularly effective during the early stages of propagation, when flame stretch is important, due to the very low ignition energies utilised in this study. Moreover, the 5 repeats undertaken for each test provide possibly the first defensible statistical information on the accuracy of burning rate data from fully confined vessels. Excellent agreement is attained in comparison with other published data from other confined bombs during the stretched flame region. However, due to the geometrical configuration of the cloud chamber utilised in this study and hence associated pressure effects, the flame speed only reaches about 90% of its maximum value, and so the maximum flame speeds measured are lower than those published in the literature. However, methods for overcoming this current limitation without having to construct a new rig have been proposed and partly appraised in preparation for future studies.

Chapters 4 & 5 demonstrated that the Cardiff cloud chamber is capable of producing mono-dispersed water droplets of characteristic size likely to be suitable for explosion mitigation, and is suitable as a combustion diagnostic facility. Hence, in this chapter the laminar burning characteristics of stretched methane-air flames with the addition of water in the form of vapour or droplets can be studied, and benchmark data generated. This data will assist in the thesis aim of appraising the efficacy of water as a suppressant for methane-air explosions.

Water as a suppressant was discussed in detail in Chapter 2; however, its effectiveness at a fundamental level particularly in the case of laboratory-scale propagating laminar methane-air flames is a notable omission from the current literature.

## **6.1 Calculation of Water vapour Fractions**

Before studies could commence, first it was necessary to determine a method of describing the proportion of water in the combustion mixture. As seen in Chapter 2, there are many different ways in defining the water concentration within a combustible mixture. It was decided that the most suitable way of representing the water present was by calculating it as a molar percentage of the total mixture.

An equation to determine the volume of water to be injected is derived below:

Consider the system as shown in Figure 6.1 below with the methane and air premixed in the confined bomb at a preset pressure and temperature and the water to be injected at ambient temperature and pressure.

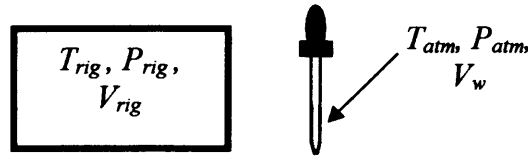


**Figure 6.1 Schematic diagram representing pre-mixing conditions of water, methane and air**

Hence, the volume of water ( $V_w$ ) to provide the required molar percentage ( $r_w$ ) of water vapour after the methane/air/water is fully mixed needs to be calculated.

A number of factors are measurable or preset before the addition of the water to the mixture, namely;

$$V_{rig}, P_{rig}, T_{rig}, T_{atm}, P_{atm}, ER, r_w, Mr_w, \rho_w$$

Therefore these values must be used to calculate the unknown quantities, namely;

$$V_w, n_w, n_a, n_m, V_{air}, V_{methane}$$

The molar percentage of water in combustion mixture may be given by (6.1):

$$r_w = \frac{n_w}{(n_{air} + n_{methane}) + n_w} \quad (6.1)$$

Rearranging (6.1):

$$\text{Using, } n_w = \frac{r_w(n_{air} + n_{methane})}{(1 - r_w)} \quad (6.2)$$

$$V_w = \frac{n_w Mr_w}{\rho_w} \quad (6.3)$$

Implemented the gas laws give:

$$P_{rig} V_{air} = n_{air} R_o T_{rig} \quad (6.4)$$

$$\text{And: } P_{rig} V_{methane} = n_{methane} RT_{rig} \quad (6.5)$$

$$V_{air} + V_{methane} = V_{rig} \quad (6.6)$$

Substituting (6.2) into (6.3) and using (6.4), (6.5) and (6.6) can be shown to give:

$$V_w = \frac{Mr_w}{\rho_w} \times \frac{P_{rig} V_{rig}}{RT_{rig}} \times \left( \frac{1}{r_w} - 1 \right)^{-1} \quad (6.7)$$

## 6.2 Experimental Programme

Following the findings of Chapter 5, it was decided that the experimental programme should again include equivalence ratios of 0.8, 1.0, 1.1 and 1.2 at initial temperatures of 50°C and 100°C so as a comprehensive comparison between ‘wet’ and ‘dry’ cases could be conducted. After thoroughly reviewing the literature and on ascertaining the limitations associated with thermodynamic conditions within the Cardiff cloud chamber, it was decided that molar fractions of 5%, 10% and 15% would be examined for the vapour cases.

The effectiveness of the facility in producing a definable, mono-dispersed water mist as shown in Chapter 4, made it possible to also investigate the effectiveness of ‘fine’ water mists as quenching agents. Various droplet diameters of 5µm, 10µm, 15µm and 20µm were chosen due to their formation properties being close to the thermodynamic conditions suitable for comparative studies. Owing to the size of the data set and other limitations (discussed later), it was decided to conduct droplet cases with an equivalence ratio of 1.0 only, with water fractions of 5% and 10%.

For the vapour cases it was decided that the programme should again assess repeatability and facilitate statistical analysis, and hence five experiments were undertaken for the majority of experimental conditions. However due to satisfactory prior tolerances and time constraints, a reduced repeatability of three data sets was used for the droplet conditions.

A summary of the full programme is presented in Table 6.1.

**Table 6.1 Schematic representation of experimental programme**

water fraction	Temperature		Droplets			
	50°C	100°C	5µm	10µm	15µm	20µm
0%						
5%				34°C		34°C
10%			48°C		48°C	
15%		ER=1.2 quench				

	Not thermodynamically possible
	5 repeats Equivalence ratios 0.8, 1.0, 1.1, 1.2
	3 repeats Equivalence ratio 1.0 (750 mbar)
	5 repeats Equivalence ratio 1.0 and 3 repeats Equivalence ratio 0.8 & 1.1

## 6.3 Results and Discussions

### 6.3.1 Ignition Energies

Although the remit of this study did not include an investigation of ignition energies for methane/air/water explosions, due to the techniques used in conducting the fundamental experiments a relatively thorough qualitative study was necessary in addition to the experimental programme specified in Table 6.1.

The ignition system used is as detailed in the section 5.1.2. After numerous trial ignitions it was noticed that both the initial energy values and the spark gap had a large influence on the initial flame propagation. It was therefore decided after some deliberation to opt for a compromise between smaller spark gap and larger ignition energy to keep the initial spark gap at 1.5mm for each of the 140 or so experiments conducted in Chapters 5 & 6.

Precise energies within the spark can not be deduced at this time due to losses, however, by using the simple correlation for capacitors given earlier (5.1) the energy in the primary coil could be deduced, representing an upper bound to the actual energy discharged across the electrodes:

As mentioned earlier, there were 3 x 0.47µF capacitors used, which were checked using a B-150 universal bridge (AVC). A total capacitance of 1.39 µF was noted, which is well

within their accepted tolerance. Thus, it was then possible to calculate the energy in the primary coil. By accepting there are losses on the secondary side, the actual energies supplied are lower than those stated here by a factor that could be ascertained in the future. However, it should be noted that these losses will change from day to day as in any electrode system owing to factors such as electrode tip cleanliness and degradation.

The spark energy used was chosen using an iterative technique in order to attain a relatively low ignition energy that would reliably ignite the mixture from day to day. After working with the rig for numerous weeks, it was found that the smallest 'reliable' spark was attainable with the high voltage power supply set to 40V (equivalent to 1.11mJ). Hence, it was decided that the lowest energy used for each experiment would be 50V (1.73mJ). This compares favourably with the literature as it is similar to those quoted by Karpov et al [85], and is an order of magnitude lower than the energies utilised by Gu et al. [87] and Bradley et al. [92] in the Leeds bomb, where energies of the order of 20-30mJ are usually quoted.

Turning the high voltage supply up in 10-volt intervals, and observing the flame quench, determined the ignition energy used for each mixture. Figure 6.2 shows a typical sequence of a flame quenching when ignition energy is insufficient to achieve self-sustained propagation.

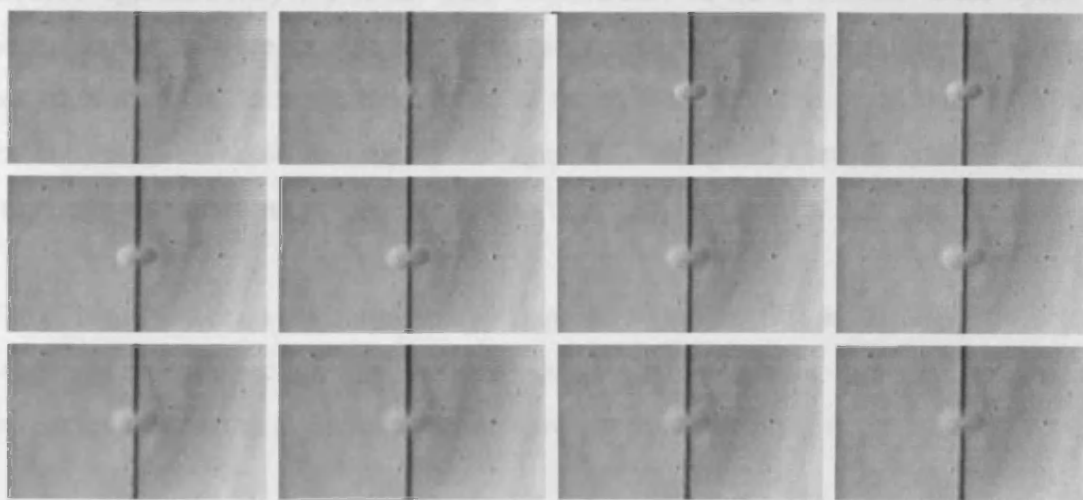


**Figure 6.2** *Schlieren sequence depicting the 'quench' of a propagating flame*

This introduces an interesting concept with regard to the definition of defining limits for quenching of a flame, and is important in interpretation of the methane/air/water data. In

fully confined vessels such as the Cardiff cloud chamber, flames develop as spherical kernels, so by definition experience greatest stretch in the earliest phases of propagation, and hence the quenching limit is a function of ignition energy. If sufficient energy is supplied, eventually ignition occurs followed by sustained flame propagation, and by plotting the flame distance-time graph, it is possible to study the sensitive propagation characteristics of strained flames near quenching conditions. The breakdown voltage was further increased by 10-15V to ensure reliable, repeatable ignition from one day to the next. Owing to the time-consuming nature of this calculation and its lack of scientific rigour, it was decided that values used for the 50°C test cases would be used also for the 100°C cases for consistency within the comparative studies.

As explained above the exact values of energy within the spark cannot be quoted at this time and the energies used are not those of the minimum ignition energy however the energies used are given by Figure 6.3.

There are a number of trends that may be drawn from examining Figure 6.3, namely that the lowest ignition energy required in initiating a reaction always occurred at an equivalence ratio around unity, with the energy required getting higher as the mixture becomes leaner or richer. The addition of water in the form of vapour has the effect of raising the energies required to overcome quenching. Typically it seems the energy required approximately triples for each 5% increase in water fraction. Once again the richest mixtures were most susceptible to flame quench thus requiring the greatest initiation energies. In the extreme case of an equivalence ratio of 1.2 and 15% water fraction, even at maximum supply voltage of 350V (86mJ) led to quenching of the propagating flame front.

The effect of water on the initial energy required to initiate full propagation seems to be dependant on both fraction and phase, as when the water is in the form of 'fine' droplets, the energy required to overcome stretch increases considerably.

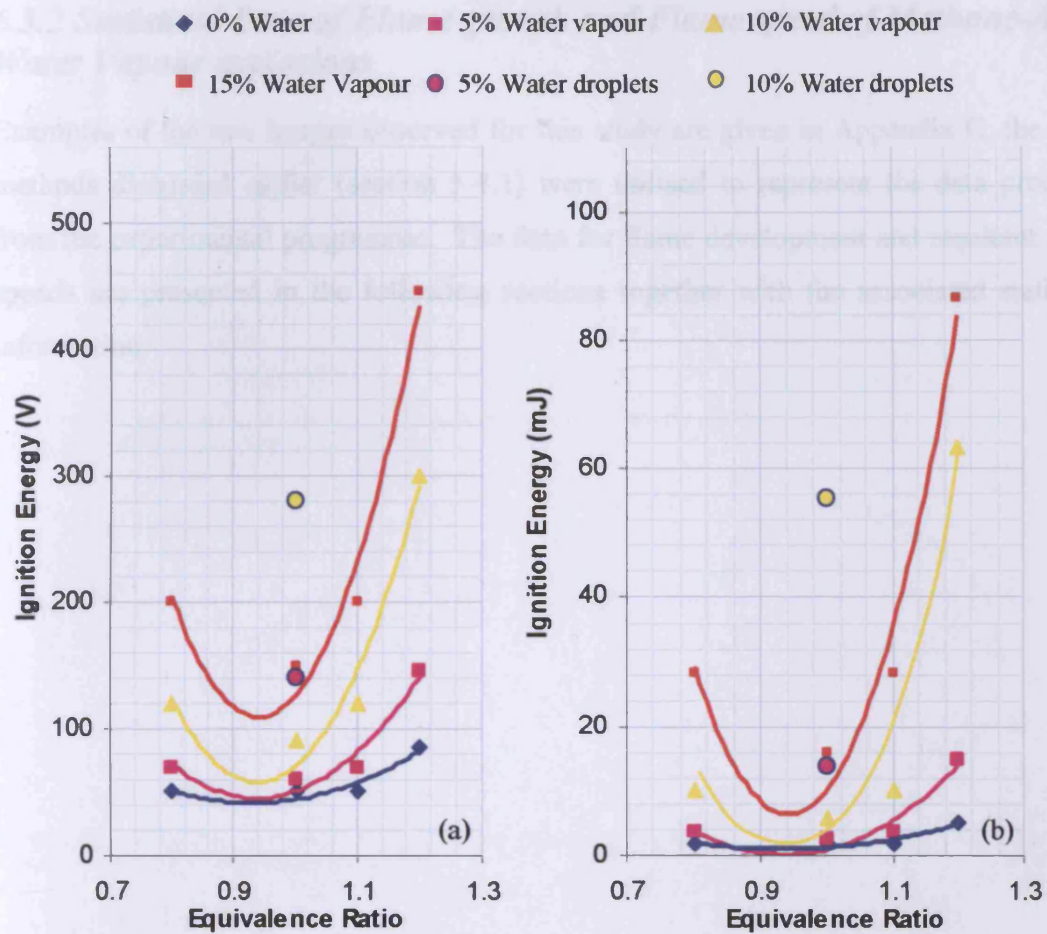


**Figure 6.3 (a&b) Ignition energies used to initiate flame propagation for various combustion mixtures represented as voltage supplied (V) and theoretical spark energy (mJ) respectively**

It may be observed that the droplet cases were only carried out at an equivalence ratio of 1.0 which will be discussed later, but it was perceived that a full data set would not be possible because of the energies required for the richer and leaner mixtures. It can be seen that the energies required are six times higher for the 5% case and nearly ten times higher for the 10% case. However this trend may not only be attributed to the droplets, as in order to create the droplet environment the pressure is reduced prior to ignition. This pressure effect however, would be similar for both the 5% and 10% cases and given that the energy required for the 10% case is 9 times greater compared to the 7 times increase required for the 5% cases then it suggests that the addition of water droplets is a definite influence. Thus it is possible to surmise that water has a greater ability to quench a stretched flame in the form of fine droplets compared with pure vapour, which reinforces the conclusions of the literature review discussed in Chapter 2.

### ***6.3.2 Statistical Data of Flame growth and Flame speed of Methane-Air-Water Vapour explosions***

Examples of the raw images observed for this study are given in Appendix C, the same methods discussed earlier (section 5.4.1) were utilised to represent the data produced from the experimental programme. The data for flame development and resultant flame speeds are presented in the following sections together with the associated statistical information.

### 6.3.2.1 Initial Temperature 50°C Water fraction 5% Vapour

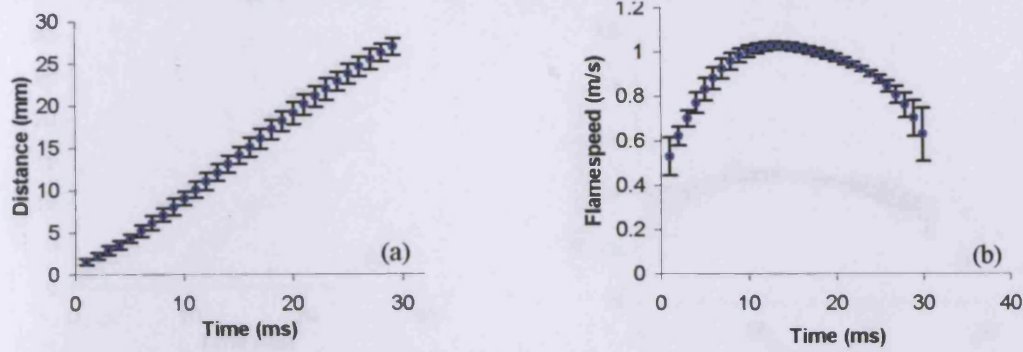


Figure 6.4.1 (a&b) Processed data for flame growth and flame speed respectively. Equivalence ratio 0.8, Ignition energy 3.5mJ, 5% Water Vapour, Initial temperature 50°C

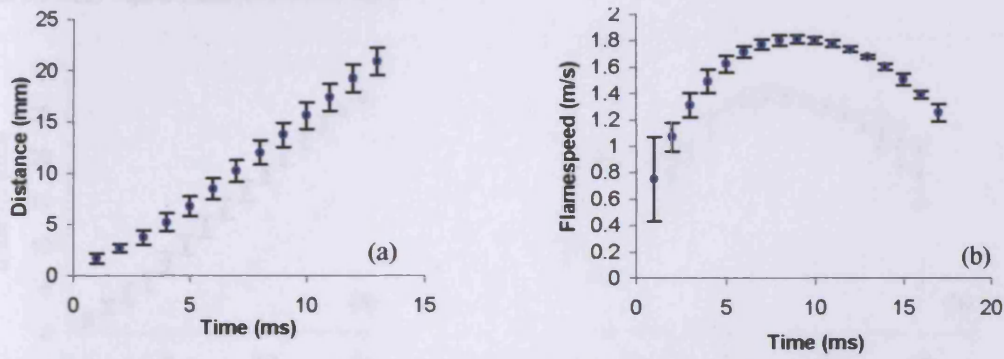


Figure 6.4.2 (a&b) Processed data for flame growth and flame speed respectively. Equivalence ratio 1.0, Ignition energy 2.5mJ, 5% Water Vapour Initial temperature 50°C

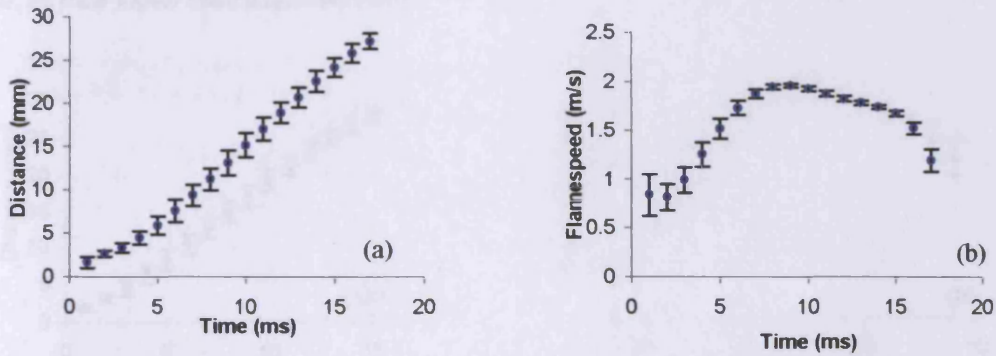


Figure 6.4.3 (a&b) Processed data for flame growth and flame speed respectively. Equivalence ratio 1.1, Ignition energy 3.5mJ, 5% Water Vapour Initial temperature 50°C

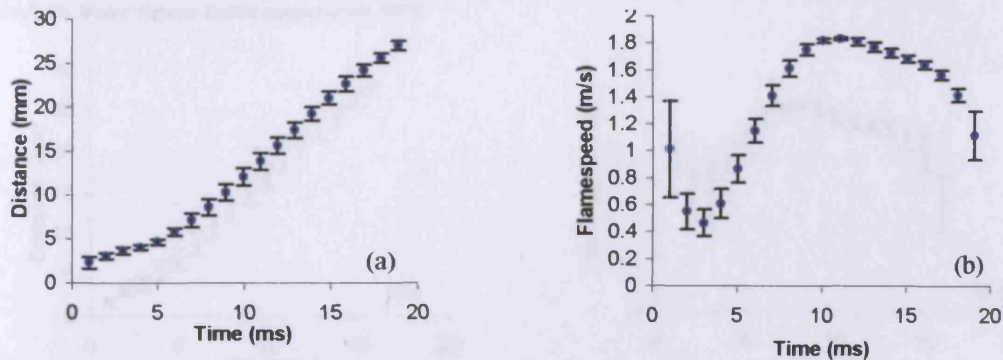


Figure 6.4.4 (a&b) Processed data for flame growth and flame speed respectively. Equivalence ratio 1.2, Ignition energy 15.9mJ, 5% Water Vapour Initial temperature 50°C

6.3.2.2 Initial Temperature 100°C Water fraction 5% Vapour

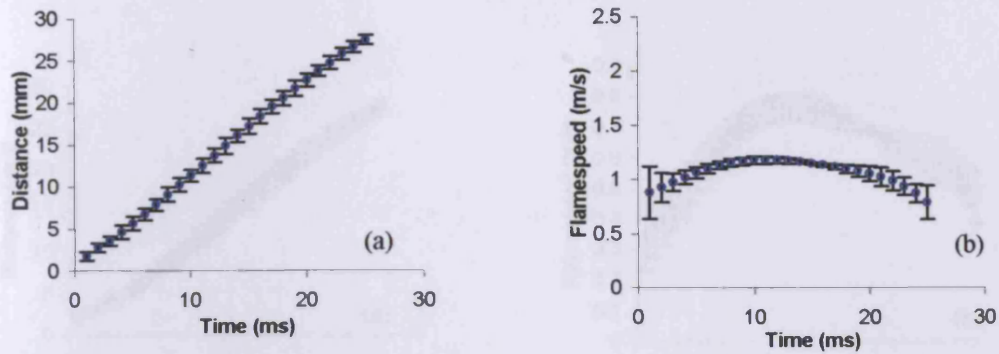


Figure 6.5.1 (a&b) Processed data for flame growth and flame speed respectively. Equivalence ratio 0.8, Ignition energy 3.5mJ, 5% Water Vapour Initial temperature 100°C

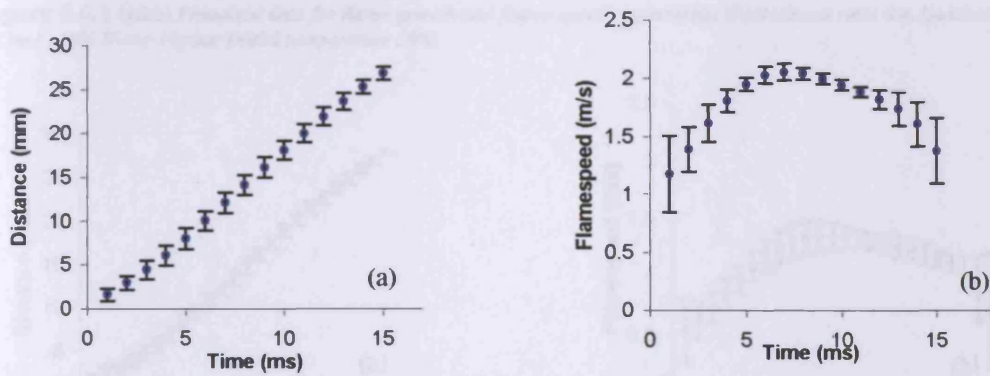


Figure 6.5.2 (a&b) Processed data for flame growth and flame speed respectively. Equivalence ratio 1.0, Ignition energy 2.5mJ, 5% Water Vapour Initial temperature 100°C

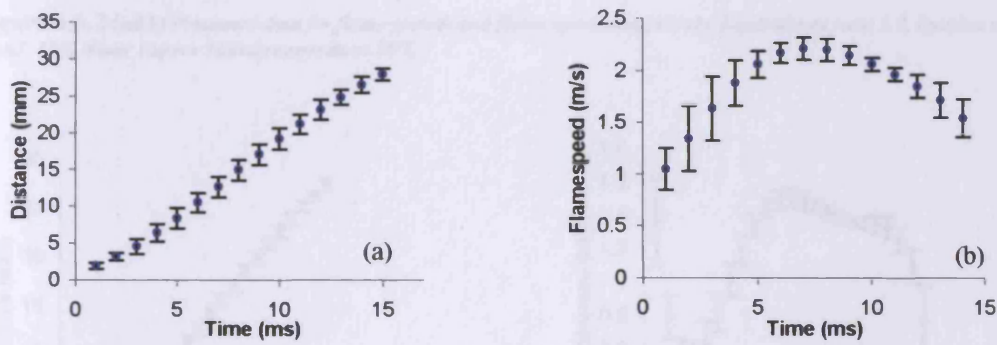


Figure 6.5.3 (a&b) Processed data for flame growth and flame speed respectively. Equivalence ratio 1.1, Ignition energy 3.5mJ, 5% Water Vapour Initial temperature 100°C

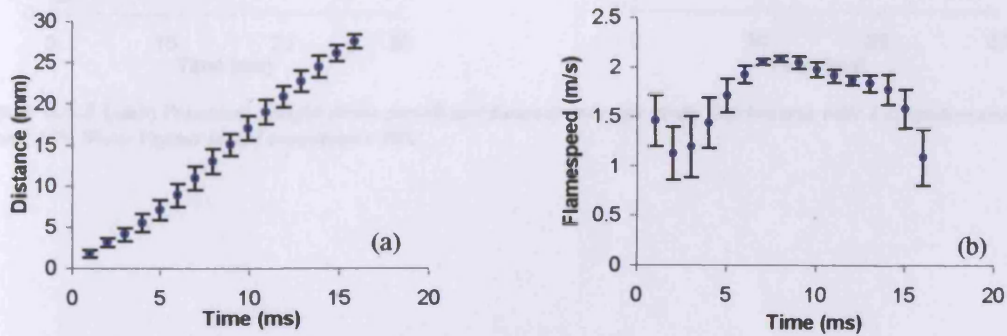


Figure 6.5.4 (a&b) Processed data for flame growth and flame speed respectively. Equivalence ratio 1.2, Ignition energy 13.8mJ, 5% Water Vapour Initial temperature 100°C

### 6.3.2.3 Initial Temperature 50°C Water fraction 10% Vapour

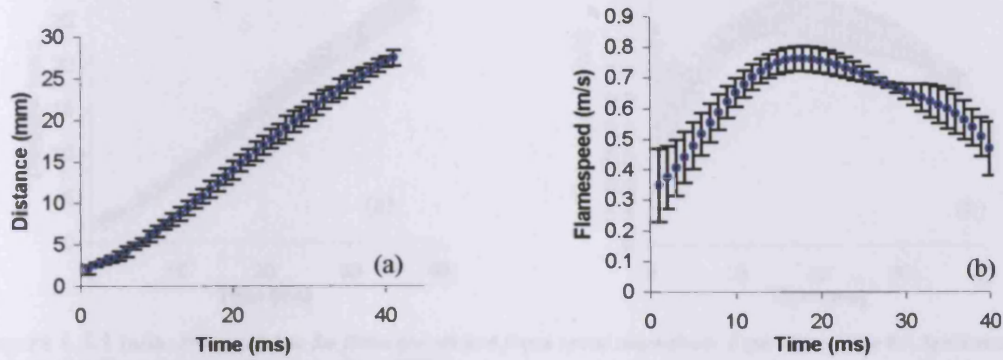


Figure 6.6.1 (a&b) Processed data for flame growth and flame speed respectively. Equivalence ratio 0.8, Ignition energy 10.2mJ, 10% Water Vapour Initial temperature 50°C

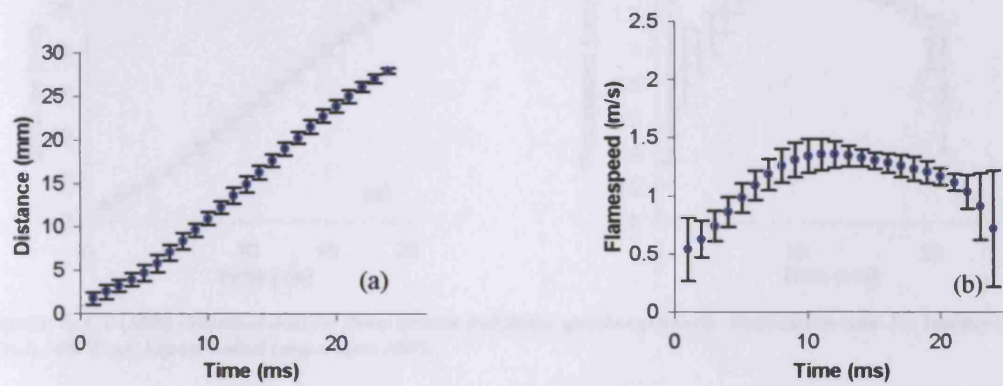


Figure 6.6.2 (a&b) Processed data for flame growth and flame speed respectively. Equivalence ratio 1.0, Ignition energy 5.7mJ, 10% Water Vapour Initial temperature 50°C

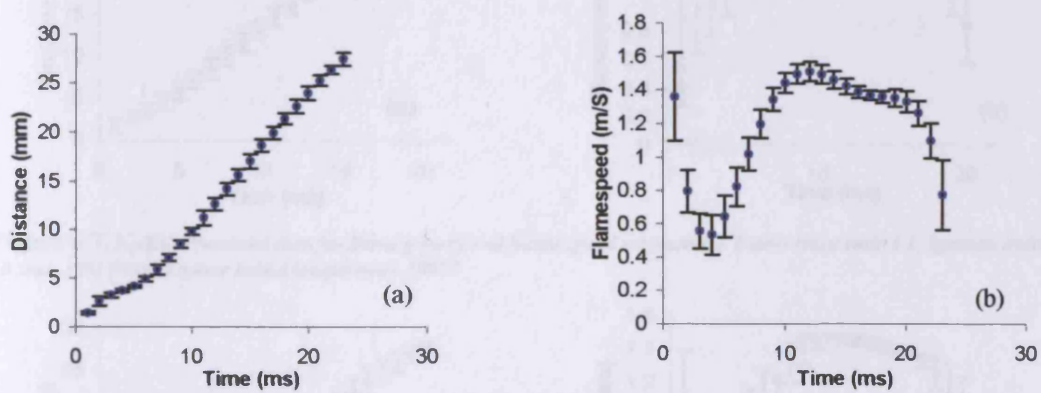


Figure 6.6.3 (a&b) Processed data for flame growth and flame speed respectively. Equivalence ratio 1.1, Ignition energy 10.2mJ, 10% Water Vapour Initial temperature 50°C

### 6.3.2.4 Initial Temperature 100°C Water fraction 10% Vapour

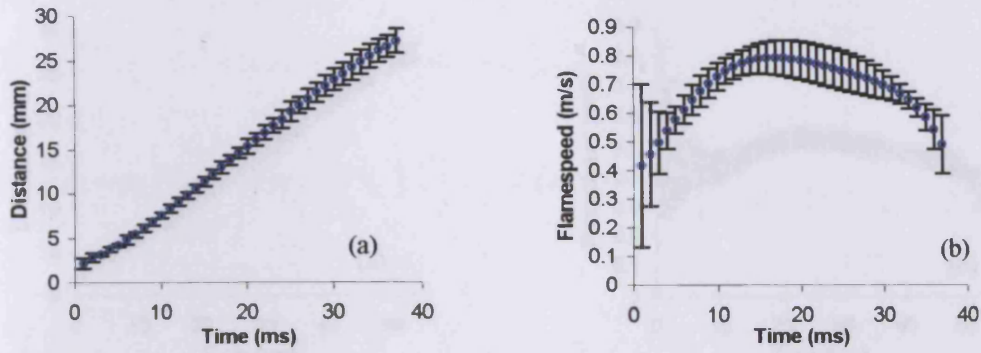


Figure 6.7.1 (a&b) Processed data for flame growth and flame speed respectively. Equivalence ratio 0.8, Ignition energy 10.2mJ, 10% Water Vapour Initial temperature 100°C

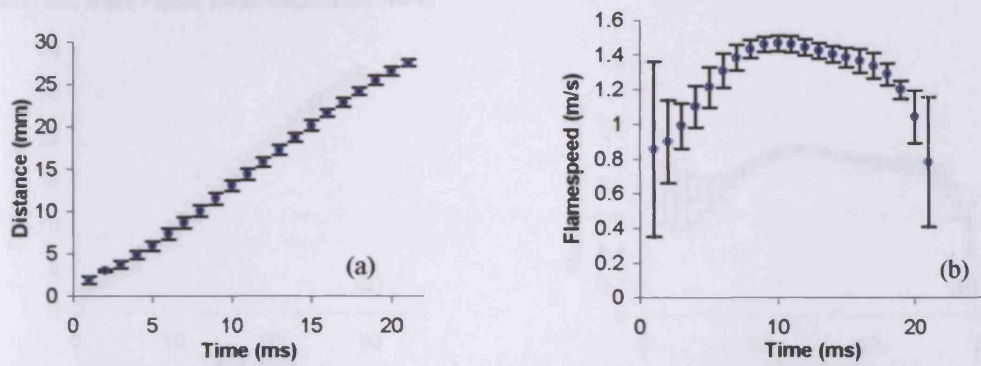


Figure 6.7.2 (a&b) Processed data for flame growth and flame speed respectively. Equivalence ratio 1.0, Ignition energy 5.7mJ, 10% Water Vapour Initial temperature 100°C

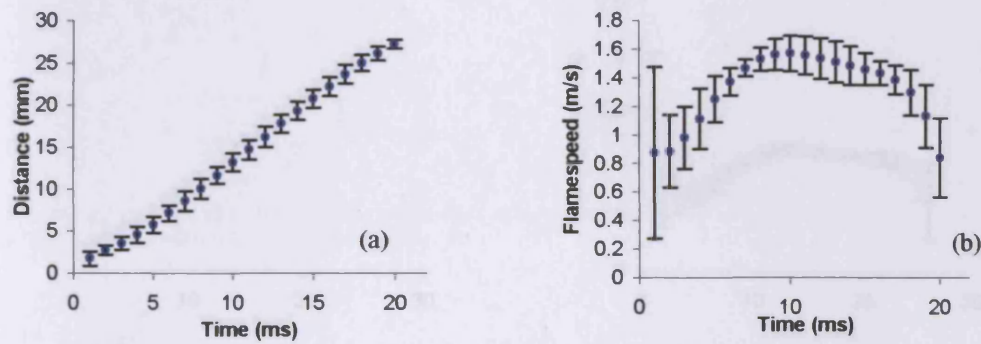


Figure 6.7.3(a&b) Processed data for flame growth and flame speed respectively. Equivalence ratio 1.1, Ignition energy 10.2mJ, 10% Water Vapour Initial temperature 100°C

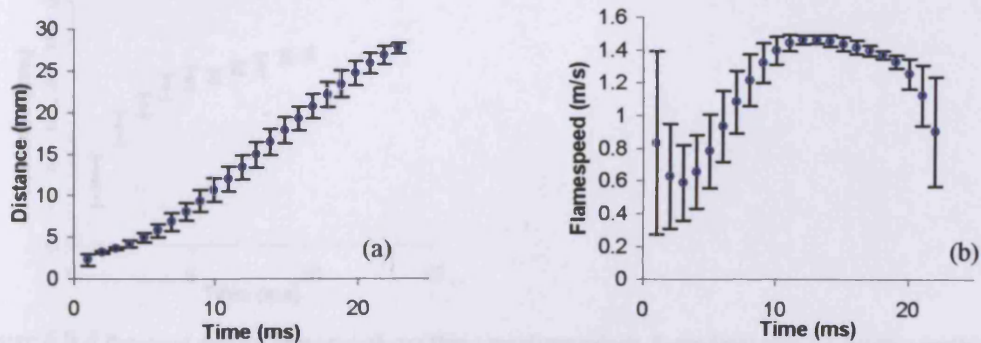


Figure 6.7.4(a&b) Processed data for flame growth and flame speed respectively. Equivalence ratio 1.2, Ignition energy 300v, 10% Water Vapour Initial temperature 100°C

### 6.3.2.5 Initial Temperature 100°C Water fraction 15% Vapour

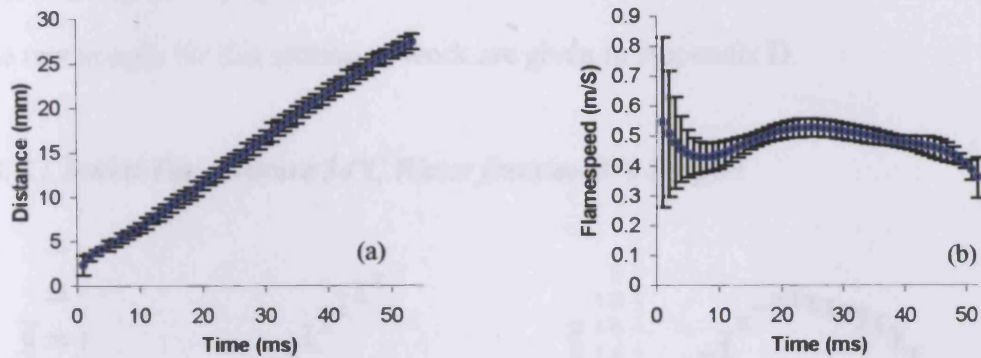


Figure 6.8.1(a&b) Processed data for flame growth and flame speed respectively. Equivalence ratio 0.8, Ignition energy 28.2mJ, 15% Water Vapour Initial temperature 100°C

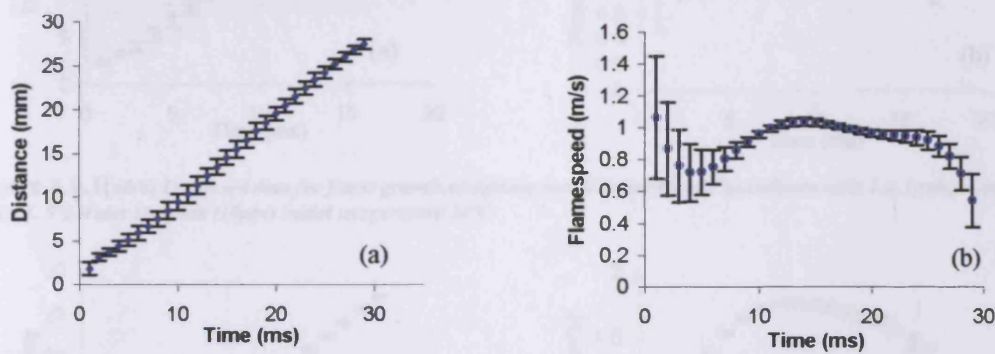


Figure 6.8.2(a&b) Processed data for flame growth and flame speed respectively. Equivalence ratio 1.0, Ignition energy 15.9mJ, 15% Water Vapour Initial temperature 100°C

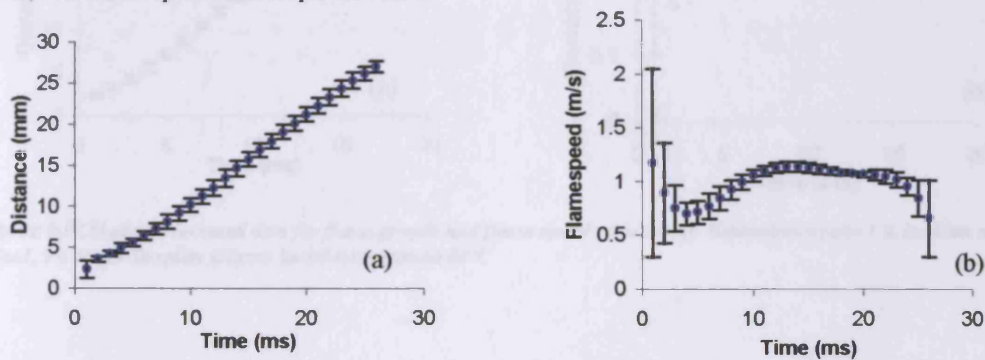


Figure 6.8.3(a&b) Processed data for flame growth and flame speed respectively. Equivalence ratio 1.1, Ignition energy 28.2mJ, 15% Water Vapour Initial temperature 100°C

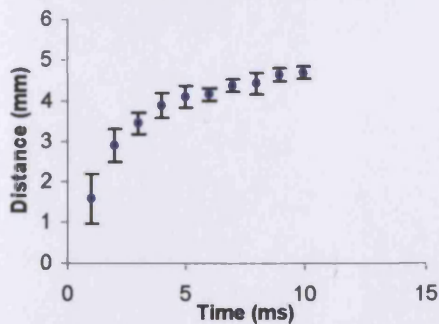


Figure 6.8.4 Processed data for flame growth and flame speed respectively. Equivalence ratio 1.2, Ignition energy 86.4mJ, 15% Water Vapour Initial temperature 100°C

### 6.3.3 Statistical Data of Flame growth and Flame speed of Methane-Air-Water Droplet explosions

The raw images for this section of work are given in Appendix D.

#### 6.3.3.1 Initial Temperature 34°C Water fraction 5% Droplet

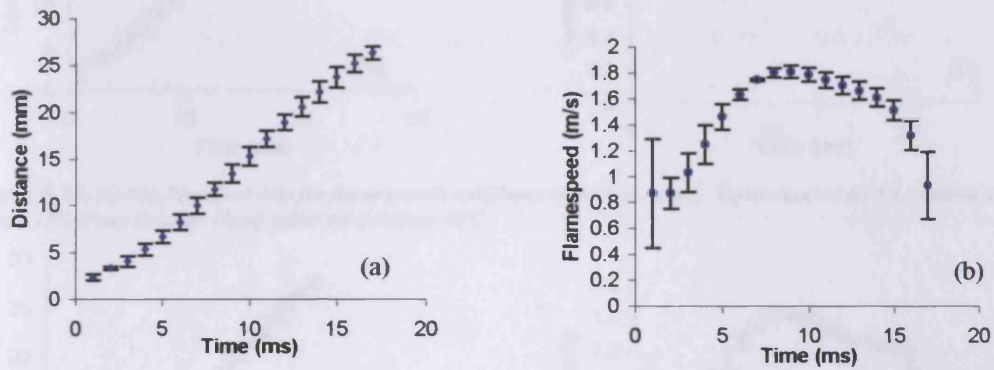


Figure 6.9.1(a&b) Processed data for flame growth and flame speed respectively. Equivalence ratio 1.0, Ignition energy 13.8mJ, 5% Water Droplets (10 $\mu$ m) Initial temperature 34°C

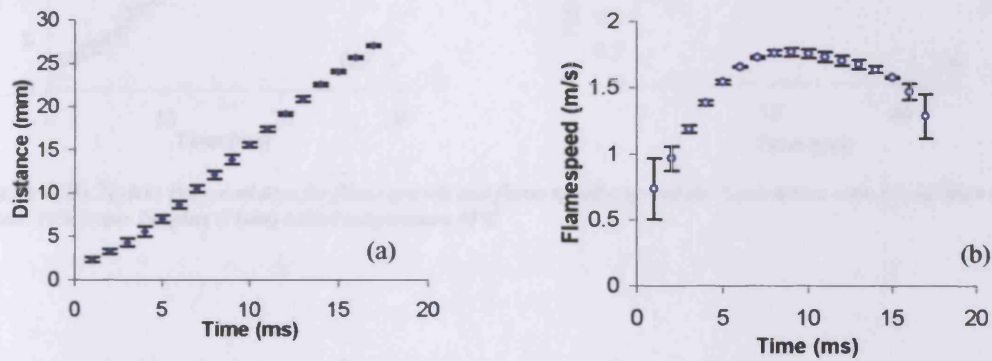


Figure 6.9.2(a&b) Processed data for flame growth and flame speed respectively. Equivalence ratio 1.0, Ignition energy 13.8mJ, 5% Water Droplets (20 $\mu$ m) Initial temperature 34°C



## 6.4 Derived Flame Speed and Burning Velocity Data

The same methods as discussed in Chapter 5 will once again be utilised to generate flame speed and burning rate data that will be directly comparable to the dry case data sets that were generated and discussed in section 5.4.3. As before burning rate calculations will be completed using expansion ratios calculated by Kwon [93]. The same CHEMKIN model developed earlier was used to generate expansion rate data for the methane-water-air systems comparable to the experiments conducted and illustrated in section 6.3. The expansion ratios generated are stated in Figure 6.11.

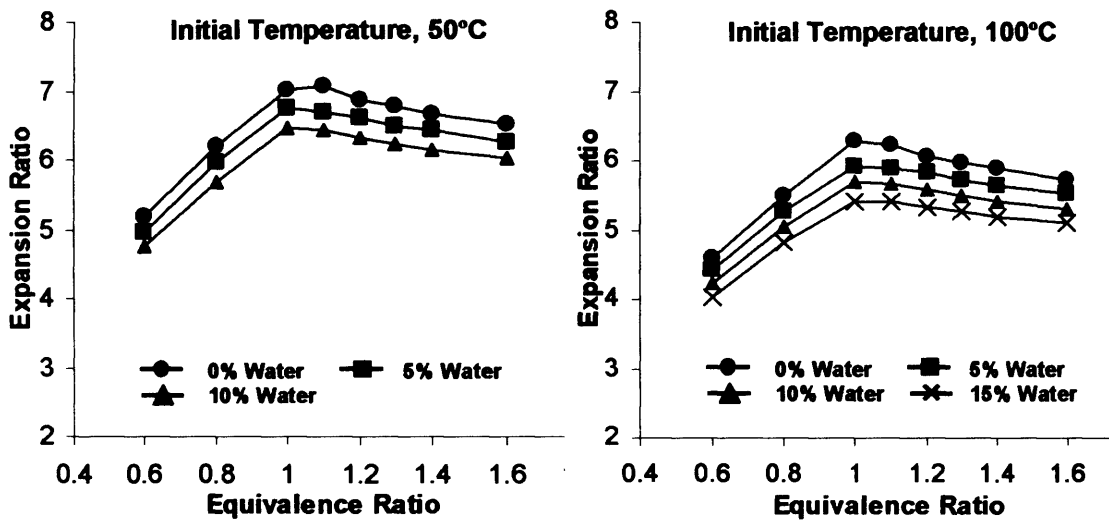


Figure 6.11 (a&b) *Derived values of expansion ratio at initial temperatures of 50°C and 100°C respectively*

The flame speed and burning rates derived from data reported in section 6.3 are given in Figure 6.12. Figure 6.12 clearly shows that the slower the flame speed and resultant burning rates are represented by the mixtures with higher water concentrations, as expected. Also it may be noted that the water droplet cases act at least as effectively as the vapour cases. As can be seen the droplet cases lie within the error bars of the vapour case, however it should be noted that in order to form the droplet case it is necessary to reduce the initial pressures and temperatures which effects the resultant burning rates as discussed later.

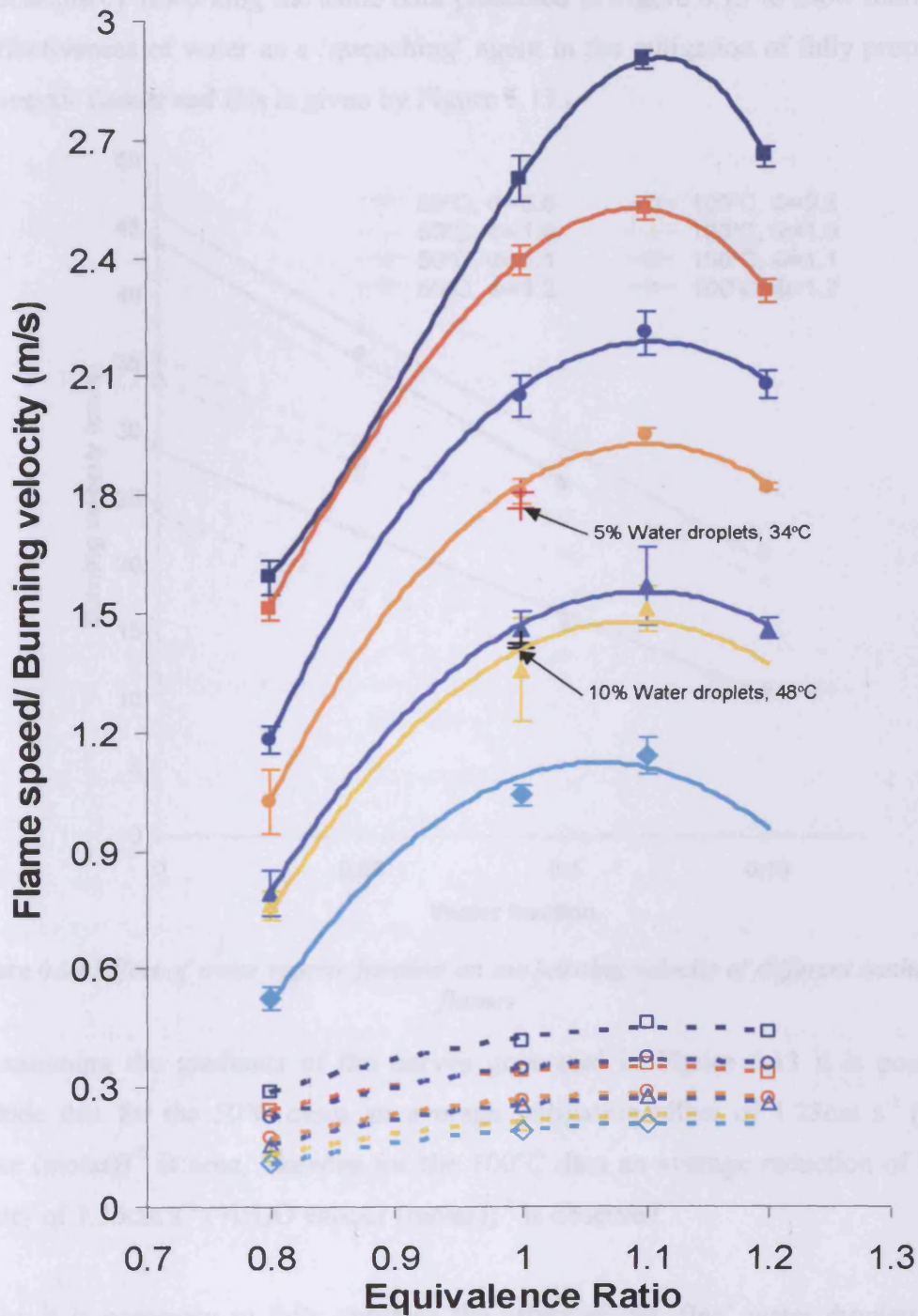


Figure 6.12 Effect of water concentration, temperature and equivalence ratio on flame speed and burning velocity of methane-air flames

It is possible by reworking the same data presented in Figure 6.13 to show more easily the effectiveness of water as a 'quenching' agent in the mitigation of fully propagating methane-air flames and this is given by Figure 6.13.

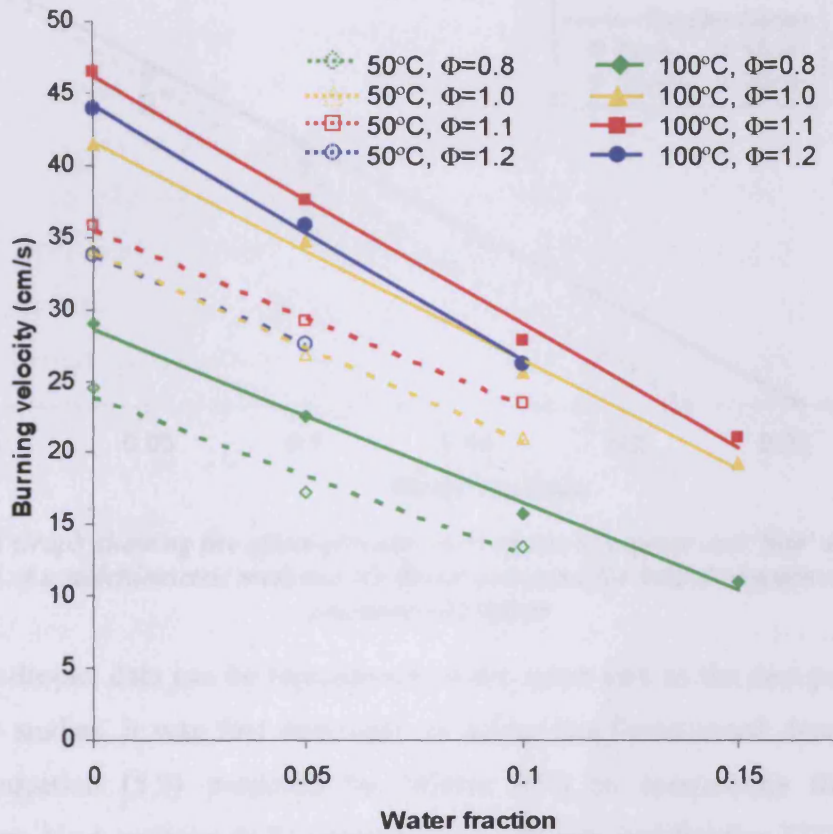
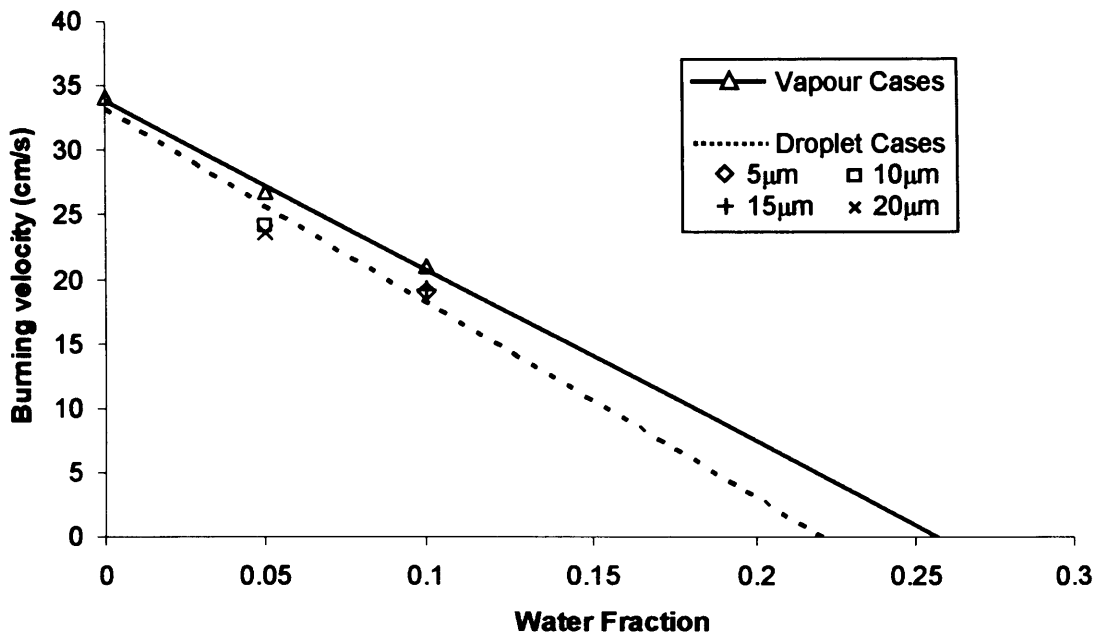


Figure 6.13 Effect of water vapour fraction on the burning velocity of different methane-air flames

By examining the gradients of the curves generated in Figure 6.13 it is possible to conclude that for the 50°C cases an average mitigating effect of  $1.23\text{cm s}^{-1} (\% \text{H}_2\text{O vapour (molar)})^{-1}$  is seen, likewise for the 100°C data an average reduction of burning velocity of  $1.56\text{cm s}^{-1} (\% \text{H}_2\text{O vapour (molar)})^{-1}$  is observed.

Finally, it is necessary to fully appraise the effect of the 'fine' water droplets on the reduction of burning velocity thus Figure 6.14 has been generated. As discussed earlier it is necessary to reduce both pressure and temperature within the Cardiff cloud chamber to produce the necessary mist of 'fine' droplets.



**Figure 6.14** Graph showing the effect of water in the form of vapour and 'fine' droplets on the mitigation of a stoichiometric methane-air flame corrected for initial temperature 50°C and pressure 1013mbar

So that the droplet data can be represented on the same axis as the data produced from the vapour studies, it was first necessary to adjust the flame speed data obtained by applying equation (5.9) proposed by Mishra [89] to compensate for the lower temperatures. Next equation (5.8) generated by Andrews and Bradley [77] was utilised to adjust for the effect of lower pressures. After correction, data points for droplet cases respective of the initial conditions of 50°C and 1013mbar are presented in Figure 6.14 and it should be observed that the droplet cases appear to be more effective than their equivalent vapour cases. The 'fine' droplets further reduce the burning velocity of the methane-air flames by approximately 10%, which is obviously advantageous in terms of developing explosion suppression systems.

As can be seen the vapour case curve crosses the x-axis at approximately 26% which is comparable to the data produced by Sapko et al. [21] which suggests that the water fraction necessary for inerting a stoichiometric methane-air mixture is 26.5% thus showing excellent agreement of data sets. If such an approximation of 'inerting' limit can be assumed then it is possible to conclude that a lower water fraction of approximately 22% water in the form 'fine' mist may be capable of making a stoichiometric methane-air mixture inert.

## 6.5 Summary

A statistically rigorous data-set providing flame propagation rate data for methane/water-vapour/air flames has been generated for the first time in a fully confined vessel. A data-set for methane/water-mist/air with homogeneous mists of characteristic droplet size between 5-20 $\mu\text{m}$  has also been provided. The data is presented in a form suitable for comparison with physical-chemical model predictions, which is currently ongoing via a complementary modelling study at Imperial College [95]. Whilst not the intention at the outset, to ensure that flames have not been significantly overdriven, it has been necessary to study in some detail the ignition energy characteristics of these mixtures. The ignition energy characteristics indicate that water and more so water-mist will be relatively more effective in quenching stretched flames, characteristic of those encountered in turbulent environments. For example, though a 20 $\mu\text{m}$  mist of 10% total molar water concentration was eventually able to support self-sustained propagation; this was only achieved when a significantly overdriven initiating flame was generated (55.3mJ), with quenching occurring for lower ignition energies. For practical purposes at this stage of understanding, the data has been reduced for presentation in simplified form to indicate the influence of water vapour fraction and water mist on the 'approximate' un-stretched burning rate of methane/air flames. This indicates that addition of every 5% molar water concentration reduces the burning rate by typically 15%, whilst introducing the water in the form of fine water mist reduces the burning rate by a further 1.5% which is an extra 10% decrease compared with the pure vapour case.

An 'inerting' limit of 26% water vapour in a stoichiometric methane-air mixture has been illustrated, which is in good agreement of past studies and the droplet data suggests that this limit may be reduced by introducing water in the form of 'fine' mists as suggested by past research.

**CHAPTER****7****Demonstration of the Effectiveness of  
'Fine' Water Mist in a Turbulent  
Environment**

The findings presented in Chapter 6, illustrating the fact that water in the form of vapour and 'fine' mist is capable of suppressing a propagating laminar methane-air flame, this provides the motivation and justification to explore the potential of fine mists as suppression/quenching systems for turbulent flames more representative of a realistic explosion. Chapter 6 showed that water appeared to be most effective at the early stages of flame growth, where flame curvature and flame stretch dominate. Moreover, droplets in the form of fine water mist under these stretched flame conditions appeared to perform more effectively than pure water vapour, and for this reason it is thought appropriate to test water in the form of 'fine' mists in a turbulent environment, where stretched flames prevail.

A turbulent flame duct designed and originally commissioned by SHELL Research Ltd. and since donated to Cardiff, is utilised in this investigation of turbulent methane-air flames and their interaction with fine water mists. The experimental facility was designed to study in detail the effect of turbulence on the resulting flame speed for gaseous fuels and fuel mixtures, and relies on an array of obstacles to generate a turbulent flame environment. The elegant design, originally based on the theory of Taylor [96], trades off turbulent flame acceleration through obstacle interaction, with venting through the roof, such that for a range of vent-ratio and obstacle grid characteristics, flames attain a constant flame velocity for a significant proportion of the propagation length along the duct.

It is the aim of this chapter to demonstrate the conclusions of Chapter 6 by introducing mists with characteristics similar to those defined in the laminar studies, within the turbulent environment generated by the Shell duct rig, to appraise whether or not it is

possible to quench the flame. It is important to emphasise that the aim is that of *demonstration* at this stage, in the anticipation that more rigorous investigations of the interaction of fine water mists with turbulent flames more generally will follow.

## 7.1 Turbulent Test Facility

The test facility shown in Figure 7.1 is best described as an obstacle filled, vented duct. The facility comprises an obstacle filled duct, a retracting roof, a gas mixing system with integrated gas analysis capabilities, an ignition system, a data recording system and an automated control system which ensures each component works in unison at the correct time affording safe reliable data sets to be achieved.

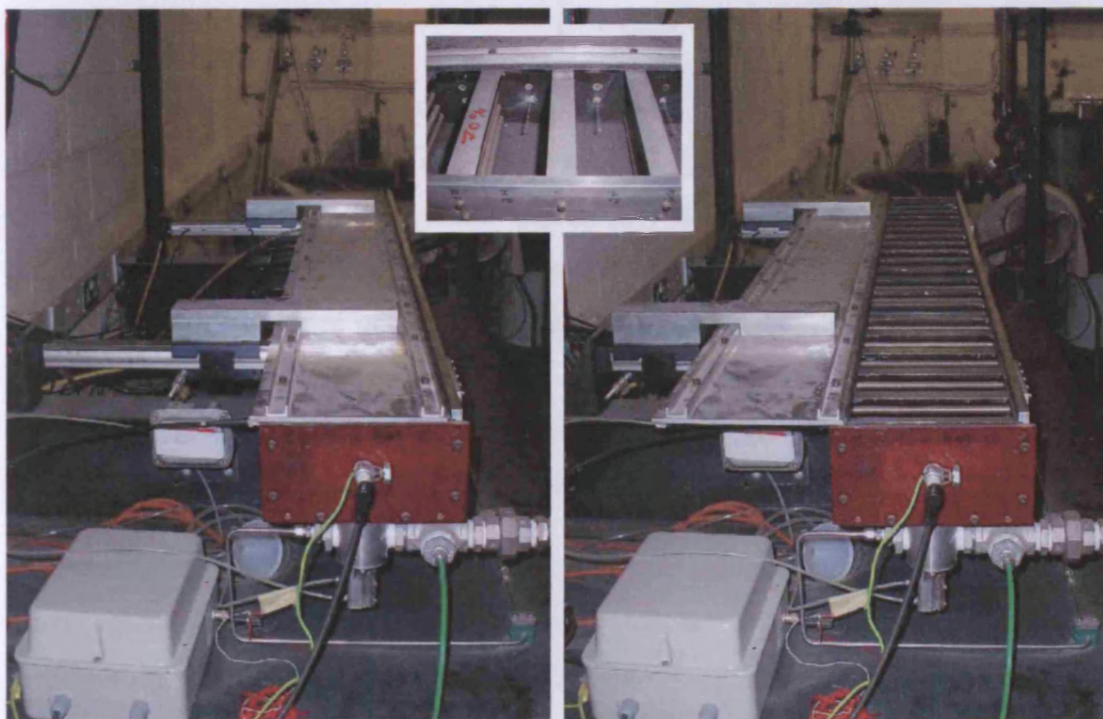


**Figure 7.1** Photographs of turbulent duct showing action of retractable roof and positioning of ignition system, obstacles, ionisation probes and roof vent

### 7.1.1 Obstacle filled Duct

The duct is constructed from 12mm aluminium plates, and has internal dimensions of 2000 x 200 x 100mm. The end plate which supports the ignition source is formed from 12mm Tufnol which is electrically insulating. Optical access is afforded for filming and laser diagnostics via quartz glass windows which can be positioned in the side and bottom walls of the duct. The construction of the duct allows for the level of turbulence

to be pre-determined by the variation of three different variables, namely the blockage ratio, blockage shape and venting ratios through the roof.

#### **7.1.1.1 Blockage Ratio**

Throughout the length of the duct are 19 internal obstacle grids, which are each interchangeable allowing the number, and geometry of each grid to be preset before ignition.

The ratio of the cross-sectional area of the obstacles to the total cross-sectional area of the duct is termed as the blockage ratio (BR), as presented below in equation (7.1),

$$BR = \text{Number of obstacles in grid} \times \left[ \frac{\text{Height of obstacle}}{\text{Height of Duct}} \right] \quad (7.1)$$

It can be observed that the blockage ratio is a non-dimensional measure of the cross sectional area of the duct that is occupied by the projected area of the solid bodies. Obstacles of 5mm and 10mm cross section are available with a maximum of four obstacles per grid. Hence, typical blockage ratios used within this rig are either 0.2 or 0.4, although other values may be achieved by lowering the number obstacles in each grid and/or by using a combination of cross sectional diameters. The higher the blockage ratio, the higher the level of turbulence generated and hence in general, the faster the achievable flame speeds for a given flammable mixture.

#### **7.1.1.2 Blockage Shape**

There are two different geometrical shapes available for obstacles utilised within the turbulent rig. These have either circular or square cross sections. For the same blockage ratio, higher flame speeds are achievable with square cross sectional blockages owing to increased obstacle drag, and hence higher levels of turbulence as the flame passes the sharp edges.

#### **7.1.1.3 Venting Ratio**

The top panel of the duct is constructed using several interchangeable vents. The venting ratio (VR) may be given by equation (7.2),

$$VR = \left[ \frac{\text{Area open to atmosphere}}{\text{Total area of top panel}} \right] \quad (7.2)$$

Once again it can be seen that this is a non-dimensional value, which represents the area open to atmosphere through the roof. There are five different vent panels' available allowing venting ratios of 100%, 70%, 30%, 20% and 10% to be utilised. The higher the venting ratio, the less the effect of expansion ratio of the hot gases and hence the slower the resulting flame speed.

### 7.1.2 Retractable Roof

A pneumatically-driven retractable roof is incorporated into the design, which remains closed to allow controllable gas-air mixing pre-ignition, but which retracts immediately before ignition to expose the vent panel with the desired vent ratio.

The roof utilises a 'hovering' design, whereupon it is held in position 0.2mm above the vent plate by the two pneumatic pistons that are used to retract the roof horizontally away from the top of the duct. For purposes of safety there are electrical switches on the pneumatic slides which ensure that ignition is not possible if the roof is closed. The roofs retraction is controlled either manually or automatically by the control system described later.

### 7.1.3 Gas mixing and Analysis

#### 7.1.3.1 Gas Mixing System

Gas mixing is achieved by a 'flow-through' system as shown in Figure 7.2, and so pre-mixing is required prior to entering the explosion duct.

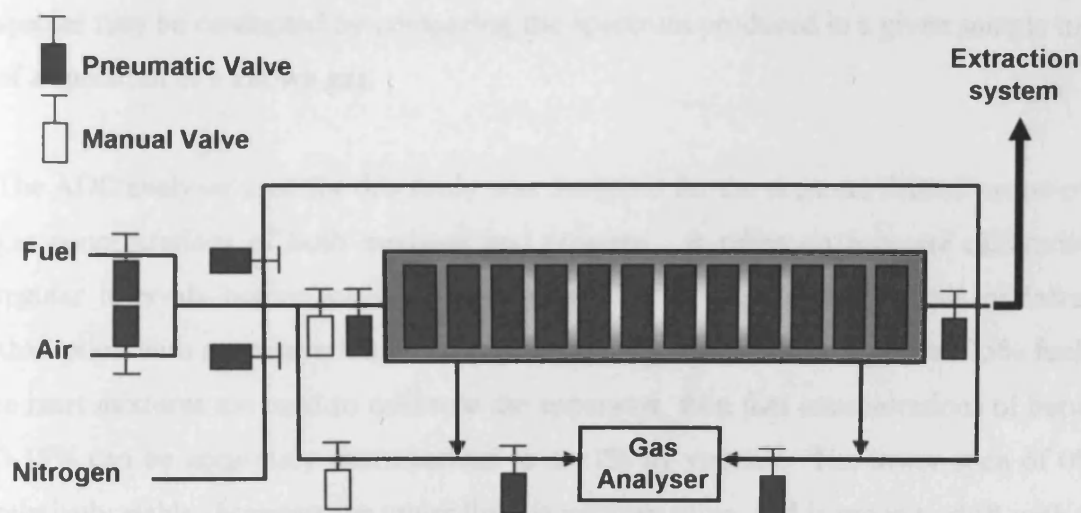


Figure 7.2 Gas mixing system of turbulent test rig

It can be seen that for single-component gas-air mixtures there are three gases required for the safe running of the turbulent duct rig. These gases are individually regulated directly at source, and so to control the mixing of the resultant flammable mixture, accurate pressure regulation is required so that the partial pressure principle can be relied upon to produce an accurate mixture concentration at the mixing point.

Nitrogen is utilised as an inert gas to purge all pipe work prior to ignition ensuring no accidental explosions occur outside of the duct, thus protecting surrounding and ancillary equipment. It can be noted that all gas flow within the system is controlled using either manual or pneumatic valves. The manual valves are safety systems necessary for the setup of the rig and during experiments are all opened. The pneumatic valves are operated via the control unit (discussed in detail later). Thus, the valves may be controlled manually through the control unit or in a fully automated mode, which is necessary for a fully reproducible experiment.

#### ***7.1.3.2 Gas Analysis***

The gas analysis conducted for this work was achieved utilising an infra-red analyser (ADC Instruments Ltd.). Infra-red spectrometry works on the principle that all molecular species absorb infra-red radiation with each species having a particular infra-red absorption spectrum. Thus, infra-red spectrometry may be used to both identify and determine a species concentration within a gaseous mixture [97].

Given that each molecule has a unique absorption spectrum, accurate determination of a species may be conducted by comparing the spectrum produced in a given sample to that of a spectrum of a known gas.

The ADC analyser used for this study was designed for the accurate determination of the gas concentrations of both methane and propane. It relies on accurate calibration at regular intervals before testing. The system relies on the linear trends of infra-red absorption with concentration. Thus, if two span gases of 0% fuel gas and 15% fuel gas in inert mixtures are used to calibrate the apparatus, then fuel concentrations of between 0-15% can be accurately characterised to a  $\pm 1\%$  by volume. The lower span of 0% is relatively stable; however the upper limit is very sensitive, and is prone to drift with time

and temperature. For these reasons the apparatus must be switched on 30 minutes before use to ensure that the internal heaters keep the temperature of the tested gases uniform, also the top span should be checked before each sample to ensure reliability of results.

There are four positions within the duct at which samples may be taken to ensure accurate mixtures of combustion gases are present throughout the test section. The first sample point is taken immediately after the mixing point, which is used to regulate the partial pressures of the combustion air and fuel to give the required mixture for the experiment. Sample points within the obstacles of the duct allow accurate determination of mixing within the test section, and then the final sample point is positioned in the extraction point. When each of the sample points is reading the same as the initial sample point it can be assumed that the entire combustion mixture is at the required AFR.

#### ***7.1.4 Ignition system***

The ignition of the combustion mixture occurs at one extremity of the duct. The system is based around a standard automotive spark plug, and is supplied by a standard 12V car battery. The initial 12V is stepped up using an automotive ignition coil as discussed in section 5.1.2. The spark occurs as a standard automotive spark across a spark gap, and is typically of the order of 30mJ.

The system is controlled by the control unit to ensure rigorous safety implications are adhered to, and will be discussed later in this section.

#### ***7.1.5 Flame Speed Determination***

In order that flame speed may be derived as discussed in Chapter 5 accurate measurement of flame position at specific times after ignition are required. Due to the geometrical configuration of the turbulent duct, filming of the resulting flame with a high-speed camera as used previously is not a viable option. For this reason a data acquisition system based around instruments placed in the flame field is required. As this is a turbulent environment an obtrusive sensor is less of an issue than would be the case in laminar studies.

Fifteen ionisation probes discussed earlier in section 3.3.2 are positioned at predetermined distances from the source of ignition. Therefore accurate recording of the time taken for the flame front to travel from one probe to the next enables an accurate determination of flame speed  $(\partial x / \partial t)$  to be calculated.

The National Instruments DAQ system described in detail in section 3.4.2 was once again utilised. As discussed earlier, the charged ionisation probes on interaction with the ionisation field associated with a flame create a positive step voltage, which can be used to determine accurately the time at which the flame passed the particular probe. By measuring accurately the linear distance between each probe, it then becomes possible to produce an accurate distance-time graph to enable flame speeds to be calculated in a manner similar to methods used in Chapters 5 & 6.

### 7.1.6 Control Unit

Due to the complexity of the test facility, for the accurate operation of the turbulent duct rig it is necessary for a centralised control unit to be capable of remotely triggering each stage of the experiment so that all personnel may work in a safe area away from the explosion. The control unit pictured below in Figure 7.3 shows the external and internal structure of the control unit.

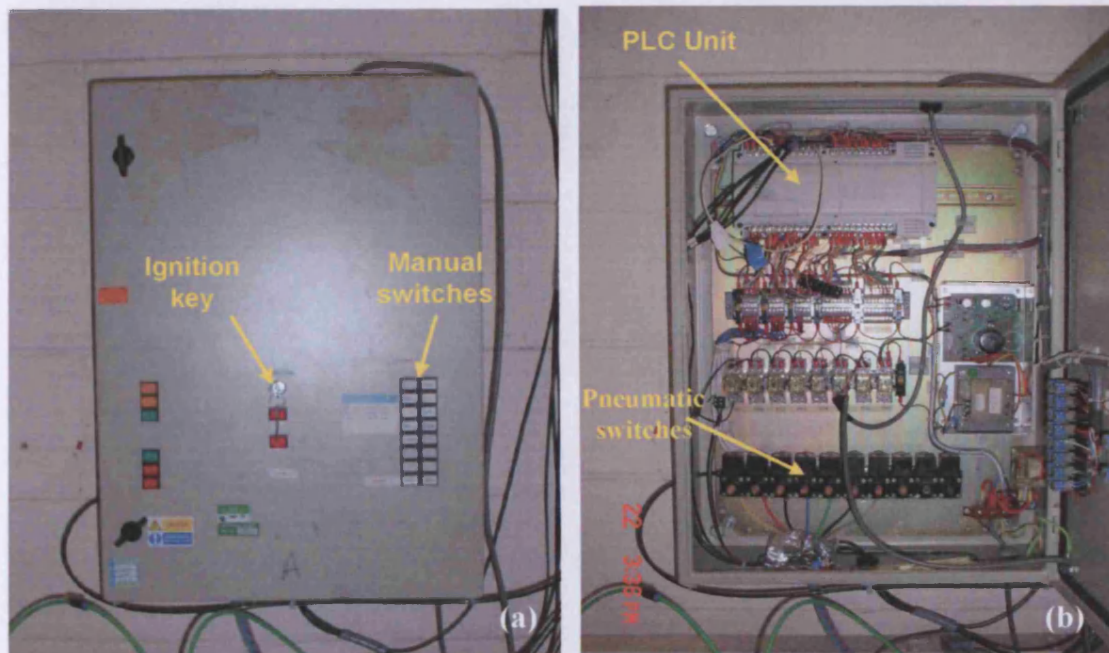
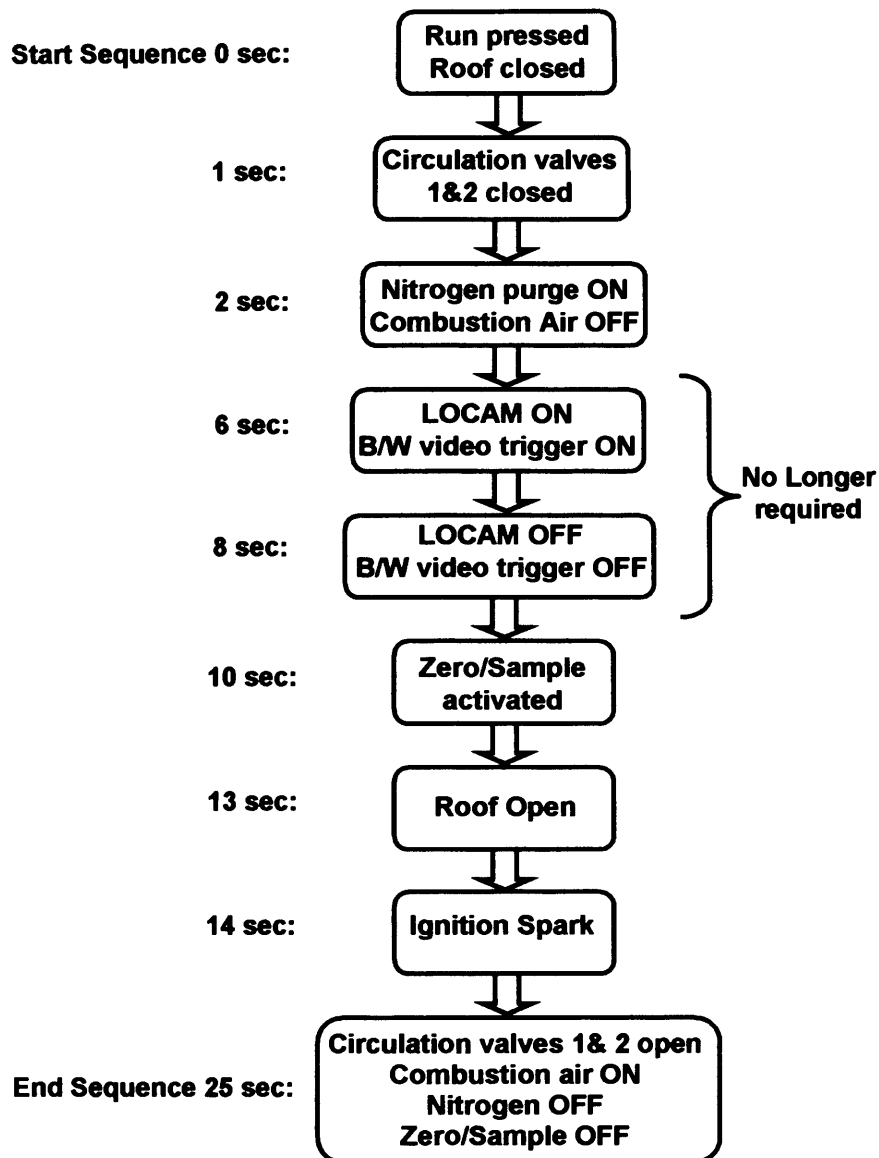


Figure 7.3 (a&b) Internal and external views of control unit of the turbulent duct rig

The electronic control unit is a custom built unit designed specifically to control the turbulent duct rig. The unit contains a Mitsubishi Melsec FX-64MR programmable logic controller (PLC), which can be programmed using Melsec Medoc software [98].

Programming can be specified in three forms namely: instruction, ladder and state diagram; due to its ease of use the programming used for this project is based around a ladder type format [99 & 100]. A comprehensive discussion of the ladder programme is given elsewhere [101 & 102] so will not be discussed here. The PLC is a black box type control unit, whereby set inputs lead to predetermined outputs which can be controlled automatically at set time intervals. In this application, the PLC is used to activate 10 pneumatic switches which control each of the necessary actions of the turbulent duct rig.

The sequence shown in Figure 7.4 is representative of the actual experiment sequence, programmed using ladder-type 'normally-open' and 'normally-closed' contacts within the PLC.



**Figure 7.4 Pre-programmed automated flow diagram**

As can be seen there is a simplistic automation routine that occurs on the depression of the automatic 'run' button. This sequence ensures that the roof opens at the correct time before ignition, and that the gas lines are pre-purged with nitrogen. Isolation of the duct from the exhaust and mixing systems is ensured by the logic programme through the correct opening and closing of the circulation valves.

There are many safety systems also incorporated into this flow-chart which safeguard against the occurrence of accidental sequences. There are safety switches associated with the pneumatic pistons of the retractable roof which if not depressed override the ignition sequence, thus ensuring that a fully confined explosion cannot occur. There are also manual operations which are not included within the automated sequence - such as

the fuel introduction and ignition which minimise the risk of explosions occurring if personnel are not present.

## 7.2 Brief Overview of Turbulent Flame Propagation

As the purpose of this chapter is demonstration of the potential for 'fine' water mists in a turbulent environment, as opposed to a detailed exploration at a more fundamental level, only a brief overview of the complex subject of turbulent flame propagation is presented here. Detailed explanations of turbulent burning are offered by Griffiths and Barnard [103], Glassman [104] and Lewis and von Elbe [105]. There are many different mechanisms in which turbulent burning can occur however Griffiths and Barnard [103] propose a concept of turbulent burning using a comparison of laminar flames.

When a laminar flame is subject to planer disturbances, the resulting 'wrinkling' may grow or decay depending on ratio of thermal diffusivity and diffusion coefficient of the deficient reactant, which is represented non-dimensionally by the Lewis number ( $Le$ ). In order to describe this effect it is necessary to refer to Figure 7.5, which shows a flame travelling between two boundaries. It can be seen that at the interface between the unburned and burned gas, the flame front stretches forming a crest on the leading edge and leaving a trough at the trailing edge.

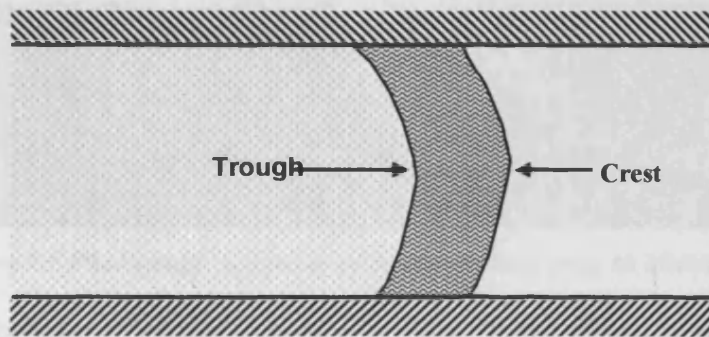
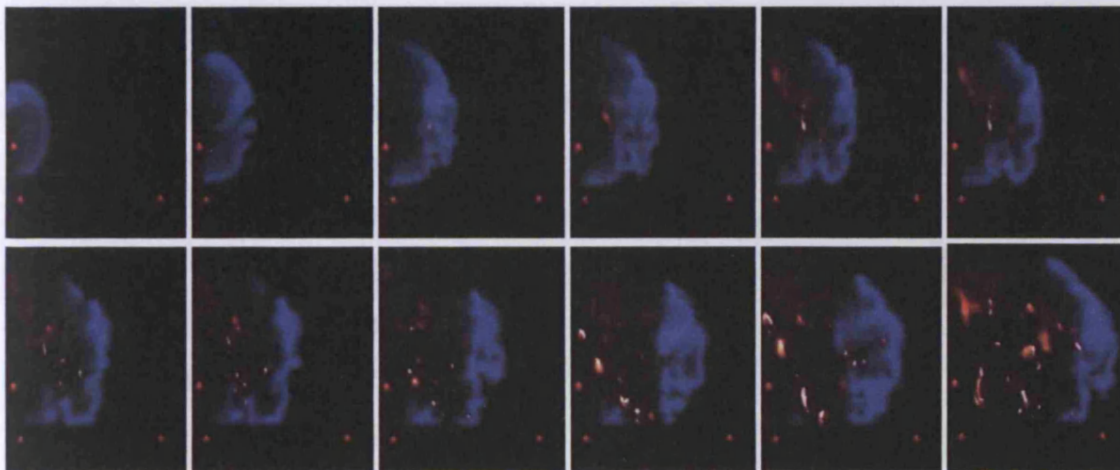


Figure 7.5 Visual depiction of flame front showing crest and trough structure

If the Lewis number is greater than unity ( $Le > 1$ ), then the thermal diffusion becomes a dominant factor thus the heat loss exceeds the mass gain. This effect means that the combustion is less intense in the crest of the flame than the trough, thus the flame structure begins to smooth forming a more laminar flame. However if the converse holds, that is the Lewis number is lower than unity ( $Le < 1$ ), then the slower burning of the trough causes an apparition of instabilities in the resultant flame structure, which can

lead to local extinctions causing a 'wrinkling' of the flame front surface. In such cases, it is thus possible to describe these turbulent flames as a system of stretched 'laminar flamelets'. Under conditions where this approximation of turbulent flames is appropriate, then extrapolating the conclusions of Chapter 6 it is anticipated that water droplets in the form of a 'fine' mist will be effective in arresting the highly stretched flames.

Within this study the effect of the obstacles are the predominant factor in the generation of turbulence, and this has been the subject of detailed studies by several authors including Lindstedt and Sakthitharan [106] and Masri and Ibrahim [107]. As the gas flow, generated by the expansion of the hot gases behind the flame front, passes over and exits each obstacle array, vortices and eddies are formed in the wake. This causes the flame front to deviate in shape leading to high levels of curvature and stretch as shown in Figure 7.6 which was filmed by SHELL Research Ltd. in a comparable obstacle filled test facility.



**Figure 7.5 Photograph sequence of flame passing over an obstacle array**

However, it should be noted that the characteristics of turbulence in a flame can greatly influence the resulting flame structure and velocity. All of these different regimes are best described and often referenced through the Borghi phase diagram, shown in Figure 7.6.

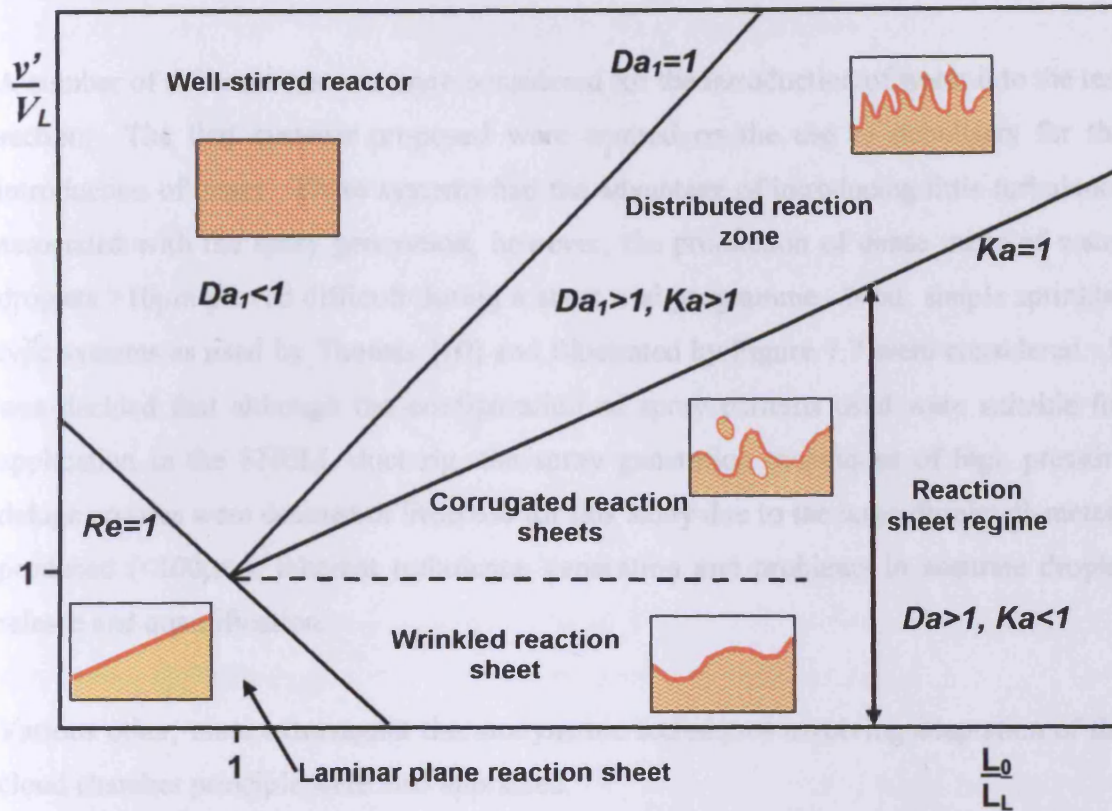


Figure 7.6 Borghi phase diagram showing different regimes in premixed turbulent combustion [11]

It can be seen from the Borghi diagram there are four distinct regimes of turbulent burning, each of which have a differing resultant flame structure. Therefore, for a rigorous study to be undertaken into the 'quenching' limit of 'fine' water mists, these regimes should be related to the types of explosions and explosion environments envisaged, to ensure that efficacy prevails in every conceivable situation.

### 7.3 Rig Development

The agreed objective of this part of the research programme was to develop a method of introducing a 'slug' of water mist into the duct after it had propagated a sufficient way along the duct to become established.

The conclusions of Chapters 2 & 6 confirm that water droplets in the size range of approximately 10-30 $\mu$ m would be the most suitable for the quenching of a propagating turbulent flame, and most likely between 20-30 $\mu$ m. It was decided that only minimal adjustment should be made to the turbulent rig to ensure that its safety and functional integrity was not compromised.

A number of different systems were considered for the introduction of water into the test section. The first systems proposed were centred on the use of nebulisers for the introduction of water. These systems had the advantage of introducing little turbulence associated with the spray generation, however, the production of dense mists of water droplets  $>10\mu\text{m}$  proved difficult during a short trial programme. Next, simple sprinkler type systems as used by Thomas [10] and illustrated by Figure 7.7 were considered. It was decided that although the configuration of spray patterns used were suitable for application in the SHELL duct rig, the spray generation techniques of high pressure deluge nozzles were deemed of little use for this study due to the large droplet diameters produced ( $<100\mu\text{m}$ ), inherent turbulence generation and problems in accurate droplet release and quantification.

Various other, more extravagant thermodynamic techniques involving adaptation of the cloud chamber principle were also appraised.

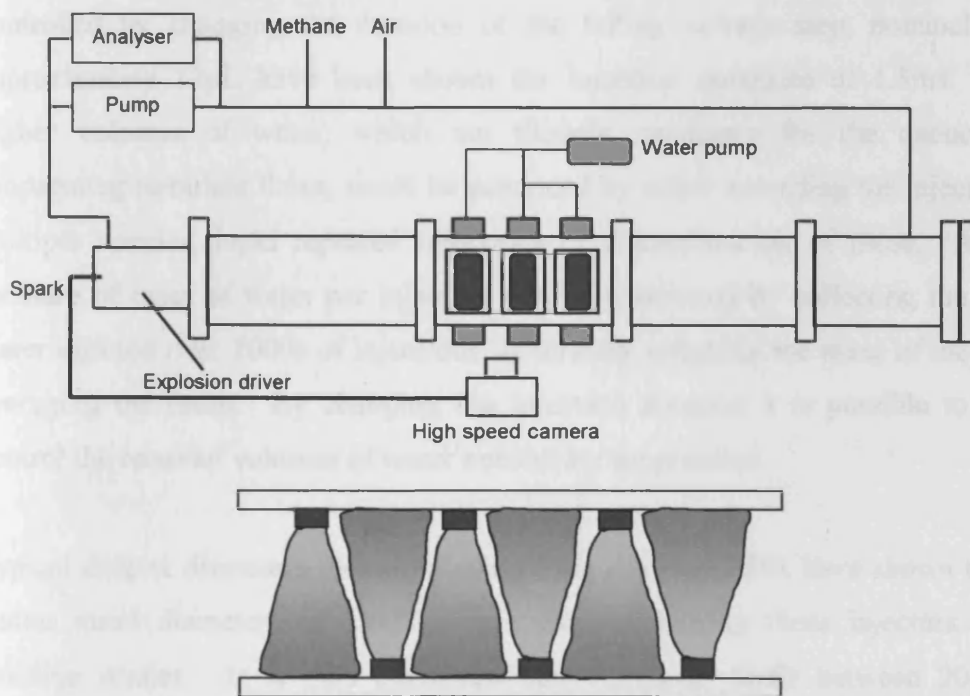


**Figure 7.7** Schematic representation of rig and spray pattern used by Thomas [10]

Finally, a solution was established involving the use of high pressure swirl nozzles usually implemented in direct injection petrol engines, where the objective is to provide sub- $20\mu\text{m}$  fuel sprays with smaller penetration than that associated with high-pressure diesel injectors.

Research carried out by colleagues within the Cardiff School of Engineering is concerned with the accurate temporal characterisation and modelling of sprays from such injectors, thus quantitative behaviour of the sprays generated with gasoline may be used in a qualitative manner to predict the sprays that may be generated when water is used [109].

The Bosch injectors capable of delivering fluid at 150mg/s are controlled by a Bosch electronic control unit (ECU). The electronic control unit relies on a falling voltage step to trigger up to 6 injectors in a configuration of three banks of two injectors. This method of water introduction therefore affords accurate control of injection time and injection duration, which ensures that precise water concentrations may be delivered into the duct at a predetermined time before the flame front arrives, hence effectively eliminating additional turbulence effects associated with spray dynamics.

For gasoline, it has been shown that mass of fluid per injection can be accurately controlled by changing the duration of the falling voltage step; nominal values of approximately 12 $\mu$ L have been shown for injection durations of 1.5ms. Therefore higher volumes of water, which are thought necessary for the quenching of a propagating turbulent flame, could be produced by either extending the injection length, multiple nozzles, rapid repeated injections or a combination of these. An accurate measure of mass of water per injection can be conducted by collecting the volume of water injected over 1000s of injections, accurately weighing the mass of the fluid, then averaging the result. By changing the injection duration it is possible to accurately control the required volumes of water needed for suppression.

Typical droplet diameters measured using time resolved PDA have shown that typical Sauter mean diameters of 15-20 $\mu$ m are generated using these injectors within the gasoline studies. It is thus perceived that values of SMD between 20-30 $\mu$ m are achievable using these injectors in conjunction with water. Accurate droplet size, which will be quantified using the Malvern Mastersizer $\chi$ <sup>TM</sup>, can be afforded by changing the supply pressure of the water.

The final design proposed for the water delivery system is given by Figure 7.8.

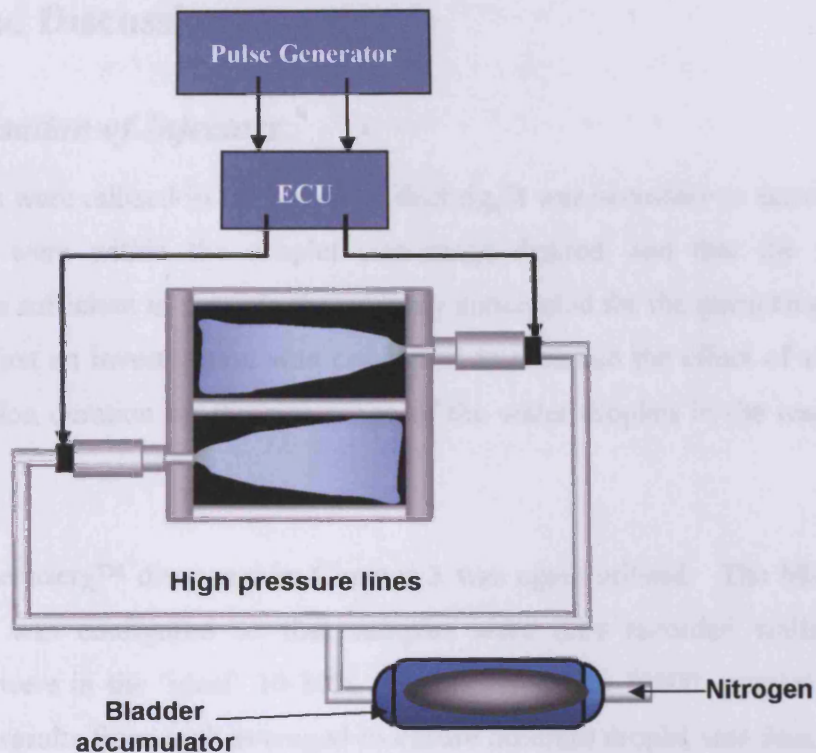


**Figure 7.8 Proposed water delivery system for turbulent duct rig**

It can be seen that the system proposed is based on two injectors positioned into opposite side walls of the duct, and offset by 100mm to ensure a better mix of mist within the section of duct in which the water 'slug' is to be positioned. The pressure of the water is generated via a bladder accumulator, which is capable of pressurising 1.5 litres of fluid and is rated to 230bar. The bladder is pressurised by a nitrogen supply, so through accurate regulation, perceived supplied pressures of 70-100bar can be achieved.

The two injectors are triggered by two falling voltage signals, generated by a dual signal pulse generator via the aforementioned ECU. By setting up the two signals with an oscilloscope, the two injectors can be triggered either in unison or independently. The mass concentration of water required to bring about quenching of the flame may then be achieved by varying the injection duration.

## 7.4 Results and Discussions

### 7.4.1 Characterisation of Injectors

Before the injectors were utilised in the turbulent duct rig, it was necessary to ensure the droplets produced were within the droplet size range desired, and that the water concentrations were sufficient to provide the quantity anticipated for the quenching of a turbulent flame. First an investigation was conducted to ascertain the effect of supply pressure and injection duration on the size range of the water droplets in the resultant mist.

The Malvern Mastersizer $\chi^{\text{TM}}$  discussed in Chapter 3 was again utilised. The Malvern sizeware software was configured so that samples were only recorded whilst the obscuration limits were in the 'ideal' 10-30% range, after which 10000 samples were then taken and the results from each averaged to ensure accurate droplet size data. The nozzle was positioned centrally a distance of 60mm from the beam, and pulsed at a rate of 5Hz for various supply pressures and injection durations.

The results gained are presented in Figures 7.9 (a&b). As can be seen the droplet sizes that are produced by the pressure swirl automotive injectors are in the ideal size range of  $D_{32}$  between 20-30 $\mu\text{m}$ .

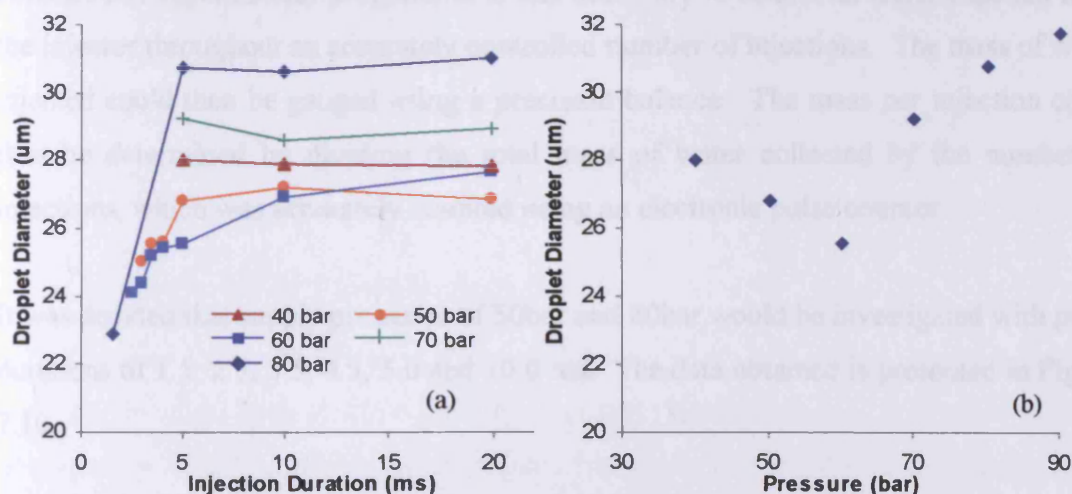


Figure 7.9 (a&b) Effect of injection duration and initial pressure on droplet size

It can be seen from Figure 7.9(a) that injection durations of greater than 5ms makes little difference to the droplet sizes produced, which suggests that the maximum opening

duration of the needle valve may be approximately 5ms, which is confirmed via the cumulative mass calculations later. However, it can be noted that droplet sizes produced are sensitive to injection length for pulse durations of less than 5ms. Figure 7.9(b), which was conducted for each pressure at pulse durations of 5ms, shows that pressure does not give a negative linear trend with droplet size as would be expected. It appears that a threshold of 60bar seems to be optimal for the production of the finest mists. It is possible that the larger droplet diameters produced at higher pressures may result due to the higher masses of water present in the swirl chamber of the nozzle, which may bring about some coalescence of droplets and hence an increase in the resulting Sauter mean diameter of the mist.

After conducting an analysis of these results, it was decided that drive pressures of 50-60bar with pulse durations <5ms would be most useful for the production of the water mists most suited to use in the turbulent duct rig. The reasoning behind this decision is that water droplets of approximately 25 $\mu$ m are produced in this range, whilst the lower pressure reduces the exit velocity of the droplets, and hence the chance of impingement on the opposite wall of the duct is greatly reduced.

A second experimental programme was then undertaken to determine the mass/volume of water ejected from the injector at particular injection durations and pressures. To conduct this experimental programme it was necessary to collect all water expelled from the injector throughout an accurately controlled number of injections. The mass of water injected could then be gauged using a precision balance. The mass per injection could thus be determined by dividing the total mass of water collected by the number of injections, which was accurately counted using an electronic pulse counter.

It was decided that supply pressures of 50bar and 60bar would be investigated with pulse durations of 1.5, 2.5, 3.5, 4.5, 5.0 and 10.0 ms. The data obtained is presented in Figure 7.10.

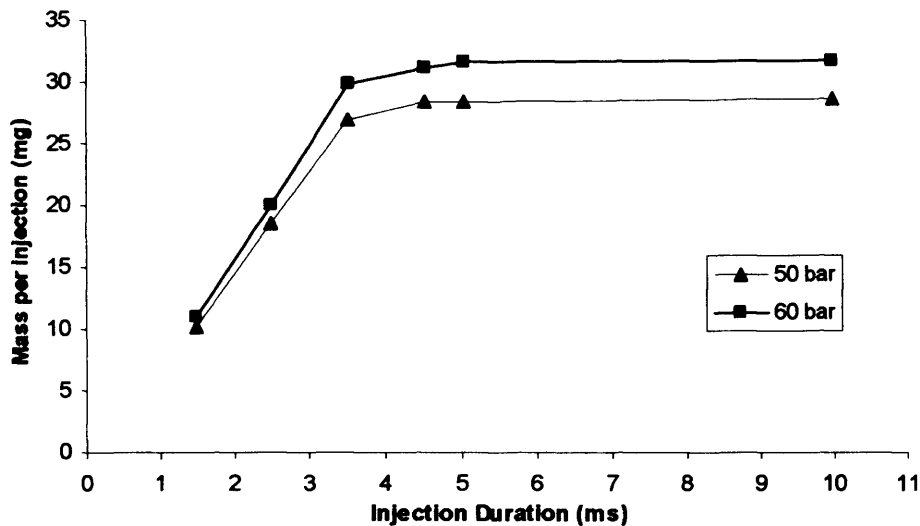


**Figure 7.10** *Effect of drive pressure and injection duration on mass of water ejected*

The conclusions of the Malvern droplet size experiments are supported by the results of Figure 7.10, showing that the injectors' maximum injection duration is approximately 5ms, so that the proposal of using long pulse durations to supply the required volumes of water will have to be reviewed and multiple shorter injections used.

It can be seen that there is a linear relationship between injection duration and mass per injection and at 50bar a mass of approximately 27mg or a volume of 27 $\mu$ l of water can be injected in 5ms. Therefore, it has been shown that the required levels of water perceived to be in the range appropriate for suppression can be easily acquired with multiple injections. The last trend shows that increasing pressure from 50-60bar only slightly increases the mass per injection, thus it is thought that the lower supply pressure of 50bar should be used as this is the most likely to give the required well mixed mist of 'fine' (25 $\mu$ m) droplets within the turbulent duct rig.

#### **7.4.2** *Suppression of Turbulent Flame*

It was decided that in order to demonstrate the usefulness of water in the form of 'fine' mists in the quenching of a propagating flame, the Shell turbulent duct rig should be configured with the round obstacles giving a blockage ratio of 0.4 and a venting ratio of 70%. An equivalence ratio of approximately 1.0 (9.5% vol.) was used as this was observed to be the least susceptible to stretch effects in Chapter 6, and thus, should prove the most difficult case to quench. It was hoped that quantifiable data would be obtained during this study, however it was found that the ionisation probes incorporated

within the structure of the rig and discussed earlier (sections 3.3.2 & 7.1.5) were not reliable enough particularly, when water was present to provide data of significant integrity to publish here. However, a simple filming of the event could be used to determine whether the water barrier was sufficient to quench the propagating flame.

An experimental programme of 8 experiments was undertaken, to determine whether a turbulent flame could be arrested by 'fine' water sprays. It was first necessary to carry out dry test cases to determine that all functions of the rig were operating correctly. An example of such a run is given by the film sequence shown in Figure 7.11.

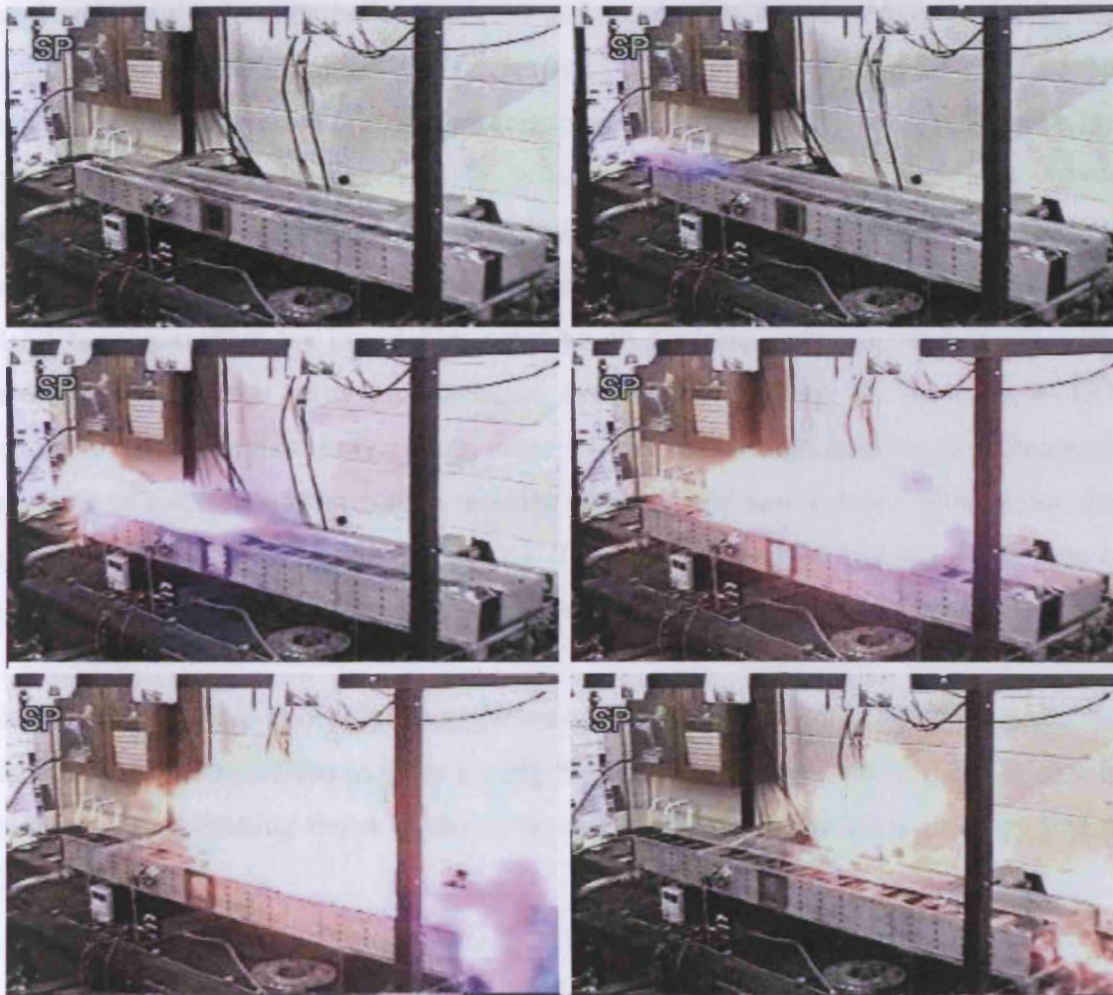


**Figure 7.11** *Film sequence of turbulent methane flame in conducted in the SHELL duct rig with no water (25fps)*

It can be seen from the above figure that a fully turbulent flame could be developed within the duct, and propagate along the full length of the duct. The video sequence facilitates an approximation of flame speed using the known data capture rate of 25Hz. Thus it can be shown that the inter frame rate of each image is 40ms, and as the flame

travels the length of the 2m duct in 4 frames then the flame speed may be given as approximately 12.5m/s. This is a 500% increase in flame speeds recorded in the laminar flame data described in Chapter 5.

After a successful commissioning of the turbulent duct rig which demonstrated that turbulent flames could be produced, it was decided that water should be injected into the rig to form a water curtain between 600-700mm from the ignition source. The water was injected into the rig at a pressure of 50bar which delivered a water mist containing droplets of Sauter mean diameter equal to 25 $\mu$ m. The water was activated approximately 6 seconds before ignition and injected at a rate of 5Hz with injection duration 5ms as was discussed earlier (section 7.4.1). Therefore it can be surmised that the mass of water injected prior to ignition approximately 1620 $\mu$ l. Using equation (6.7) it can be shown that to obtain the 25% molar concentration required to inert a volume within the section of the duct into which the injectors spray approximately 995 $\mu$ L of water is needed. However, recent impingement studies undertaken at Cardiff [108 & 109] have quantified the liquid film residing on a surface and size of droplets in the secondary spray after spray impingement, the latter specifically for the types of GDI injectors utilised in this study. From these studies, it has been possible to estimate the quantity of secondary spray which remains airborne and active post impingement, and this figure has been estimated to be 50%. Therefore, it is estimated that at the time of ignition there is a slug of water mist with concentration of approximately 21%.

It was perceived that in order to stop the water curtain being pushed out of the top of the duct, it would be beneficial to place a cling film barrier across the top of the duct prior to ignition. The resulting flame is shown by the sequence of film clips given by Figure 7.12.

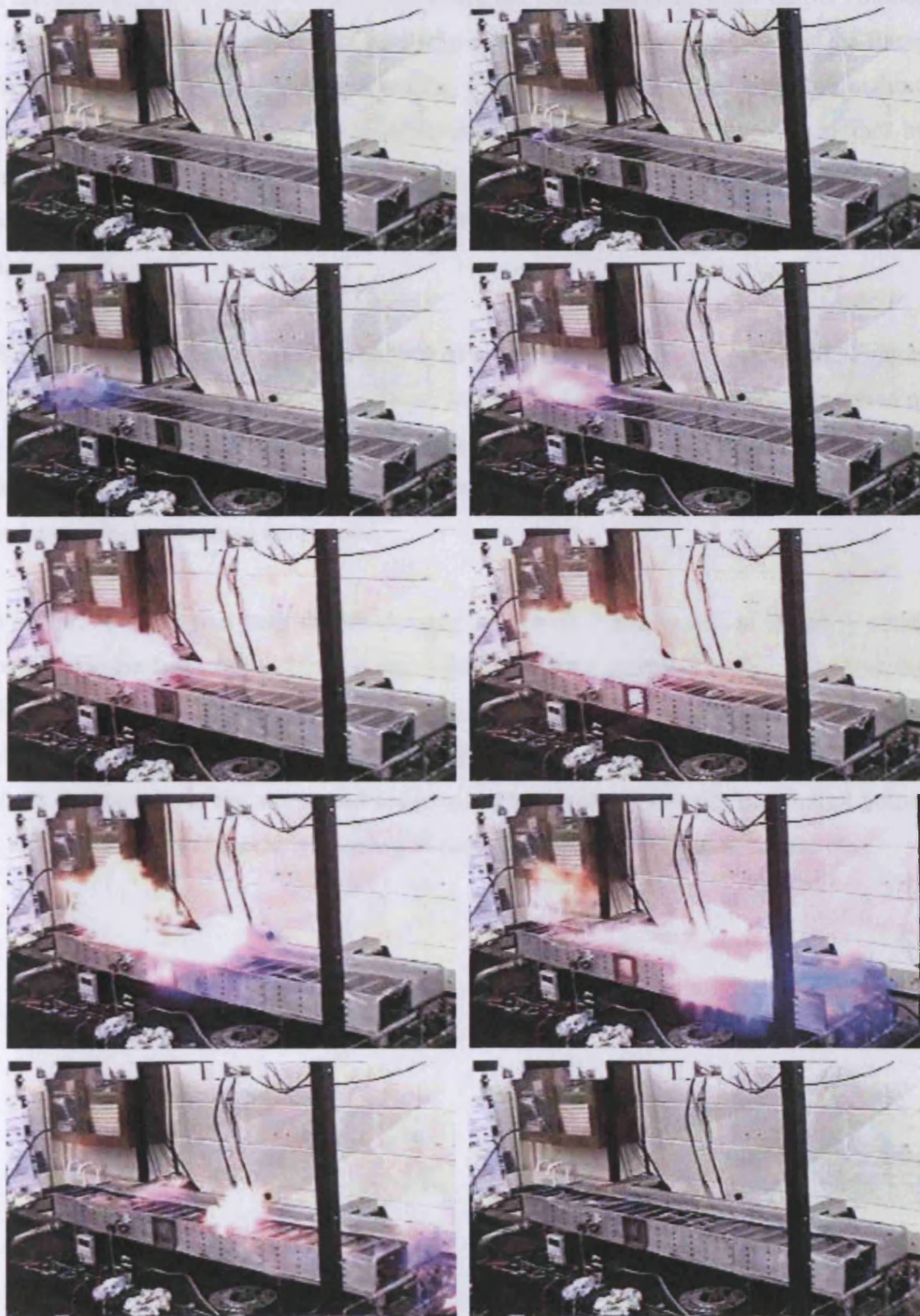


**Figure 7.12** *Film sequence of turbulent methane flame in conducted in the SHELL duct rig with water mist barrier*

It can be clearly seen that at the location where the flame meets the water barrier (frames 4-6), there is a definite retardation in flame speed. However, it appears that the flame then either 'penetrates' or circumvents the water barrier, and reaccelerates throughout the remainder of the duct. It was then decided that the cling film may in fact be hampering the dispersion of the water droplets, allowing the curtain to be breached and so it was decided that further experiments should be conducted without the use of cling film.

Without the cling film, a complete quench of a propagating flame was achieved. Figures 7.13 (a&b) shows a comparison of a flame travelling down the duct without the action of a water spray compared to one with a water curtain. The experiment where the water mist completely quenched the turbulent propagating flame was successfully repeated under nominally identical conditions.

It should be noted that both flames develop at similar flame speeds in the early stage, however in the case of there being a water barrier present as shown in Figure 7.13(a), the flame is fully arrested at the point of the water mist barrier. Another interesting observation is the time of ignition compared to the position of the roof. This shows a slight discrepancy in the automated sequence, which will require slight appraisal before a full rigorous study into the quenching of turbulent flames can be undertaken.



**Figure 7.13 (a&b) Film sequences of turbulent methane flame in conducted in the SHELL duct rig with water mist barrier and without water barrier respectively**

This quenching effect can be seen more clearly by observing the event from a different viewing angle. Figure 7.14 illustrates the quenching effect of the water barrier, which is highlighted by the red dashed box. The relative position of the injectors on the side of the duct can also be noted.

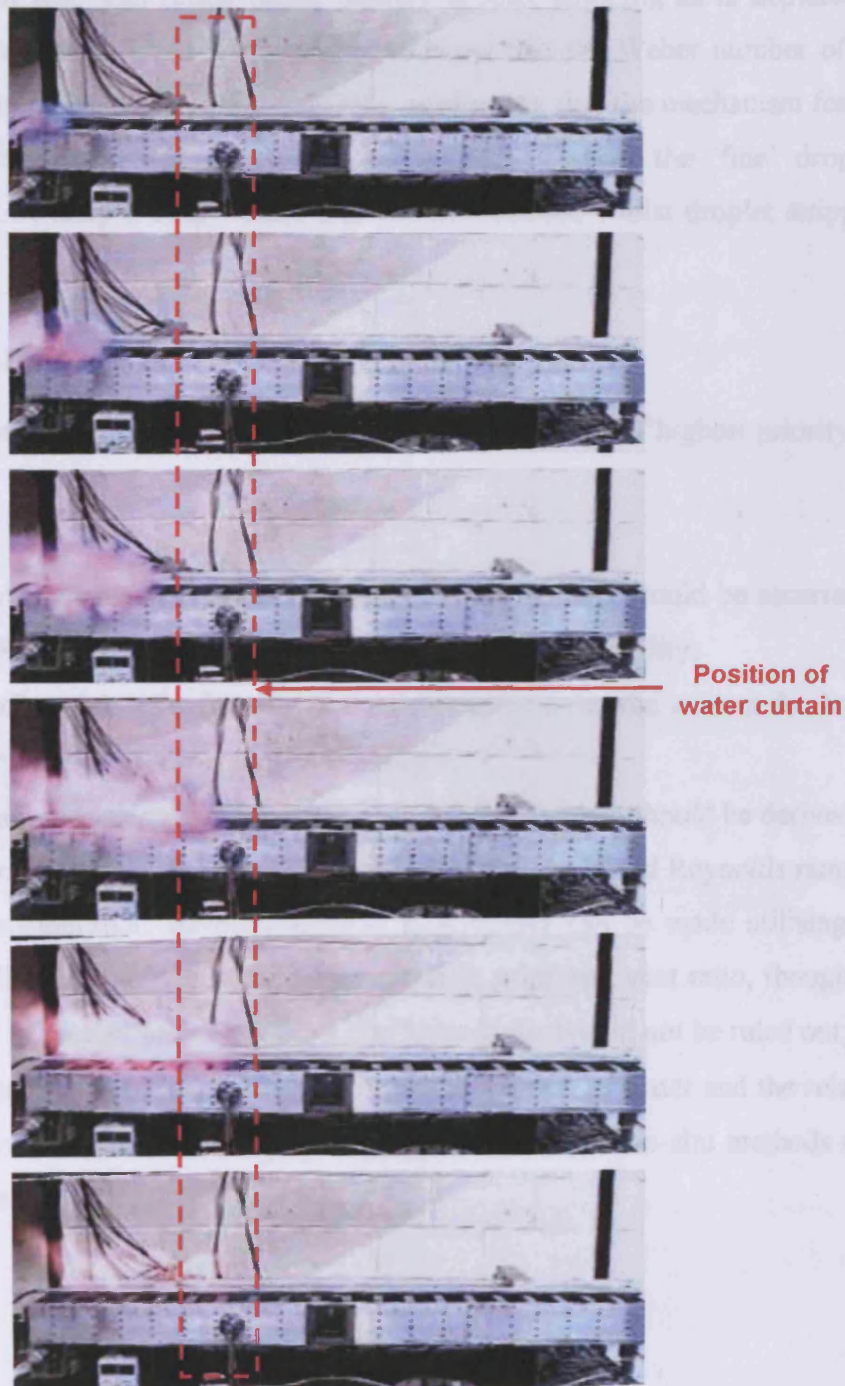


**Figure 7.14** Film sequence showing total quench of a propagating turbulent flame

The findings of this study has shown that water in the form of ‘fine’ droplets can be used to completely arrest a propagating stoichiometric turbulent methane flame. It should be stressed that previous work, as discussed in Chapter 2, has shown that water systems have been capable of quenching turbulent flames, however in these cases it was a different mechanism that was relied upon, namely droplet stripping as is depicted in Figure 2.4. Using equation (2.1) it is possible to show that the Weber number of the droplets in this study is less than 12 ( $We=0.005$ ), confirming that the mechanism for the extinction of the flames in this study is a quenching effect of the ‘fine’ droplets ( $D_{32}=25\mu\text{m}$ ) is that of simple evaporation and dilution effects, whilst droplet stripping will not occur.

## 7.5 Future work

The potential for further work is considerable, so here only those of highest priority are discussed.

- The minimum quantity of water for successful quenching should be ascertained for the low-Re flame utilised in the current turbulent duct facility;
- Flame-speed/burning rate data should be generated from the current facility to allow improvements in terms of quantification;
- The minimum quenching water concentration for fine mists should be derived for other types of turbulent flames, particularly those at increased Reynolds number. Certainly considerable developments in this respect can be made utilising the current facility through variation of the obstacle grids and vent ratio, though the requirement of an alternative rig for a complete study should not be ruled out;
- Improved methods for quantifying the airborne fraction of water and the relative phase fraction should be developed, with the possibility of in-situ methods (e.g. LIF) explored.

## 7.6 Summary

The conclusions derived in Chapter 6 concerning the effectiveness of 'fine' water mists in quenching stretched, laminar propagating flames, have been developed to provide a demonstration of the effectiveness of 'fine' water mists in quenching an established (though low Reynolds number) propagating flame. The SHELL turbulent duct rig has facilitated this demonstration showing 'fine' water mist (25 $\mu$ m SMD generated from source, hence considerably below the critical Weber number governing aerodynamic break-up) as being capable of quenching propagating turbulent flames, characteristic of some categories of gaseous explosions. In absolute terms, approximately 1.6cm<sup>3</sup> of distilled water was sufficient to quench the turbulent stoichiometric methane-air flame propagating along the 200 x 100mm, cross-section duct at approximately 13 m/s. Moreover, utilising some assumptions concerning dispersion and impingement characteristics of fine mists, based on studies from other two-phase industrial problems (e.g. stratified charge GDI engines), facilitates an estimate of the effectiveness of water as a suppression system for this specific low-Re turbulent flame. Based on these assumptions, an estimate of water fraction (on a molar basis) of about 20% is derived, which if substantiated, means that the 'active' mist in suspension is less than the established quench limit of water vapour (26%) for un-stretched laminar flames. This would be consistent with the conclusions of Chapter 6, where it was shown that stretched laminar flames quench in the presence of water vapour, and even more effectively for water mist, at molar concentrations below the 22% vapour limit. Moreover, in this demonstration the quantity of water injected was not minimised, and so it is highly likely that successful quenching would be achieved with even less than 22% concentration utilised here. This is believed to be the first time that this important conclusion concerning quenching turbulent flames has been demonstrated for low Weber number water mists. Further work is required to determine whether these results hold for other categories of turbulent flames, particularly those at higher Reynolds numbers.

## Characterisation of Large Scale Releases of 'Fine' Mists

The research and laboratory scale experiments detailed in previous chapters suggest that water can be used as an explosion suppressant. As discussed in Chapters 2, 6 & 7 if water is to be used as an 'inerting' system then the water has to be in the form of water vapour or as a mist of small droplets ( $<30\mu\text{m}$ ).

The methods used to generate the water mists discussed in Chapters 6 & 7 are obviously not applicable for use in supplying protective water mists of the scale necessary to protect those typical in industrial applications. For this reason, this chapter describes a proposed method of large-scale water mist deployment. Various plausible methods for characterising such sprays are utilised, assessed and analysed to provide an insight into the formation and suitability of the water mists for explosion suppression.

### 8.1 Creation of Large-Scale Releases

The sponsors of this research have invested in a technique potentially capable of developing suitable water mists in the form of the 'Micromist' atomiser. Accurate characterisation of these systems has yet to be conducted. Hence, the focus of this chapter is to develop tools and techniques suitable for characterising such a large-scale atomiser, and providing the most complete and reliable characterisation currently possible.

#### 8.1.1 'Micromist' Flashing Jet Technology

The Micromist atomiser is a proposed system that may be suitable to provide water mists to provide protection against hydrocarbon explosions. The system that will be tested for the majority of this study is illustrated below in Figure 8.1.

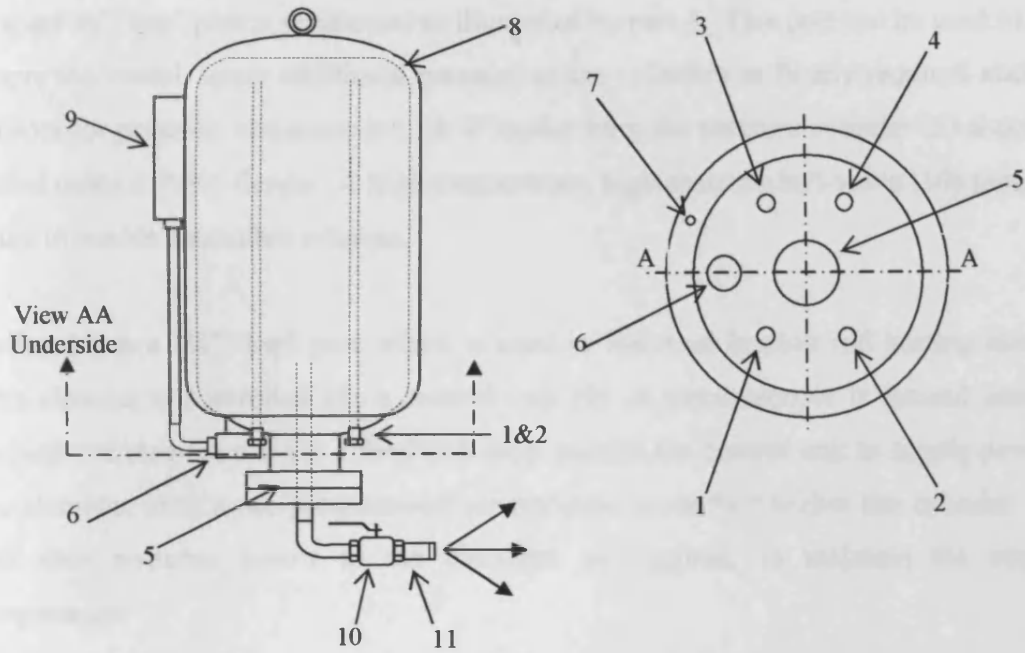


**Figure 8.1** *Technical Drawing of Micromist system used for this report.*

The Micromist atomiser is constructed from two stainless steel cylinders positioned one within the other, thus generating a double-skinned pressure vessel. There are six ports entering the internal cylinder which are utilised to ensure safe use of the apparatus.

Parts 1 & 2 are identical  $\frac{1}{2}$ " 'bsp' openings that are used for the fill and level of the rig. Internal pipe work ensures that the correct level of water is achieved in the rig, which ensures adequate head space to accommodate the expansion of water on heating. To fill the tank, both ports should be opened and a water supply of suitable domestic quality (non corrosive and chloride free) attached to one port. Water should be passed into the tank until water runs out of the level port, after which both ports should be sealed using the correct tapered fittings and PTFE tape.

Port 3 is another  $\frac{1}{2}$ " 'bsp' configuration and should be fitted with a 12bar bursting disc (brass assembly, nickel alloy). This safety device ensures that unforeseen overpressures that may be generated in the event of a temperature control failure, would not lead to the damage of the pressure cylinders, surrounding structures or personnel. This safety disc should be inspected and tested in accordance with the relevant burst test certificate regulations.

A spare ½” ‘bsp’ port is positioned as illustrated by part 4. This port can be used to fully empty the vessel, apply additional pressure to the cylinders or fit any required ancillary sensors for pressure measurement. A 4” outlet from the pressure cylinder (5) should be sealed using a PN16 flange. A high temperature, high-pressure ball-valve (10) should be fitted to enable controlled releases.

Socket (6) is a 1½” ‘bsp’ port which is used to insert an Incoloy rod heating element. This element is controlled via a control unit (9). A thermocouple is located centrally through the element and via a feedback loop enables the control unit to supply power to the elements until a pre-programmed temperature is reached within the cylinder. The unit then switches power to the elements as required, to maintain the required temperature.

To reduce energy consumption required for the heating of the mass of water, a vacuum is formed in the space formed between the two cylinders (8). This vacuum can be formed using a vacuum pump, which may be attached via the vacuum bleed (7).

A range of different nozzles can be attached (11); the discharge orifices are described later. Full operating instructions and guidelines are outlined and documented in detail elsewhere [110].

The Micromist system relies on ‘flashing’ technology. The phenomenon known as flashing occurs when a liquid is heated to above its boiling point under pressure. On release to atmospheric conditions, the liquid (in this case is water) undergoes a change in phase - Figure 8.2 [111].

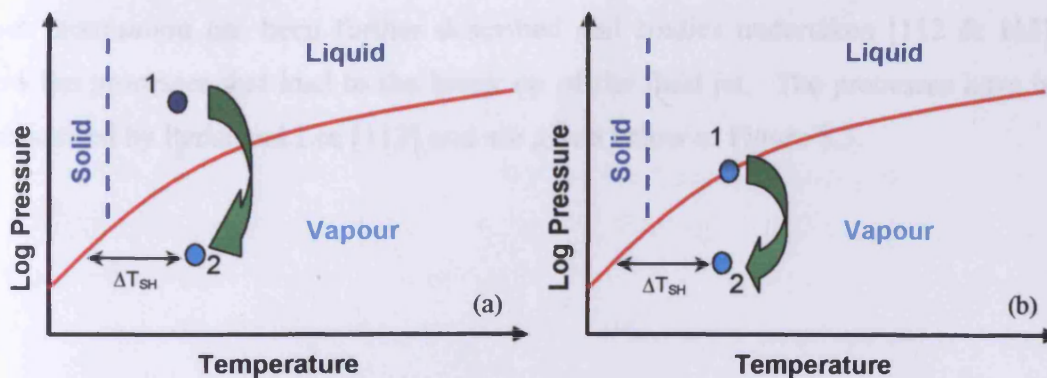


Figure 8.2 (a&b) Thermodynamic boundary conditions in relation to saturated conditions required for (a) flashing liquid release and (b) two phase flashing

To initiate a flashing jet, water upstream of the exit orifice -in the case of the Micromist atomiser, within the internal pressure cylinder- has to be pressurised above the liquid/vapour transition curve. This point is shown by point 1 in Figures 8.2 (a&b) and is often referred to as the stagnation condition.

Upon release of water to the atmosphere (shown by the arrow), the conditions drop down to the far-field atmospheric conditions. The degree of superheat ( $\Delta T_{SH}$ ) which, in the case of the Micromist atomiser provides the drive pressure, may be calculated from the distance from point 2 to the liquid/vapour transition curve as shown in Figures 8.2 (a&b). This can be represented by the following equation;

$$\Delta T_{SH} = T_{st} - T_{sat}(P_a) \quad (8.1)$$

In the case of the Micromist atomiser, due to the fact that the release conditions are always to ambient atmospheric conditions, the superheat temperature is given by;

$$\Delta T_{SH} = T_{st} - T_b \text{ or } \Delta T_{SH} = T_{st} - 373 \text{ (K)} \quad (8.2)$$

In the event (as shown by Figure 8.2b) that point 1 is actually on the transition curve (under saturated condition), then the release at the orifice will be released as a two-phase mixture of water liquid and water vapour.

The Micromist atomiser utilised in this study is capable of a maximum degree of superheat of approximately 80°C at a drive pressure of approximately 10bar. However, the design ensures that the stagnation pressure is not independent of temperature. Suggested improvements concerning this and other design issues are presented later.

Flash atomisation has been further described and studies undertaken [112 & 113] to show the processes that lead to the break up of the fluid jet. The processes have been summarised by Parks and Lee [113] and are given below in Figure 8.3.

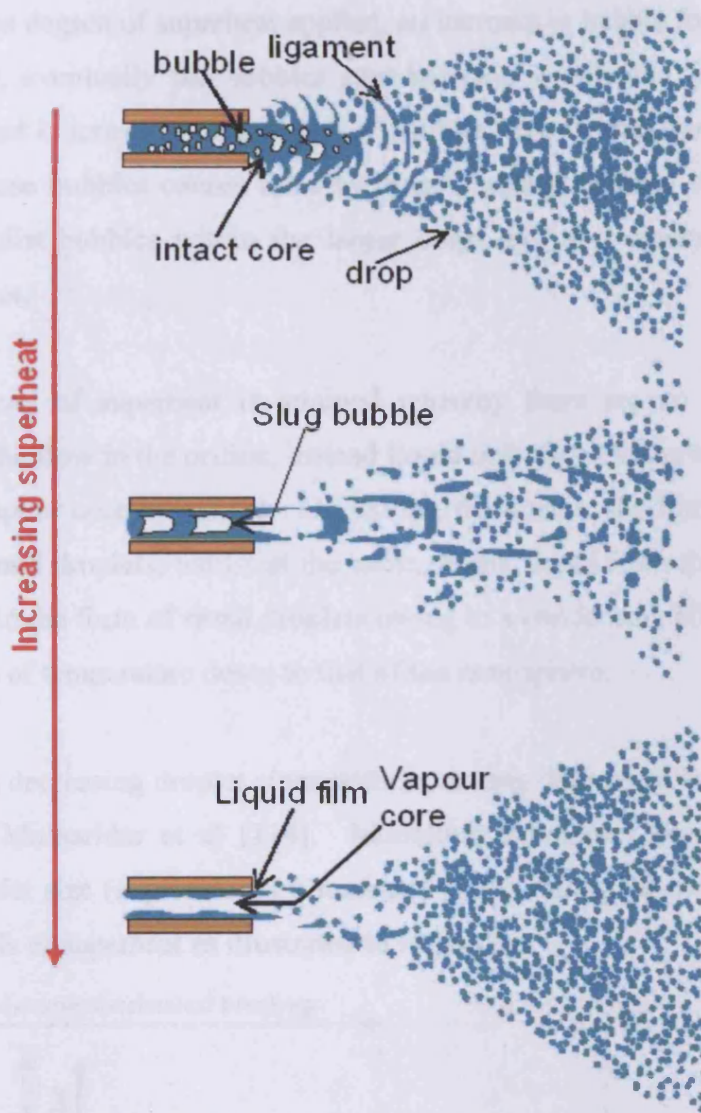


**Figure 8.3** *Dependence of spray characteristics on upstream flow conditions*

As can be seen from Figure 8.3, flashing atomisation is brought about by the formation of bubbles within the liquid flow. The formation mechanism of the bubbles is directly linked to the degree of superheat applied to the liquid at its stagnation condition, but is also dependant on such factors as nozzle shape, size and manufacture.

It can be seen that for low degrees of superheat, bubbles appear within the flow near the orifice, and as the liquid flows out to atmosphere these bubbles grow due to the decrease in pressure. Under these conditions, an intact liquid core remains beyond the nozzle exit, and so mechanical break-up remains influential with the bubbles only shattering at the edge of the core. This leaves a flow of drops with a large range of droplet diameters in the spray with a large central core of larger droplets.

By increasing the degree of superheat applied, an increase in bubble formation is caused within the flow, eventually the bubbles start merging within the orifice causing the formation of what is termed a 'slug flow' of bubbles. On exiting the orifice, the rapid expansion of these bubbles causes them to literally shatter, casting off both large and small drops, whilst bubbles within the larger drops will also expand causing further break up of the jet.

Eventually a level of superheat is attained whereby there are no longer individual bubbles within the flow in the orifice, instead liquid only flows at the walls of the nozzle and a central vapour core is formed. On exiting the nozzle, the film of liquid readily atomises into small droplets, whilst at the same instant liquid from the vapour phase is condensing out in the form of small droplets owing to a condensing effect brought about by the reduction of temperature down to that of the atmosphere.

Trends showing decreasing droplet sizes with increasing degrees of superheat have also been noted by Mulharidur et al [114]. Modelling techniques showed that apparent changes in droplet size (expressed as a rainout fraction during the work) are witnessed for varying levels of superheat as illustrated in Figure 8.4.

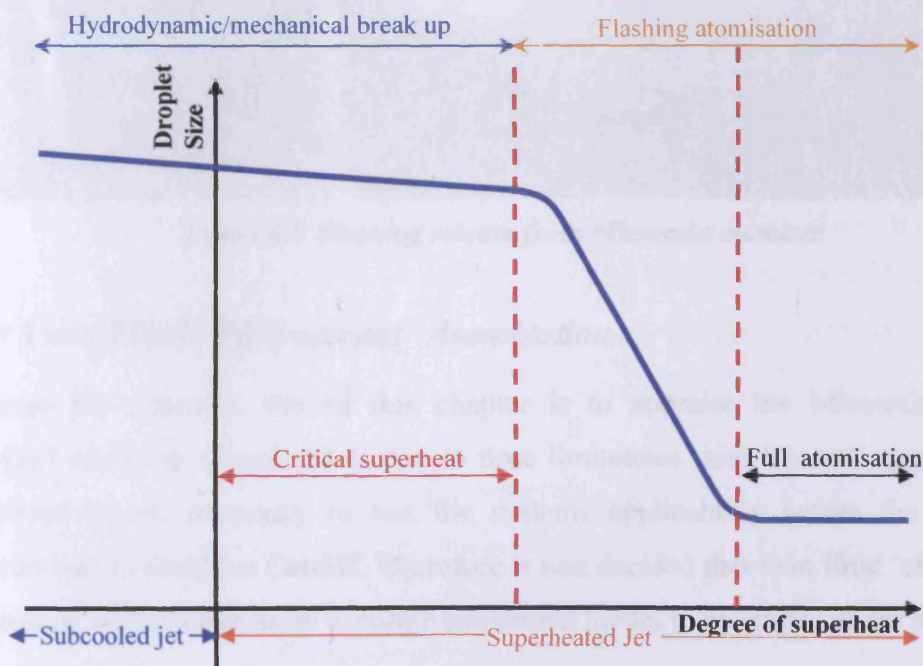


**Figure 8.4 Schematic of flashing and non-flashing regions in relation to droplet size**

It can be concluded from Figures 8.3 & 8.4 that increasing the degree of superheat will decrease the resultant droplets released to atmosphere. Therefore, for this study the

Micromist atomiser will be utilised at a maximum stagnation temperature ( $T_{ST} = 180^{\circ}\text{C}$ ), which has the best chance of producing a mist with a Sauter mean diameter in the region of 20-30 $\mu\text{m}$ , conducive to that required for the mitigation of explosions as shown in Chapters 2, 6 & 7.

A photograph of the Micromist atomiser discharging under fully flashing conditions is given by Figure 8.5. As can be seen, the mist is of a very dense nature which proves problematic for characterisation techniques.



**Figure 8.5** *Flashing release from Micromist atomiser*

### **8.1.2 Twin Fluid ‘Effervescent’ Atomisation**

Although the foremost aim of this chapter is to appraise the Micromist atomiser described earlier in section 8.1.1, due to time limitations with ‘loaned’ specialist laser equipment it was necessary to test the systems applicability before the Micromist atomiser was available at Cardiff. Therefore it was decided that twin fluid ‘effervescent’ atomisation would serve as an accurate isothermal model to generate similar mists.

Similar two-phase flow to superheated flow is produced by twin fluid 'effervescent' atomisation, and so it was decided that this would be a satisfactory tool to test the laser systems applicability.

### 8.3.2 Effervescent

The effervescent atomiser relies on phenomenological processes similar to those of flashing atomisation. A 'bubbly' flow is also used to produce small droplets, however instead of utilising superheat to provide these bubbles; compressed air is entered into the pressurised water stream in an isothermal process upstream of the orifice as shown in Figure 8.6.

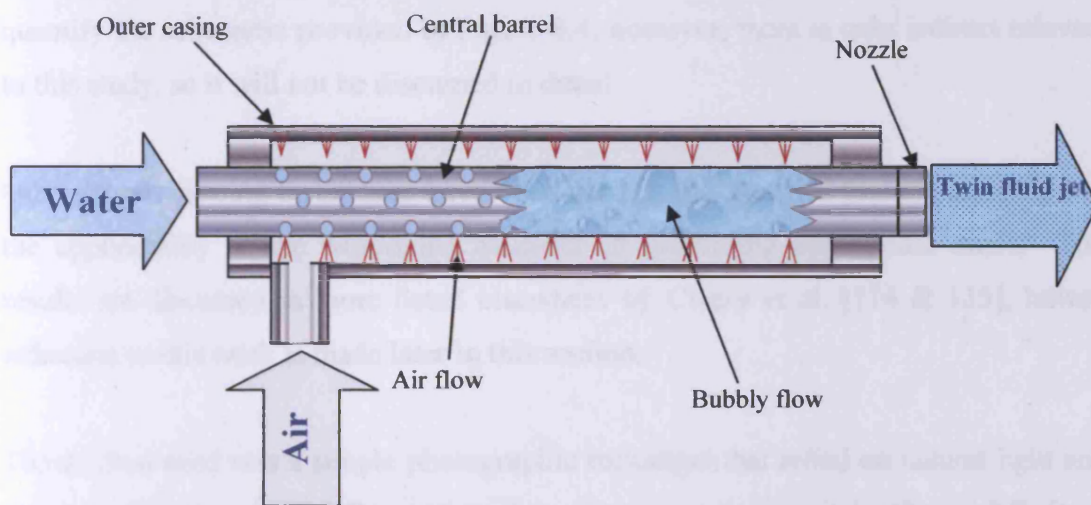


**Figure 8.6 Schematic diagram of twin phase atomiser used for PDA appraisal**

The effervescent atomiser used for the appraisal was of the form shown in Figure 8.6. The twin fluid jet is created by feeding both pressurised water and air into the atomiser. The water passes to the nozzle through a centrally located barrel, which has a series of holes through its walls. When the supply pressure of the air exceeds that of the water, pressurised air bubbles are formed in the central water core as the air passes through the holes.

On exiting the orifice, the bubbles depressurise and rapidly expand, thus shattering the water column and producing an effervescent jet of relatively small water droplets.

## **8.2 Results of Different Methods for Characterisation of Water Mist Release**

### ***8.2.1 Visualisation***

The easiest method of studying a large scale release is to simply observe its global characteristics. This can be achieved in a number of different ways, but all are based around a photographic technique. In previous studies [111 & 112] high-speed close up backlit methods have been used to describe the formation of flashing jets. Similar filming techniques are being carried out at present in Cardiff University to try to quantify the schematic provided in Figure 8.4; however, there is only indirect relevance to this study, so it will not be discussed in detail.

Other simple filming techniques have been used in this study to provide an insight into the applicability of the Micromist atomiser in generating appropriate mists. These results are discussed in more detail elsewhere by Cleary et al. [114 & 115], however reference to this work is made later in this section.

The method used was a simple photographic technique that relied on natural light and a standard digital camera. By setting the camera up as shown in Figure 8.7, it was possible to determine the influence of variables such as initial stagnation temperature, pressure and orifice size on the size and shape of the resultant jet formed, which may be of use in the design of the suppression systems delivery nozzles. Also it gives an idea of the global scale required in preparation for more accurate characterisation measurements within the spray.

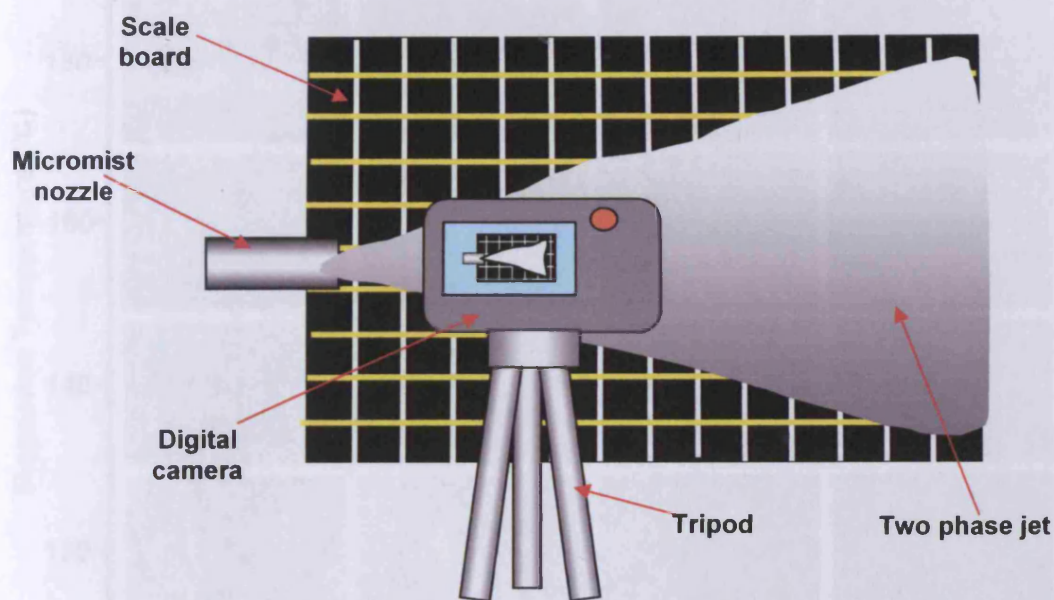


**Figure 8.7** *Illustration of camera setup to enable visualisation of shape of flashing jet*

This is the most basic form of photographic setup, but still enables an accurate image and scaling of resultant two phase jets. Spray cone angles and relative mist densities can be clearly derived.

Simple photographing of the different ‘flashing’ jets created via each of the different initial conditions is of considerable value. It can be seen by analysing all of the pictures that initial conditions and discharge orifice have a large bearing on the types of jet produced by the Micromist atomiser.

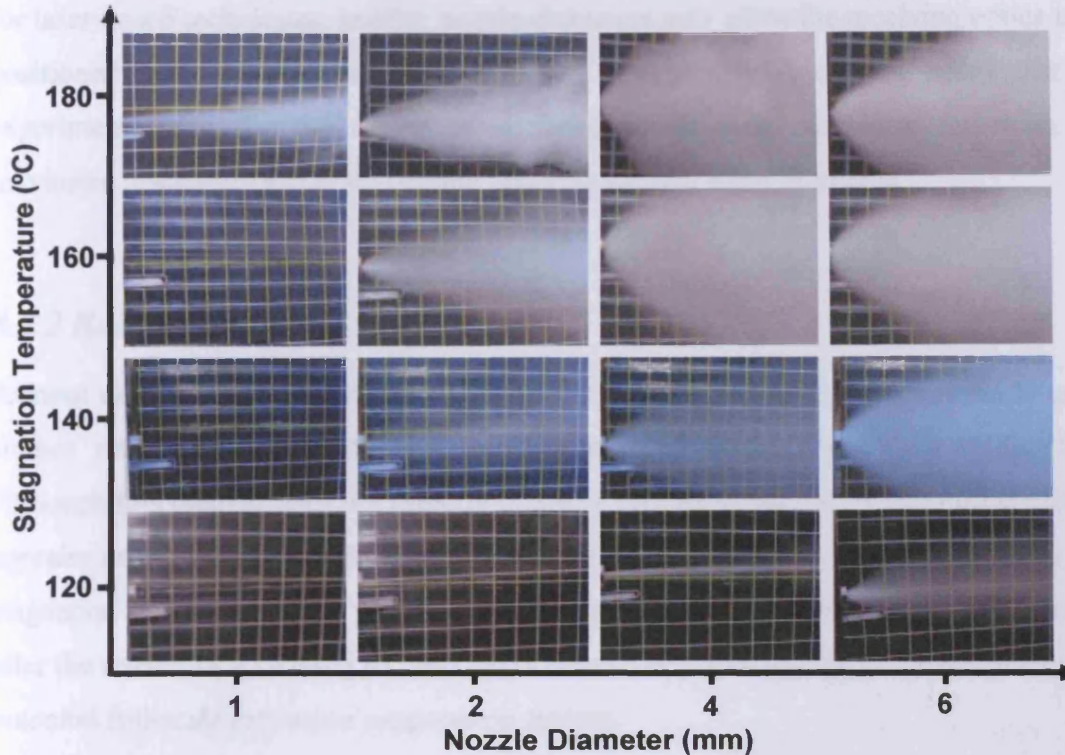


**Figure 8.8** *Graphic showing effects of both stagnation temperature and orifice diameter on flashing jet*

As can be seen from Figure 8.8, the two-phase flashing jet produced by the Micromist atomiser changes in a number of ways as both temperature and orifice sizes are increased. Correlations for this change in cone width and angle have been proposed and documented by Cleary [115].

It can be seen that as temperature is increased, the degree of ‘flashing’ appears to increase along with the density of spray. Likewise the cone angle increases up until 160°C. However, as pressure increases in conjunction with temperature, it is not possible to fully decouple the effects of these two control variables.

Increasing the orifice diameter also causes an increase in cone angle and density of spray. Once again this proposal should be treated with caution as studies conducted by Cleary [115] and Jones [117] have shown that the actual temperature at the nozzle is closer to that of the stagnation temperature for the larger the orifices. Thus, by increasing nozzle diameter the effective degree of superheat in the jet is also increased.

Other useful facts that can be deduced from the photographic evidence are things which will aid in the construction of the other experimental programmes. For example, clearly

for laser-based techniques, smaller nozzle diameters may allow the receiving optics to be positioned nearer the centre of the spray. Conversely it can be noted that for experiments requiring the filling of enclosed rooms then maximum superheat and maximum discharge orifice will create the densest most rapid discharge.

### ***8.2.2 Rainout Data***

Rainout data was not generated as part of this programme, so reference is made to the studies conducted by Jones [117] and documented further by Cleary et al. [116]. Although this method does not directly measure droplet sizing which is required to fully appraise an explosion systems viability, it does offer an insight concerning the effects of stagnation temperature and pressure on the amount of water that stays in suspension after the release of a flashing jet, and helps determine a strategy for the development of a potential full-scale explosion suppression system.

The work was conducted within the Cardiff School of Engineering, and involved carrying out a number of full-scale releases for differing degrees of superheat, supply pressures and nozzle arrangements. The work was conducted externally, so factors which are not directly relevant to this work such as wind speed and direction were examined, but are not discussed here.

There were two basic methods for determining the rainout fraction that occurred on the releases. The first method was based on a 'patternator' design, which allows the quantification of both rainout fraction and spatial distribution. This is not of great interest for the purposes of this report, so only results from the second method will be reviewed.

The method used to generate the results (detailed later) is based on a very simple but effective method of collecting rainout from full-scale releases. It simply involved releasing the jet over a large raised polythene sheet, which caused any rainout to collect in a pool which could then be measured to determine a volume of water that had not remained in suspension.

An image of the setup is given in Figure 8.9, and shows the Micromist atomiser being released in the open atmosphere over the tarpaulin sheet, which has a dimension of 6 x 4 meters.

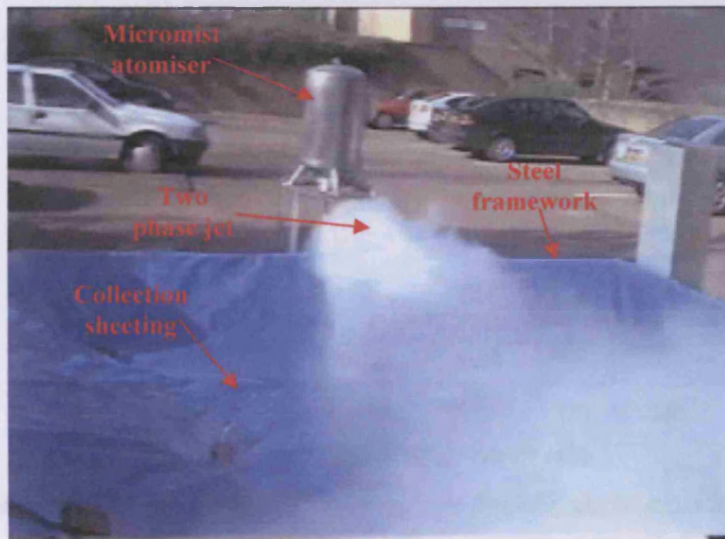


**Figure 8.9** Photograph of rainout experiment conducted with Micromist atomiser

The jet is released in the horizontal plane, which is not the probable direction of an explosion suppression system, but still gives an insight to the effect of initial conditions so results may still be used in a qualitative manner.

The crude method proposed provided good repeatable results that are comparable to results produced by the Centre for Chemical Process Safety (CCPS), which is reviewed thoroughly by Ramsdale and Tickle. [118].

The data presented here can be used to show the effects of both stagnation temperature and discharge orifice on the respective rainout. The effects of temperature on rainout are illustrated in Figure 8.10.

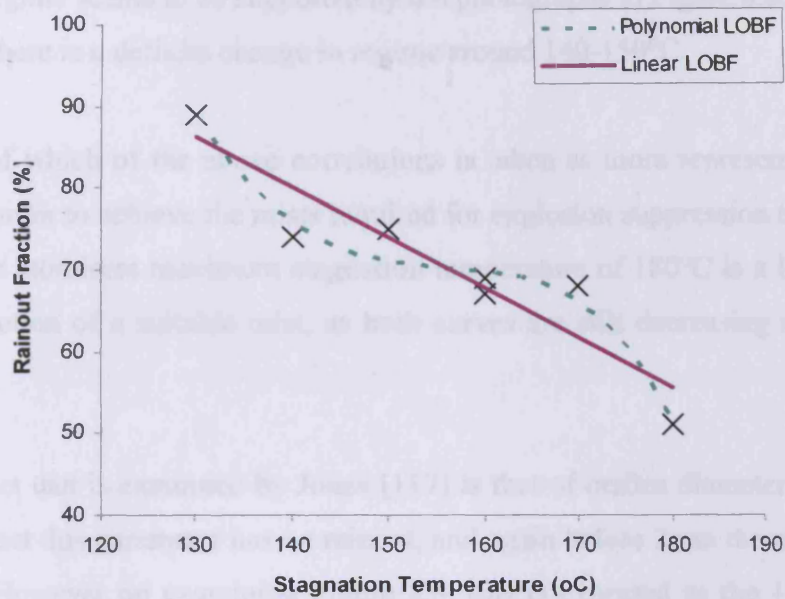


**Figure 8.10** Rainout against stagnation temperature for Micromist atomiser orifice diameter 4mm

As can be seen from the data above, rainout fraction and stagnation temperatures are inversely proportional. The exact correlation can be represented in a number of different ways as shown by the two different lines of best fits imposed onto this graph. The linear trend would imply that the break-up mode for all of the points is that of 'flashing' so that by increasing superheat the ferocity of the flashing process escalates, thus decreasing the size of the droplets produced. This in turn will cause there to be less rainout owing to the fact that each droplet is more likely to remain in suspension due to the fact that it is more buoyant and also more likely to evaporate because of its large surface area to volume ratio.

If the polynomial trend-line is more characteristic, then this could be explained by a change of modes of break-up mechanism from mechanical break-up at the lower temperatures, into a full flashing regime at the highest temperatures. The shape of the curve would thus indicate that at the lower temperatures, larger droplets are being produced owing to the lower jet pressures associated with the Micromist atomiser at low temperature. As the temperature increases the pressure also increases causing a reduction in droplet size even though the mechanism is still that of mechanical break-up. There is then a transition point at approximate stagnation temperature of 160°C whereby the predominant mode of break-up is that of flashing, hence the sudden drop in rainout fraction/droplet size.

The second regime seems to be supported by the photographs in Figure 8.8, which seems to show that there is a definite change in regime around 140-150°C.

Irrespective of which of the above correlations is taken as more representative, it does show that in order to achieve the mists required for explosion suppression then at present the Micromist atomisers maximum stagnation temperature of 180°C is a limiting factor for the production of a suitable mist, as both curves are still decreasing rapidly at this point.

The next effect that is examined by Jones [117] is that of orifice diameter. Figure 8.11 shows the effect this parameter has on rainout, and again before 2mm there appears to be a transition. However on examining Figure 8.8, this is expected as the 1mm orifice at 160°C does not flash, and so by adding the jet regime onto the figure produced by Jones [117] is considered likely to present a fairer depiction of the correlation.

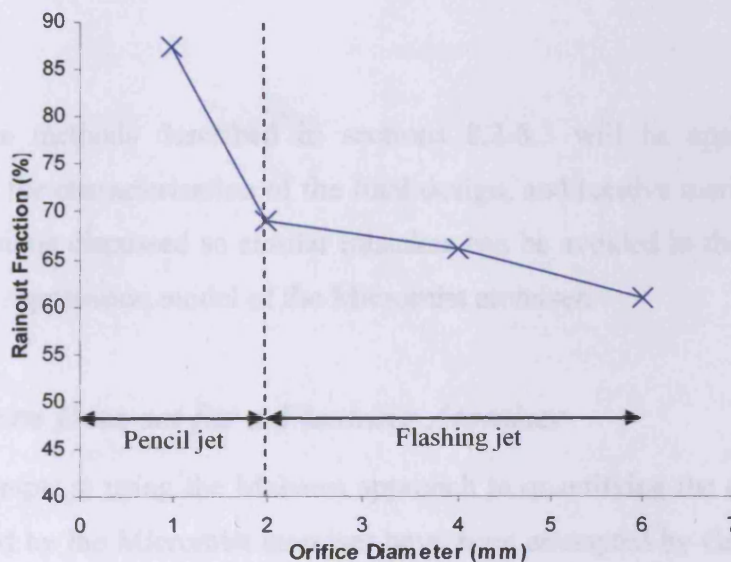


**Figure 8.11** Rainout fraction compared with discharge orifice for Micromist atomiser at stagnation temperature of 160°C

The data points for 2, 4 & 6mm seem to display a linear trend, which indicates that increasing orifice slightly decreases the rainout fraction for the Micromist atomiser. This trend does not seem to link directly to the CCPS data, which observes little correlation between orifice diameter and rainout. The decrease noted in this data is once again due to the actual degree of superheat measured at the nozzle, as explained earlier

and documented [115 & 116] the larger the orifice diameter, the nearer the nozzle temperature is to that of the stagnation temperature.

Larger orifice diameters also produce larger cone angles, as discussed in section 8.2.1, so the likelihood of droplets being carried onto the tarpaulin after exit is increased owing to the direction of discharge over the collection section, thus to witness a drop in rainout fraction supports the fact that jets produced through large orifices driven by high stagnation temperatures give the smallest droplets and highest vapour containing mists.

This study has proven invaluable for a number of different reasons, namely; there is little value in trying to fully characterise an experimental Micromist atomiser used for this work, as mist produced from a explosion suppression system which will probably incorporate a higher stagnation temperature to ensure smaller droplets with a larger orifice size in the order of 10's of centimetres, to ensure a very fast discharge time, and so will not be fully representative of those created in this study with the prototype atomiser.

Therefore the methods described in sections 8.2-8.3 will be appraised as to their usefulness in the characterisation of the final design, and relative merits and weaknesses in each technique discussed so similar mistakes can be avoided in the final appraisal of an explosion suppression model of the Micromist atomiser.

### ***8.2.3 Malvern Data-set for a Flashing Atomiser***

Previous attempts at using the Malvern approach to quantifying the characteristics of a mist produced by the Micromist atomiser have been attempted by Galloway University on behalf of Micromist Ltd [110]. A summary of the data obtained is given in Figure 8.12, and details for the three trialled delivery systems given in Table 8.1.

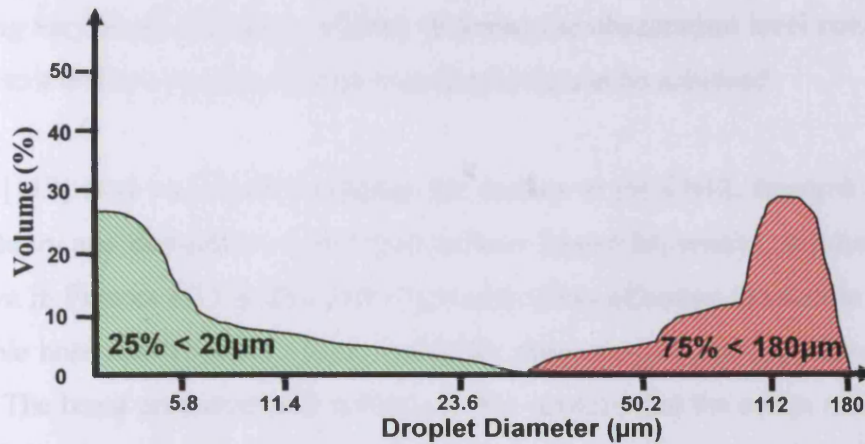


**Figure 8.12** Representation of data produced from Malvern Mastersizer $\chi^{\text{TM}}$  for Micromist atomiser

As can be seen from the above figure, only 25% of the volume of the spray seems to be in the range required to be effective as an explosion suppressant. However, some scepticism should be shown with respect to these results, as the number of sample points taken throughout the spray is not stated and in order to achieve these usable obscuration levels, it is presumed that some form of shielding must have been used.

**Table 8.1** Volume Analysis for Micromist atomiser using Malvern Mastersizer $\chi^{\text{TM}}$

Orifice Diameter (mm)	D <sub>0.5</sub> (µm)	D <sub>0.9</sub> (µm)	Obscuration
5	92.5	181	0.44
5	49.2	141.3	0.33
5	No result	20	0.52

As can be seen from results Table 8.1, three different delivery systems were characterised and the results obtained from each differ considerably once again iterating that to fully characterise a trial atomiser is of limited use for the aim of this study.

In order to fully analyse the usefulness of the Malvern Mastersizer $\chi^{\text{TM}}$  in the characterisation of a fully-flashing jet, a full scale release was attempted at Cardiff University. Major problems were encountered in generating meaningful results with the current facilities. Fogging of the optics was a major problem in large scale releases, and although it was proposed that using shields and beam protectors could have resolved this problem, at maximum superheat the obscuration levels were of the order of 90+%, which leaves the data very prone to error, as discussed in Chapter 3.

By using very small discharge orifices (0.5mm) the obscuration level could be lowered but not to a level acceptable for any meaningful data to be achieved.

Clary [119] used a specially designed test facility at the ENEL research centre in Pisa (Italy) to try and characterise a full scale release from a Micromist atomiser. The facility is shown in Figures 8.13 (a&b) with slight alterations allowing the nozzle to be fitted to a flexible hose and traverse, which allows for accurate positioning of the spray into the beam. The beam protectors and deflection fins ensured that the optics remained dry and reduced the obscuration by reducing the size of the sample area. All of the mist is then extracted into the expansion vessel, and vented away from the instrumentation.

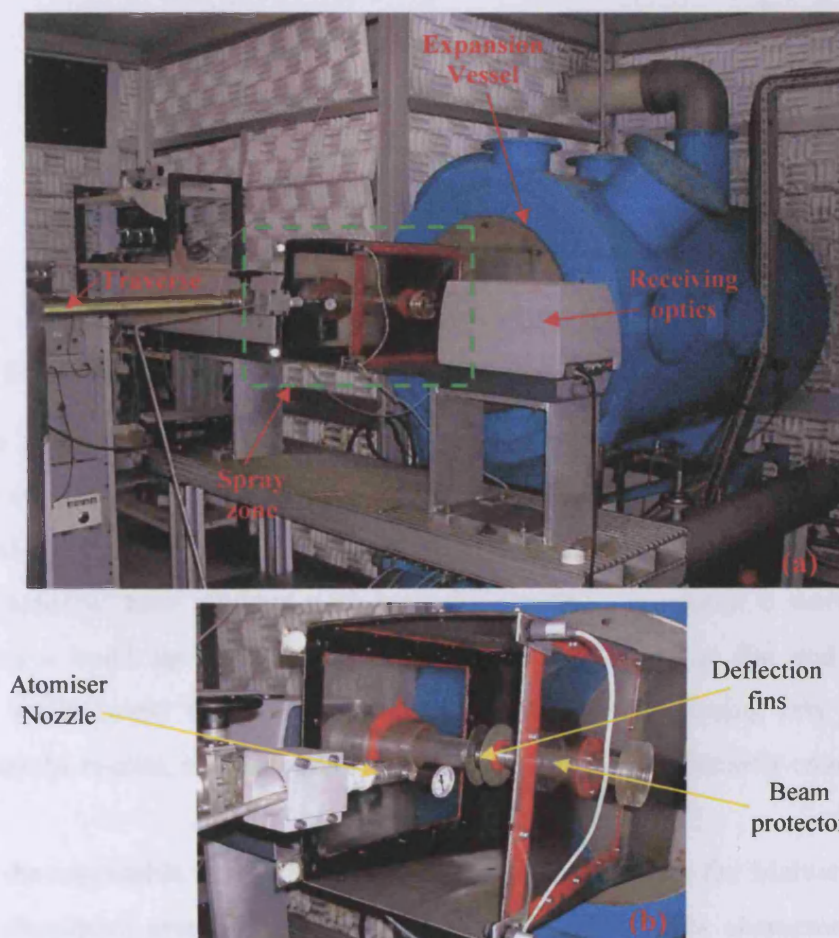


**Figure 8.13 (a&b) ENEL Malvern Mastersizer<sup>TM</sup> large scale spray rig (a) and close up of the spray zone (b)**

Even with this advanced spray rig, obscuration proved to be a problem thus to try and reduce this, and owing to time constraints, a data set was attempted at a low stagnation temperature of 140°C, which gave a nozzle temperature of 125°C. Therefore the jet was not fully-flashing, so larger droplet diameters were to be expected.

### 3.2.4 PDA Diagnostics for a Turbine Fuel Atomiser

By positioning the traverse, droplet sizes were taken at three axial positions of 350mm, 400mm and 450mm, with a number of radial sample points being taken at 10mm increments around the centreline. The results are given in Figure 8.14.

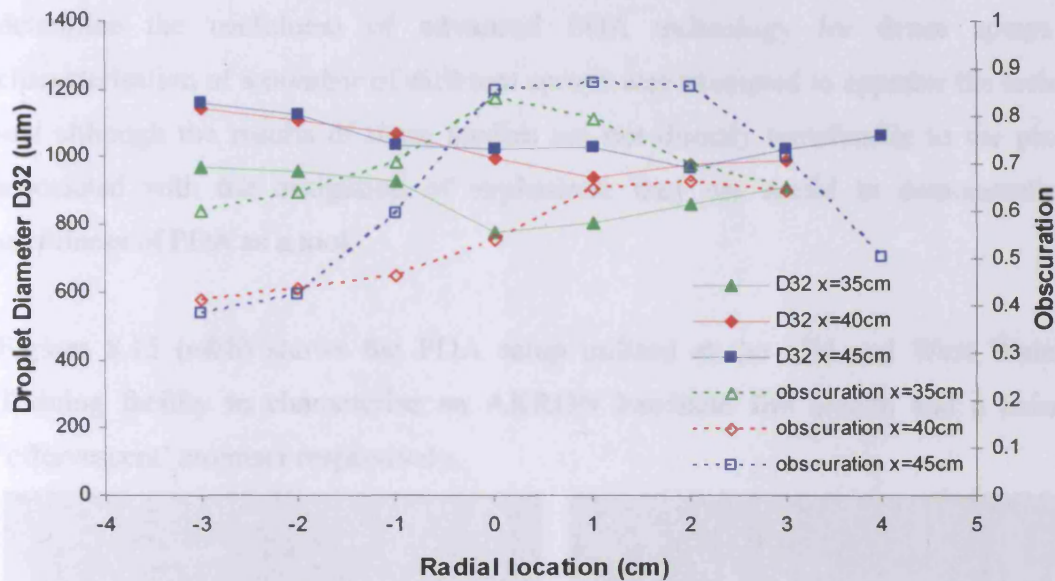


**Figure 8.14** Malvern Mastersizer results obtained for Micromist atomiser

As can be seen from the data, the obscuration levels even with the shielding and low superheat are still too high. The droplet sizing as can be seen is very high even for a mechanical break up regime. Cleary [119] suggests a number of sources of error with this setup namely; those inherent with laser diffraction as discussed in section 3.2.3, also he suggests a build up fluid on the metal disks positioned at the end of the beam protectors which could 'drip' into the path of the laser beam causing very large droplets to enter into the results, and potentially skew the Sauter mean diameter considerably.

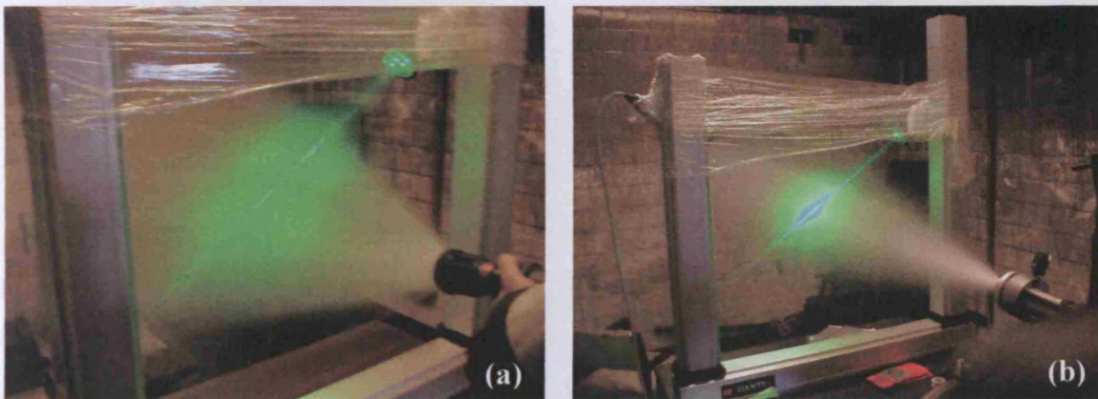
Owing to the unsuitable principle for dense sprays upon which the Malvern Mastersizer is based, alternative methods of characterisation are sought for characterisation of the final Micromist explosion vessel.

### **8.2.4 PDA Data-set for a Twin Fluid Atomiser**

The Phase Doppler Anemometry method (discussed in Chapter 2) provides a powerful technique for the characterisation of large-scale water jets.

A simple 1 point system was set up at the Mid and West Wales Fire Training Centre to determine the usefulness of advanced PDA technology for dense sprays. The characterisation of a number of different sprays was attempted to appraise the technique, and although the results of these studies are not directly transferable to the problems associated with the mitigation of explosions, they are useful in demonstrating the usefulness of PDA as a tool.

Figures 8.15 (a&b) shows the PDA setup utilised at the Mid and West Wales Fire Training facility to characterise an AKRON handheld fire branch and a twin fluid 'effervescent' atomiser respectively.



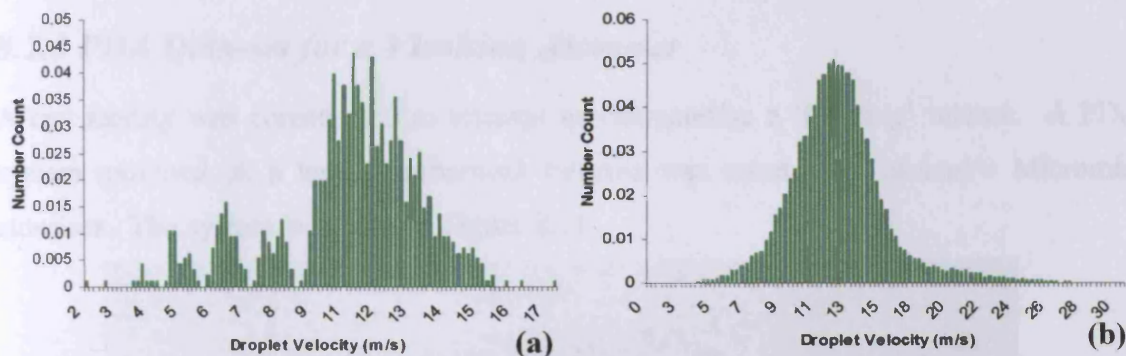
**Figures 8.15 (a&b) Fixed PDA System Utilised for the Appraisal of Characterisation of Large-scale Water Spray work with Fire Branch and Twin Fluid Atomiser Respectively**

It can be seen in the Figures 8.15 (a&b) above that the sprays utilised are fairly large and dense, and so it was decided that if valid results could be obtained for these types of sprays, then that its application was likely to be suitable for attempting to characterise full-scale 'flashing' releases.

As these tests were undertaken to appraise the apparatus, no processed results are presented here. However, by looking at the processed results certain conclusions/lessons have been learned.

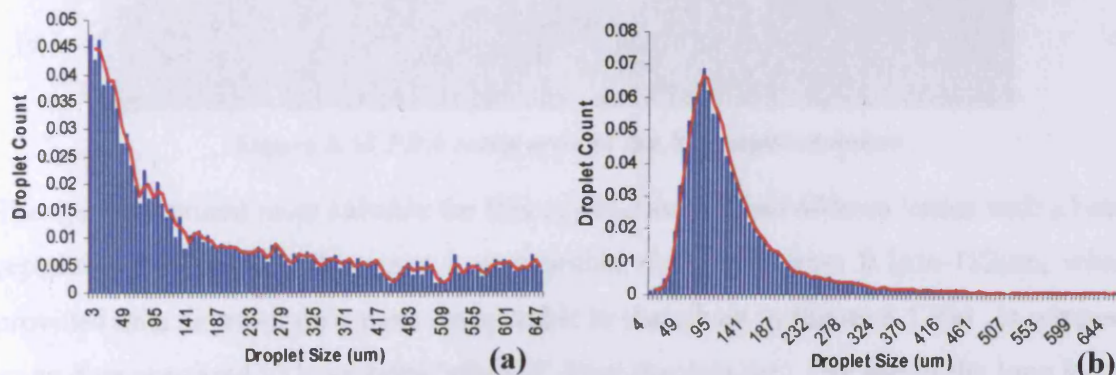
Due to the fact that only one data point is recorded for each spray then it is not possible to use the results as comparative purposes, but such things as data count indicate the types of spray that can best be characterised by PDA systems.

Figure 8.16(a) demonstrates that it is crucial that a comparatively large sample count is used, as in this case only a few hundred sample points were taken compared with the thousands taken for the other hose data sets (Figure 8.17b). This may explain the multimodal appearance of the velocity distribution compared with the Gaussian distributions witnessed for the other data sets.



**Figure 8.16 (a&b) PDA Droplet velocity distributions for a fire hose demonstrating the need for large data sets**

The preliminary study also demonstrated the necessity of appropriate beam separation and lenses are crucial. Figure 8.17(a) shows that if the limits are not sufficiently broad, then data will be missed at either the upper or lower limits. In this case large droplets present in the spray are missing from the data because they are outside the limits of measurement for this particular set up, thus when Sauter mean diameters are calculated it will be unrepresentative of the actual spray, giving a value lower than the actual one.



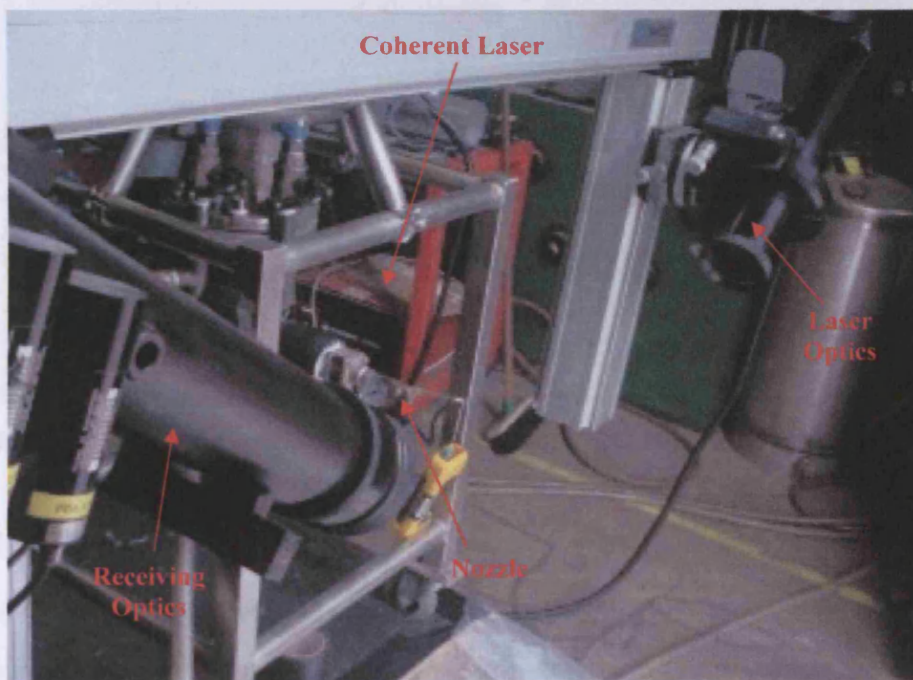
**Figure 8.17 (a&b) PDA Droplet size distributions for a twin fluid 'effervescent' jet demonstrating the need for the correct optical arrangement**

Figure 8.17(b) then demonstrates that with the correct optical arrangement all droplets within the spray can be measured thus affording an accurate measure of the Sauter mean diameter within the spray.

Undertaking these preliminary studies also indicated that appropriate data and validation rates could be achieved in these dense full-scale releases. Furthermore, with a more powerful laser as used within Cardiff University, coupled with an optimised set up it would be possible to attempt to characterise a Micromist release.

### **8.2.5 PDA Data-set for a Flashing Atomiser**

A test facility was constructed to attempt to characterise a ‘flashing’ release. A PDA system mounted on a large mechanical traverse was constructed around a Micromist atomiser. The system is shown in Figure 8.18.



**Figure 8.18 PDA setup around the Micromist atomiser**

The system deemed most suitable for this application utilised 600mm lenses with a beam separation of 70mm. This gave a measurable size range from  $0.1\mu\text{m}$ - $182\mu\text{m}$ , which provided data distribution curves comparable to that given in Figure 8.17(b), is adequate so no data appeared to have been ‘clipped’ from the data set. The use of the long lenses ensured that the lenses did not become fogged up by spray as the distance meant they were kept well out of the spray field.

The large mechanical traverse allowed for measurements to be taken axially for a distance of up to 8000mm from the nozzle and radial measurements could be taken for  $\pm 1500$ mm from the centreline of the spray. This allowed for investigations into the droplet sizing throughout the whole spray.

The control volume was passed through the mist as shown by Figure 8.19. 20,000 sample points were attempted at 33 different points throughout each jet with a 45 second timeout function added to ensure that the whole spray could be characterised.

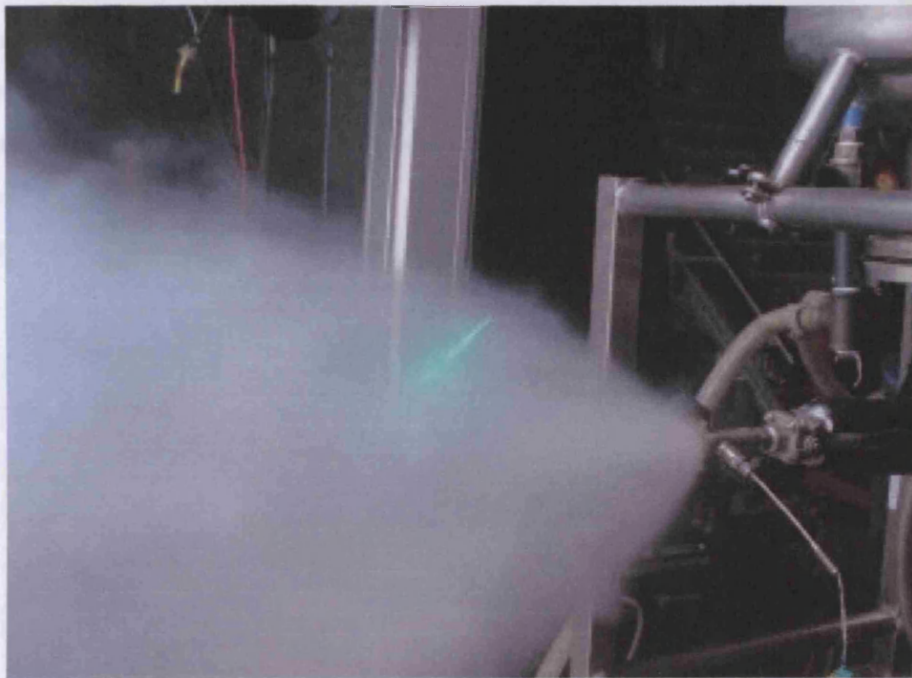


**Figure 8.19 PDA control volume passing through a full scale 'flashing' release**

#### **8.2.5.1 'Flashing' Jet results 180°C with 0.75mm Nozzle**

The raw data collected from the DANTEC 'SIZEWARE' version 2.3' software was exported into Microsoft Excel, where it was processed to produce the graphs of the type illustrated by Figures 8.16 & 8.17. This data was then exported into AXUM and put through a MathCAD programme in order to summarise all of the data in the form of a pictorial representation of the flashing release. Results can be represented in a number of different ways each with their own merits.

The first data shown in Figure 8.20 gives details of the mean droplet diameter ( $D_{10}$ ) throughout the spray. The two graphs represent the same data in different forms. The

upper graph shows pictorially the actual measurements made at each point. As can be seen a majority of the  $D_{10}$  values are under 40 microns and the axial speed of the droplets drops from 8m/s at 250mm to 1m/s at 750mm.

The lower portion of Figure 8.20 is an interpolated result so a prediction for the whole spray is generated from the 33 data points, as can be seen by the large mass of dark blue that there is a definite trend of the larger drops migrating due to gravity.

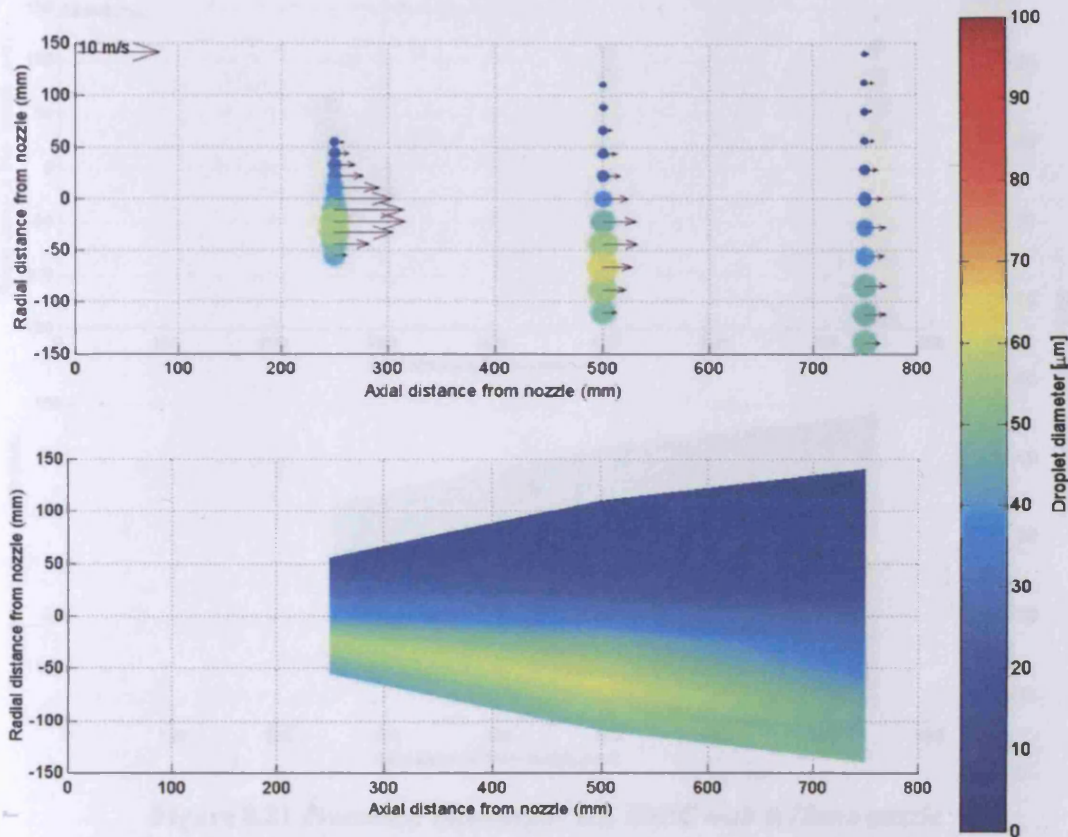


**Figure 8.20 Processed Results for  $D_{10}$  values  $180^{\circ}\text{C}$  with  $0.75\text{mm}$  nozzle**

The same data can however be represented in the form of Sauter mean diameter ( $D_{32}$ ) as

depicted by Figure 8.21.  $D_{32}$  is given by  $\frac{\sum d^3}{\sum d^2}$  so represents the spray as a droplet of a

given volume to surface area ratio. This value is how most sprays are represented for heat or mass transfer application; however it is susceptible to being swayed towards a larger size by relatively few large drops. In the case of a mist capable of suppressing an explosion, these droplets would rain out of the mist early on after release, thus are of no consequence to their effect on the suppression.

As can be seen at the position of axial 500mm, radial -50mm in Figures 8.19 and 8.20, some large droplets are witnessed compared with all other areas. This either represents a growth in droplets via coalescence, or more probably that this is the trajectory of the rainout of large droplets, thus there are a high percentage of the larger droplets in this area of the spray which elevates the mean diameters, particularly the Sauter mean diameter.

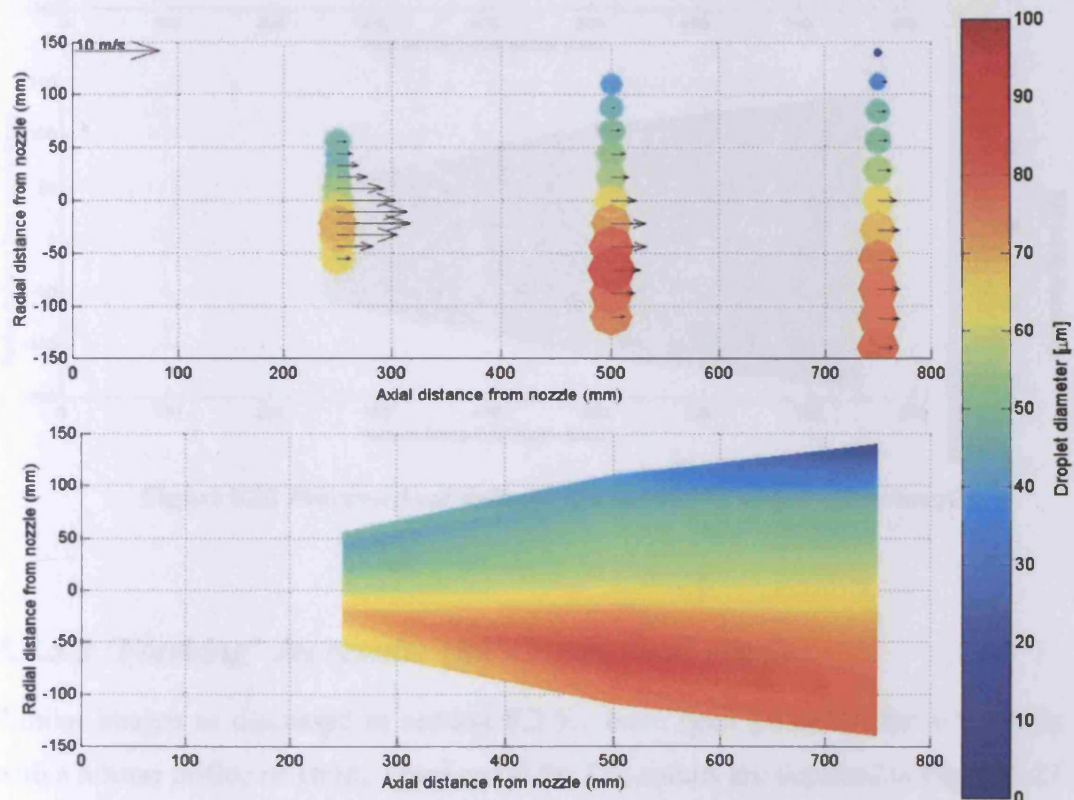


**Figure 8.21 Processed Results for  $D_{32}$  180°C with 0.75mm nozzle**

As can be seen from Figure 8.22, high validation rates of 90-100% are seen throughout the entire spray for both validation and sphericity. This demonstrates that the setup used for the PDA system is a reliable one. However, if needed these values could have been compromised slightly to allow for either a larger control volume or a higher data rate which may be required for a different spray.

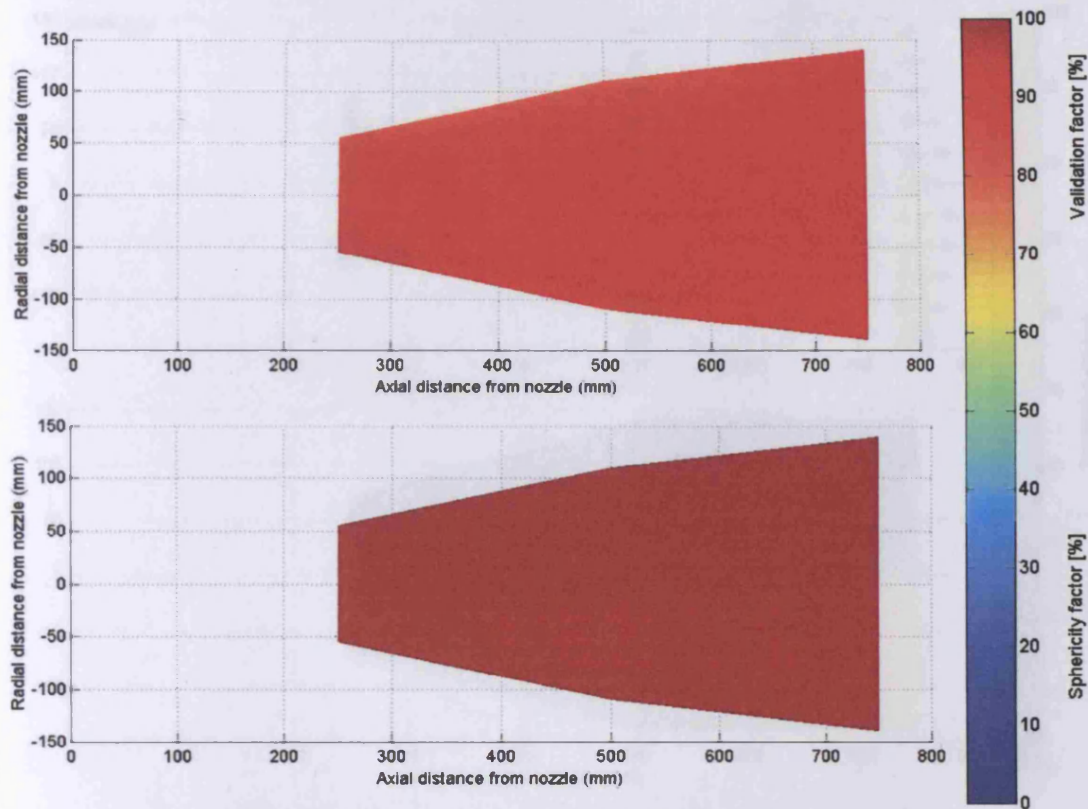


**Figure 8.22 Processed validation rates for 180°C with 0.75mm nozzle**

### 8.2.5.2 'Flashing' Jet results 180°C with 1mm nozzle

Similar images as discussed in section 8.2.5.1 have been generated for a 'flashing' jet with a release orifice of 1mm. Once again the  $D_{10}$  results are depicted in Figure 8.23.

As can be seen through the predominant colourings of blues and yellows, nearly all droplets are in the 0-60 $\mu$ m range. And once again the smaller droplets appear to be in the upper half of the spray.

It can also be seen that the droplet velocities within the spray are higher than that witnessed for the 0.75mm orifice.

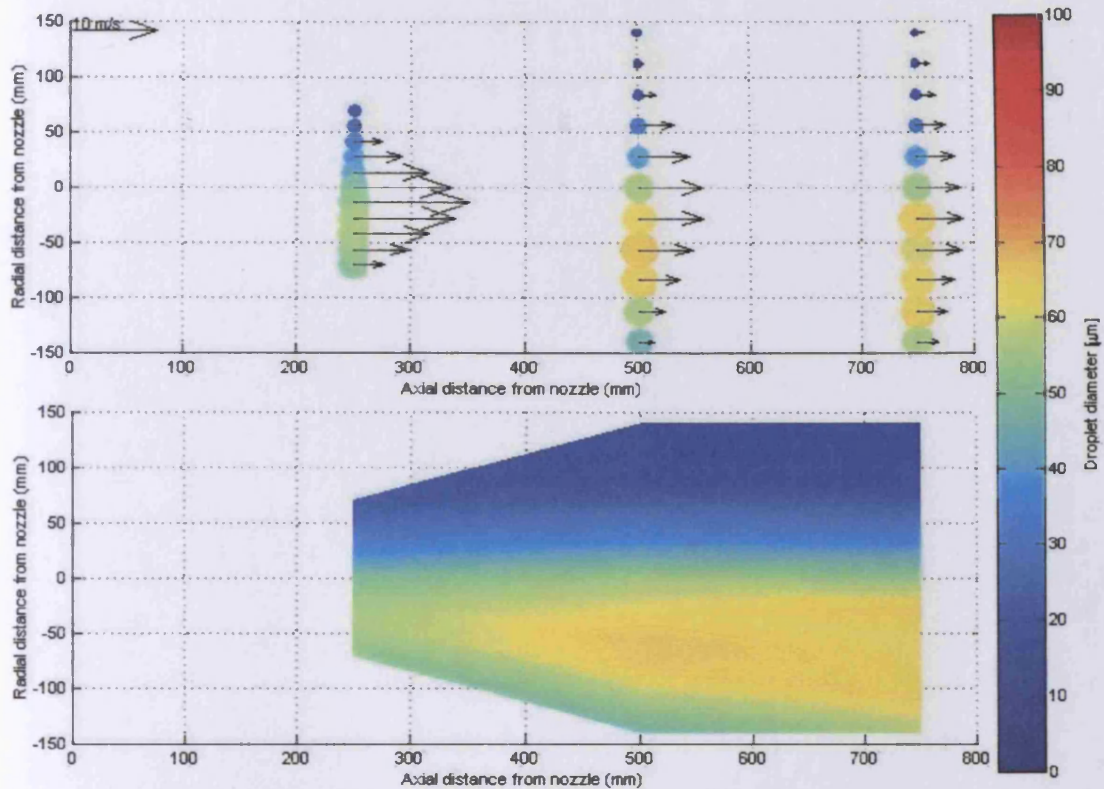


**Figure 8.23 Processed results  $D_{10}$  180°C with 1mm nozzle**

It should be noted that there seems to be a larger portion of yellow within Figure 8.23 compared to that of Figure 8.20, however as can be seen owing to the outer ranges of the traverse used, radial data at the edges of the spray after 500mm was not possible. Thus data which would have contained predominantly small droplets is missing from this data set.

When converting the data to represent droplets in terms of  $D_{32}$  for this data set (Figure 8.24) it can be seen that the droplets appear to be much larger than those given in the 0.75mm data (Figure 8.21). This is surprising as the  $D_{10}$  values are similar, but this divergence of data shows the sensitivity of the  $D_{32}$  value to a few very large droplets. There are many reasons why these large droplets may be present in the data set and these will be discussed later in section 8.4.

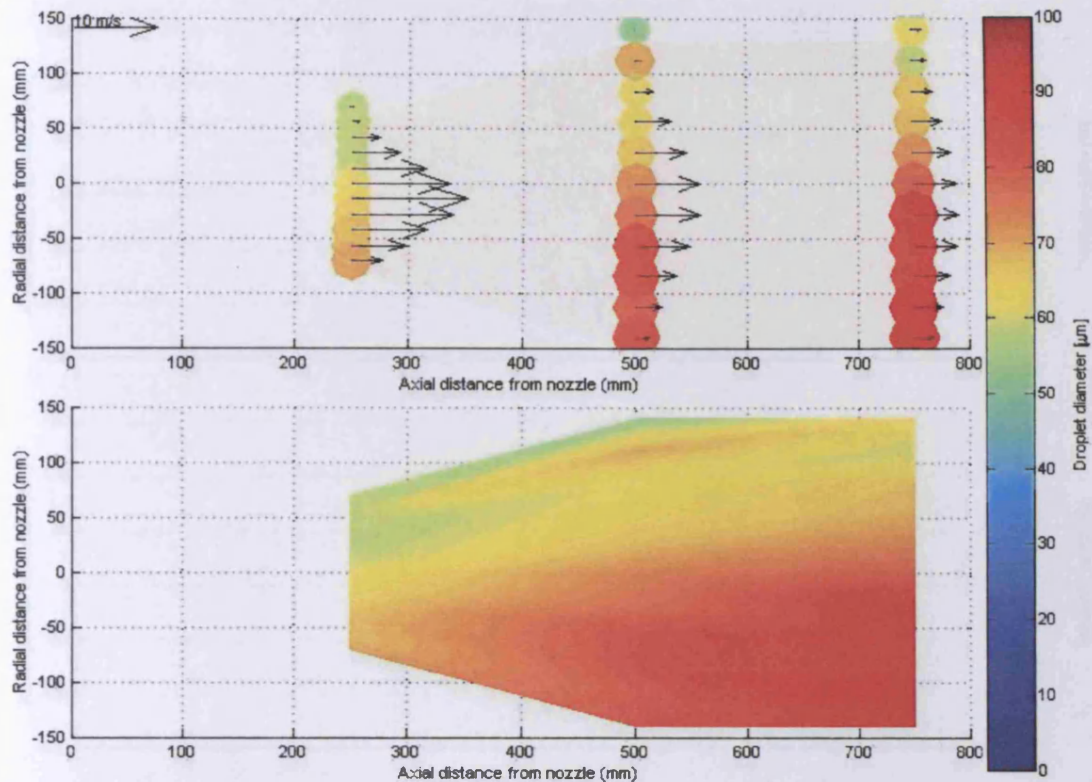


**Figure 8.24 Processed results for D32 180°C with 1mm nozzle**

Figure 8.24 indicates that the droplet diameters within this spray are predominantly greater than  $60\mu\text{m}$ . However, on examining the raw data files it can be seen that there are large numbers of droplets for each data point that are less than  $60\mu\text{m}$ . This demonstrates that statistical analysis of droplet counts must be treated with caution.

The validation results for the 1mm data shown in Figure 8.25 are lower than those given for the 0.75mm data, which is to be expected, as there are higher data rates due to the higher density of the spray. The validation rates are still in the high 80-90% region which shows that there is still a good setup for the PDA system. The drop in validation rate could be caused by a number of factors such as multiple occupancy of the control volume, or some very large droplets being out of range of the control volume. The sphericity factor is still once again nearly 100%, which shows a competent setup and reliability of the data.

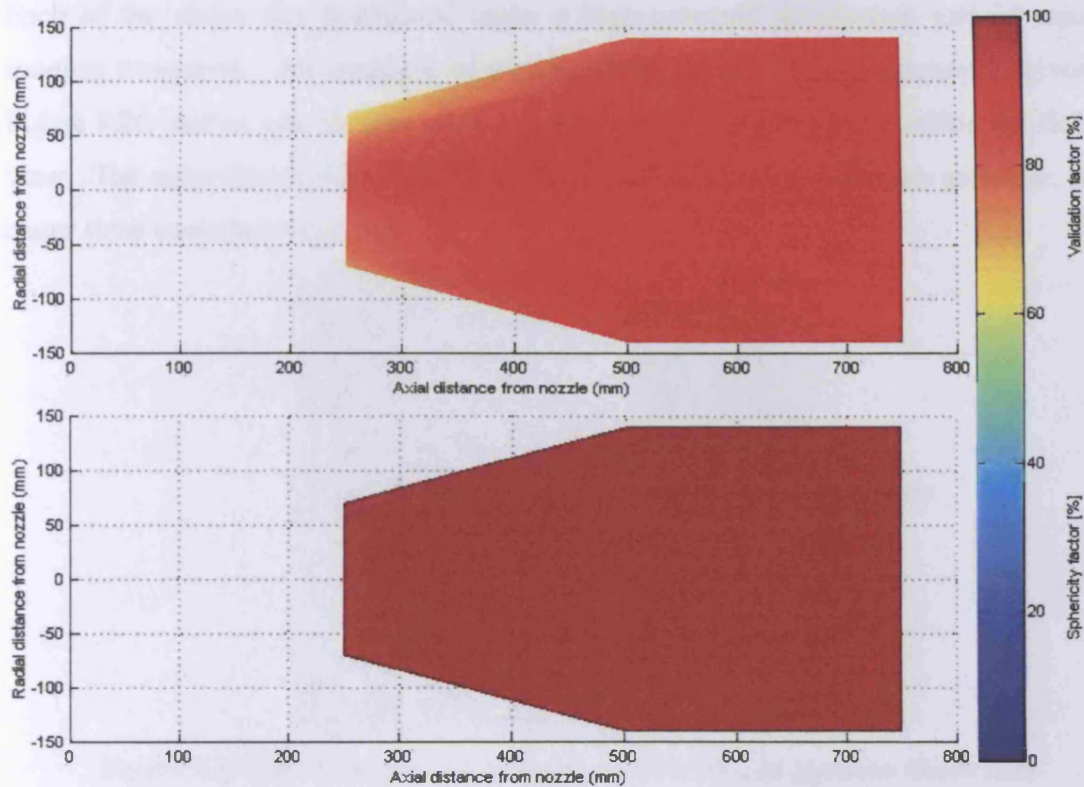


**Figure 8.25** *Processed validation rates 180oC with 1mm nozzle*

### 8.2.6 Magnesium oxide data

Two different experiments were derived to examine whether the magnesium oxide method discussed earlier (Chapter3) were of use for the characterisation of large scale two phase releases in terms of droplet sizing and distribution.

The first was to examine if the method could be used to actually measure droplets during a release, and the second to examine if the technique would be of use in determining the effect of time on the rain out of a mist in a closed environment (section 8.3.2).

The first investigation was undertaken within Cardiff University. The Micromist atomiser was heated to 180°C and released through a 2mm orifice. After the jet was observed to fully flash, magnesium oxide slides were placed into the spray at distances of 1, 2, 3 & 4 meters from the orifice and then placed into a sealed box so they could be examined later.

Each of the slides was positioned under a high powered microscope and 36 random droplets measured. An example of a slide viewed under the microscope is given in Figure 8.26, and as can be seen, there are a number of craters visible within the field of view. The outer rim of the crater is measured and sized using computer software; these crater sizes were then recorded.

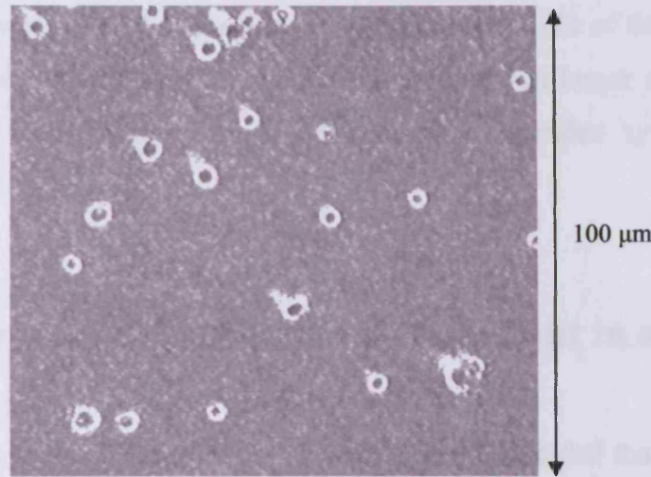


**Figure 8.26** View of craters left by water droplets on a Magnesium Oxide slide

As the crater is not directly representative of the actual size of the droplet, it is necessary to add a scaling factor (as discussed in Chapter 3). After correction of the measured droplet diameters, it was then possible to plot the distribution of droplet sizes against distance from the orifice as presented in Figure 8.27.

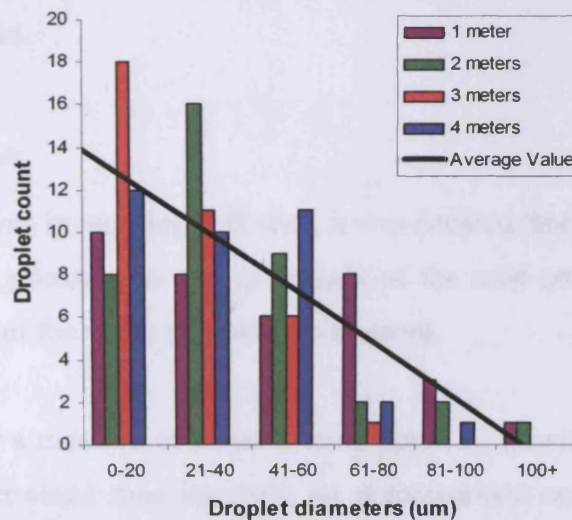


**Figure 8.27** Droplet distribution from Micromist atomiser as determined

These results suggest that up to 3 meters from the release all the large >100µm droplets have rained out of the mist. It can also be seen that nearly 65% of all droplets counted

within this area of release were under the size of 40 $\mu$ m and 33% of the droplets counted were under the size of 20 $\mu$ m.

This study has obvious fundamental flaws with respect to accurate data; namely the low sample rate and crude analysis of the data. However, these limitations are easily overcome with the investment of extra time into the analysis side of this technique. If automated counting and sizing of the droplets was created then larger sample numbers could be recorded so that sample sizes of the order recommended by DalaValle [56] could be constructed.

### **8.3 Results of droplet dispersion and settlement in a confined release**

Following the success of the flashing release studies, it was decided that it was of value to employ forms of visualisation and Magnesium Oxide techniques to evaluate a full-scale confined release. A suitable humidity chamber was chosen at the Mid and West Wales Fire Training facility, the dimensions of which were 3.2 x 4.4 x 3.4 meters giving a total volume for saturation of just under 48m<sup>3</sup>. Although the intention was to conduct a fully enclosed release, this proved impossible owing to the density of mist requiring an external door to be opened primarily for additional light, which, was required to ensure the safety of personnel.

#### **8.3.1 Visualisation**

Due to time constraints in working 'off site', it was decided that video images would be recorded during the releases, so that an insight of the mist could be used to visually record the residency of the water mist within the room.

It was surmised that a measure of concentration could be generated by taking stills off the video at predetermined time intervals, so a comparison could be drawn. This is given by the series of photographs detailed in Figure 8.28.

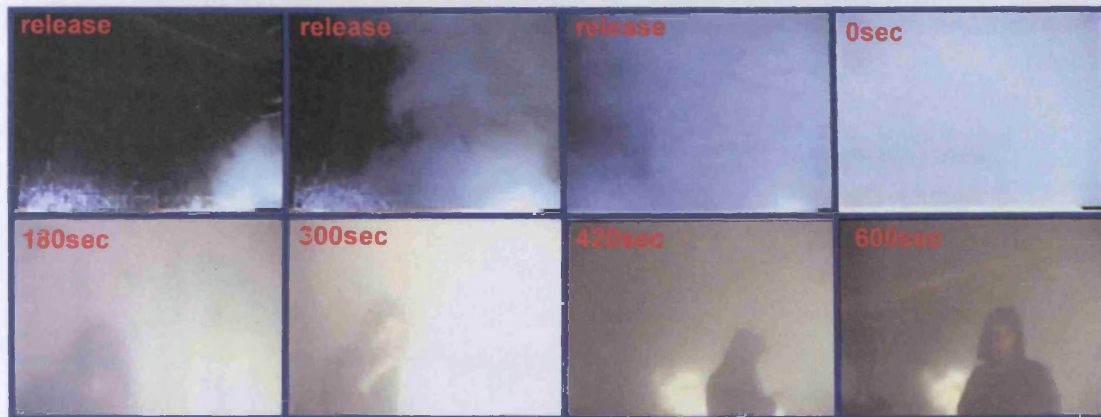


Figure 8.28 Video sequence of enclosed release

Although this technique can obviously not be used quantitatively from a qualitative point of view, it is clearly observed that the density of the mist reduces with time, as would be expected. This change of density is actually accelerated owing to the fact that an external door needed to be opened as discussed earlier.

Examination of these films does provoke thoughts of likely problems associated with a mist based system for explosion suppression systems. The mist itself was completely harmless to personnel who were in the room throughout the release; however there are other problems that would need to be addressed concerning visibility. Also, after observing the density of mist, immediate concerns with respect to electrical isolation would have to be appraised.

### 8.3.2 Magnesium Oxide Data-set for a Flashing Jet

The Micromist atomiser was once again heated to maximum superheat ( $T_{\text{stag}} = 180^{\circ}\text{C}$ ), and it was decided that the largest discharge orifice available of 6mm would be used, which would be most representative of probable explosions systems which would require a rapid discharge of mist. It was proposed that magnesium oxide slides would be exposed to the mist at a number of different locations, namely; low corner, high corner, centre and low centre of the room. This would give an appreciation of whether the mist gets convected around the entire volume.

It was known that the release would take approximately 45 seconds, and so it was decided that samples should be taken at time intervals of 0.5, 1, 1.5, 2, 3, 5, 7.5 and 10 minutes after the end of the discharge.

The processed and corrected results collected from this experiment are summarised in Figure 8.29,

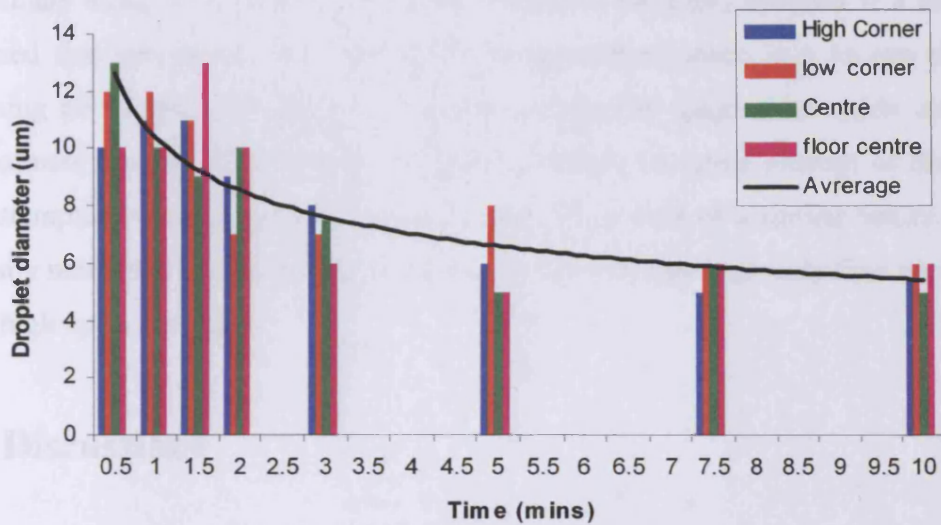


**Figure 8.29** Droplet diameter versus time for confined release at different internal positions

All average droplet diameters recorded were lower than 20µm. Although this seems very low, however it should be noted that due to the high stagnation temperature coupled with the fast discharge, the likelihood of the production of small droplets increases. Also, the rainout of large droplets would have occurred during the 30 seconds before the first sample was taken, this can be shown from the first experiment (detailed in section 8.2.6), which showed that a large proportion of droplets had fallen out of the spray within a few meters of the orifice.

The droplet diameter averaged for each time band suggests that the average droplet size decreases according to a power law. This is as would be expected, as larger droplets will settle faster due to gravity. Evaporation of the droplets will also occur as the room temperature rises to fully saturate the vapour fraction, and then over the next few minutes, the buoyancy of the smallest remaining droplets will keep them airborne.

There are once again fundamental flaws in this data set, most notably the low data samples and low repeatability of experiment, however once again this test has shown that the method could be of considerable use in the quantification of droplets in a full-scale confined release.

There is an extension of this method, which could be developed to quantify the actual concentration of the droplets within the mist. The method of sampling in this preliminary study was to simply wave the slides in the mist, however if a device was designed that passed the slide through a known arc of space in a known time, then assuming all droplets in this space impacted into the magnesium oxide coating, an approximate number concentration could be derived. A crude attempt of this method was attempted by assuming all 'swipes' of the slides were of a similar nature. It could be easily noted that the most densely impacted slides occurred at early time recordings at areas high up in the room.

## **8.4 Discussions**

### ***8.4.1 Appraisal of different techniques in the characterisation of the Micromist atomiser***

The course of this study has largely been achieved with the characterisation of the prototype explosion suppression Micromist atomiser. Five different methods for characterisation described in Section 8.2 were attempted and their appraisal shows that in all cases, with the exception of the Malvern Mastersizer<sup>TM</sup>, the techniques had relative merits in the characterisation of a full-scale 'flashing' release.

The visualisation techniques, although not quantifiable for droplet sizing, proved invaluable in the understanding of the effect of stagnation temperature and release orifice on the resultant jet. The results given in section 8.2.1 can be used to surmise that larger orifice diameters with higher degrees of superheat increase the density and 'flashing' effect witnessed in the resulting jet. These studies suggest that using stagnation temperatures of less than 140°C is of little use in the study of 'flashing' technology.

The next method proposed was that of rainout. This simple cost-effective method proved possibly the most valuable technique in the remit of this report. Although it does not give the actual size of droplets in the mist produced, it does allow for the calculation of the volumes of water that remain in suspension and thus the active portion of water that is expelled during a 'flashing' release.

The rainout data given in Figure 8.10 shows that in order to generate a mist of predominantly small droplets higher stagnation temperatures are favourable. This data also shows that the Micromist in its current design is not working as efficiently as it could be in terms of delivering mists that remain airborne. At present, the maximum stagnation temperature recommended is 180°C, corresponding to a maximum achievable nozzle temperature of less than 170°C. At this temperature 50% of all water is remaining in suspension.

The shape of the lines of best fit suggests that a further increase in stagnation temperature, which would require a higher pressure rating of the Micromist atomiser, would allow for a mist of finer droplets and higher vapour fraction to be produced, which would ensure that a greater fraction of the water would stay in suspension.

The next method utilised was that of the Malvern Mastersizer<sup>™</sup>, which was the least effective method appraised, as in order to achieve any meaningful data obtrusive beam protectors are necessary. These obstructions are likely to skew the data to such an extent as to derive the data as unrepresentative.

The Magnesium Oxide slide method proved useful in the characterisation of a confined mist. With a few improvements this method could be adapted to give all the required data needed to fully characterise a full-scale release. The droplet sizes within a mist can be given accurately if a large enough data set could be measured. By producing a mechanism that passes the slide through a known sweep area over a known time frame, an accurate representation of concentration could also be given. The only reservation with this system at present is the highly labour intensive method of measurement, and the possibility that some droplets do not impact onto the surface. This could possibly lead to the loss of small droplets from the data set. However, average droplet diameters of down to 6 microns are recorded in Figure 8.29, which are as small as would be expected for such a release.

The PDA method for measuring an actual release proved very valuable, as it can be used to show the size and concentrations of droplets within a spray. The PDA system currently available at Cardiff School of Engineering is capable of characterising 'flashing' jets produced by the Micromist atomiser with orifice diameters of both

0.75mm and 1mm. With the setup utilised, it proved harder to characterise larger orifice sizes for a number of different reasons namely; the high density of the resulting jets, the increased velocity ranges, the physical size of the jet produced and the reduced times in which the entire contents of the atomiser were released.

These problems could possibly be overcome by changing the setup of the PDA system to produce a more suitable control volume. By changing the orientation of the discharge it would also be made possible to take sample points nearer the release.

The data that was collected for this report given in sections 8.2.5.1 & 8.2.5.2 shows that large numbers of 'small' droplets are produced by the Micromist atomiser. There are some discrepancies in the data produced from the PDA compared with models proposed from the rainout data. The data for the  $D_{32}$  given by the PDA results suggests that the larger orifice diameter produces a mist of larger droplets compared with that of the smaller orifice; however, the  $D_{10}$  values seem very similar.

This suggests that there are some large droplets within the spray produced through the 1mm orifice. These droplets could be produced for a number of different reasons namely; measurement before full 'flashing' temperature has been reached, imperfections with the 1mm nozzle, ill alignment of the nozzle or a build up of water on the nozzle plate that drips into the spray. The latter effect can be illustrated by current work which is being carried out with high speed filming techniques (Figure 8.30).

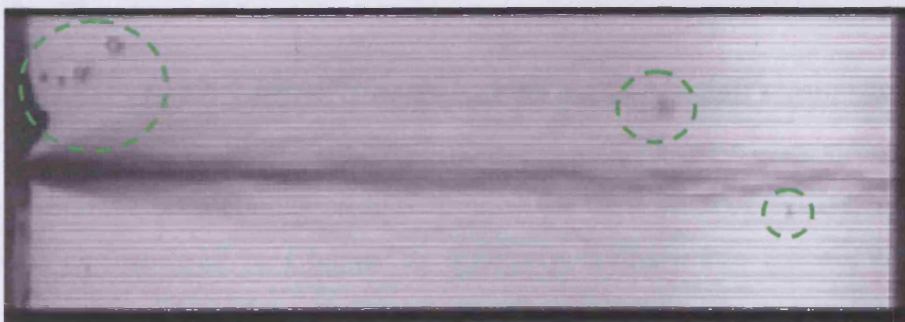


**Figure 8.30 High speed close up of 'flashing' jet illustrating large droplets that may sway  $D_{32}$  values**

As can be seen highlighted, there are some large droplets being formed at the edge of the nozzle and these on release get carried with the spray, possibly through the measurement volume. These are dependant on nozzle manufacture and not orifice size, which demonstrates that orifice diameter alone is only one of the variables, and the effect of

nozzle material and manufacture have been demonstrated as very important by Maragkos [108].

There may also be another cause of this over-sizing of the  $D_{32}$  value. Whilst researching the standard PDA system that was utilised for the Micromist work, it was found that DANTEC [120] have seen similar over predictions as in the following Figure 8.31(a&b).

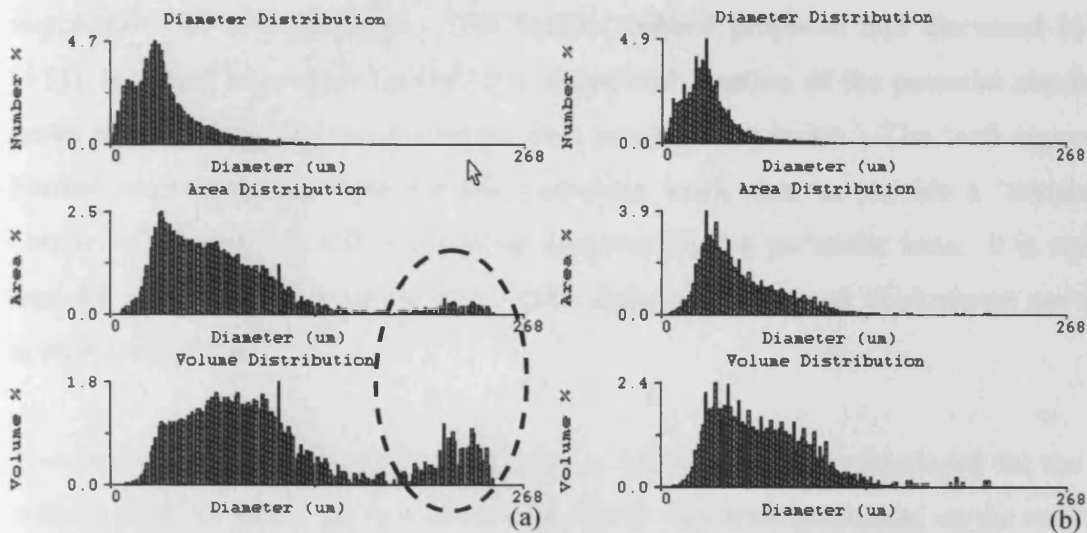


**Figure 8.31 (a&b) PDA data for spray using standard PDA and dual PDA respectively**

It can be seen that the standard PDA, as used for this study, can give unrepresentative data in terms of both area and volume measurements, which is highlighted in the standard PDA data. This addition of large droplets could be a factor that is affecting the 1mm data - set.

#### **8.4.2 Usefulness of Micromist atomiser as an explosion suppressant system**

Many studies have been conducted to determine the usefulness of water as an explosion suppressant as discussed in Chapter 2. Similarly, a study into the use of ‘flashing’ technology was conducted by the Steel Construction Institute on behalf of the HSE [121]. The study concluded that these sorts of devices, if developed in a suitable manner could be used to control explosions in offshore modules, and could also be made to operate at lower costs than competitor systems. However, it was expressed that medium-scale studies should be undertaken, and that ‘objections’ made to the systems

maintenance and accidental releases should be addressed before a system is made fully available.

The Micromist atomiser has already been tested as a ‘quenching’ agent as described by Tam et al [122]. The experiments detailed in this work were aimed to show whether the Micromist atomiser could be used as a ‘soft suppressive barrier’. A test schedule conducted at the Christian Michelsen Research facility involved the attempted suppression of 20 explosions. The barrier method proposed and discussed by Tam [123], is aimed at controlling the size, shape and location of the potential combustion gases thus limiting the consequences of a resultant explosion. The ‘soft suppressive barrier’ technique employed for this particular work aims to provide a ‘curtain’-like barrier, which restricts self propagating combustion to a particular zone. It is surmised that for this technology to be successful, rapid detection and deployment are of the utmost importance.

The medium-scale CMR M24 test rig (8m x 2.5m x 2.5m) was employed for the study and four Micromist units were utilised of which, two were positioned on the roof of the rig with their nozzles facing down and the remaining two were placed in the rig with horizontally facing nozzles. Measurements of pressure and flame front position were tracked using both pressure transducers and ionization probes. However, possibly due to the water interaction the ionization probes proved unreliable. Stoichiometric methane was utilised as the flammable cloud, ignited either centrally at an end wall and various deployment strategies and timings investigated. Exact concentrations and sizing of the water cloud could not be made, although it is estimated that between 2% and 15% by molar fraction of 20µm droplets were present.

Dry case tests were first undertaken to determine the extent of the unimpeded explosion, so that so as a comparison could be made when the atomisers were applied. A measure of performance was given by the control efficiency ( $C_E$ ), given by the following equation:

$$C_E = \frac{(P_u - P_s)}{P_u} \quad (8.3)$$

where,  $P_u$  is the highest recorded pressure in the dry case experiments, and  $P_s$  is the maximum recorded pressure in ‘suppressed’ explosion. It can be seen that the maximum control efficiency ( $C_E=1$ ) could only be achieved if there was no recorded pressure signal and owing to the system under investigation, which was a barrier technique this was not physically achievable. Therefore for a successful suppressive effect from a barrier type system, the  $C_E$  should be as near to unity as possible.

In the studies undertaken, the  $C_E$  values calculated ranged between 25% and 80% and owing to the type of system the maximum theoretical value possible for total suppression is of the order of 85%, showing the Micromist atomiser to be of great use in the suppressing of self-propagating flames.

A total suppression of a methane flame by a ‘soft passive barrier’ is illustrated by Figure 8.32, which shows the full extent of the flame within the test rig.



**Figure 8.32** *Photograph showing the maximum extent of flame through water mist barrier generated by Micromist atomisers*

However, some conclusions drawn from the study indicate that in the case of an incomplete mist curtain, the explosion can easily pass out of the module. In practice this could cause a reacceleration of the flame after the barrier as was witnessed in the case depicted by Figure 7.12 in Chapter 7.

For the above reasons and in addition to the conclusions drawn in Chapters 2 & 6 it is possible to deduce that Micromist technology could be best used to provide explosion protection against a methane-air explosion in the form of an ‘inerting’ system.

As is detailed in Chapter 2 the complexities in ‘quenching’ a self propagating methane flame are much greater than those encountered in the ‘inerting’ of the environment. It is also stated that 26% water vapour by volume is required to render a stoichiometric methane mixture inert. The most recent data from the literature states that 10µm droplets act as a vapour, and that droplets of in the size range of 15-30µm may be more effective than a simple vapour case.

Chapter 6 has shown that for a small scale ideal methane explosion that droplets in the range of 5-20µm are more effective at suppressing a methane-air flame than an equivalent water vapour case.

Therefore it is possible to suggest that an ideal ‘inerting’ system should be capable of delivering both high levels of water vapour and a large number of droplets in the 0-30µm size range. It can be seen from the results in this report that the Micromist technology could be used to supply such a mist. The rainout data suggests that by increasing the degree of superheat by another 50-60°C would increase the volumes of both vapour and small droplets considerably. In order that a room is made safe from explosion 26% water vapour / fine mist must be present. By adapting the equation (6.7) derived in Chapter 6, to include an atomiser efficiency function ( $A_E$ ) it is possible to calculate the volume of an enclosure ( $V_{enc}$ ) that could be made inert, as given by equation 8.4.

$$V_w \times A_E = \frac{Mr_w}{\rho_w} \times \frac{P_{atm} V_{enc}}{R_o T_{atm}} \times \left( \frac{1}{r_w} - 1 \right)^{-1} \quad (8.4)$$

By using values that have been derived from this study in Chapters 6 & 8 for the required water fraction required for inerting ( $r_w = 0.26$ ) and the approximate atomiser efficiency derived by the rainout data ( $A_E = 0.5$ ) it is possible by substituting in ambient conditions that the 35 Litre Micromist atomiser used for this study could protect an enclosure of approximately 65m<sup>3</sup>. However, it should be noted that over time water in the form of droplets will gradually rainout or condense out of the vapour phase, as shown by results in section 8.3.1. The timescale over which this happens would need to be precisely known to ensure there is ample water in saturation for the duration of protection time required.

As with all systems, there are associated problems with the implementation of the proposed system, namely; the added danger of pressure vessels, the associated risk of water around electrical equipment, the reduced visibility of personnel in a space requiring rapid evacuation and the fact that the system is only as reliable as the sensors that would be required for successful triggering. Owing to the nature of this system, if there were regular accidental triggers then there would be large periods of time when there would be little or no protection because the heat up times of the atomiser is in the region of hours rather than seconds.

### ***8.4.3 Future work***

As has been previously discussed, the Micromist atomiser could be an effective tool in making a potentially explosive environment safe. However, further research should investigate the effect higher superheat would have on the efficiency of the spray to act as a suppressant. By taking the maximum stagnation temperature of the Micromist atomiser up to  $>250^{\circ}\text{C}$  it is thought that data produced from a simple rainout data set, would show that a much higher fraction of the water would stay in suspension.

When a minimum value of rainout is found, confined release experiments with the proposed system should be carried out to ensure that droplet sizes and concentrations are in the correct ranges. The best method for this at present seems to be the Magnesium Oxide slide method, as this could be used to determine droplet size and concentration within a closed environment with respect to time. If this method was also coupled with a transient rainout experiment, then vapour fractions could also be estimated accurately. PDA data with the system in its present configuration would prove hard to attain, fast releases through very large orifices as would be required for a rapid deployment, would produce large dense releases that would cause rapid fogging of optics and low validation rates. However it is thought that an updated PDA system capable of positioning nearer the orifice could offer some insight into the actual droplets produced at source.

If it was found that nozzle diameter could be used in some way to give a more accurate droplet size range. Then a multi-hole orifice could be used to give all the required characteristics needed, in such a case then PDA could be used as a powerful tool in determining the droplet characteristics of the mist exiting the nozzle.

New sizing and concentration techniques are currently being made commercially available [124]; these techniques can be compared to a photographic version of the Magnesium Oxide method. These techniques rely on a thin laser sheet illuminating droplets in a spray, digital images of the drops can be taken within the spray and due to differing diffraction patterns and offset optics the size of the droplet can be determined directly from the number of bands witnessed. The number concentration can then be simply found from a number count. An example of such an image is given by Figure 8.33.

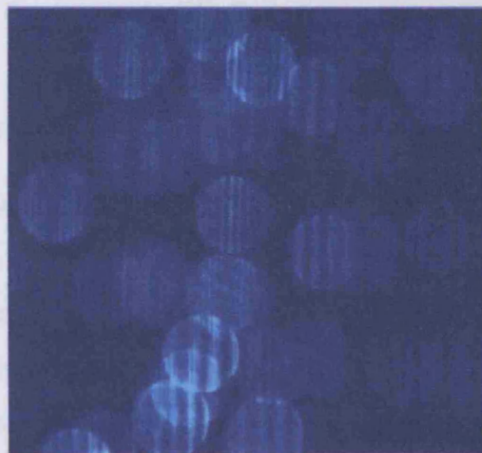


**Figure 8.33** *Image of droplets using particle interferometry sizing technique*

This technique could be of high value if optics could be protected from the enclosed mist, and could be very useful in determining a mists concentration with time.

## **8.5 Summary**

The conclusions of Chapter 8 have shown using a number of different characterisation techniques that there is potential for the Micromist atomiser to be commissioned as an explosion suppression system. The results obtained in this study demonstrate that the current Micromist prototype is capable of delivering approximately 50% of the stored water in a form which facilitates the ‘quenching/inerting’ of a combustible mixture of methane-air.

The study has highlighted possible ways in which the atomiser could be improved in terms of increasing its efficiency namely, increased superheat and orifice diameters. However, a number of perceived problems have also been illustrated but it is felt that these with careful consideration could be eliminated.

## Conclusions and Suggestions for Further Work

A number of valuable conclusions have been gained during the remit of this study allowing each of the aims and objectives described in Chapter 1 to be achieved. Each of these conclusions is given below along with suggestions for further work.

### 9.1 Main Achievements of Work

In the following section is a review of all the conclusions drawn from the previous chapters of this study:-

- A thorough literature review was undertaken which demonstrated that water in the form of 'fine' mists (10-30 $\mu$ m) could be very useful in the suppression of fully propagating methane-air explosions. The review highlighted the need for fundamental studies into the interaction of water in the forms of vapour and 'fine' mists on early flame propagation.
- The cloud chamber approach has been shown suitable for fundamental studies of interaction of 'fine' water mists with propagating laminar flames. The original Cardiff cloud chamber has been redesigned and undergone significant development to facilitate rigorous water-mist/flame propagation quantification studies.
- The operation of the cloud chamber has been analysed to develop towards calibrated operation. The dependence of mono-disperse mean droplet size on the primary control variables of expansion rate and expansion ratio has been quantified for the first time, so that simple empirical guidelines can now be proposed. The operation of the cloud chamber has also been described via an appropriate thermodynamic process equation, through temporal quantification of rate of expansion and pressure. A method for temporal quantification of

temperature variation during expansion requires further refinement. This work has been presented and published in the Proceedings of the ICLASS meeting [70] (12<sup>th</sup>-17<sup>th</sup> July, Sorrento, (2003)).

- Utilising the redesigned cloud chamber facility, laminar flame speeds and burning rates have been derived for methane-air explosions for a range of equivalence ratios and initial temperatures. Data generated has been compared with other published work, and shows reasonable agreement. Improvements compared with previous datasets include:
  - i). Undertaking five repeat experiments, so facilitating a statistical analysis for stretched laminar flames, possibly for the first time.
  - ii). Minimising the ignition energy utilised, hence reducing the effect of initial spark overdrive, and so allowing more detail of the early development of the stretched flame kernel, particularly useful for modelling purposes.
- A comprehensive dataset has been generated for laminar stretched burning rate of water-vapour methane-air mixtures, in a form suitable for model appraisal. Results have been derived for a range of equivalence ratios, water-vapour concentrations and initial temperatures. Reductions in laminar burning rate due to the water vapour fraction have been quantified. Furthermore, even for water-vapour concentrations significantly less than the ‘inerting’ limit, increased ignition energy was required to overdrive the flames during the early, highly stretched phase of propagation. This indicates that stretched laminar flames quench at significantly lower water vapour concentrations than for their unstretched counterparts. This conclusion is likely to be significant for studies of water interaction with turbulent flames, which are highly stretched by definition.
- Studies of the influence of fine mono-disperse water mists (<25 $\mu$ m) on propagating laminar methane-air flames showed slightly enhanced burning rate reductions to those observed for the equivalent water-vapour mixtures. Moreover, higher overdrive energies were required to initiate the water mist

propagation compared with the water vapour, indicating that stretched flames are likely to be more susceptible to quenching by water mist than water vapour.

- The conclusions of the laminar studies have been demonstrated within a turbulent environment. A dispersed barrier (1.6 cm<sup>3</sup> total water injected) of fine (25µm) water mist was introduced ahead of a propagating, stoichiometric turbulent methane/air flame, which propagated at about 12-13 m/s due to obstacle-induced turbulence before the mist. Particular turbulent flames completely quenched upon encountering the water-mist section. Estimates of the air-borne fraction of 'active' water mist, taking into account reasonable estimates for loss mechanisms such as impingement, indicate indeed that the molar concentration is likely to have been about 20%, less than the established 'inerting' limit of 25% for water vapour, and hence consistent with the conclusions from the laminar studies.
- Finally, the possibility of rapidly providing very large quantities of fine mist through the thermodynamic method of superheated or 'flash' atomisation has been appraised utilising a broad range of diagnostic techniques, including laser-based particle size and velocity measurements, water rainout, and mist residency within a confined space using multiple impact slides. All techniques indicate that sufficient quantities of 'fine' mist (about 50% by volume) is generated by the superheated methodology demonstrating that this technology is a very strong candidate as a successful, practical system for explosion inerting, quenching of suppression.

## 9.2 Further Work

This study has illustrated that there is considerable scope for water to be used as an explosion suppressant, however for this to be fully appraised a number of further studies would be of use to supplement these findings.

- The laminar studies have demonstrated the effectiveness of water in the form of vapour and ‘fine’ mists. This data is particularly informative during early flame formation during the high curvature/stretch regime and is currently being used to validate computer models. However, a number of subtle changes to the Cardiff cloud chamber would allow for a better data set to be achieved. The internal volume of the chamber should be maximised to allow more data to be attained before pressure effects take control. Also a higher filming rate would afford more crucial information for the calculation of flame speed.
- A comprehensive ignition study should be implemented within the Cardiff cloud chamber to determine the exact volumes of water necessary to quench a propagating flame or inert a combustible mixture. Also this would provide more valuable data for the investigation of flame stretch particularly in methane-water-air mixtures.
- Currently only methane-air flames have been appraised. However, for water based alternatives to be fully implemented in the replacement of current Halon based systems, other fuels such as propane and hydrogen should be investigated thus ensuring water is a genuine contender for Halon replacement.
- The demonstration in a turbulent environment proved water is capable of being used for the quenching of a propagating turbulent flame. This data set was limited thus further work should be conducted to determine the exact volumes of water required to ‘quench’ a range of turbulent flames, and comparable studies should be undertaken using Halon 1301 so as direct comparisons of the two suppressants may be drawn.

- A fundamental weakness in all studies concerning the use of water in the forms of droplets and vapour is the measurement of exact water loading, at present it is possible to fully characterise the droplet fraction and to a lesser extent the vapour fraction, however to accurately characterise both in-situ at present is problematic. Therefore a system capable of defining water vapour concentration, water droplet concentration and water droplet size distribution on a real time basis should be designed.
- Finally, further work should be centred on large-scale systems capable of generating water mists capable of inerting a flammable cloud and suppressing a propagating turbulent flame. The systems produced should be comprehensively trialled to ensure they are highly efficient, thus ensuring their effect on the environment is as limited as possible. The final systems should be tested in large-scale explosion tests to ensure there are no scaling problems which may lead to their failure in actual applications.

## References

- [1] **Pitblado, R. and Turney, R.**, Risk Assessment in the Process Industries, *second edition, IChem<sup>E</sup>, Warwickshire (1996)*
- [2] **Bimson, S.J., Bull, D.C., Cresswell, T.M., Marks, P.R., Masters, A.P., Prothero, A., Puttock, J.S., Rowson, J.J. and Samuels, B.**, *4<sup>th</sup> International Colloquium on the Dynamics of Explosions and Reactive Systems*, August 1<sup>st</sup> - 6<sup>th</sup>, Coimbra, Portugal, (1993).
- [3] **Health and Safety Executive**, 'The Flixborough Disaster : Report of the Court of Inquiry', *HMSO, ISBN 0113610750, (1975).*
- [4] **The Hon. Lord Cullen.**, The Public Enquiry into the Piper Alpha Disaster, (*The Cullen Report*) in 2 volumes, *HMSO (1990).*
- [5] **Gann, R., G.**, Annual Report 'Next Generation Fire Suppression Technology Program (NGP)' NIST FY (2001)
- [6] **Nolan, M.**, Regulations on Halon '*Halon Phase Out Conference*' London (2000)
- [7] **Grosshandler, W. L., Gann, R. G., and Pitts, W. M.**, Evaluation of Alternative In Flight Suppressants for Full-Scale Testing in Aircraft Engine Nacelles and Dry Bays, *NIST SP-861, (1994)*
- [8] **Platt, U. and Honninger, G.**, The role of Halogen species in the troposphere *Chemosphere 52 pp325-338 (2003)*
- [9] **Powell, R., L.**, CFC phase-out: have we met the challenge? *Journal of fluorine chemistry 114 pp237-250 (2002)*
- [10] **Thomas, G., O.**, On the conditions required for explosion mitigation by water sprays, *IChemE, 78(B) pp 339-354 (2000)*
- [11] **HSE Source**, <http://www.ukooa.co.uk/issues/PiperAlpha-> Accessed-18/03/2003
- [12] **Tam, V., H., Y.**, Discussion on proposed safety systems, *Private communication, (2004)*

- [13] **Acton, M., R., Sutton, P. and Wickens, M., J.**, An investigation of the mitigation of gas cloud explosions by water sprays, *Piper Alpha- Lessons Learned for Life-cycle Safety Management Symposium, London, Sept 26-27 (IChemE)*122 pp166-173 (1990)
- [14] **Bowen, P., J.**, Large-scale appraisal of water sprays for explosion suppression, *Private communication* (2003)
- [15] **Gerstein, M., Carlson, E., R. and Hill, F., U.**, Natural gas-air explosions at reduced pressure: detonation velocities and pressures. *Ind. Eng. Chem.* **46(12)** pp2558 (1954)
- [16] **Fells, I. and Rutherford, A., G.**, Burning Velocity of Methane-Air Flames, *Combust. Flame*, **13** pp130-138 (1969)
- [17] **Carlson, L., W., Knight, R., M. and Henrie, J., O.**, Flame and detonation initiation and propagation in various hydrogen-air mixtures with and without water spray. *Internal Report, Atomics International Division, Rockwell International.* (1973)
- [18] **Lieberman, A., Richmond, J., K. and Grumer, J.**, Proc. 16<sup>th</sup> Int. Conf. On Coal Mine Safety Research, Washington, DC, September 22-26<sup>th</sup> (1975)
- [19] **Eggleston, L., Herrera, W., R. and Pish M., D.**, Water spray to reduce vapour cloud spray, *Loss Prevention* **10** pp31 (1976)
- [20] **Richards, R., C. and Sheehan, D.**, Explosion suppression systems for marine applications, 8<sup>th</sup> Annual Offshore Technology Conference, Houston Texas paper N<sup>o</sup>: OTC 2561 may 3-6<sup>th</sup> (1976)
- [21] **Sapko, M., J., Furno, A., L. and Kuchta, J., M.**, Quenching methane-air ignitions with water sprays, *Bureau of Mines Report of Investigations 8214, US Dept. of Interior* (1977)
- [22] **Zalosh, R., G. and Bajpai, S., N.**, Water fog inerting of hydrogen-air mixtures. *Proc 2<sup>nd</sup> Int. Conf. On the Impact of Hydrogen on Water Reactor Safety*, 709 (1982)

- [23] **Lutz, A., E., Marx, K., D. and Dwyer, H., A.** A model of flame interactions with water droplets, *AIAA 2<sup>nd</sup> Aerospace Sciences Meeting, Reno Nevada, Jan 9-12<sup>th</sup> (1984)*
- [24] **Pilch, M. and Erdman, C., A.** Use of break-up time data and velocity history data to predict the maximum size of stable fragment for acceleration – induced break-up of a liquid drop, *International Journal of Multiphase Flow* **13(6)** pp741-757 (1987)
- [25] **Thomas, G., O., Edwards, M., J. and Edwards, D., H.** Studies of detonation quenching by water sprays, *Combust. Sci. and Tech.*, **71** pp 233-245 (1990)
- [26] **Bjerketvedt, D. and Bjorkhaug, M.** Experimental Investigation: Effect of water sprays on gas explosions, *Report prepared by the Christian Michelson Institute, Uk Dept. of Energy HMSO: OTH90 316 (1991)*
- [27] **Thomas, G., O., Jones, A. and Edwards, M., J.** Influence of water sprays on explosion development in fuel-air mixtures, *Combust. Sci. and Tech.* **80** pp47-61 (1991)
- [28] **Jones, A. and Thomas, G., O.** The mitigation of small-scale hydrocarbon-air explosions by water sprays, *Trans IChemE*, **70(A)** pp 197-199 (1992)
- [29] **Ewan, B., C., R. and Swithenbank, J.** The study of fluid injection for the mitigation of gaseous explosions, *Internal Report Dept. of Mechanical and Process Engineering, University of Sheffield (1992)*
- [30] **Jones, A. and Thomas, G., O.** The action of water sprays on fires and explosions: A review of experimental work, *Trans. IChemE*, **71(B)** pp 41-49 (1993)
- [31] **Catlin, C., A., Gregory, C., A., J., Johnson, D., M. and Walker, D., G.** Explosion mitigation in offshore modules by general area deluge. *Trans. IChemE*, **71(B)** pp 101-111 (1993)

- [32] **Health and Safety Executive**, Feasibility study of practical gas explosion/suppression system for offshore installations, *Report prepared by Chubb Fire Engineering and British Gas PLC, Offshore Technology Report – OTO 92 016 (1993)*
- [33] **Brenton, J., R., Thomas, G., O. and Al-Hassan, T.**, Small-scale studies of water spray dynamics during explosion mitigation tests, *European Advances in Process Safety, UMIST Manchester, Apr 19-21 (1994)*
- [34] **Jones, and Nolan**, Discussions on the use of fine water sprays or mists for fire suppression, *J. Loss Prev. Process Ind.*, **8** pp17-22 (1995)
- [35] **van Wingerden, K. and Wilkins B.**, The influence of water sprays on gas explosions. Part 1: water-spray-generated turbulence, *J. Loss Prev. Process Ind.*, **8:2** pp 53-59 (1995)
- [36] **van Wingerden, K., Wilkins B., Bakken, J. and Pedersen, G.**, The influence of water sprays on gas explosions. Part 2: mitigation, *J. Loss Prev. Process Ind.*, **8:2** pp 61-70 (1995)
- [37] **Moore, P., E.**, Suppressants for the control of industrial explosions, *J. Loss Prev. Process Ind.* **9:1** pp 119-123 (1996)
- [38] **Zheng, R., Bray, K., N., C. and Rogg, B.**, Effect of sprays of water and NaCl-water solution on the extinction of laminar premixed methane-air counter-flow flames, *Comb. Sci. Tech.* **126** pp 389-401 (1997)
- [39] **Lentati, A., M, and Chelliah, H., K.**, Dynamics of water droplets in a counterflow field and their effect on flame extinction, *Combustion and Flame* **115** pp 158-179 (1998)
- [40] **Grant, G., Brenton, J. and Drysdale, D.**, Fire suppression by water spray, *Prog. Energy Comb. Sci.* **26** pp 29-130 (2000)
- [41] **Lazzarrini, A., K., Krauss, R., H. and Chelliah, H., K.**, Extinction conditions of non-premixed flames with fine droplets of water and water/NaOH solutions, *Proc. Comb. Institute*, **28** pp 2939-2945 (2000)

- [42] **Fuss, S., P., Dye, D., J., Williams, B., A. and Fleming, J., W.**, Inhibition of premixed methane-air flames by submicron water mists, *Proc. HOTWC, Albuquerque, NM. (2000)*
- [43] **Mesli, B. and Gökalp, I.**, Optimisation of water mist efficiency for the extinction of turbulent premixed flames, *Proc. ILASS, Zurich, 2-6 September (2001)*
- [44] **Shimizu, S., Tsuzuki, M., Yamazaki, Y. and Hayashi, A., K.**, Experiments and numerical simulation on methane flame quenching by water mist, *J. Loss Prev. Process Ind. 14 pp 603-608 (2001)*
- [45] **Catlin, C.**, Passive explosion suppression by blast-induced atomisation from water containers, *J. Hazardous Materials, 94(A) pp 103-132 (2002)*
- [46] **Thomas, G., O.**, The quenching of laminar methane-air flames by water mists, *Combustion and Flame 130 pp 147-160 (2002)*
- [47] **Yang, W. and Kee, R., J.**, The effect of monodispersed water mists on the structure, burning velocity, and extinction behaviour of freely propagating, stoichiometric, premixed, methane-air flames, *Combustion and Flame 130 pp 322-335 (2002)*
- [48] **Fuss, S., P., Chen, E., F., Yang, W., Kee, R., J., Williams, B., A. and Fleming, J., W.**, Inhibition of premixed methane/air flames by water mist, *Proc. Comb. Institute, 29 pp 361-365 (2002)*
- [49] **Chelliah, H., K., Lazzarini, A., K., Wanigarathne, P., C. and Linteris, G., T.**, Inhibition of premixed and non-premixed flames with fine droplets of water and solutions, *Proc. Comb. Institute, 29 pp 369-376 (2002)*
- [50] **Swithenbank, J., Beer, J., M., Taylor, D., S., Abbot, D. and McCreath, G., C.** A Laser Diagnostic Technique for the Measurement of Particle and Droplet Size Distribution, *AIAA pp76-99 (1976)*
- [51] **Trotman, A.**, Diffraction Training Course Notes Malvern Instruments (1999)

- [52] **Durst, F. and Zare, M.**, Laser-Doppler Measurements in Two-Phase Flows. *Proceedings of the LDA-Symposium, Copenhagen, pp 403-429 (1975)*
- [53] **Bates, C., J., and Ayob, R.**; Annular two-phase flow measurements using phase Doppler anemometry with scattering angles of  $30^{\circ}$  and  $70^{\circ}$ ; *Flow Measurement and Instrumentation. 6:1, pp.21-28 (1995)*
- [54] **May, K., R.**, The measurement of Airborne Droplets by the Magnesium Oxide Method *Journ. Sci. Instr.* **27** pp 128-130 (1949)
- [55] **Yeomans, A., H.**, Directions for Determining Particle Size of Aerosols and Fine Sprays *US Dept. of Agriculture Bureau of Entomology and Plant Quarantine ET-267 (1949)*
- [56] **DalaValle, J., H.**, Micrometrics *New York (1943)*
- [57] **Dept. of Scientific and Industrial Research**, Schlieren Methods, *Notes on applied science 31, H.M.S.O. (1963)*
- [58] **Nac-1000 Operating Manual**, *Nac (1990)*
- [59] **National Instruments Catalogue**, *National Instruments (2000)*
- [60] **Wilson C., T., R.**, Condensation of water vapour in the presence of dust-free air and other gases, *Proc. Royal Soc. pp 265-307 (1897)*
- [61] **Cameron, L., R., J.**, Aerosol Explosion Hazard Quantification, *PhD Thesis, University of Wales, Cardiff, December (1999)*
- [62] **Cameron, L., R., J. and Bowen, P., J.**, Novel Cloud Chamber Design for 'Transition Range' Aerosol Combustion Studies, *Trans. IChemE. 79 pp197-205 (2001)*
- [63] **Hayashi, S. and Kumagai, S.**, Flame propagation in droplet-vapour-air mixtures, *Fifteenth (International) Symposium on Combustion, (1974)*
- [64] **Hayashi, S. and Kumagai, S.**, Flame structure of Droplet-Vapour-Air Mixtures, *Archiwum Termodynamiki i Spalania, 6, pp. 479 (1975).*

- [65] **Hayashi, S., Kumagai, S. and Sakai, T.**, Propagation Velocity and Structure of flames in Droplet-Vapour-Air mixtures, *Combust. Sci. Tech.*, **15** pp 169-177 (1976)
- [66] **Kwon, S-I., Arai, M., and Hiroyasu, H.** Effects of Cylinder Temperature and Pressure on Ignition Delay in Direct Injection Diesel Engine, *J.MESJ.* **18** pp 3-16 (1990)
- [67] **Brinkworth, B., J. and Hughes, T., D., R.**, Accelerated response of thermopile pyrometers, *J. Solar Energy*, **18** pp 403-404 (1976)
- [68] **Poling, Prausnitz, O'Connel.** The Properties of gases and liquids. *5th ed., App.A, McGraw-Hill, New York, (2001)*
- [69] **Perry's Chemical Engineers' Handbook, McGraw-Hill.**
- [70] **Crayford, A., P., Bowen, P., J., Coughlin, A., Kwon, S., I., Tizzano, G. and Griffiths, A., J.** Characterisation of a Mist through Cloud Chamber Technology, *Proceedings of ICLASS 12<sup>th</sup>-17<sup>th</sup> July, Sorrento, (2003)*
- [71] **Dreizler, A., Lindenmaier, S., Maas, U., Hult, J., Alden, M. and Kaminski C., F.**, Characterisation of a spark ignition system by planar laser-induced fluorescence of OH at high repetition rates and comparison with kinetic calculations, *Appl. Phys. B* **70** pp. 287-294 (2000)
- [72] **Andrews, G., E. and Bradley, D.**, Determination of burning velocities: A critical review, *Combustion and Flame*, **18** pp. 133-153 (1972)
- [73] **Rallis, C., J. and Garforth, A., M.**, The determination of laminar burning velocity, *Prog. Energy Comb.*, **6** pp. 303-329 (1980)
- [74] **Linnett, J.**, Methods of measuring burning velocities, *Fourth (Int.) Symp. Combust.* pp. 20-35 (1953)
- [75] **Eschenbach, R., C. and Agnew, J., T.**, Use of the constant-volume bomb technique for measuring burning velocity, *Combustion and Flame* **2** pp. 273-285 (1958)

- [76] **Bradley, D. and Hundy G, F**, Burning velocities of methane-air mixtures using hot-wire anemometers in closed vessel explosions, *Thirteenth (Int.) Symp. Combust.* pp. 575-583 (1971)
- [77] **Andrews, G., E. and Bradley, D.**, The burning velocity of methane-air mixtures, *Combustion and Flame* **19** pp. 275-288 (1972)
- [78] **Bradley, D. and Mitcheson, A.**, Mathematical solutions for explosions in spherical vessels, *Combustion and Flame* **26** pp. 201-217 (1976)
- [79] **Garforth, A., M. and Rallis, C., J.**, Laminar burning velocity of stoichiometric methane-air: pressure and temperature dependence, *Combustion and Flame* **31** pp. 53-68 (1978)
- [80] **Agrawal, D., D.**, Experimental determination of burning velocity of methane-air mixtures in a constant volume vessel, *Combustion and Flame* **42** pp. 243-252 (1981)
- [81] **Toshio, I. and Tadao, T.**, Effects of temperature and pressure on burning velocity, *Combustion and Flame* **65** pp. 35-43 (1986)
- [82] **Tseng, L., K., Ismail, M., A. and Faeth, G., M.**, Laminar burning velocities and Markstein numbers of hydrocarbon/air flames, *Combustion and Flame* **95** pp. 410-426 (1993)
- [83] **Taylor, S., C. and Smith, D., B.**, Brief Communication, Comment on "Laminar burning velocities and Markstein numbers of hydrocarbon/air flames" by Tseng, L., K., Ismail, M., A. and Faeth, G., M., *Combustion and Flame* **102** pp. 523-525 (1995)
- [84] **Bradley, D., Gaskell, P., H. and Gu, X., J.**, Burning velocities, Markstein lengths, and flame quenching for spherical methane-air flames: A computational study, *Combustion and Flame* **104** pp. 176-198 (1996)
- [85] **Karpov, V., P., Lipatnikov, A., N. and Wolanski, P.**, Finding the Markstein number using the measurements of expanding spherical laminar flames, *Combustion and Flame* **109** pp. 436-448 (1997)

- [86] **Hassan, M., I., Aung, K., T. and Faeth, G., M.**, Measured and predicted properties of laminar premixed methane/air flames at various pressures, *Combustion and Flame* **115** pp. 539-550 (1998)
- [87] **Gu, X., J., Haq, M., Z., Lawes, M. and Woolley, R.**, Laminar burning velocity and Markstein lengths of methane-air mixtures, *Combustion and Flame* **121** pp. 41-58 (2000)
- [88] **Dahoe, A., E. and de Goey, L., P., H.**, On the laminar burning velocity from closed vessel gas explosions, *Journal Loss Prev.* **16** pp. 457-478 (2003)
- [89] **Mishra, D., P.**, Effects of initial temperature on the structure of laminar CH<sub>4</sub>-air premixed flames, *Fuel*, **82** pp 1471-1475 (2003)
- [90] **Egolfopoulos, F., N., Cho, P. and Law, C., K.**, Laminar flame speeds of methane-air mixtures under reduced and elevated pressures, *Combustion and Flame*, **76** pp375-391 (1989)
- [91] **Stone, R., Clarke, A. and Beckwith, P.**, Correlation for laminar burning velocity of methane/diluent/air mixtures obtained in free-fall experiments, *Combustion and Flame*, **114** pp 546-555 (1998)
- [92] **Bradley, D., Hicks, R., Lawes, M., Sheppard, C., G., W. and Woolley, R.**, The measurement of laminar burning velocities and Markstein numbers for iso-octane-air and iso-octane-n-heptane-air mixtures at elevated temperatures and pressures in an explosion bomb, *Combustion and Flame*, **115** pp126-144 (1998)
- [93] **Kwon, S-I.**, Chemkin Premix model of methane-air-water mixtures, *Private communication*, (2003)
- [94] **Aung, K., T., Tseng, L., K., Ismail, M., A. and Faeth, G., M.**, Response to comment by S.C. Taylor and D.B. Smith on "Laminar Burning Velocities and Markstein Numbers of Hydrocarbon/Air Flames" *Combustion and Flame*, **102** pp 526-530 (1995)
- [95] **Lindstedt, R., P.**, Comparison of experimental data with produced model, *Private communication*, (2003)

- [96] **Taylor, P., H. and Hirst, W., J., S.**, *Proceedings of 22<sup>nd</sup> Symp. Int. Comb.*, (1989)
- [97] **Robinson, J., W.** Undergraduate Instrumental Analysis, *fifth edition Marcel Dekker Inc.*, (1995)
- [98] Melsec Medoc Programming and Documentation System for Melsec PC Systems, *Mitsubishi Electric UK Ltd.* (1991)
- [99] **Parr, E., A.** Programmable Controllers an Engineers Guide, Butterworth-Heinemann Ltd. *2<sup>nd</sup> Edition* (1999)
- [100] **Bolton, W.** Programmable Logic Controllers and Introduction, Butterworth-Heinemann Ltd. (1996)
- [101] **More, N., J.** Suppressing Explosions using Water Mists, Final year Project, Cardiff School of Engineering, Systems Division (2002)
- [102] **Fernandez- Martinez, S.**, Commissioning of Shell Turbulent Duct rig, *Escuela Tecnica Superior de Ingenieros Industrials, Universidad Politecnica de Valencia* (2003)
- [103] **Griffiths, J.F. and Barnard, J.A.**, Flame and Combustion, *Third edition, Published by Blackie Academic & Professional, an imprint of Chapman & Hall, Glasgow*, (1995).
- [104] **Glassman, I.**, Combustion, *Second edition, Academic Press, Orlando*, (1987).
- [105] **Lewis, B and von Elbe, G.**, Combustion Flames and Explosions of Gases, *second edition, Academic press, New York*, (1961).
- [106] **Linstedt, R., P. and Sakhithran, V.**, Time Resolved and Turbulence Measurements in Turbulent Gaseous Explosions, *Combust. Flame*, **114** pp469-483 (1998)
- [107] **Masri, A., R., Ibrahim, S., S., Nehzat, N., and Green, A., R.** Experimental study of premixed flame propagation over various solid obstructions, *Experimental Thermal and Fluid Science*, **21:1-3** pp 109-116 (1995)

- [108] **Marakos, A.**, Combustion Hazard Quantification of Accidental Releases of High- Flashpoint Liquid Fuels , *PhD Thesis, University of Wales, Cardiff, September (2002)*
- [109] **Kay, P.**, Characterisation of direct injection systems. *Private communication (2004)*
- [110] **O'Connell, M.**, Micromist, Fire suppression Agent, *Micromist Ltd. Cork Ireland (2000)*
- [111] **Bowen, P., J. and Witlox H.**, Flashing liquid jets and two-phase dispersion, *Contract Research Report, (2001)*
- [112] **Reitz, R., D.**, A Photographic Study of Flash Boiling Atomisation, *Aerosol Science and Technology. 12 pp561-569 (1990)*
- [113] **Parks, B., S., and Lee, S., Y.**, An Experimental Investigation of the Flash Atomisation Mechanism, *Atomisation and Sprays 4 pp159-179 (1994)*
- [114] **Muralidhar, R., Jersey, G., R., and Krambeck, F., J.**, A Two-Phase Release Model for Quantifying Risk Reduction for Modified HF Alkylation Catalysts, *Journal of Hazardous Materials. 44 pp141-183 (1995)*
- [115] **Cleary, V.**, Development of modelling approaches for large scale superheated fuel jets, *Euroflam Report N° 2910, Cardiff School of Engineering (2002)*
- [116] **Cleary, V., Bowen, P., J. and Maragkos, A.**, Jet Transition and Rainout from Large Superheated Spray Releases, Proceedings of *ICLASS 12<sup>th</sup>-17<sup>th</sup> July Sorrento (2003)*
- [117] **Jones, G., H.**, Assessment of the validity of previous models that have been proposed for rainout fraction in flashing water jets and associated criteria, *Internal Final Year Project, Cardiff School of Engineering (2002)*
- [118] **Ramsdale, S. and Tickle, G.**, Review of RELEASE rainout model and the Centre for Chemical Process Safety (CCPS) data, *HSE/AEA Technology plc., HSE Books. (2000)*

- [119] **Cleary, V.**, Characterisation of Superheated Flashing Jets Using Laser Diffraction Droplet Size Analysis, *Euroflam Report, Cardiff School of Engineering (2002)*
- [120] **DANTEC DYNAMICS**, Principles of PDA Systems, *Educational Lecture Notes*
- [121] **Steel Construction Institute**, The assessment of pressure hot water explosion suppression system, *HSE Book, OTH 93 406, (1993)*
- [122] **Tam, V., H., Y., O'Connell, M., Pederson G. and Renwick, P.**, Testing of the Micromist device: an active soft barrier for explosion control, *J. Loss Prev. Process Ind. 16 pp 81-88 (2003)*
- [123] **Tam, V., H., Y.**, Barrier methods for gas explosion control, *ERA Conference, London, (1999)*
- [124] **DANTEC DYNAMICS**, *Promotional Literature, Dantec website, accessed November (2003)*

## Appendix A: Calculation of Combustion mixtures for Cardiff Cloud Chamber

The mixing methodology may be assumed as shown in Figure A.1, whereby a known volume of fuel at ambient conditions is passed from a gas tight syringe into a fully sealed container of preset volume, temperature and pressure.

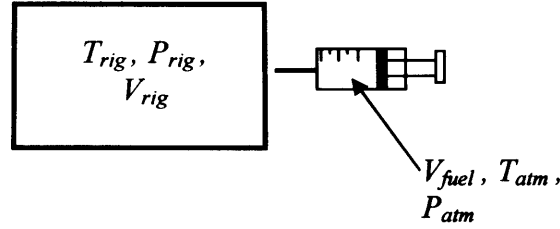


**Figure A.1 Schematic diagram representing pre-mixing conditions of methane and air**

To enable an accurate volume of methane to be calculated for a specified equivalence ratio, it is first necessary to calculate the mass of air and methane required using the following equations.

$$AFR_{actual} = \frac{M_{air}}{M_{fuel}} \quad (A.1)$$

$$ER = \frac{AFR_{stoich}}{AFR_{actual}} \quad (A.2)$$

Thus, re-arranging (5.3),

$$AFR_{actual} = \frac{AFR_{stoich}}{ER} \quad (A.3)$$

By using,

$$M_{air} = \rho_{air} \times V_{air} \quad (A.4a) \quad M_{fuel} = \rho_{fuel} \times V_{fuel} \quad (A.4b)$$

and,

$$\rho_{air} = \frac{P_{rig}}{T_{rig} R_{air}} \quad (A.5a) \quad \rho_{fuel} = \frac{P_{fuel}}{T_{fuel} R_{fuel}} \quad (A.5b)$$

By substituting (A.5) into (A.4),

$$M_{air} = \frac{P_{rig} V_{rig}}{T_{rig} R_{air}} \quad (A.6a) \quad M_{fuel} = \frac{P_{fuel} V_{fuel}}{T_{fuel} R_{fuel}} \quad (A.6b)$$

Substituting (A.6a&b) into (A.1),

$$AFR_{actual} = \frac{\left( \frac{P_{rig} V_{rig}}{T_{rig} R_{air}} \right)}{\left( \frac{P_{fuel} V_{fuel}}{T_{fuel} R_{fuel}} \right)} \Rightarrow AFR_{actual} = \frac{P_{rig} V_{rig} T_{fuel} R_{fuel}}{P_{fuel} V_{fuel} T_{rig} R_{air}} \quad (A.7)$$

Using,

$$R_{air} = \frac{R}{Mr_{air}} \quad (A.8a) \quad R_{fuel} = \frac{R}{Mr_{fuel}} \quad (A.8b)$$

Rearranging (A.7) then substituting into (A.3),

$$V_{fuel} = \frac{(ER) P_{rig} V_{rig} T_{fuel} R_{fuel}}{(AFR_{stoich}) P_{fuel} T_{rig} R_{air}} \quad (A.9)$$

Substituting (A.8a&b) into (A.9)

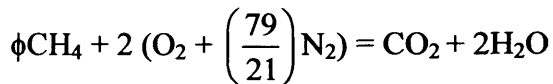
$$V_{fuel} = \frac{(ER) P_{rig} V_{rig} T_{fuel} Mr_{air}}{(AFR_{stoich}) P_{fuel} T_{rig} Mr_{fuel}} \quad (A.10)$$

As can be seen from (A.9) the only unknown variable is the Air-Fuel-Ratio at stoichiometric conditions.

To find the  $AFR_{stoich}$ ,

Let Equivalence Ratio (ER) =  $\phi$

The equation for combustion of Methane is



If all of above are gaseous then 1 mole of methane reacts with 2 moles of oxygen and 2

$\times \left( \frac{79}{21} \right)$  moles of Nitrogen

Calculation of Molar Masses

Combustion side:-

Using Molar Masses            C =12.011  
    H = 1.00794  
    O = 15.9994  
    N = 14.00674

∴ Molar mass Methane            = 12.011 + 4(1.00794)  
    = 16.04276

∴ Molar mass of Air            = 2 × (2(15.9994) + 2 ×  $\left(\frac{79}{21}\right)$  (14.0674)  
    = 2 × (31.9988 + 105.3840438)  
    = 274.7656876

∴ For Equivalence Ratio  $\phi = 1.0$

$$AFR_{stoich} = \frac{Mr_{air}}{Mr_{fuel}} = 17.12708335 \tag{A.11}$$

Finally (A.11) may be substituted into (A.10) to give,

$$V_{fuel} = \frac{(ER)P_{rig} V_{rig} T_{fuel} Mr_{air}}{(17.12708335)P_{fuel} T_{rig} Mr_{fuel}} \tag{A.12}$$

## Appendix B: Flame Growth Methane-Air Flames Dry

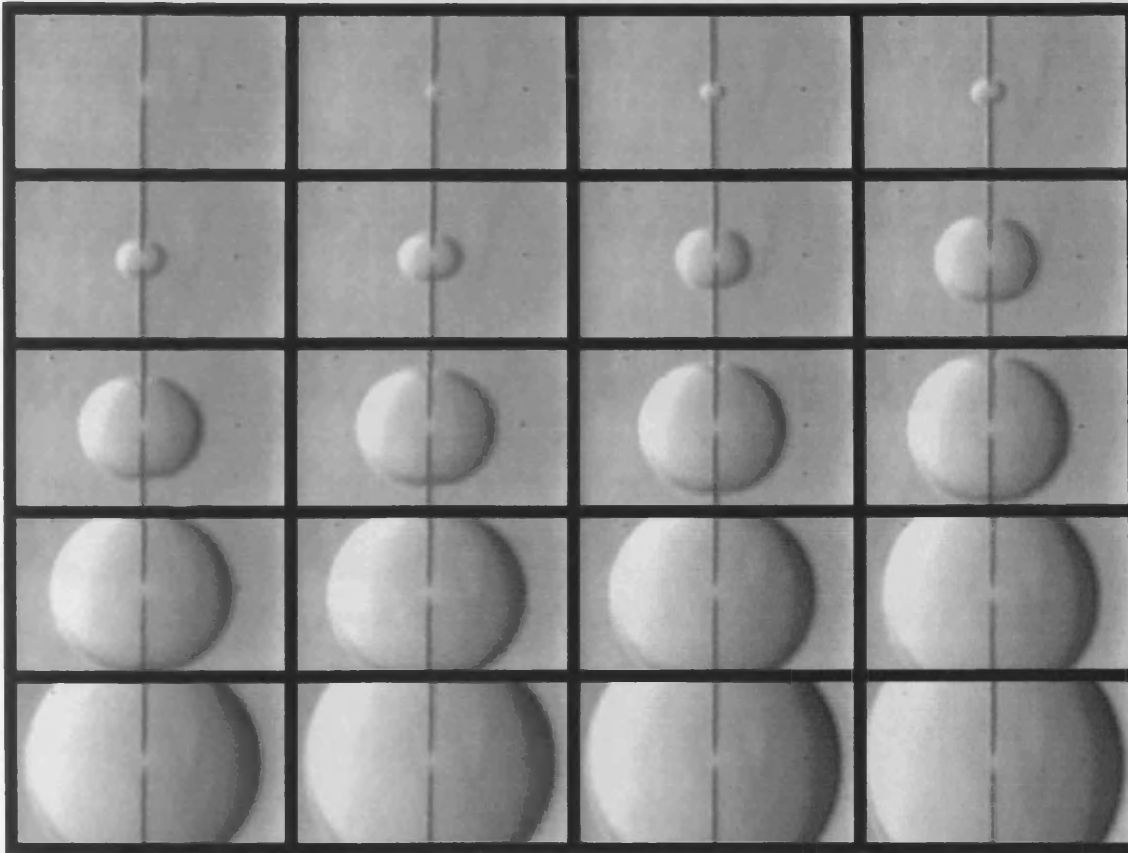


Figure B1.1 *Flame growth of methane-air flame, ER=0.8,  $T_{rig}=50^{\circ}\text{C}$ , water 0%, 1000fps*

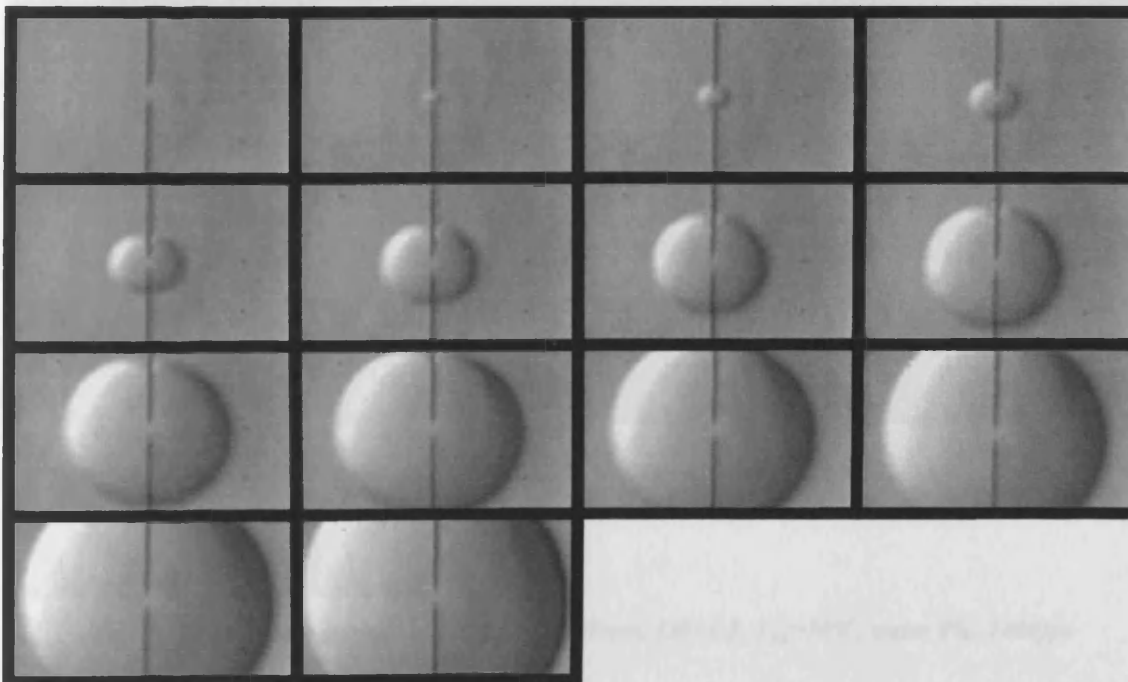
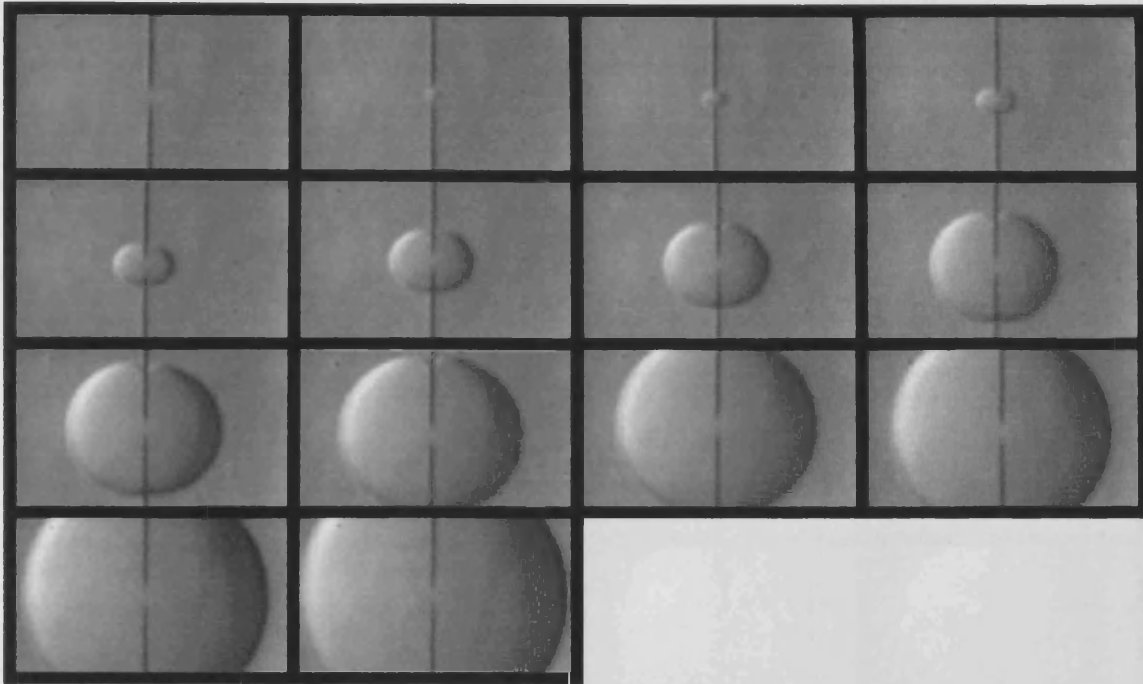
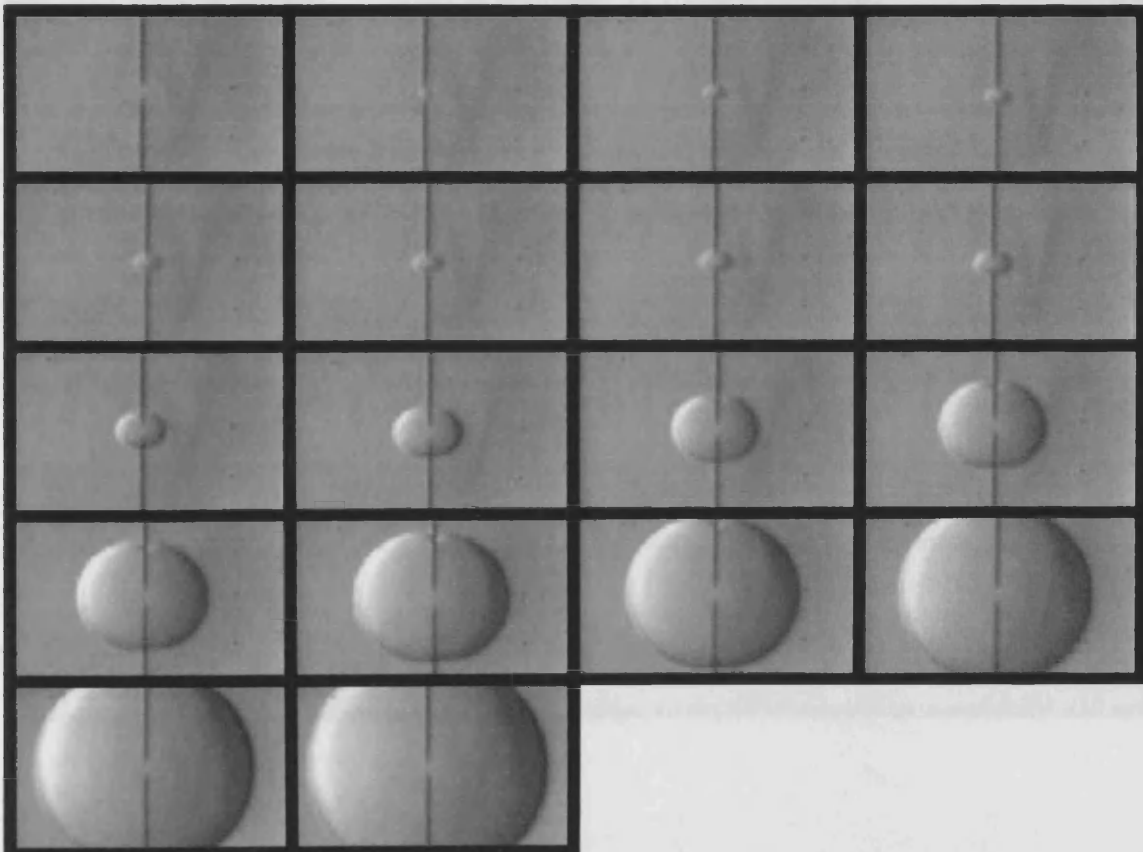


Figure B1.2 *Flame growth of methane-air flame, ER=1.0,  $T_{rig}=50^{\circ}\text{C}$ , water 0%, 1000fps*



**Figure B1.3** Flame growth of methane-air flame,  $ER=1.1$ ,  $T_{rig}=50^{\circ}C$ , water 0%, 1000fps



**Figure B1.4** Flame growth of methane-air flame,  $ER=1.2$ ,  $T_{rig}=50^{\circ}C$ , water 0%, 1000fps

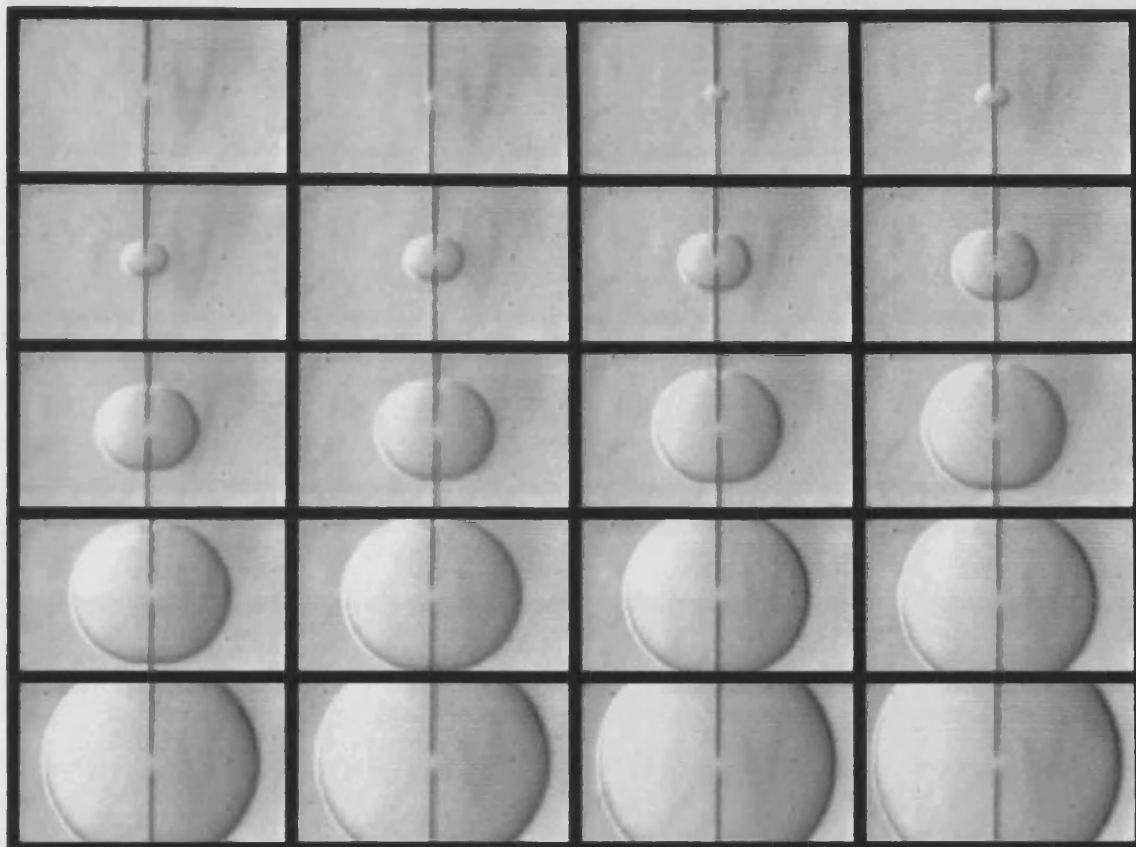


**Figure B2.1** Flame growth of methane-air flame,  $ER=0.8$ ,  $T_{rig}=100^{\circ}C$ , water 0%, 1000fps

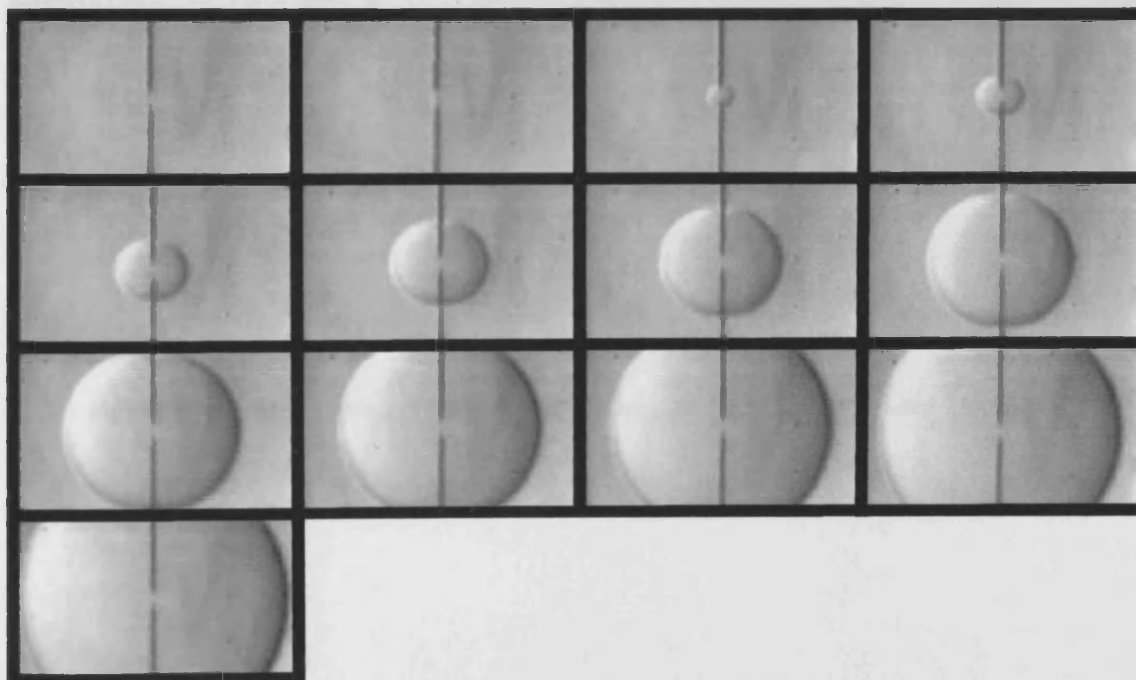


**Figure B2.2** Flame growth of methane-air flame,  $ER=1.0$ ,  $T_{rig}=100^{\circ}C$ , water 0%, 1000fps

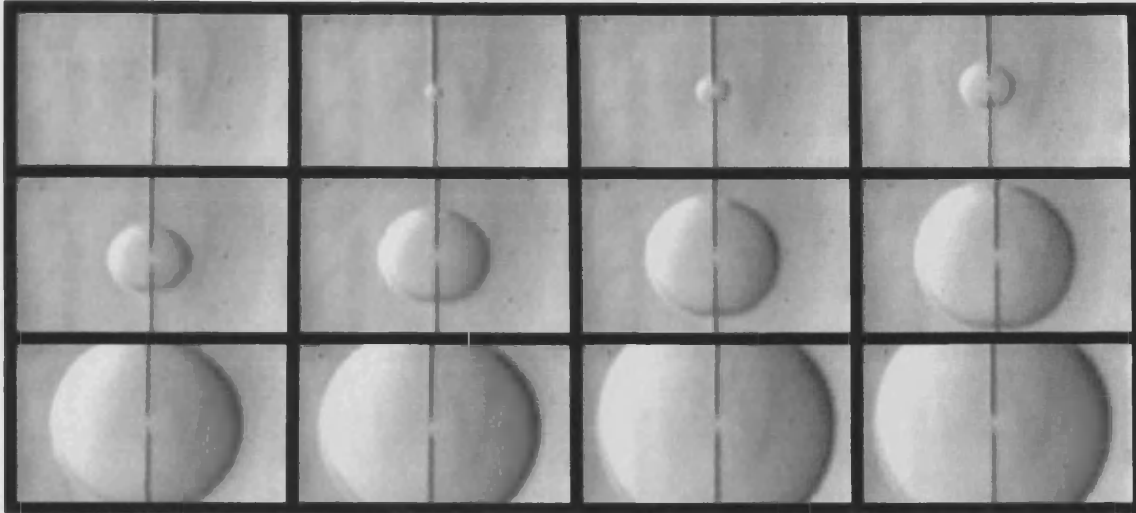


**Figure B2.3** *Flame growth of methane-air flame,  $ER=1.1$ ,  $T_{rig}=100^{\circ}C$ , water 0%, 1000fps*

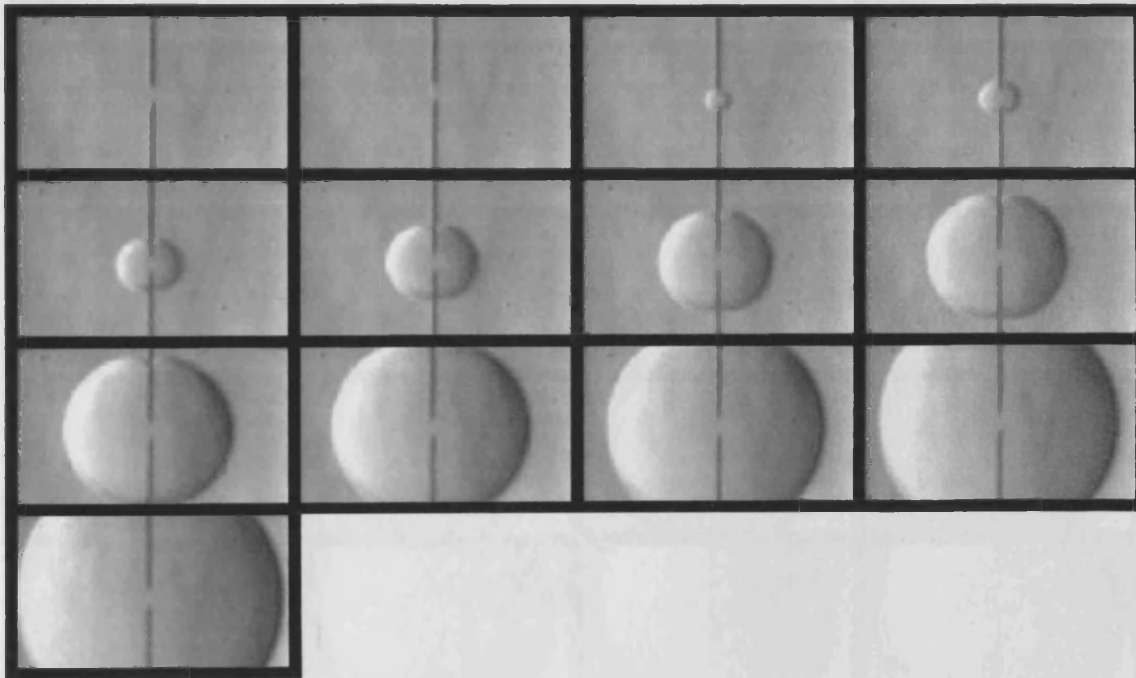


**Figure B2.4** *Flame growth of methane-air flame,  $ER=1.2$ ,  $T_{rig}=100^{\circ}C$ , water 0%, 1000fps*

## Appendix C: Flame Growth Methane-Air-Water Flames Vapour

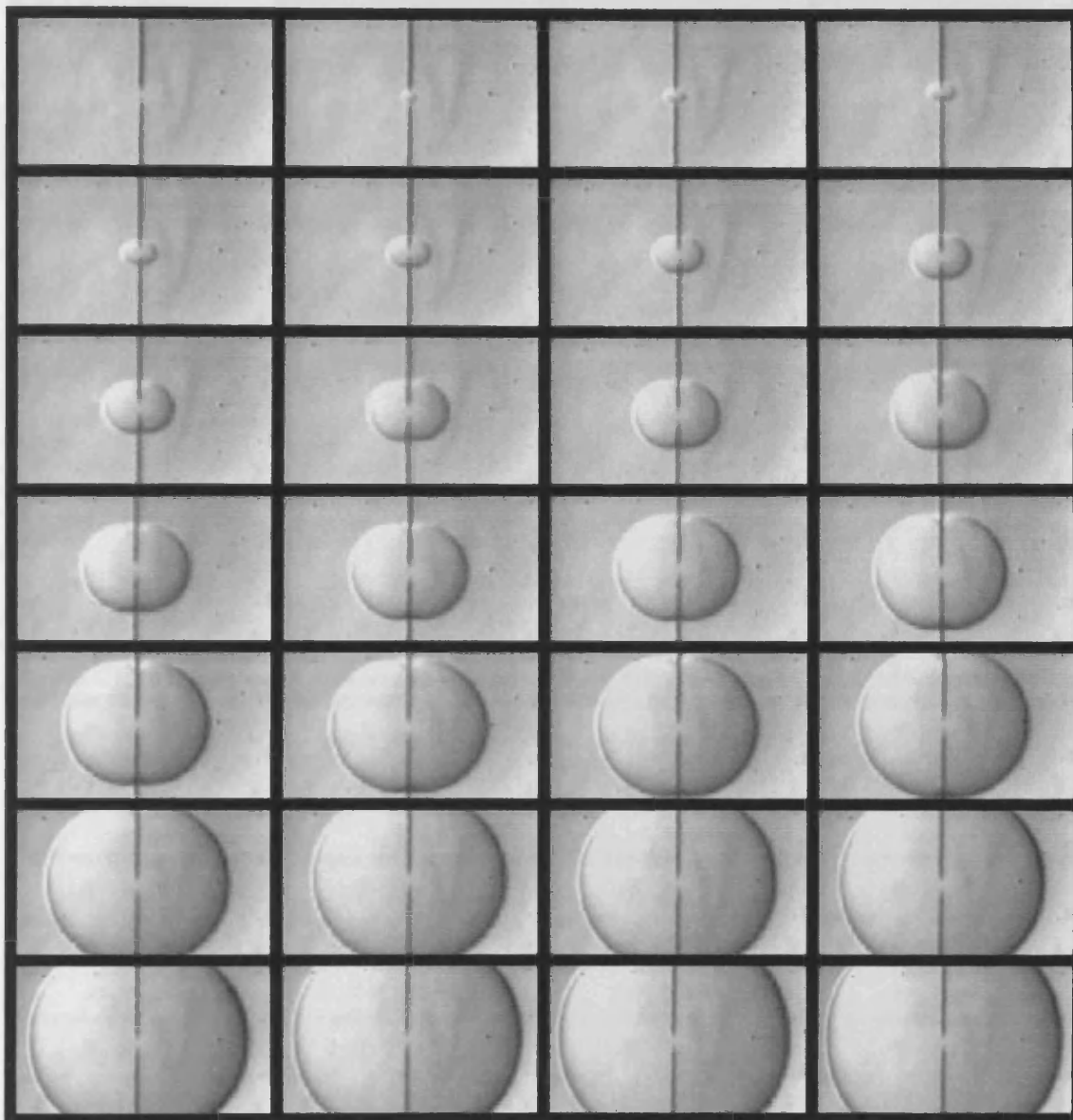


Figure C1.1 Flame growth of methane-water-air flame,  $ER=0.8$ ,  $T_{rig}=50^{\circ}C$ , water 5% vapour, 1000fps

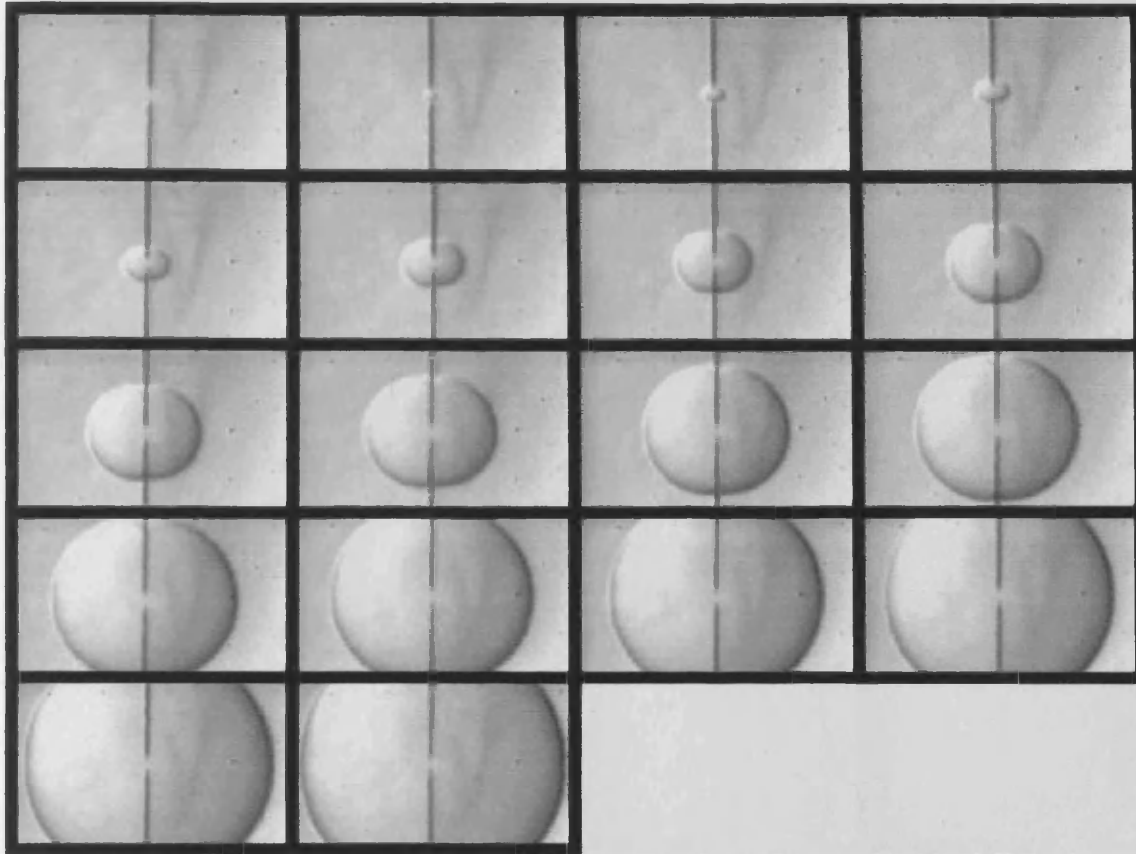


Figure C1.2 Flame growth of methane-water-air flame,  $ER=1.0$ ,  $T_{rig}=50^{\circ}C$ , water 5% vapour, 1000fps

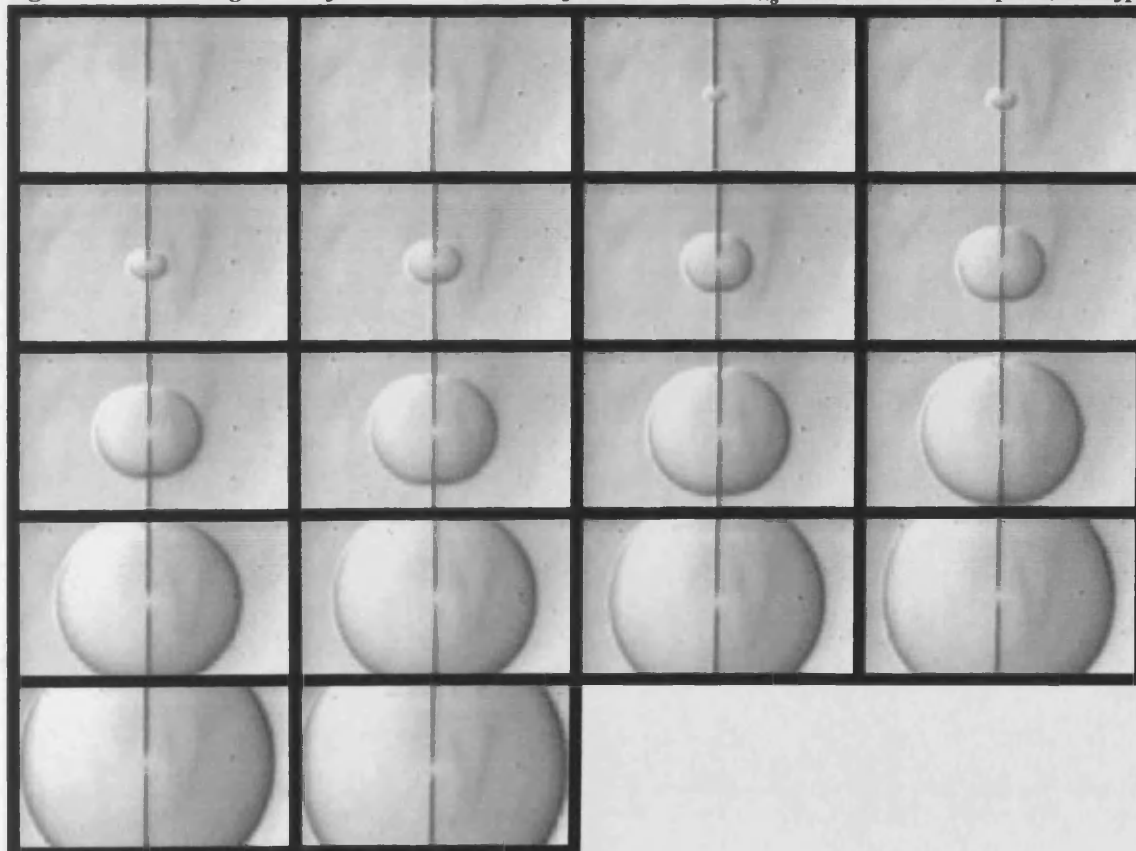
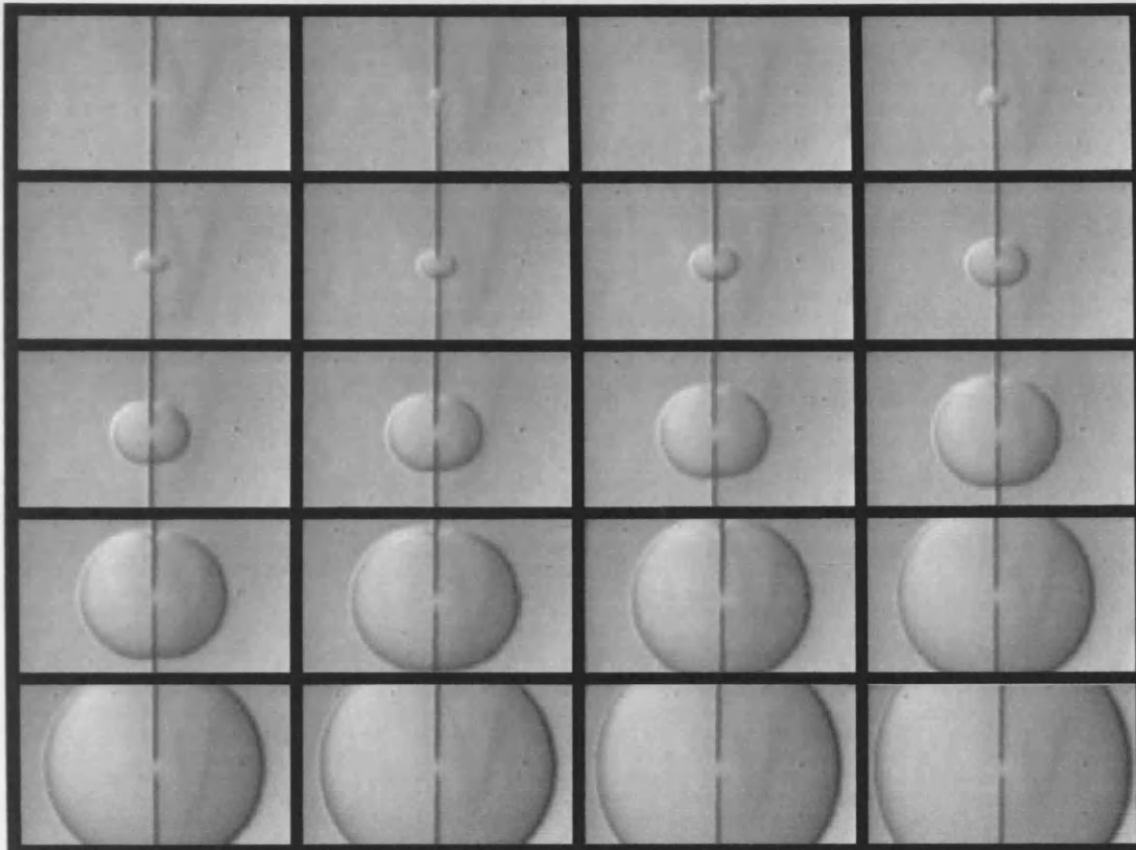
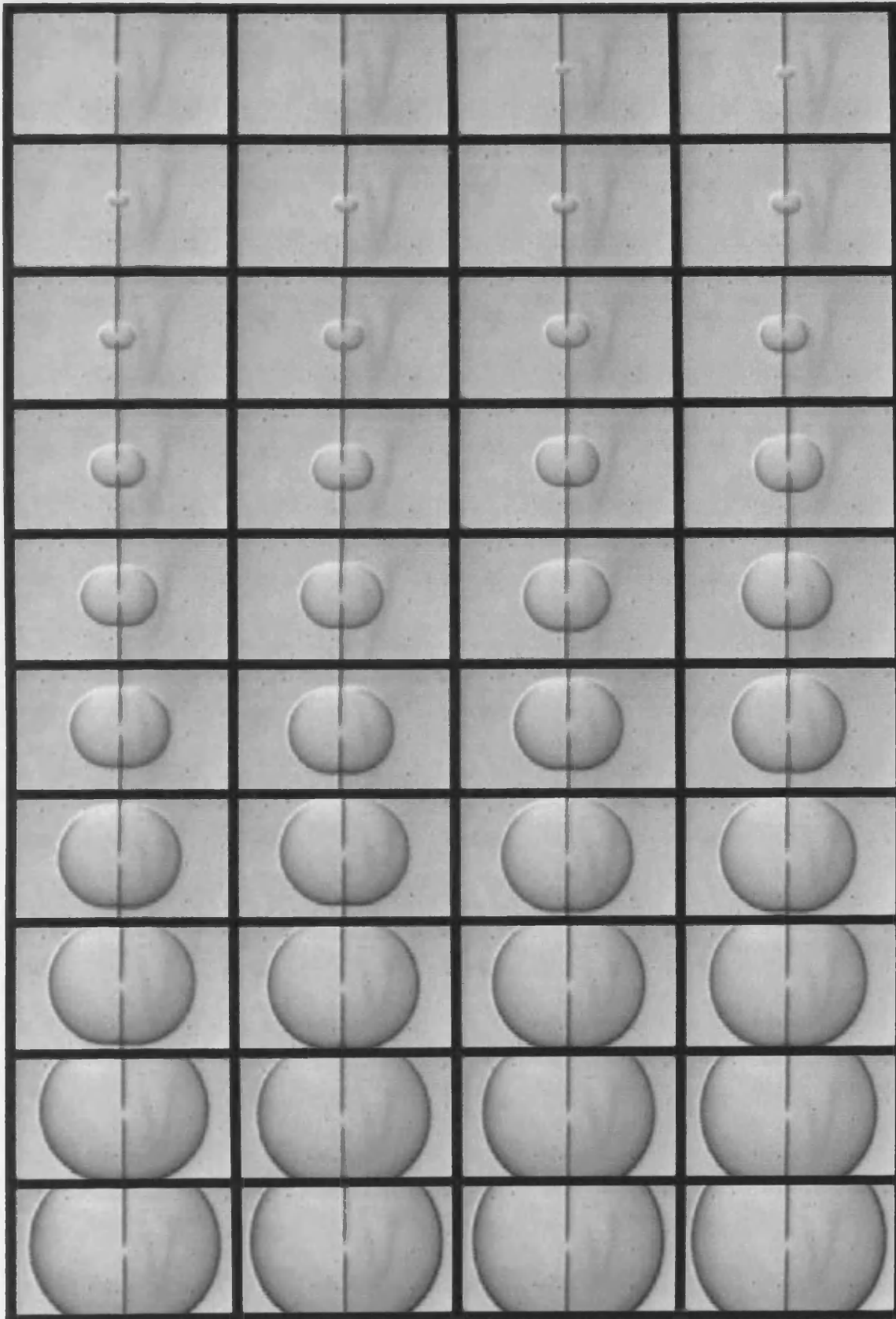


Figure C1.3 Flame growth of methane-water-air flame,  $ER=1.1$ ,  $T_{rig}=50^{\circ}C$ , water 5% vapour, 1000fps



**Figure C1.4** *Flame growth of methane-water-air flame,  $ER=1.2$   $T_{rig}=50^{\circ}C$ , water 5% vapour, 1000fps*



**Figure C2.1** Flame growth of methane-water-air flame,  $ER=0.8$   $T_{rig}=50^{\circ}C$ , water 10% vapour, 1000fps

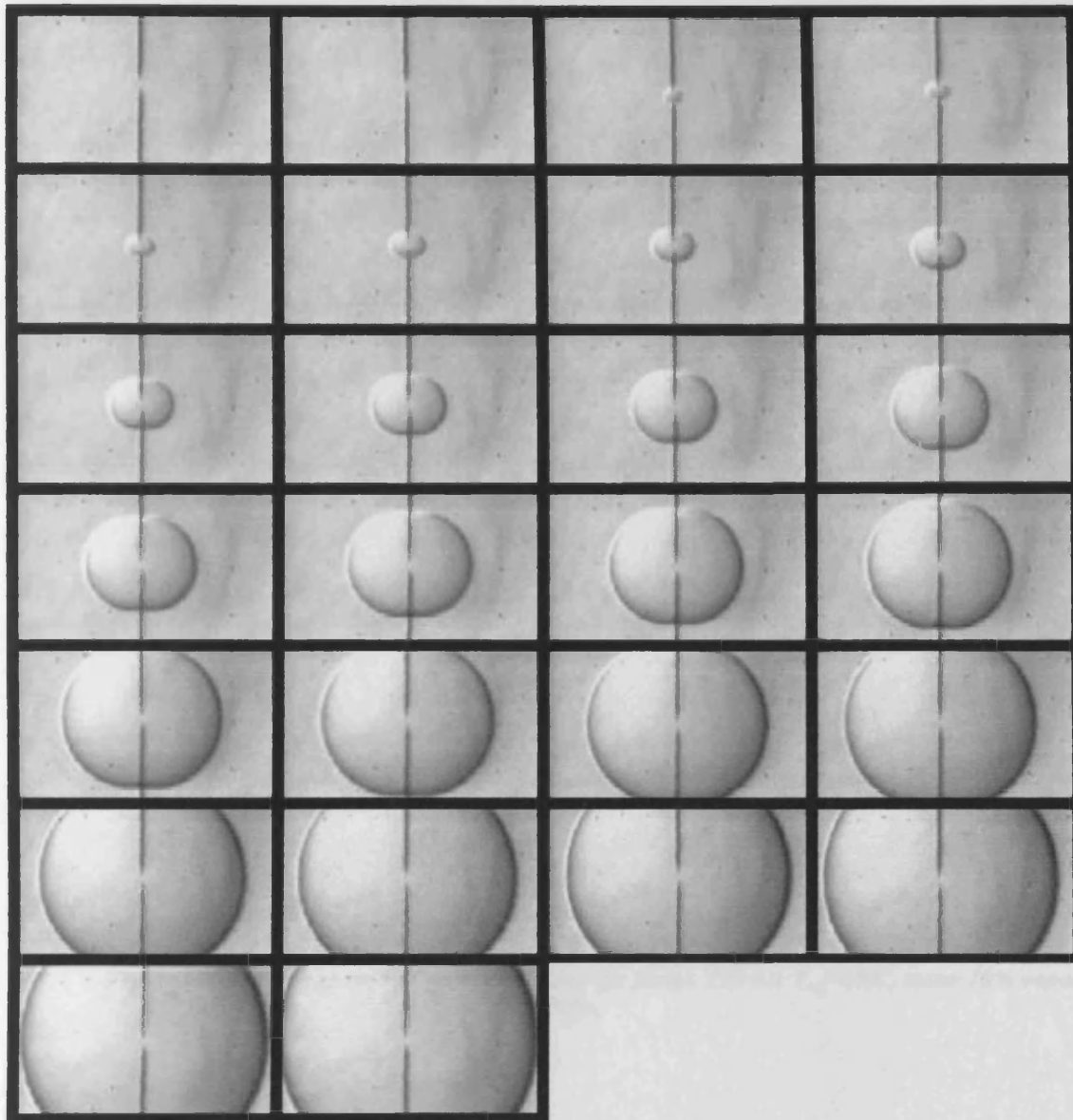


**Figure C2.2** *Flame growth of methane-water-air flame,  $ER=1.0$   $T_{rig}=50^{\circ}C$ , water 10% vapour, 1000fps*

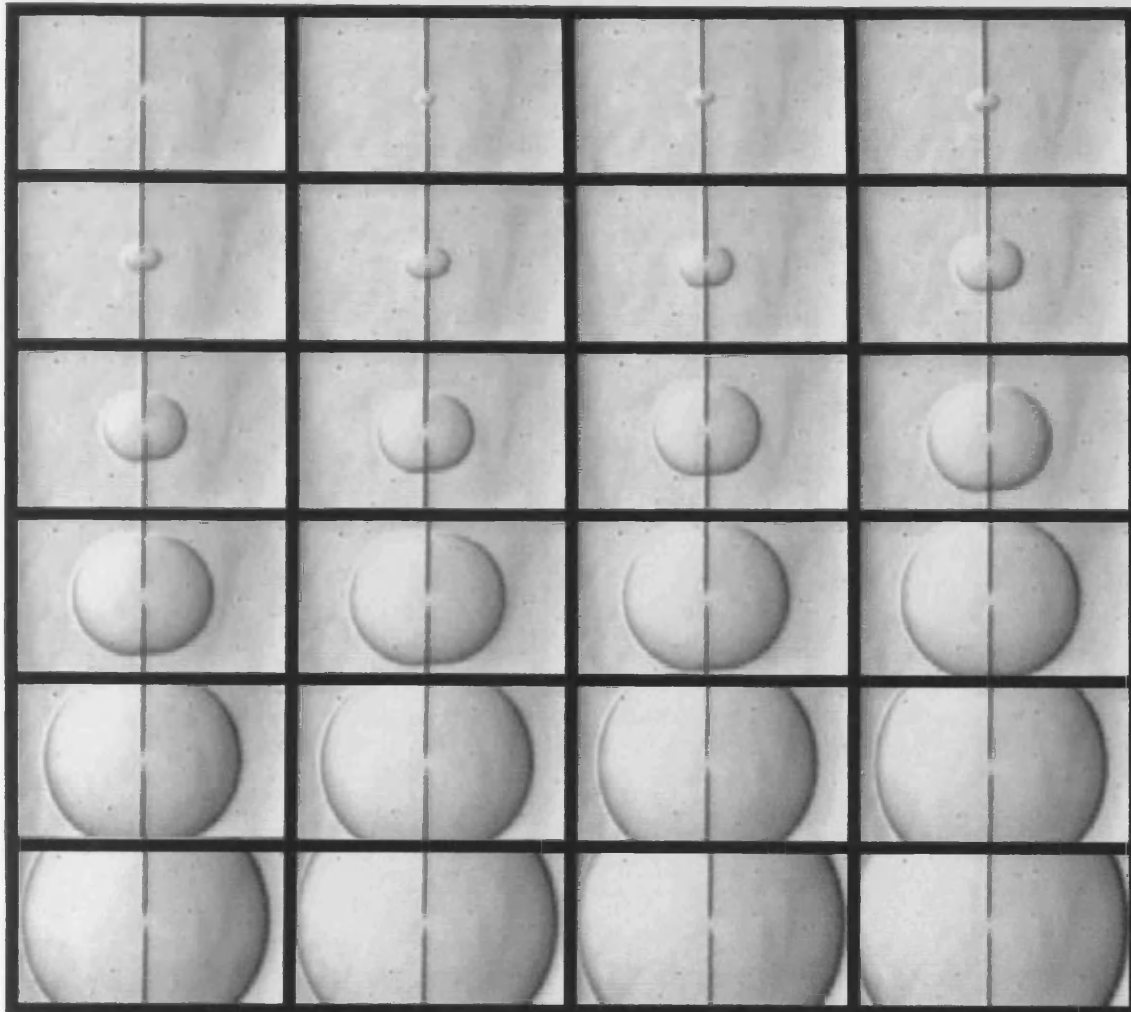


**Figure C2.3** *Flame growth of methane-water-air flame,  $ER=1.1$   $T_{rig}=50^{\circ}C$ , water 10% vapour, 1000fps*

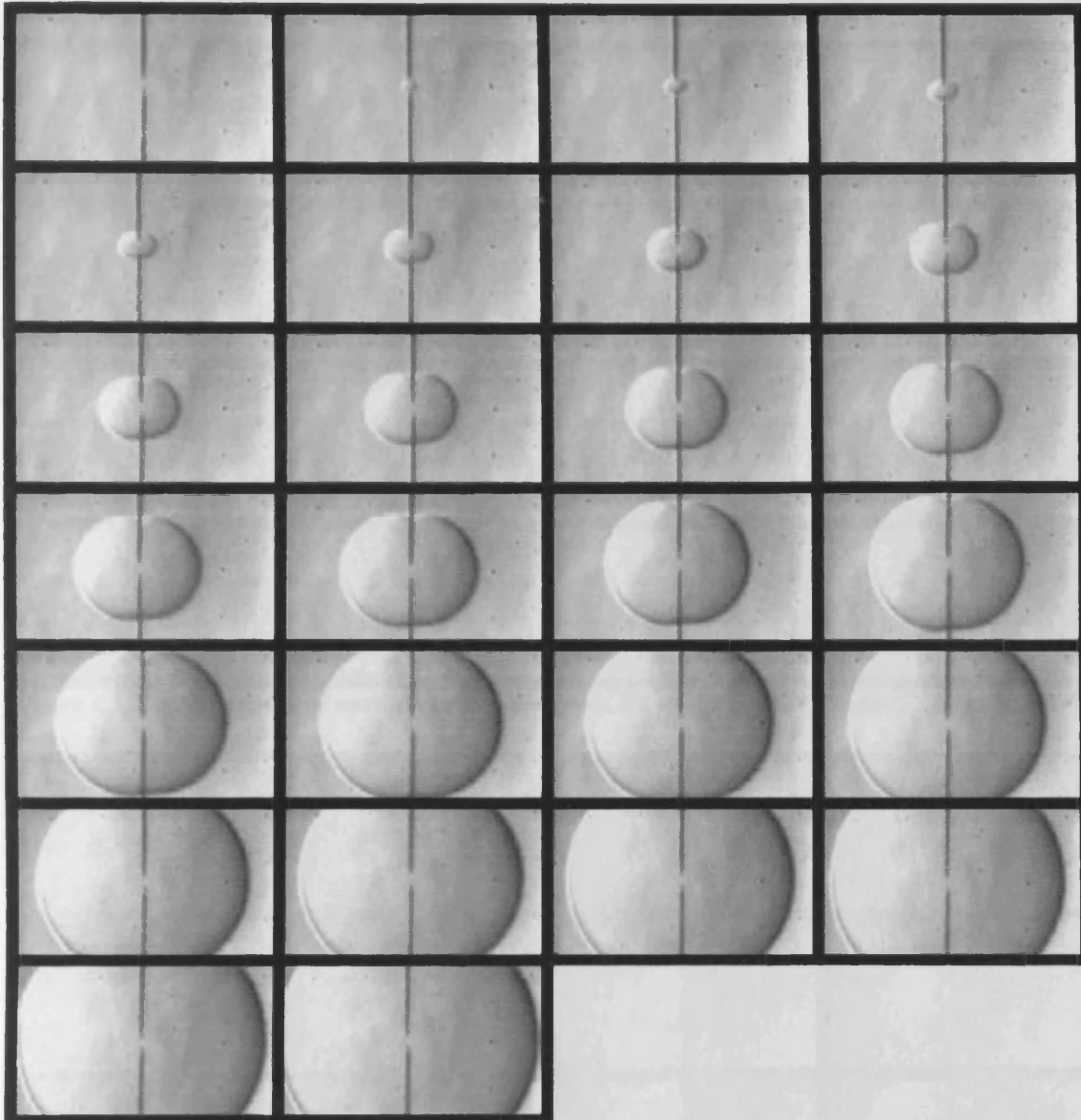


Figure C3.1 *Flame growth of methane-water-air flame,  $ER=0.8$   $T_{rig}=100^{\circ}C$ , water 5% vapour, 1000fps*

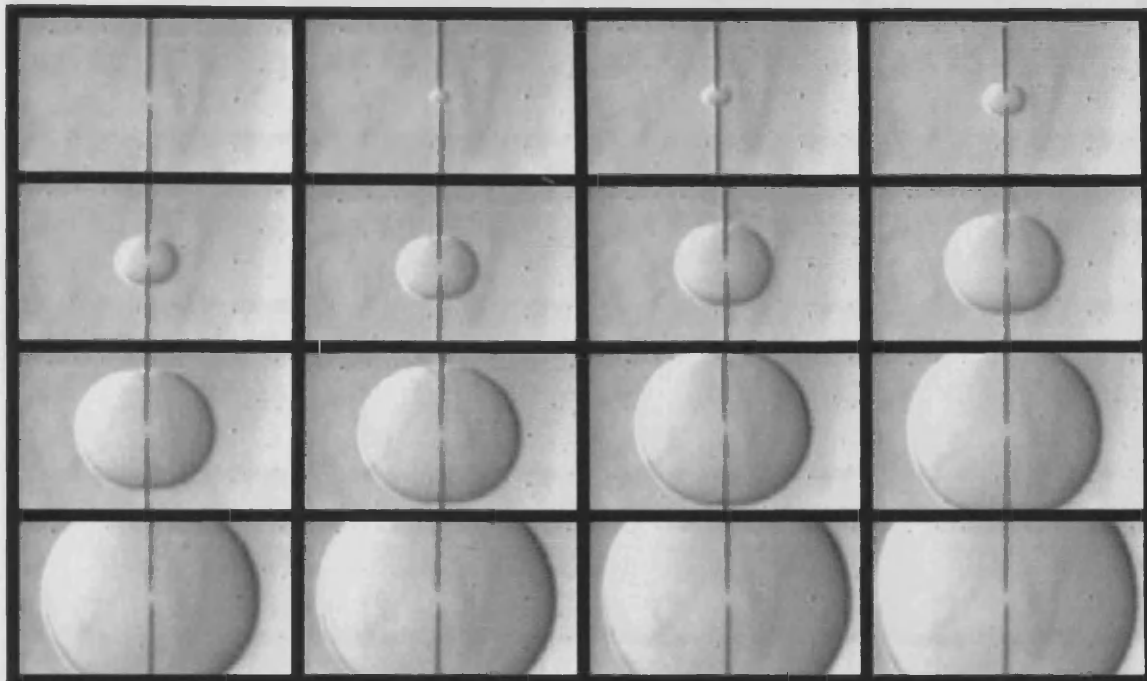


Figure C3.2 Flame growth of methane-water-air flame,  $ER=1.0$   $T_{rig}=100^{\circ}\text{C}$ , water 5% vapour, 1000fps

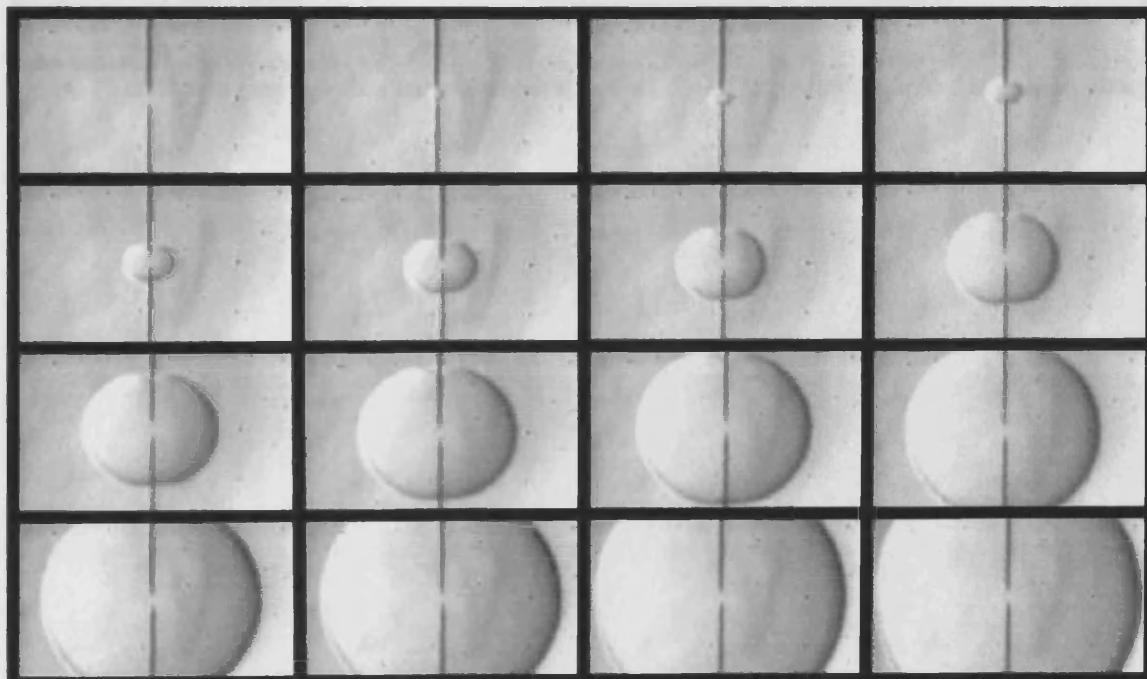


Figure C3.3 Flame growth of methane-water-air flame,  $ER=1.1$   $T_{rig}=100^{\circ}\text{C}$ , water 5% vapour, 1000fps

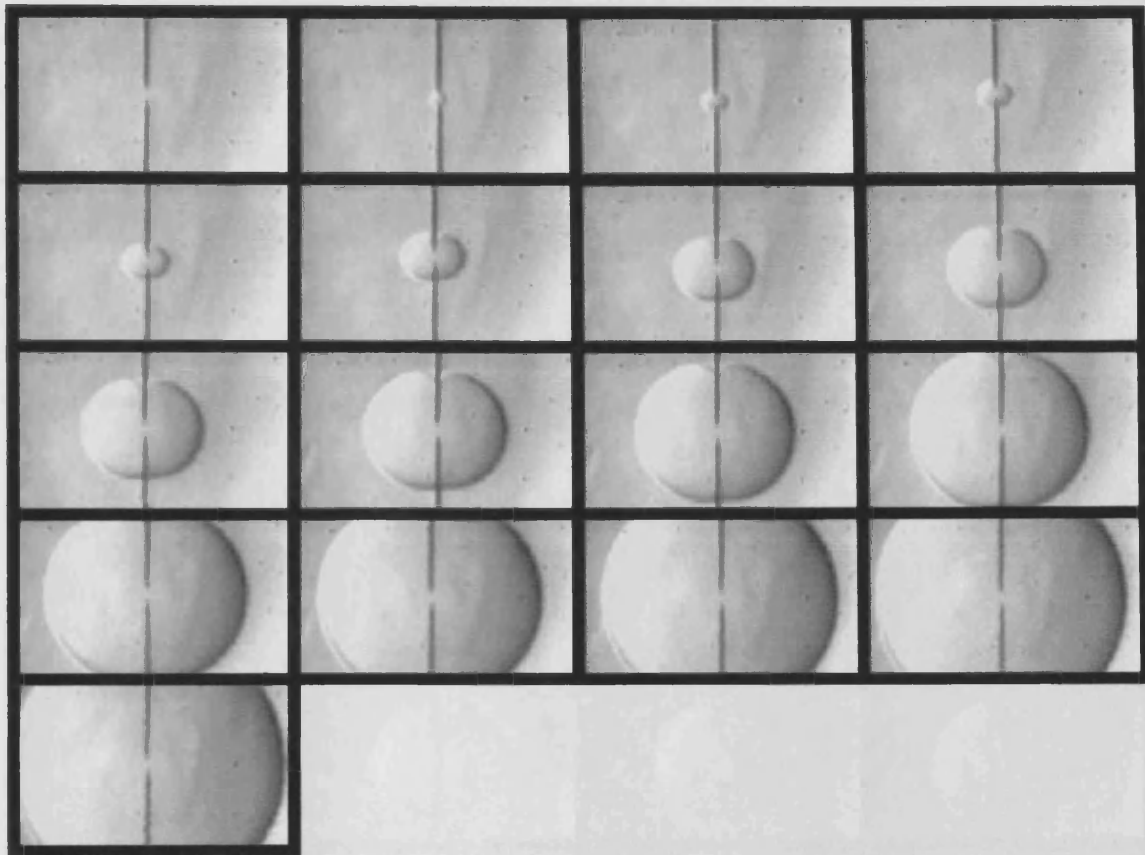
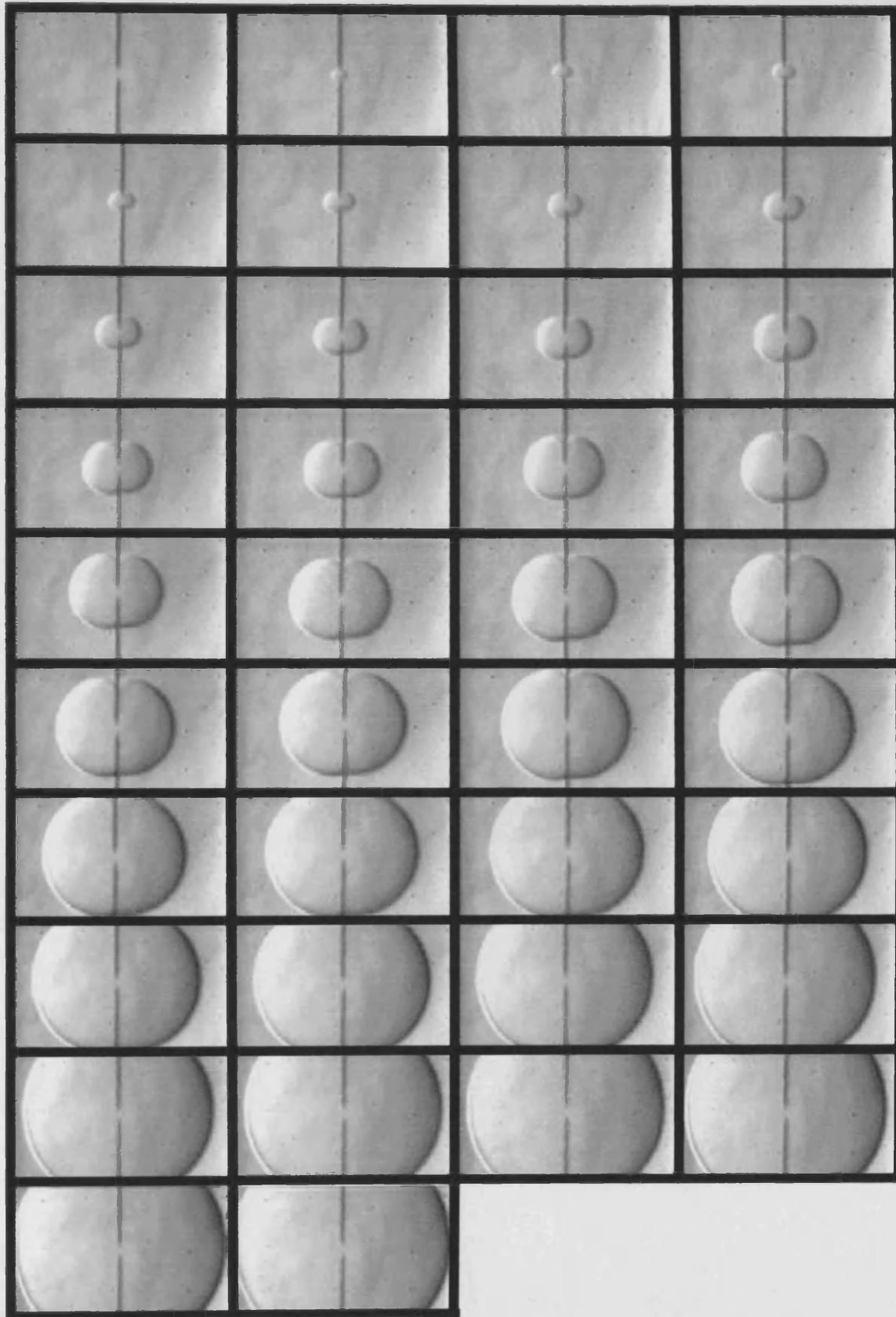
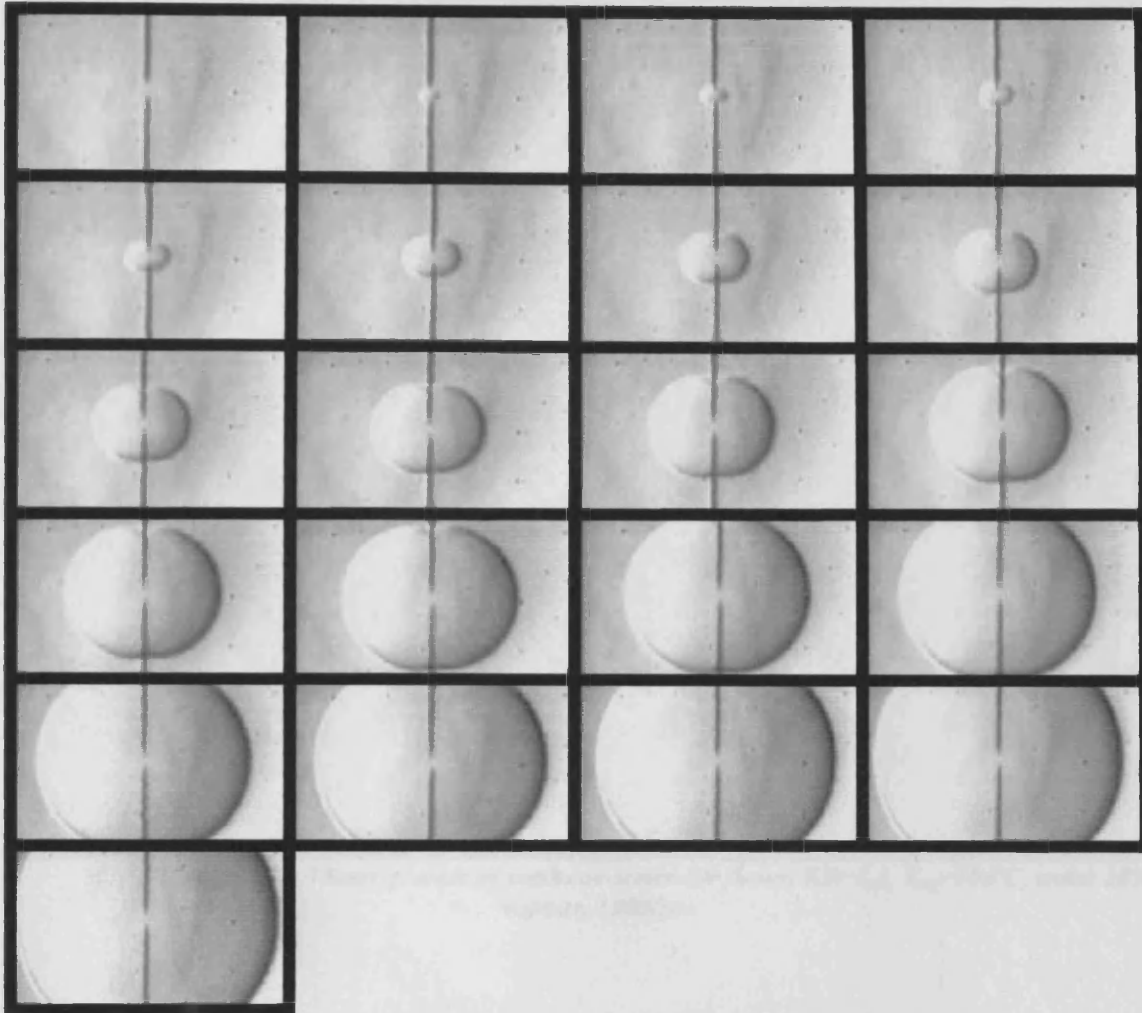


Figure C3.3 Flame growth of methane-water-air flame,  $ER=1.2$ ,  $T_{rig}=100^{\circ}C$ , water 5% vapour, 1000fps



**Figure C4.1** *Flame growth of methane-water-air flame,  $ER=0.8$ ,  $T_{rig}=100^{\circ}\text{C}$ , water 10% vapour, 1000fps*



**Figure C4.2** *Flame growth of methane-water-air flame,  $ER=1.0$ ,  $T_{rig}=100^{\circ}\text{C}$ , water 10% vapour, 1000fps*

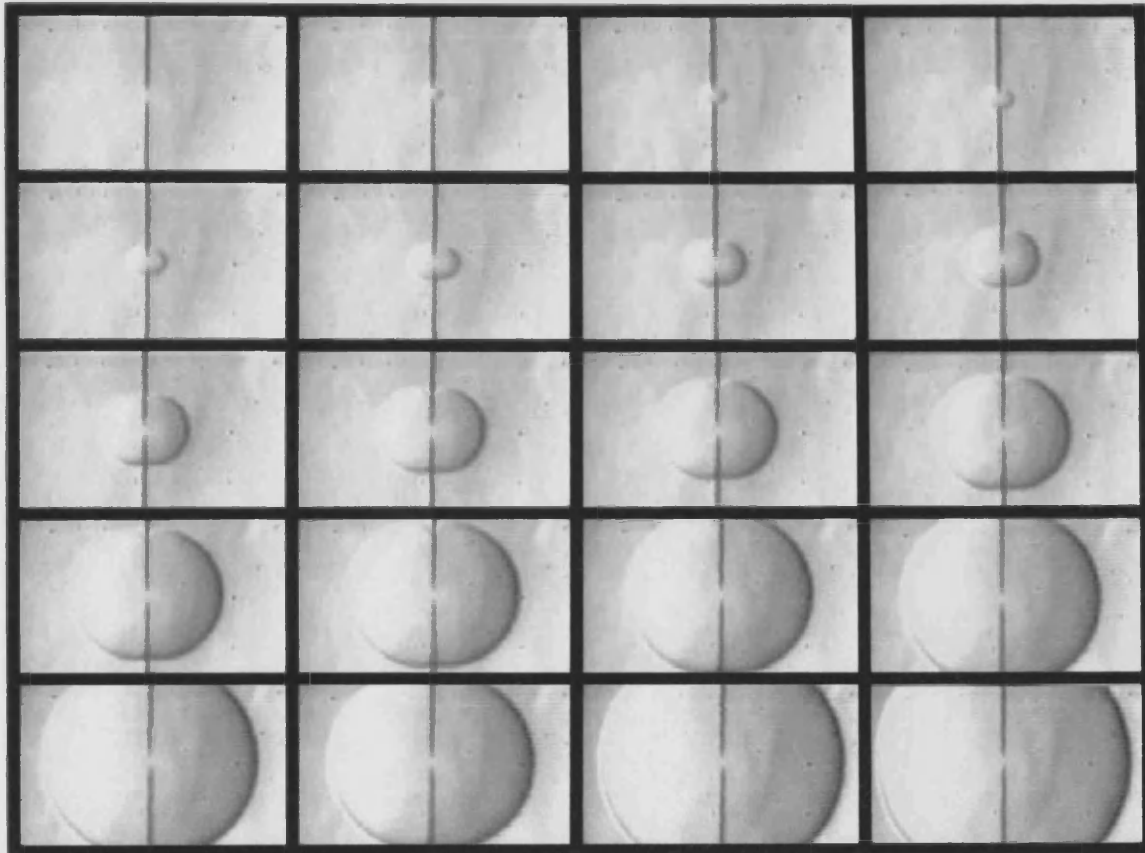


**Figure C4.3** *Flame growth of methane-water-air flame,  $ER=1.1$ ,  $T_{rig}=100^{\circ}\text{C}$ , water 10% vapour, 1000fps*

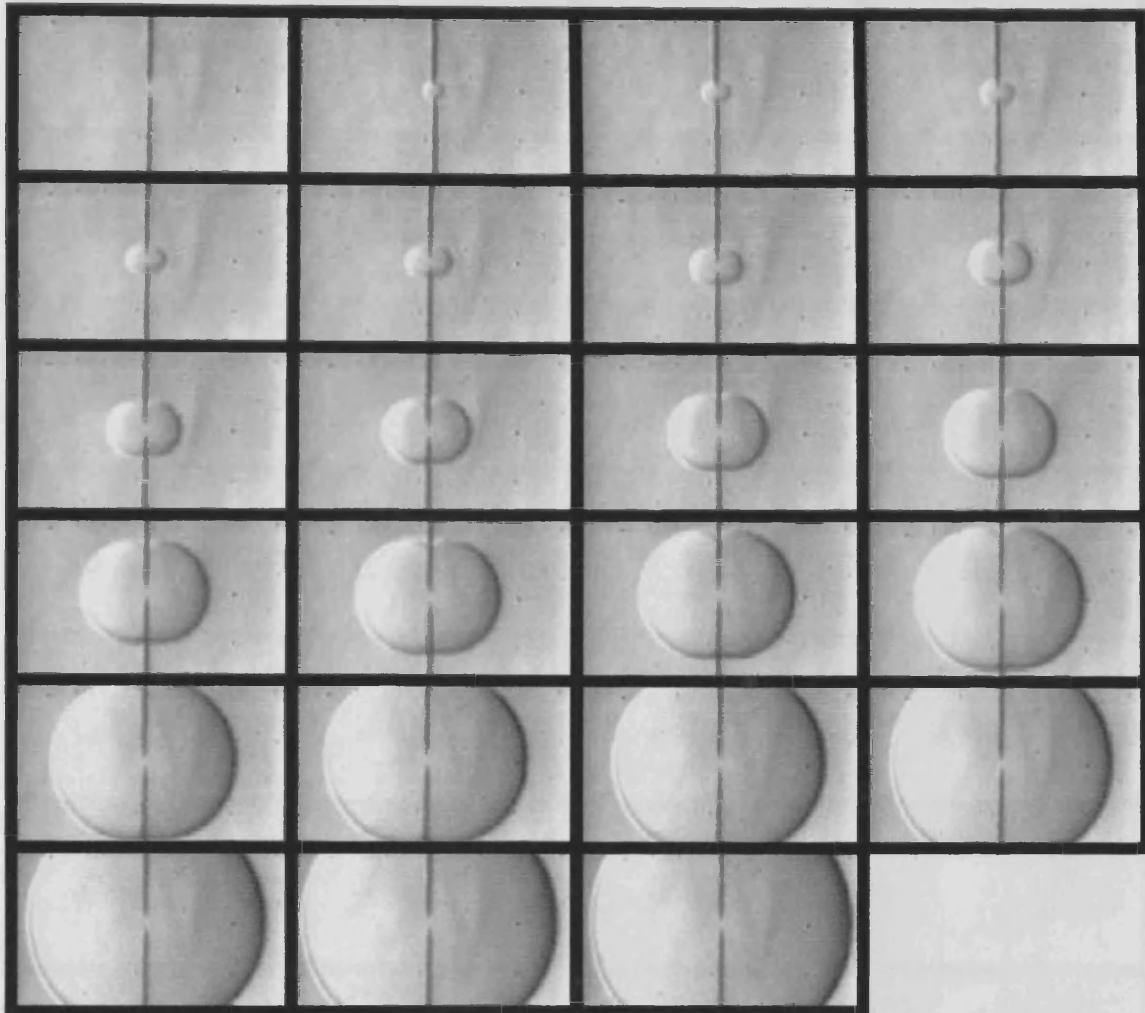


**Figure C4.4** *Flame growth of methane-water-air flame,  $ER=1.2$ ,  $T_{rig}=100^{\circ}C$ , water 10% vapour, 1000fps*

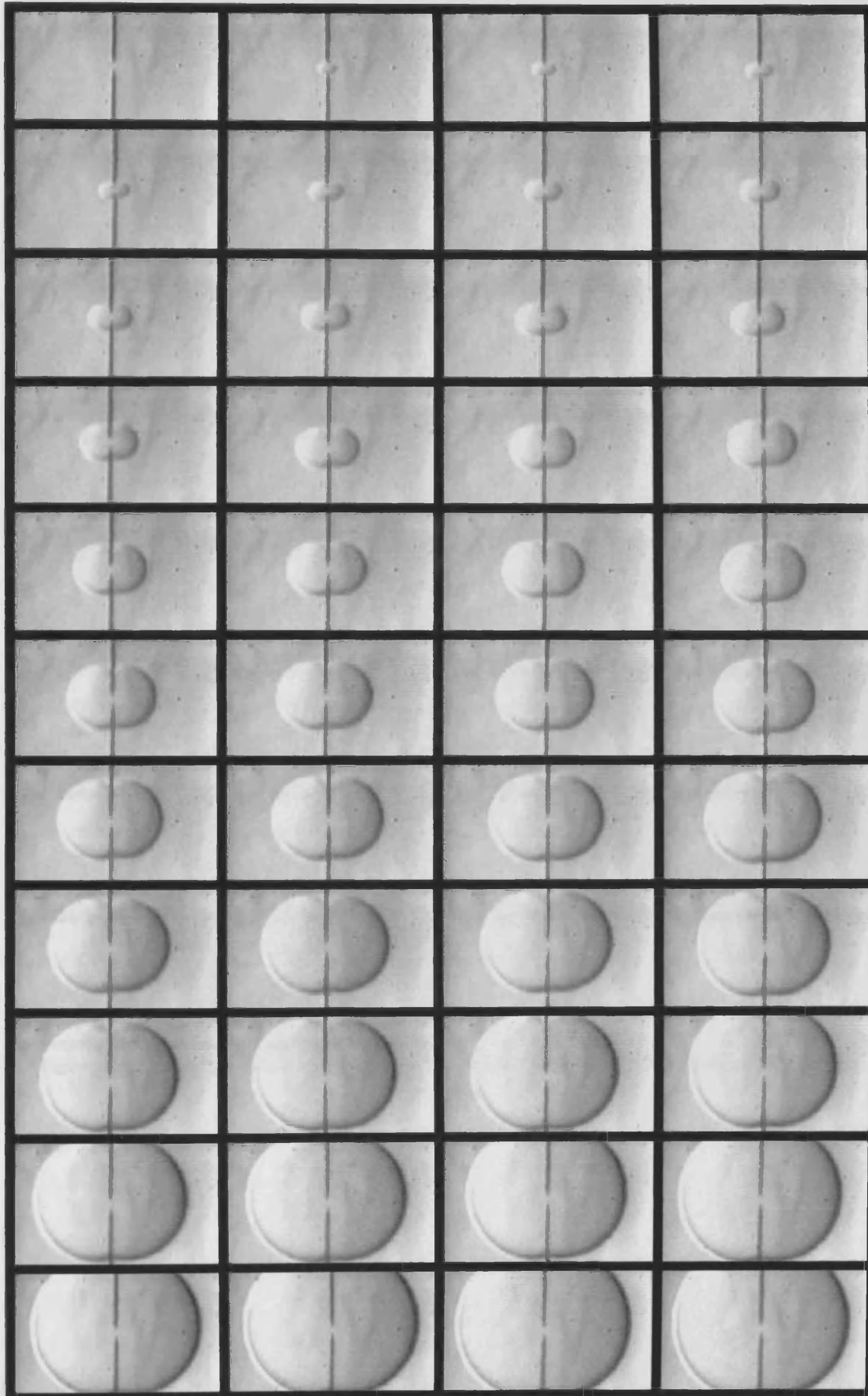
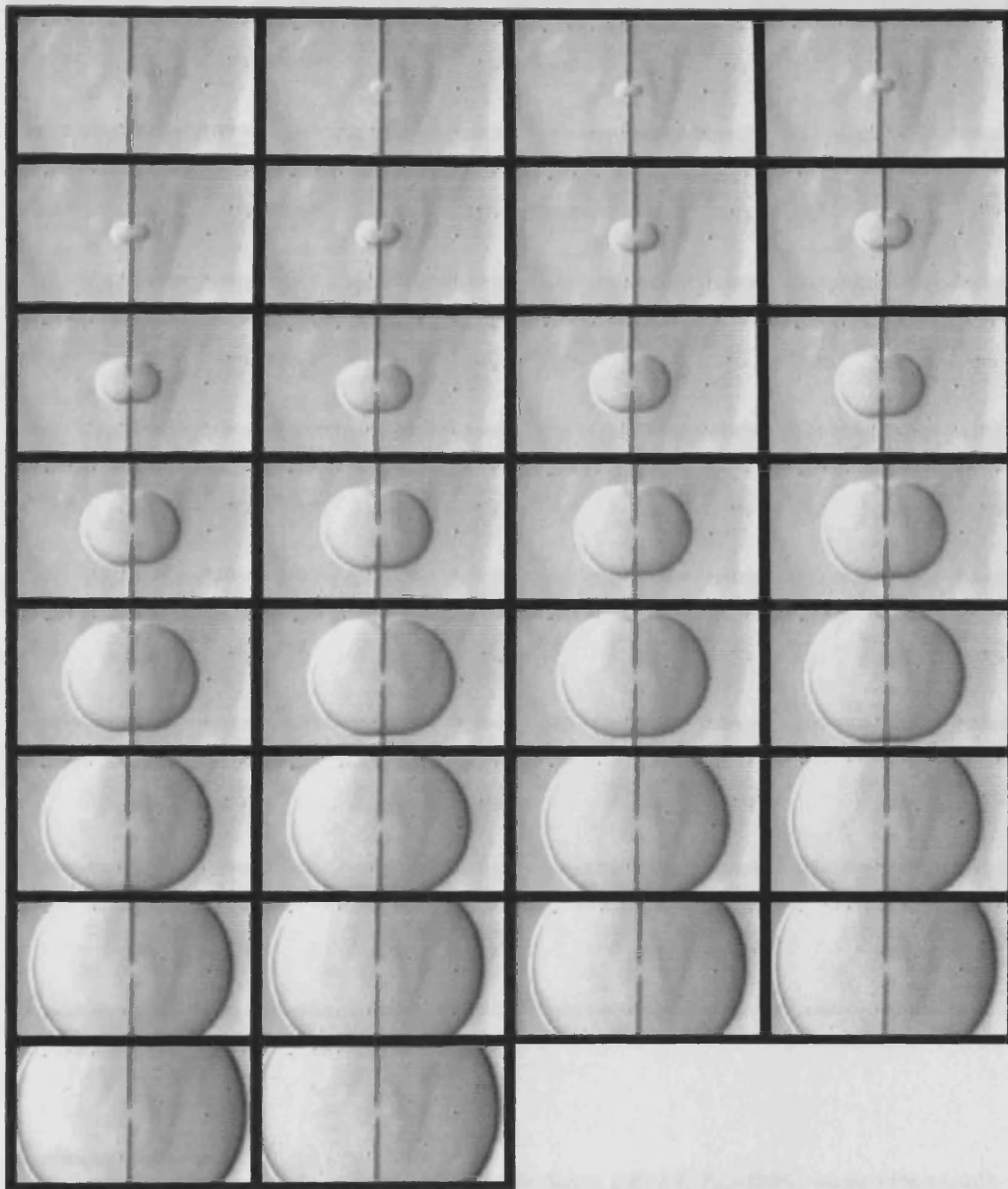
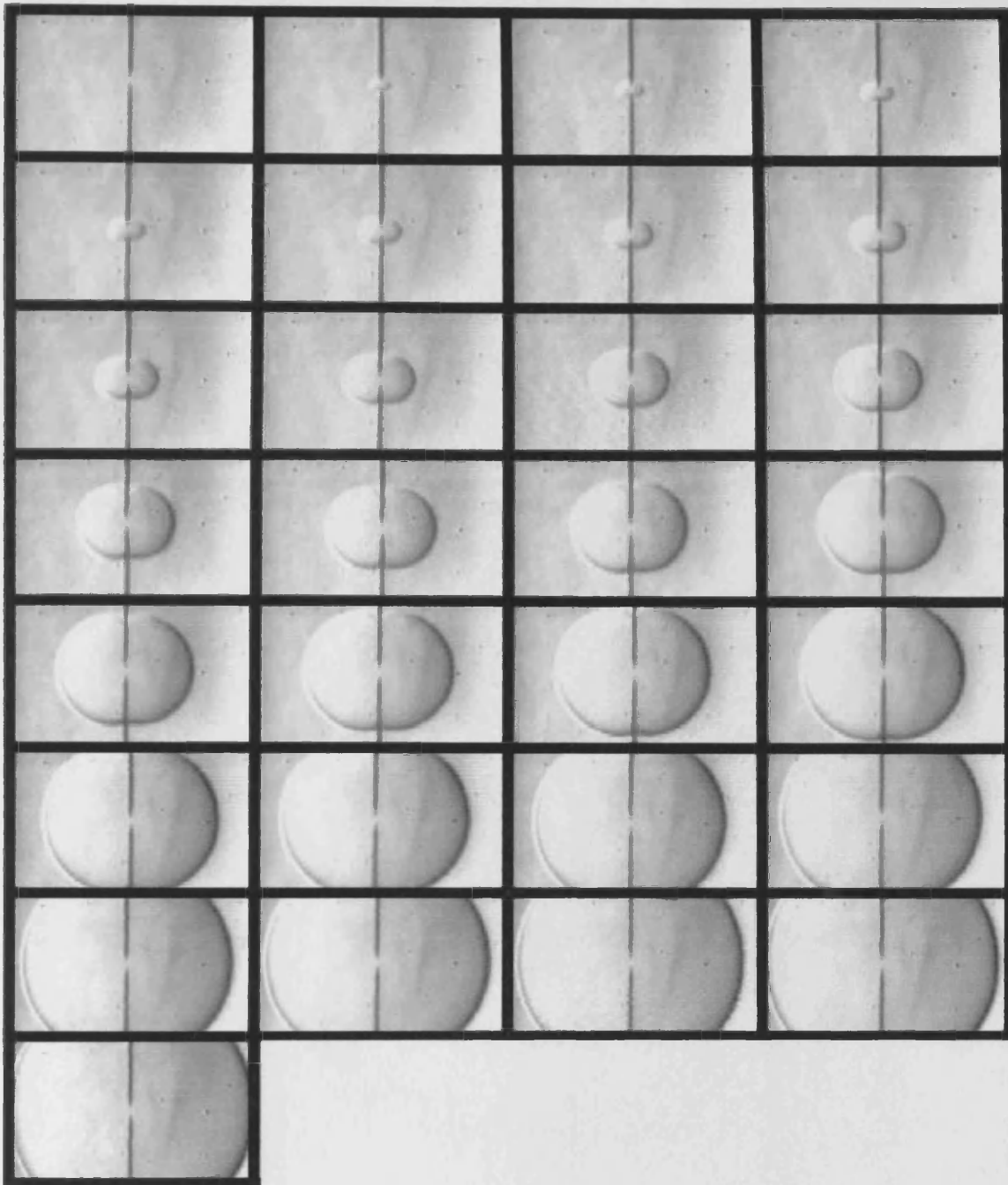


Figure C5.1 Flame growth of methane-water-air flame,  $ER=0.8$ ,  $T_{rig}=100^{\circ}\text{C}$ , water 15% vapour, 1000fps



**Figure C5.2** *Flame growth of methane-water-air flame,  $ER=1.0$ ,  $T_{rig}=100^{\circ}\text{C}$ , water 15% vapour, 1000fps*



**Figure C5.3** *Flame growth of methane-water-air flame,  $ER=1.1$ ,  $T_{rig}=100^{\circ}\text{C}$ , water 15% vapour, 1000fps*

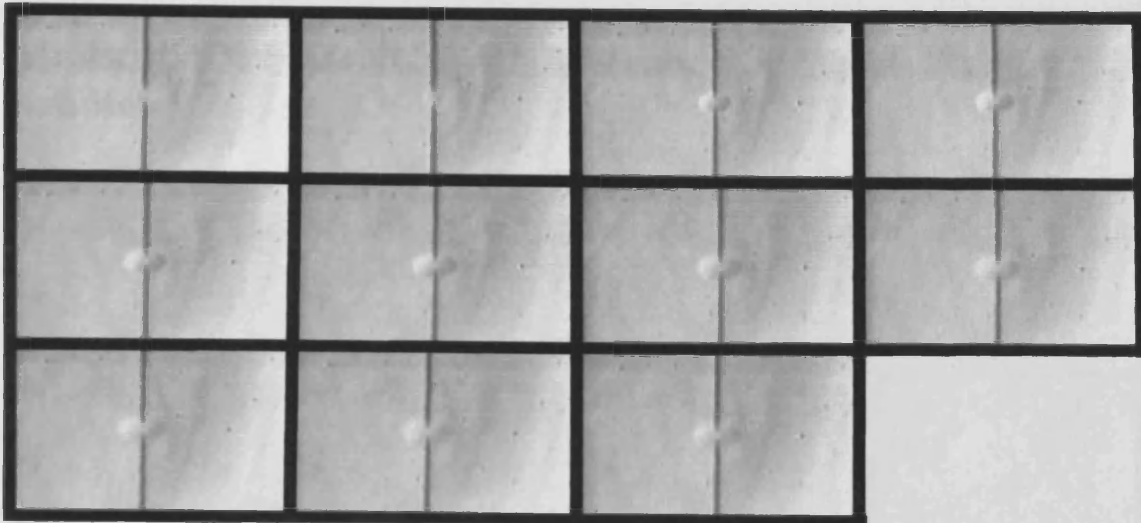


**Figure C5.4** *Flame growth of methane-water-air flame,  $ER=1.2$ ,  $T_{rig}=100^{\circ}C$ , water 15% vapour, 1000fps*

## Appendix D: Flame Growth Methane-Air-Water Flames Droplets

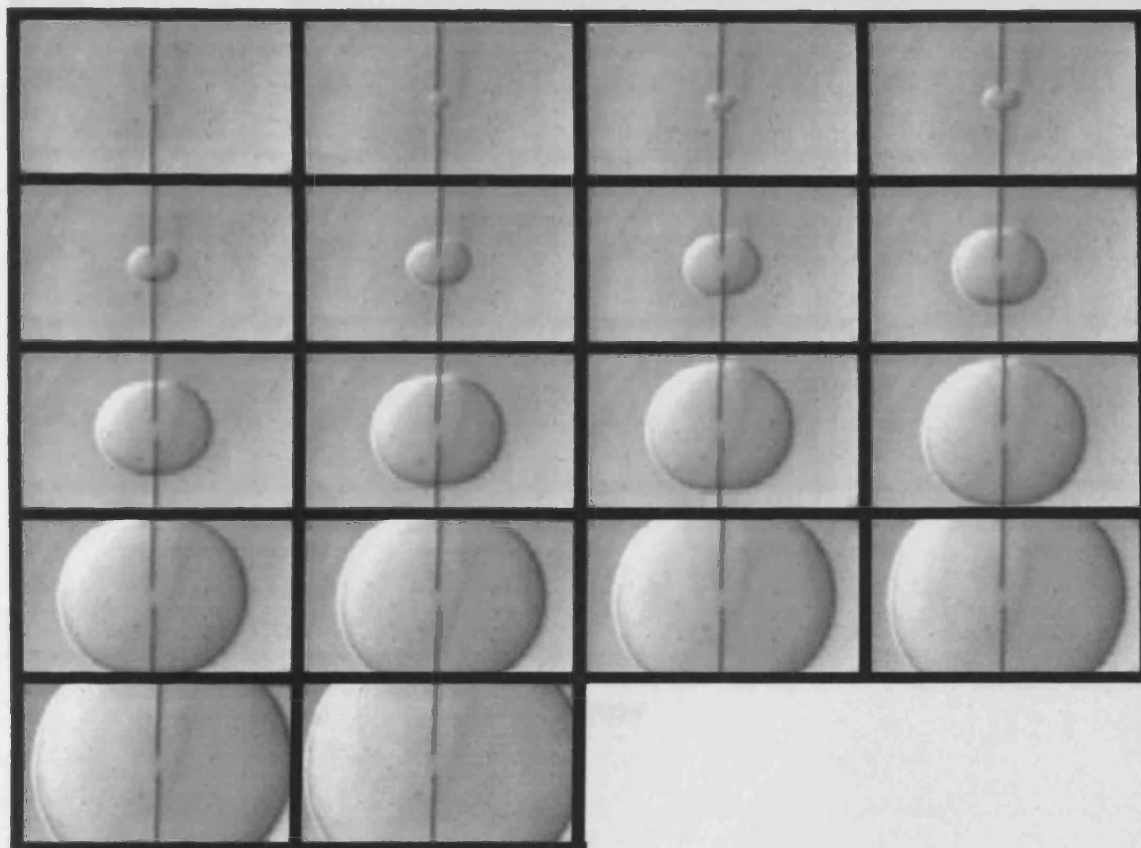
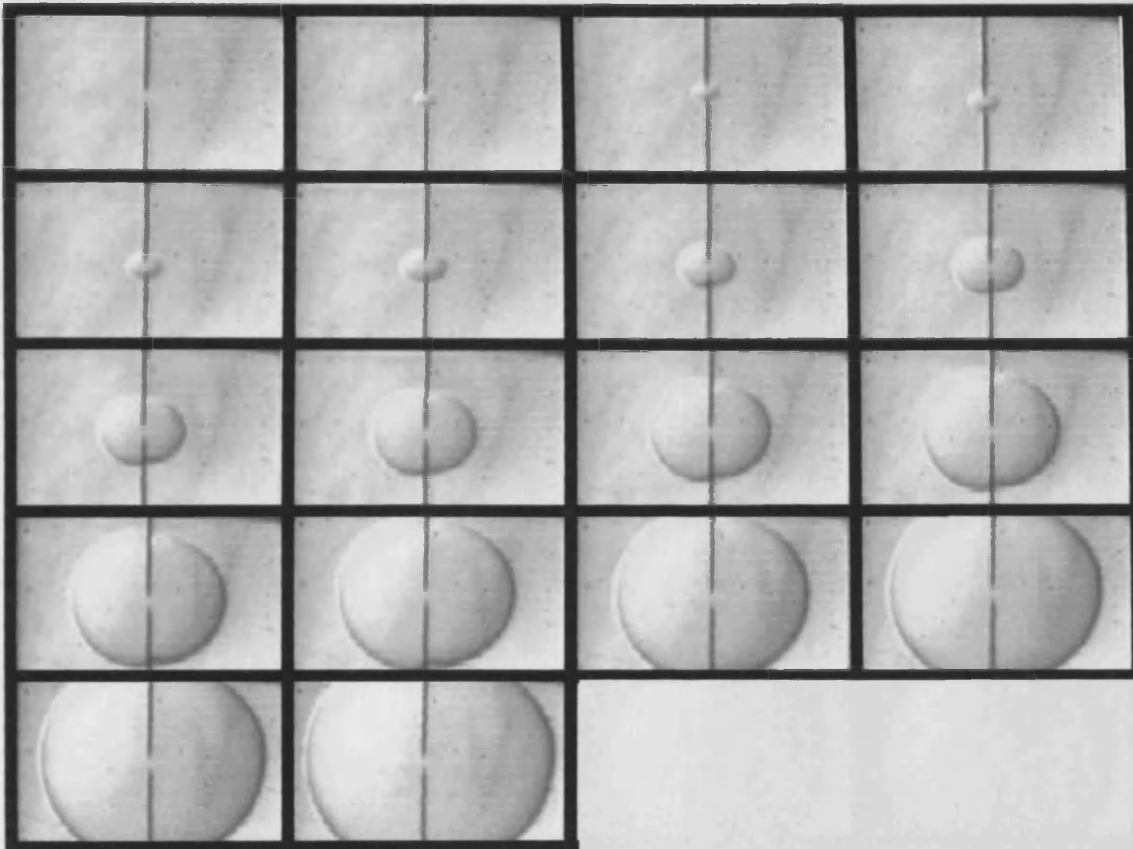
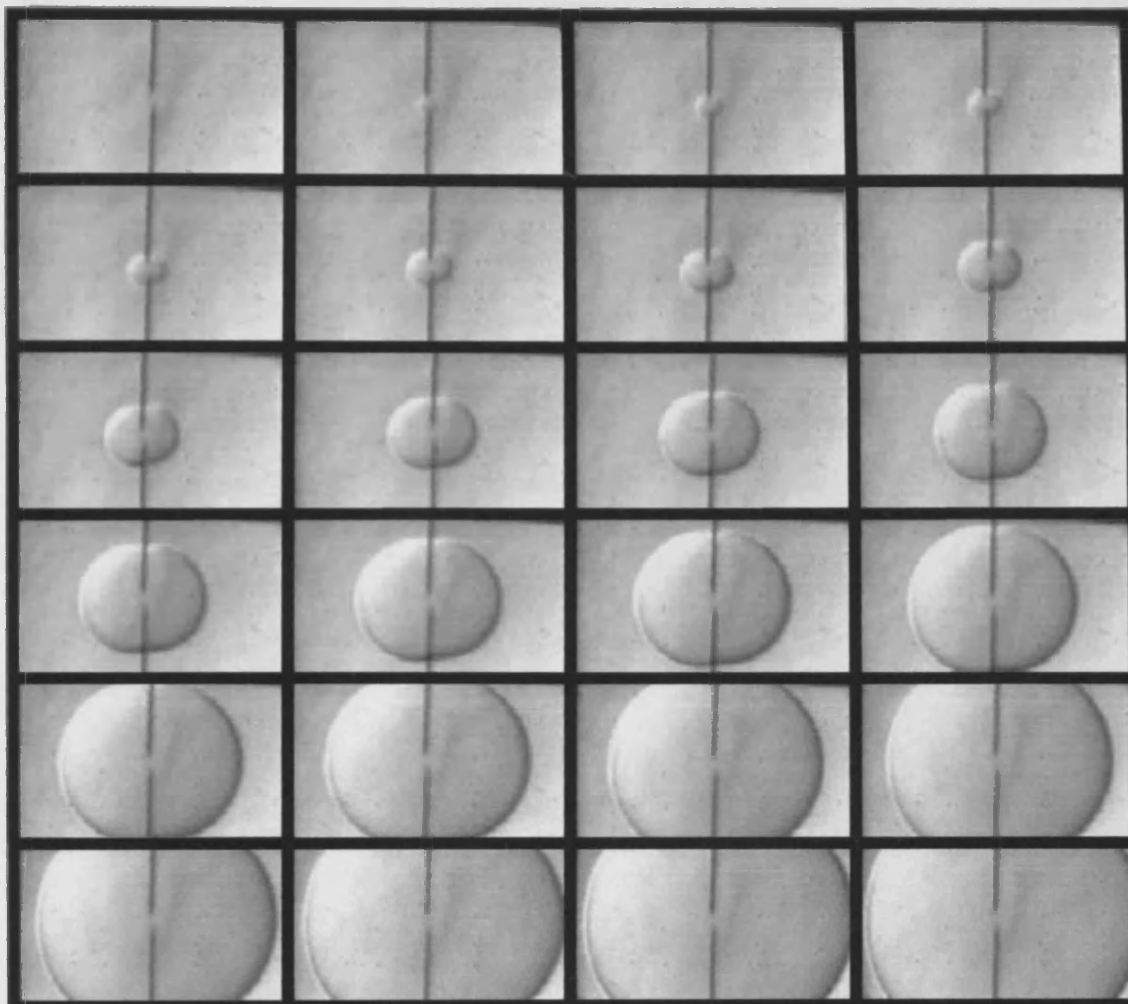


Figure D1.1 *Flame growth of methane-water-air flame,  $ER=1.0$ ,  $T_{rig}=34^{\circ}C$ , water 5%, 20µm-droplets, 1000fps*



**Figure D1.2** *Flame growth of methane-water-air flame,  $ER=1.0$ ,  $T_{rig}=34^{\circ}C$ , water 5%,  $10\mu m$ -droplets, 1000fps*



**Figure D2.1** *Flame growth of methane-water-air flame,  $ER=1.0$ ,  $T_{rig}=48^{\circ}C$ , water 10%, 15 $\mu$ m-droplets, 1000fps*

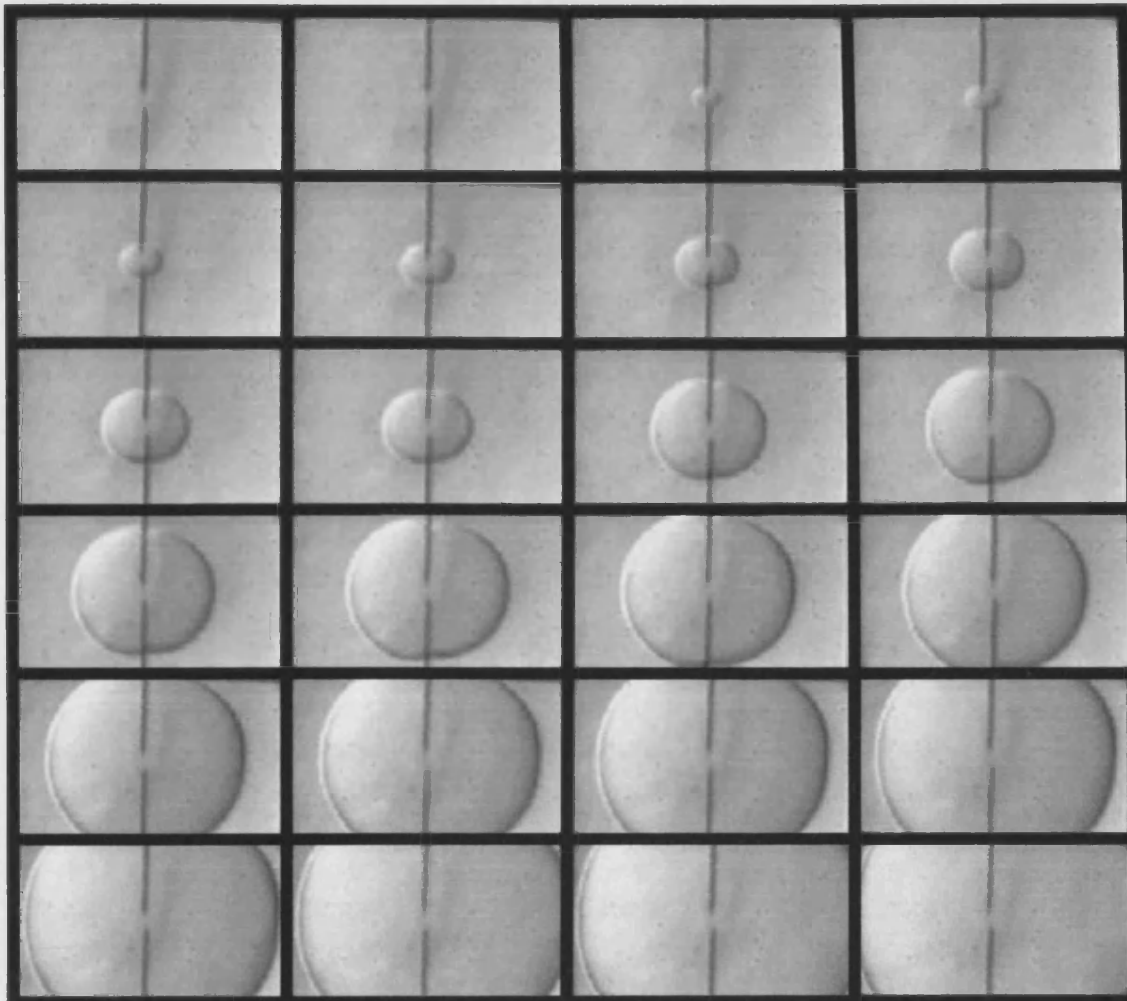


Figure D2.21 *Flame growth of methane-water-air flame,  $ER=1.0$ ,  $T_{rig}=48^{\circ}\text{C}$ , water 10%,  $5\mu\text{m}$ -droplets, 1000fps*

